ISSN 2074-272X

науково-практичний журнал

2025/1

Електротехніка і Електромеханіка

Electrical Engineering & Electromechanics

Електротехнічні комплекси та системи
Теоретична електротехніка
Техніка сильних електричних та магнітних полів, інженерна електрофізика

Журнал включено до найвищої категорії «А» Переліку фахових видань України

З 2019 р. журнал індексується у Scopus

З 2015 р. журнал індексується у Web of Science Core Collection: Emerging Sources Citation Index

Electrical Engineering & Electromechanics

Scientific Journal was founded in 2002
Co-founders: National Technical University «Kharkiv Polytechnic Institute» (Kharkiv, Ukraine);
Anatolii Pidhornyi Institute of Power Machines and Systems of NAS of Ukraine (Kharkiv, Ukraine)

From no. 1 2019 Journal «Electrical Engineering & Electromechanics» is indexing in **Scopus**
and from no. 1 2015 Journal is indexing in **Web of Science Core Collection: Emerging Sources Citation Index (ESCI)**
Also included in DOAJ (Directory of Open Access Journals), in EBSCO's database, in ProQuest's databases – Advanced Technologies & Aerospace Database and Materials Science & Engineering Database, in Gale/Cengage Learning databases.

Editorial office address:
National Technical University «Kharkiv Polytechnic Institute», Kyrpychova Str., 2, Kharkiv, 61002, Ukraine
phone: +380 67 3594696, **e-mail:** a.m.grechko@gmail.com (**Grechko O.M.)**
ISSN (print) 2074-272X
ISSN (online) 2309-3404

Approved for printing on 28 December 2024. Format 60 × 90 ⅛. Paper – offset. Laser printing. Edition 50 copies.
Printed by Printing house «Madrid Ltd» (18, Gudanova Str., Kharkiv, 61024, Ukraine)

Electrical Engineering & Electromechanics
Scientific Journal

no. 1, 2025

Table of Contents

Electrotechnical Complexes and Systems

Theoretical Electrical Engineering

High Electric and Magnetic Fields Engineering, Engineering Electrophysics

UDC 621.3.013 https://doi.org/10.20998/2074-272X.2025.1.01

I.I. Alnaib, A.N. Alsammak

Optimization of fractional PI controller parameters for enhanced induction motor speed control via indirect field-oriented control

Introduction. *Induction Motors (IM) possess advantages such as stability, reliability, and ease of control, making them suitable for many purposes; the literature elucidates control methodologies for IM drives, primarily focusing on scalar and vector control techniques; the conventional method utilized in manufacturing is scalar control, which unfortunately demonstrates optimal performance solely in steady-state conditions. The absence of significant instantaneous torque control restricts flux and dissociated torque, resulting in subpar dynamic responsiveness. Indirect Field Oriented Control (IFOC) for IM drives has proven beneficial for various industrial applications, particularly electric vehicle propulsion. The primary advantages of this approach include the decoupling of torque and flux characteristics and its straightforward implementation.* ***The novelty*** *of the work consists of a proposal for a driving cycle model for testing the control system of electric vehicles in Mosul City (Iraq), and using a Complex Fractional Order Proportional Integral (CFOPI) controller to control IMs via IFOC strategies, the Artificial Bee Colony (ABC) algorithm was applied, which is considered to be highly efficient in finding the values of controllers.* ***Purpose.*** *Improvement IFOC techniques for the regulation of IM speed.* ***Methods.*** *Using the ABC algorithm in tuning the two unique CFOPI controller, and a Real Fractional Order Proportional Integral (RFOPI) controller, to regulate the speed of a three-phase IM via IFOC techniques.* ***Results.*** *The CFOPI controller outperforms the RFOPI controller in obtaining the best performance in controlling the IM.* ***Practical valu****e. The CFOPI controller demonstrates superiority over the RFOPI controller, as evidenced by the lower integral time absolute error in motor speed tracking during the driving cycle 2.1004 for the CFOPI controller compared to 2.1538 for the RFOPI controller.* References 27, tables 5, figures 4.

Key words: **complex fractional order proportional integral controller, real fractional order proportional integral controller, artificial bee colony algorithm, indirect field oriented control.**

Вступ*. Асинхронні двигуни (АД) мають такі переваги, як стабільність, надійність і легкість керування, що робить їх придатними для багатьох цілей; література пояснює методології керування приводами АД, головним чином зосереджуючись на методах скалярного та векторного керування; звичайний метод, який використовується у виробництві, – це скалярне керування, яке, на жаль, демонструє оптимальну продуктивність лише в стаціонарних умовах. Відсутність значного миттєвого контролю крутного моменту обмежує потік і дисоційований крутний момент, що призводить до низької динамічної чутливості. Непряме поле-орієнтоване керування (IFOC) для приводів АД, довело свою користь для різноманітних промислових застосувань, зокрема для двигунів електромобілів. Основні переваги цього підходу включають відокремлення характеристик крутного моменту та потоку та його пряме впровадження.* ***Новизна*** *роботи полягає в пропозиції моделі циклу водіння для тестування системи керування електромобілями в місті Мосул (Ірак), і використання контролера комплексного дробового порядку пропорційного інтегралу (CFOPI) для керування АД за допомогою стратегій IFOC, було застосовано алгоритм штучної бджолиної колонії (ABC), який вважається високоефективним у пошуку значень контролерів.* ***Мета****. Удосконалення методики IFOC для регулювання швидкості АД.* ***Методи****. Використання алгоритму ABC для налаштування двох унікальних контролерів CFOPI та контролера реального дробового порядку пропорційного інтегралу (RFOPI) для регулювання швидкості трифазного АД за допомогою методів IFOC.* ***Результати****. Контролер CFOPI перевершує контролер RFOPI в отриманні найкращої продуктивності в управлінні АД.* ***Практична цінність****. Контролер CFOPI демонструє перевагу над контролером RFOPI, про що свідчить менша абсолютна похибка інтегрального часу у відстеженні швидкості двигуна під час циклу руху 2.1004 для контролера CFOPI порівняно з 2.1538 для контролера RFOPI.* Бібл. 27, табл. 5, рис. 4.

Ключові слова: **пропорційно-інтегральний контролер комплексного дробового порядку, пропорційно-інтегральний контролер дійсного дробового порядку, алгоритм штучної бджолиної колонії, непряме поле-орієнтоване керування.**

Introduction. Induction motors (IM) have advantageous characteristics like robustness, reliability, and ease of control, and are used in many different types of applications [1, 2]. These applications electric and hybrid vehicles, the literature clarified control methodologies for IM drives, predominantly encompassing scalar and vector control approaches [3, 4]. The lack of significant instantaneous torque control inhibits flux and dissociated torque, leading to suboptimal dynamic responsiveness [5]. In contrast, Field Oriented Control (FOC) regulates the frequency, amplitude, and instantaneous location of the flow linkage vectors of current and voltage [6, 7]. Therefore, it is effective for each stability and enhanced dynamic performance [8, 9]. The two fundamental groups of FOC methods are direct and indirect operations, defined by Blaschke in 1972 and Hasse in 1968, respectively [10].

The aim of the paper is using Indirect Field Oriented Control (IFOC) strategies for speed control of IM and decision the mathematical model of the system. Proposal for a driving cycle model for testing the control system of electric vehicles in Mosul City, Iraq. Applying the Artificial Bee Colony (ABC) algorithm to identify optimal certain elements for fractional order PI controllers.

Review of the literature. The authors compared the complex fractional order PI controller against the real fractional order PI controller to control the speed of the IM via the IFOC technique. The results showed that the Complex Fractional Order Proportional Integral (CFOPI) controller improved the Real Fractional Order Proportional Integral (RFOPI) controller by achieving a minimal error between the reference and actual speeds. Nevertheless, the controller variables were found by using trial and error [11]. The research presented here differentiates between the two different RFOPI speed controllers (FOPI and FO[PI]) of the IM drive. The results show the superiority of the FO[PI] controller compared to the FOPI and integer order PI under identical stability boundary constraints [12]. This study elucidates the use of Particle Swarm Optimization (PSO), Teaching Learning Based Optimization (TLBO) and Jaya optimization algorithms for the calibration of PI and RFOPI controllers employed in the IM driving model with comparison of the results from the aforementioned optimization. This indicates that Jaya yields superior reduction outcomes compared to the other two strategies [13]. An intelligent hybrid control system for scalar IM control use ANFIS optimization [14]. This study confirms the efficacy as well as the upside of a CFOPI model for ascertaining the parameters of a PID controller that manages the common rail tension in the injection system of a compressed fossil fuel engine. Parameters are derived by PSO process that

integrates a cost factor evaluating effectiveness and reliability metrics [15]. A review of previous work in the field indicates that a few researchers have used CFOPI controllers to control IMs via IFOC strategies. Those who have investigated this type of controller utilized the trial and error method to ascertain optimal parameter values.

Materials and methods. The control architecture of IFOC (Fig. 1) is a vector control method widely accepted in high performance drive vehicles. The theory fundamentally relies on decoupling flux and torque by regulating the stator current component [16, 17]. The components of the control circuit in Fig. 1 are next [2, 18]: R_r is the rotor resistance, L_r is the rotor self-inductance, T_m is the electromagnetic torque, p is the number of pole pairs, L_m is the magnetizing inductance, ψ_{dr} is the rotor flux, ω is the angular frequency, I_{abc} is the IM current, i_d, i_q are the rotating currents in d-q axis; ω_r is the IM angular speed.

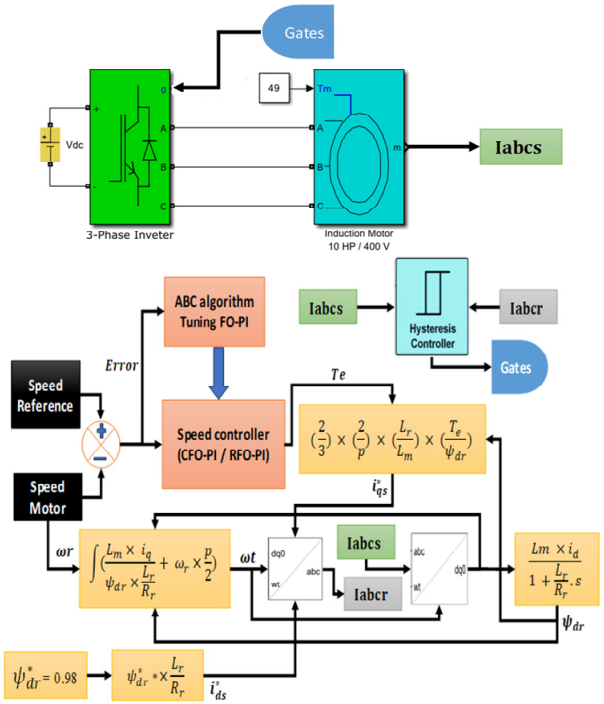

Fig. 1.The control architecture of IFOC of IM

Types of FOPI controllers. FOPI controllers are extensively utilized in various control projects to attain accurate system efficiency [19]. The bulk of the controllers possess real and complex components with fractional order integrals [20].

The general CFOPI controller is represented as [21, 22]:

$$G_c(s) = K_p + K_i \cdot \left(\frac{1}{s}\right)^{\alpha+j\beta}, \quad (1)$$

where K_p is the proportional value; K_i is the integral value; α, β are the non integer number (fractional values); s is the fractional operator.

The complex integrator can be written as:

$$\left(\frac{1}{s}\right)^{\alpha+j\beta} = \left(\frac{1}{s}\right)^{\alpha} \cdot \left(\frac{1}{s}\right)^{j\beta}; \quad (2)$$

$$\left(\frac{1}{s}\right)^{\alpha+j\beta} = \left(\frac{1}{s}\right)^{\alpha} \cdot e^{j\beta \ln\left(\frac{1}{s}\right)}; \quad (3)$$

$$\left(\frac{1}{s}\right)^{\alpha+j\beta} = \left(\frac{1}{s}\right)^{\alpha} \cdot \left(\cos\left(\beta \ln\left(\frac{1}{s}\right)\right) + j\sin\left(\beta \ln\left(\frac{1}{s}\right)\right)\right). \quad (4)$$

If the complex operator is applied to a real input it will result in a complex response. So, in practice, it is realized by extracting the real part. The transfer function of CFOPI controller denoted as [23]:

$$\left(\frac{1}{s}\right)^{\alpha+j\beta} = \left(\frac{1}{s}\right)^{\alpha} \cdot \cos\left(\beta \ln\left(\frac{1}{s}\right)\right). \quad (5)$$

According to (1), when the real and imaginary parts are fractional values, the transfer function of the fractional controller has a real and imaginary form, as expressed as:

$$CFOPI(s) = K_p + K_i \cdot \left(\frac{1}{s}\right)^{\alpha} \cdot \cos\left(\beta \ln\left(\frac{1}{s}\right)\right). \quad (6)$$

The transfer function of RFOPI controller is:

$$RFOPI(s) = K_p + K_i \cdot \left(\frac{1}{s}\right)^{\alpha}. \quad (7)$$

According to (1), when the imaginary component is null, the transfer function of the fractional controller has a real style, as articulated in the subsequent equation:

ABC algorithm is engineered to mimic the actions of wild bees to get best solutions for constrained scenarios. The core ABC idea comprises 3 categories of bees: worker bees, spectator bees and spy bees. 50 % of the swarm consists of hired bees, while the other 50 % consists of observation bees. Just one artificial hired bee is supposed to exist for each food source [24]. The quantity of worker bees in the group correlates with the food sources in proximity to the hive. Foraging bees access their food supply and thereafter return to the hive to perform a dance in this area. The employed bee that has forsaken its food reserve metamorphoses into a scout and starts the search for a fresh source of food. Scouts methodically investigate their environment to identify a novel food source, driven by personal motivation, environmental indicators, or serendipity. Onlooker bees stay within the hive and assess which kind of food to utilize depending on the knowledge supplied by forager bees [25]. Table 1 explains the parameters of ABC algorithm.

Table 1

Selection of the settings for the ABC algorithm

Parameters	Values
No. of bees and limit	15 and 30
No. of food sources	Round (no. of bees/2)
Population size and iteration number	15 and 15
Range of K_P and K_i	$0 \le K_P \le 200$ and $0 \le K_i \le 200$
Range of real and imaginary part of CFO-PI controller	$0 \le \alpha \le 1$ and $0 \le \beta \le 1$

Driving cycle for Mosul City (Iraq). Definition of a driving cycle collection of data points illustrating vehicle speed in relation to time. Several driving cycles are employed globally for homologation, including the FTP-75 in the USA, the NEDC in Europe, and the J10-15 in Japan [26]. These cycles frequently encompass additional sub phases designed to illustrate low and high speed sequences or various driving environments such as urban, rural or freeway settings [27]. The proposed driving model was used to test the best type of fractional PI controllers and find the most efficient controller for tracking the required speeds of Mosul City's driving cycle. The proposed driving cycle includes reversing the electric vehicle's speed. The characteristics of the Mosul driving cycle the test duration is 12 min (Fig. 2). The load of 7.46 kW is kept constant during the driving cycle's execution and consists of the following durations as detailed in Table 2.

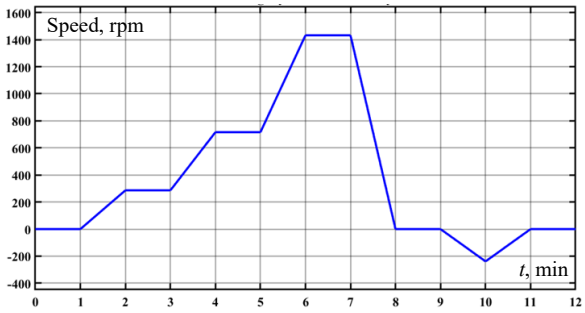

Fig. 2. Mosul City driving cycle

Table 2

Clarify the features of the driving cycle test for a control system in an electric vehicle

Duration, min	Speed case, rpm	Duration, min	Speed case, rpm
[0–1]	Turn off speed	[7–8]	Decrease speed (breaking mode) [1432–0]
[1-2]	Increase speed [0–286]	[8–9]	Turn off speed
[2–3]	Constant at 286	[9–10]	Reverse speed direction [0–238]
[3–4]	Increase speed [286–716]	[10–11]	Decrease speed [238–0]
[4–5]	Constant at 716	[11–12]	Turn off speed
[5–6]	Increase speed [716–1432]		
[6–7]	Constant at 1432		

Simulation and results. This section shows the simulation method for controlling the speed of an electric vehicle using a three-phase IM, which parameters are shown in Table 3.

Table 3

Parameters of the IM

Parameters	Value
Rated power P, HP	10
Voltage V, V	400
Frequency f, Hz	50
Angular speed ω_r, rpm	1440
Stator resistance R_s, Ω	0.7384
Stator self-inductance L_s, mH	3.045
Rotor resistance R_r, Ω	0.7402
Rotor self-inductance L_r, mH	3.045
Magnetizing inductance L_m, H	0.1241
Inertia J, kg·m^2	0.0343
Friction factor F, N·m·s	0.000503
Number of pole pairs p	2

It implements an IFOC technique with the proposed FOPI controller types. For an electric vehicle was developed to examine the different kinds of FOPI controllers by using performance Integral Time Absolute Error (ITAE) index:

$$ITAE = \int_0^t t \cdot \left| error(t) \mathrm{d}t \right|. \quad (8)$$

The performance index showed that the CFOPI controller outperformed the RFOPI controller in obtaining the best results in tracking the driving cycle signal with the slightest error. Table 4 shows the parameters of all FOPI types by tuning ABC algorithm and identify the optimal variant, reflecting the characteristics of the roadways in Mosul (Iraq).

Table 4

Tuning the all types of FOPI controller using ABC algorithm

Controller types	Transfer function	ITAE
CFOPI	$62.928 + 200 \cdot \left(\frac{1}{s}\right)^{0.982 + j0.587}$	2.1004
RFOPI	$59.724 + 198.565 \cdot \left(\frac{1}{s}\right)^{0.9}$	2.1538

Figure 3 shows the IM characteristics, when Mosul driving cycle is applied to the IM using the CFOPI controller by tuning parameters ABC algorithm.

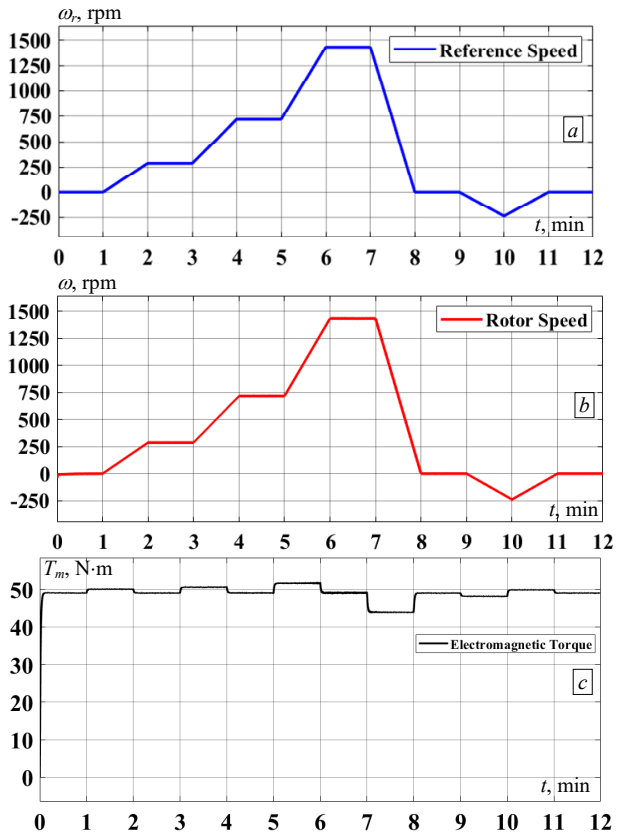

Fig. 3. The driving cycle response of the IM using the CFOPI controller: *a* – driving cycle reference; *b* – driving cycle of rotor speed IM; *c* – electromagnetic torque response

The different kinds of fractional controllers were evaluated using specific reference speeds (for lower-speed and high speed ranges) to facilitate a comparison among controllers. Table 5 indicates that the CFOPI controller surpassed the RFOPI controller, and Fig. 4 illustrates the time response for each reference speed.

Table 5

Comparison of fractional controllers at different reference speeds in terms of the time characteristics of the speed response

Types of FOPI controller	Speed reference, rpm	Overshoot, %	Peak time, s	Settling time, s	Steady state error, %
RFOPI	250	8	0.012	0.13	0
	750	5.6	0.016	0.717	0
	1200	5.67	0.024	0.95	0
	1440	6.18	0.068	0.98	0
CFOPI	250	7.6	0.012	0.12	0
	750	4	0.016	0.4	0
	1200	3.66	0.024	0.74	0
	1440	3.95	0.074	0.92	0

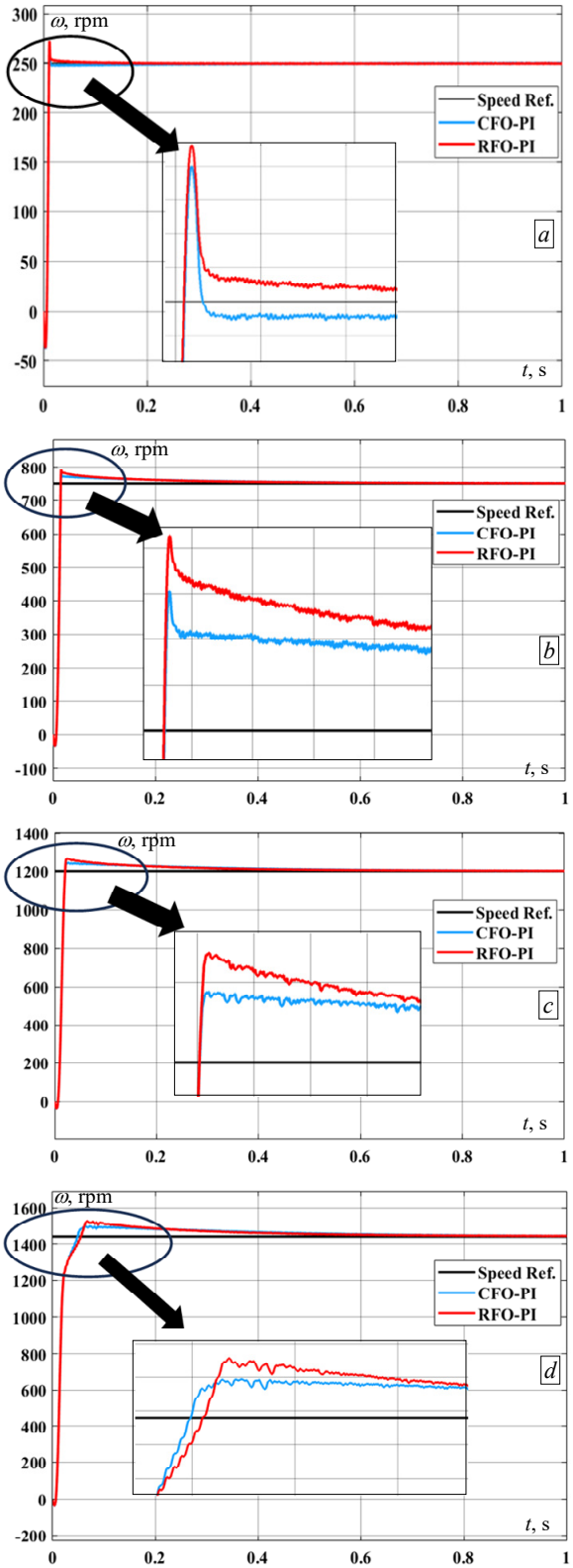

Fig. 4. Speed response of IM by CFOPI and RFOPI controllers for speed references:
a – 250 rpm; *b* – 750 rpm; *c* – 1200 rpm; *d* – 1440 rpm

Conclusions. IFOC strategy that uses 2 types of fractional controllers was used to control the speed of the three-phase IM via the voltage source inverter circuit, where the firing signal is generated using the hysteresis current method. It is comparative between the proposed controllers using the proposed driving cycle for the city of Mosul (Iraq), which includes several levels of speed values in both directions. And the other pattern is different reference speed levels, where low and high speeds were chosen in order to cover all cases of speed to using the IM in electric vehicle and using the ABC algorithm to find the parameters of the controllers through the results of the simulation turns out the superiority the CFOPI controller over the RFOPI controller, where the lowest ITAE in tracking the motor speed for driving cycle for the CFOPI controller is 2.1004, for the RFOPI controller is 2.1538.

The superiority of the CFOPI controller over the RFOPI controller where the overshoot in speed the limit that is considered one of the most. Important factor to speed control where the controller was CFOPI (7.6 %) and RFOPI (8 %) for reference speed 250 rpm; at reference speed 750 rpm (4 %) and (5.6 %), for 1200 rpm was (3.66 %) and (5.67 %) and for 1440 rpm was (3.95 %) and (6.18 %) respectively.

Acknowledgements. The authors would like to sincerely thank the College of Engineering Department of Electrical at the University of Mosul for the tremendous help they provided during this work.

Conflict of interest. The authors declare that there is no conflict of interest.

REFERENCES

1. Alitasb G.K. Integer PI, fractional PI and fractional PI data trained ANFIS speed controllers for indirect field oriented control of induction motor. *Heliyon*, 2024, vol. 10, no. 18, art. no. e37822. doi: https://doi.org/10.1016/j.heliyon.2024.e37822.

2. Nemouchi B., Rezgui S.E., Benalla H., Nebti K. Fractional-based iterative learning-optimal model predictive control of speed induction motor regulation for electric vehicles application. *Electrical Engineering & Electromechanics*, 2024, no. 5, pp. 14-19. doi: https://doi.org/10.20998/2074-272X.2024.5.02.

3. Adamczyk M., Orlowska-Kowalska T. Postfault Direct Field-Oriented Control of Induction Motor Drive Using Adaptive Virtual Current Sensor. *IEEE Transactions on Industrial Electronics*, 2022, vol. 69, no. 4, pp. 3418-3427. doi: https://doi.org/10.1109/TIE.2021.3075863.

4. Adigintla S., Aware M.V. Robust Fractional Order Speed Controllers for Induction Motor Under Parameter Variations and Low Speed Operating Regions. *IEEE Transactions on Circuits and Systems II: Express Briefs*, 2023, vol. 70, no. 3, pp. 1119-1123. doi: https://doi.org/10.1109/TCSII.2022.3220526.

5. Ndiaye A., German R., Bouscayrol A., Gaetani-Liseo M., Venet P., Castex E. Impact of the User Charging Practice on the Battery Aging in an Electric Vehicle. *IEEE Transactions on Vehicular Technology*, 2024, vol. 73, no. 4, pp. 4578-4588. doi: https://doi.org/10.1109/TVT.2024.3356116.

6. Adigintla S., Aware M.V., Bingi K., Das S. Novel Complex Fractional Order Speed Controller for IM Drive Under Varying Operating Conditions With Enhanced Robustness. *IEEE Transactions on Industrial Electronics*, 2024, vol. 71, no. 8, pp. 8438-8447. doi: https://doi.org/10.1109/TIE.2023.3314864.

7. Alsammak A.N.B., Al-Kaoaz H.N.A. Design of a fuzzy distance relay taking into consideration the impact of using a unified power flow controller. *Eastern-European Journal of Enterprise Technologies*, 2023, vol. 2, no. 5 (122), pp. 6-19. doi: https://doi.org/10.15587/1729-4061.2023.277343.

8. Altamura A., Lino P., Maione G., Kapetina M., Rapaic M.R., Jelicic Z.D. On PID Controllers for a Complex-Order Fractional Model of an Automotive Injection System. *IFAC-PapersOnLine*, 2024, vol. 58, no. 12, pp. 119-124. doi: https://doi.org/10.1016/j.ifacol.2024.08.177.

9. Alsammak A.N.B., Ghanim A.S. Performance Enhancement and Assessment of the Dual Stator Induction Motor. *Przegląd Elektrotechniczny*, 2023, no. 10, pp. 171-177. doi: https://doi.org/10.15199/48.2023.10.33.

10. Blaschke F. The Principle of Field Orientation as Applied to the NEW Transvector Closed-Loop System for Rotating-Field Machines. *Siemens Review*, 1972, vol. 34, no. 3, pp. 217-220.

11. Gomes R.R., Pugliese L.F., Silva W.W.A.G., Sousa C.V., Rezende G.M., Rodor F.F. Speed Control with Indirect Field Orientation for Low Power Three-Phase Induction Machine with Squirrel Cage Rotor. *Machines*, 2021, vol. 9, no. 12, art. no. 320. doi: https://doi.org/10.3390/machines9120320.
12. Kumar D.M., Mudaliar H.K., Cirrincione M., Mehta U., Pucci M. Design of a Fractional Order PI (FOPI) for the Speed Control of a High-Performance Electrical Drive with an Induction Motor. *2018 21st International Conference on Electrical Machines and Systems (ICEMS)*, pp. 1198-1202. doi: https://doi.org/10.23919/ICEMS.2018.8549407.
13. Raj A., Khan Y.A., Verma V. Comparative Evaluation of PSO, TLBO, and JAYA based Adaptive PI and FOPI Controllers for Vector Controlled Induction Motor Drive. *2021 IEEE 4th International Conference on Computing, Power and Communication Technologies (GUCON)*, pp. 1-6. doi: https://doi.org/10.1109/GUCON50781.2021.9573705.
14. Mohammed H.A., Alsammak A.N.B. An Intelligent Hybrid Control System using ANFIS-Optimization for Scalar Control of an Induction Motor. *Journal Européen Des Systèmes Automatisés*, 2023, vol. 56, no. 5, pp. 857-862. doi: https://doi.org/10.18280/jesa.560516.
15. Sayed S., Elmenshawy M., Elmenshawy M., Bader Q., Iqbal A. Comparison of Direct Torque Control and Indirect Field-Oriented Control for Three-Phase Induction Machine. *Lecture Notes in Electrical Engineering*, 2021, vol. 723 LNEE, pp. 131-141. doi: https://doi.org/10.1007/978-981-33-4080-0_13.
16. Wang H., Yang Y., Ge X., Zuo Y., Yue Y., Li S. PLL- and FLL-Based Speed Estimation Schemes for Speed-Sensorless Control of Induction Motor Drives: Review and New Attempts. *IEEE Transactions on Power Electronics*, 2022, vol. 37, no. 3, pp. 3334-3356. doi: https://doi.org/10.1109/TPEL.2021.3117697.
17. Abed K., Zine H.K.E. Intelligent fuzzy back-stepping observer design based induction motor robust nonlinear sensorless control. *Electrical Engineering & Electromechanics*, 2024, no. 2, pp. 10-15. doi: https://doi.org/10.20998/2074-272X.2024.2.02.
18. Ghanim A.S., Alsammak A.N.B. Modelling and simulation of self-excited induction generator driven by a wind turbine. *Eastern-European Journal of Enterprise Technologies*, 2020, vol. 6, no. 8 (108), pp. 6-16. doi: https://doi.org/10.15587/1729-4061.2020.213246.
19. Amieur T., Taibi D., Kahla S., Bechouat M., Sedraoui M. Tilt-fractional order proportional integral derivative control for DC motor using particle swarm optimization. *Electrical Engineering & Electromechanics*, 2023, no. 2, pp. 14-19. doi: https://doi.org/10.20998/2074-272X.2023.2.03.
20. Wang J., Du C., Yan F., Duan X., Hua M., Xu H., Zhou Q. Energy Management of a Plug-in Hybrid Electric Vehicle Using Bayesian Optimization and Soft Actor-Critic Algorithm. *IEEE Transactions on Transportation Electrification*, 2024, pp. 1-1. doi: https://doi.org/10.1109/TTE.2024.3398046.
21. Warrier P., Shah P. Design of an Optimal Fractional Complex Order PID Controller for Buck Converter. *Journal of Robotics and Control (JRC)*, 2023, vol. 4, no. 3, pp. 243-262. doi: https://doi.org/10.18196/jrc.v4i3.17446.
22. Warrier P., Shah P. Fractional Order Control of Power Electronic Converters in Industrial Drives and Renewable Energy Systems: A Review. *IEEE Access*, 2021, vol. 9, pp. 58982-59009. doi: https://doi.org/10.1109/ACCESS.2021.3073033.
23. Zellouma D., Bekakra Y., Benbouhenni H. Field-oriented control based on parallel proportional–integral controllers of induction motor drive. *Energy Reports*, 2023, vol. 9, pp. 4846-4860. doi: https://doi.org/10.1016/j.egyr.2023.04.008.
24. Wang K., Li X., Gao L., Li P., Sutherland J.W. A Discrete Artificial Bee Colony Algorithm for Multiobjective Disassembly Line Balancing of End-of-Life Products. *IEEE Transactions on Cybernetics*, 2022, vol. 52, no. 8, pp. 7415-7426. doi: https://doi.org/10.1109/TCYB.2020.3042896.
25. Yao G., Wu Y., Huang X., Ma Q., Du J. Clustering of Typical Wind Power Scenarios Based on K-Means Clustering Algorithm and Improved Artificial Bee Colony Algorithm. *IEEE Access*, 2022, vol. 10, pp. 98752-98760. doi: https://doi.org/10.1109/ACCESS.2022.3203695.
26. Wang Z., Song C., Zhang L., Zhao Y., Liu P., Dorrell D.G. A Data-Driven Method for Battery Charging Capacity Abnormality Diagnosis in Electric Vehicle Applications. *IEEE Transactions on Transportation Electrification*, 2022, vol. 8, no. 1, pp. 990-999. doi: https://doi.org/10.1109/TTE.2021.3117841.
27. Da Silva D.C., Kefsi L., Sciarretta A. Closed-Form Expression to Estimate the Hydrogen Consumption of a Fuel Cell Hybrid Electric Vehicle. *IEEE Transactions on Vehicular Technology*, 2024, vol. 73, no. 4, pp. 4717-4728. doi: https://doi.org/10.1109/TVT.2024.3350351.

Received 01.11.2024
Accepted 06.12.2024
Published 02.01.2025

I.I. Alnaib[1]*, MSc., Lecturer,*
A.N. Alsammak[1]*, PhD, Professor,*
[1] Electrical Engineering Department,
College of Engineering, University of Mosul, Iraq,
e-mail: ibrahim-85353@uomosul.edu.iq (Corresponding Author);
ahmed_alsammak@uomosul.edu.iq

How to cite this article:
Alnaib I.I., Alsammak A.N. Optimization of fractional PI controller parameters for enhanced induction motor speed control via indirect field-oriented control. *Electrical Engineering & Electromechanics*, 2025, no. 1, pp. 3-7. doi: https://doi.org/10.20998/2074-272X.2025.1.01

UDC 621.3 https://doi.org/10.20998/2074-272X.2025.1.02

B. Alouache, M. Helaimi, A.B. Djilali, H.A. Gabbar, H. Allouache, A. Yahdou

Optimal tuning of multi-stage PID controller for dynamic frequency control of microgrid system under climate change scenarios

Introduction. *In recent years, the use of renewable energy has become essential to preserve the climate from pollution and global warming. To utilize renewable energy more effectively, the microgrid system has emerged, which is a combination of renewable energies such as wind and solar power. However, due to sudden and random climate fluctuations, energy deviation and instability problems have arisen. To address this, storage systems and diesel engines have been incorporated. Nevertheless, this approach has led to another issue: frequency deviation in the microgrid system. Therefore, most recent studies have focused on finding ways to reduce frequency deviation. The* ***goal*** *of this work is to study and compare various improvement methods in terms of frequency deviation.* ***Methodology****. We first simulated the microgrid system using the PID controller based on the following algorithms: krill herd algorithm (KHA) and cuckoo search algorithm (CSA). In the second phase, we replaced the PID controller with the multi-stage PID controller and optimized its parameters using the KHA and the CSA. In the final phase, we tested the response of the microgrid system to these methods under a range of influencing factors.* ***Results.*** *The results initially showed the superiority of the KHA over the other algorithms in improving the parameters of the PID controller. In the second phase, the results showed a significant advantage of the multi-stage PID controller in terms of speed and stabilization time, as well as in reducing the frequency deviation compared to the PID controller.* ***Practical value****. Based on the tests conducted on the microgrid system, we can conclude that the multi-stage PID controller based on the KHA can be relied upon to solve these types of problems within the microgrid system.* References 36, tables 4, figures 10.

Key words: **microgrid, multi-stage PID controller, frequency control, renewable energy sources, krill herd algorithm, cuckoo search algorithm.**

Вступ*. В останні роки використання відновлюваної енергії стало необхідним для збереження клімату від забруднення та глобального потепління. Для більш ефективного використання відновлюваної енергії з'явилася система мікромереж, яка є комбінацією відновлюваних джерел енергії, таких як енергія вітру та сонця. Однак через раптові та випадкові коливання клімату виникли проблеми відхилення та нестабільності енергії. Для вирішення цієї проблеми були включені системи зберігання та дизельні двигуни. Проте цей підхід призвів до іншої проблеми: відхилення частоти в системі мікромереж. Тому більшість останніх досліджень було зосереджено на пошуку способів зменшення відхилення частоти.* ***Метою*** *роботи є вивчення і порівняння різних методів поліпшення з погляду відхилення частоти.* ***Методологія****. Спочатку ми змоделювали систему мікромереж з використанням ПІД-регулятора на основі наступних алгоритмів: алгоритм стада криля (KHA) та алгоритм пошуку зозулі (CSA). На другому етапі ми замінили ПІД-регулятор багатоступінчастим ПІД-регулятором та оптимізували його параметри з використанням KHA та CSA. На заключному етапі ми протестували реакцію мікромережевої системи на ці методи при низці факторів, що впливають.* ***Результати*** *спочатку показали перевагу KHA над іншими алгоритмами поліпшення параметрів ПІД-регулятора. На другому етапі результати показали значну перевагу багатоступеневого ПІД-регулятора з точки зору швидкості та часу стабілізації, а також зниження відхилення частоти в порівнянні з ПІД-регулятором.* ***Практична цінність****. На підставі випробувань, проведених на мікромережевій системі, ми можемо зробити висновок, що багатоступеневий ПІД-регулятор на основі KHA може бути використаний для вирішення цих типів проблем мікромережевої системи.* Бібл. 36, табл. 4, рис. 10.

Ключові слова: **мікромережа, багатоступеневий ПІД-регулятор, частотне керування, відновлювані джерела енергії, алгоритм стада крилів, алгоритм пошуку зозулі.**

Introduction. In recent decades, the world has observed an increase in the concentration of CO_2 in the atmosphere, which can be attributed to the heavy reliance on fossil fuels and their derivatives to meet energy needs. This pollution has a number of adverse effects, including detrimental impacts on human health and the climate. These include rising temperatures and an increase in the frequency of natural disasters [1]. Consequently, it has become imperative to identify sustainable solutions to eliminate traditional sources of pollution. One potential solution is to rely on renewable energy sources, such as wind and solar power. These sources are regarded as environmentally benign, pollution-free, widely accessible, and sustainable. Following the technological advancements in renewable energy sources, a novel concept has emerged: the microgrid. This is an innovative solution that integrates various renewable energy sources, in addition to storage systems. A microgrid is a small electrical system that can operate independently or in parallel with the main power grid. It can be argued that microgrid represent a significant advancement in the pursuit of sustainable and clean energy [2].

The primary challenge confronting the microgrid is the maintenance of frequency and energy stability, given the unpredictable random fluctuations in energy production from renewable sources. These results in an imbalance between the energy demand and the total energy produced. Consequently, storage systems for the microgrid, such as plug-in hybrid electric vehicle (PHEV), have become indispensable due to their efficacy in buffering and their capacity for rapid charging and efficient energy storage [3]. They function as reservoirs for storing energy and as energy suppliers in the event of a deficit in renewable energy sources to power the load. Nevertheless, this approach is not always secure or sustainable for supplying energy to the load [2], which is why a diesel generator (DEG) is added. Although it is a pollutant, it is considered the last resort when solar, wind energy, and storage batteries fail to supply the load with energy [3].

The proposed microgrid system in this study is comprised of a set of photovoltaic (PV) solar cells, wind turbine generators (WTG), and storage systems represented by PHEV [3]. The batteries are charged when there is a surplus of energy from renewable sources and are used to supply energy when there is a deficit from renewable sources to meet the load demand. Furthermore, DEG has been included to provide energy in the event that all

renewable energy sources fail to meet the load demand. This solution ensures that the microgrid used in this study can provide energy in all operating conditions [4, 5].

Once the energy supply for loads had been secured, a further issue emerged in the form of frequency deviation, which was caused by random climate fluctuations. Consequently, the majority of researchers have recently focused their attention on the development of control strategies for microgrid systems, employing a variety of controllers and adjusting their parameters through the use of different optimization algorithms. The PID controller has been employed in the majority of industrial applications, primarily due to its simplicity, reasonable cost, and desirable performance. PID controller based on the genetic algorithm has been studied for frequency deviation control in [6, 7] proposed optimizing the parameters of the PID controller using the grey wolf optimization. In [8] proposed optimizing the parameters of the PID controller based on the harmony search algorithm. In [9], frequency control in the microgrid was achieved using the PID controller based on the fruit fly algorithm. In [10] was proposed to control the frequency in the microgrid system using PID based on the algorithm particle swarm optimization (PSO). All the aforementioned research used the PID controller. However, this choice has inherent limitations and is not suitable for these parameters. It may lead to solutions where the values of the optimizers or the controller parameters are minimal. Consequently, the methodology has been revised to incorporate the fractional order PID (FOPID) controller as an alternative to the PID controller. This work was addressed in [11], where he controlled the frequency of the AC microgrid system using the FOPID controller based on a set of optimization algorithms. In [12] was optimized the parameters of the FOPID controller based on the PSO algorithm with the objective of controlling frequency deviation oscillations as well as power. Nevertheless, when examining this type of controller, it became evident that there were still some limitations in applying optimization algorithms to adjust the parameters of the PID controller [10]. Consequently, another controller was employed by other researchers, namely the multi-stage PID (MPID) controller, comprising two distinct controllers, namely PD and PI. In [13] was applied fuzzy logic to determine the parameters of the MPID controller for frequency control of the microgrid. Despite the fact that the fuzzy logic method is considered classical compared to modern optimization algorithms, this study yielded good results. In [14] was used the MPID controller to control the frequency of the isolated microgrid using a set of optimization algorithms. This research resulted in a prompt and effective response to frequency stability issues. In addition, in [15] was investigated frequency and power stability using the MPID controller based on the smell agent optimization. Following the aforementioned studies, the researchers proposed the use of the MPID controller in this study.

MPID is a controller comprising two distinct controllers connected in series. The initial PI controller is tasked with ensuring rapid response and the minimization of undesired distortions. Subsequently, the second PID controller is responsible for maintaining accuracy and reducing the error rate. This type of controller is highly flexible and capable of handling complex systems such as microgrid. In order to achieve an optimal design of the MPID controller, it is necessary to utilize optimization algorithms in order to determine the optimal values of its parameters [16].

In order to achieve enhanced and more desirable stability in the microgrid system, it is essential to determine the optimal values of the MPID controller constants. In order to achieve this objective, two optimization algorithms were subjected to investigation: the krill herd algorithm (KHA) and the cuckoo search algorithm (CSA) were considered. These are distinct algorithms that belong to the category of nature-inspired or evolutionary algorithms. The fundamental principles of these algorithms have been elucidated in [17–23]. KHA is slower in finding solutions due to its complex calculations related to krill movement. Nevertheless, it is regarded as more efficacious in addressing intricate systems and attaining optimal solutions in comparison to the CSA [17, 18]. Conversely, the CSA is relatively straightforward to implement due to its simplicity in application and design, and it requires minimal information to search the solution space [15, 21–23]. In order to enhance the frequency deviation in the microgrid, a study was conducted to assess the efficacy of these two algorithms when employed with the MPID controller. Consequently, a series of simulations were conducted in MATLAB with the objective of comparing the two algorithms and achieving a stable system. A series of scenarios representing potential operating conditions of the microgrid were conducted. The scenarios included:

1) Scenario I. Evaluation of technical response KHA-PID compared to PSO-PID and CSA-PID against disturbance load ΔP_L.

2) Scenario II. Evaluating the response of the MPID controller and comparing it with the PID controller using the KHA and CSA against disturbance load ΔP_L.

3) Scenario III. In this scenario we compared the two approaches proposed in this research MPID-KHA and MPID-CSA under different possible operating conditions ΔP_L, ΔP_{PV}, ΔP_{WTG} in the microgrid.

4) Scenario IV. In this scenario we pointed out the role and effectiveness of electric car batteries in improving and controlling frequency deviation in microgrid.

Microgrid concept. Figure 1 shows a microgrid used in remote electric vehicle charging stations, consisting of two renewable energy sources: solar energy and wind energy.

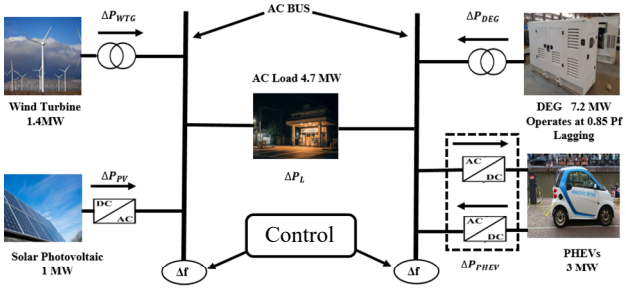

Fig. 1. Structure overview on proposed isolated microgrid system Bella Coola

Due to the random fluctuations in climate that affect energy production and stability [15], storage systems and a

DEG have been incorporated into the system to ensure stability. However, these additions are not sufficient to regulate the frequency deviation of the microgrid. Therefore, the implementation of control systems such as the PID controller and the MPID controller is essential [24].

Modeling of different generation components. In order to analyze small signals in order to verify the reliability and stability of frequency deviation for the microgrid system, models can be designed. These models can include PV, WTG, DEG and PHEV, which can be modeled by the first-order transfer function. First, starting from Fig. 1, the energy balance equation for the energy released by the microgrid can be written as [14, 15]:

$$P_S = P_{PV} + P_{WTG} + P_{DEG} - P_{PHEV}, \quad (1)$$

where P_S is the total average power generation.

The generation-load balance equation is:

$$\Delta P_L = \Delta P_{PV} + \Delta P_{WTG} + \Delta P_{DEG} - \Delta P_{PHEV}. \quad (2)$$

From (2) we infer that variations in power generation have a significant impact on frequency deviation in the system. Therefore, frequency deviation Δf can be expressed from [25, 26]:

$$TF_S = \frac{\Delta f}{\Delta P_L} = \frac{1}{k_S(1 + S \cdot T_S)} = \frac{1}{M \cdot S + D}, \quad (3)$$

where M, D are the equivalent inertia constant and damping constant, respectively; Δf is the frequency deviation; k_S is the gain constant of the microgrid; T_S is the time constant; TF_S is the transfer function of the microgrid; S is the Laplace variable.

From (3), (4) the frequency deviation of the microgrid system can be expressed as:

$$\Delta f = \frac{1}{M \cdot S + D}\left[\Delta P_{PV} + \Delta P_{WTG} + \Delta P_{DEG} - \Delta P_{PHEV}\right]. \quad (4)$$

In order to study the variations in frequency deviation, it is necessary to examine each element of the energy sources connected to the microgrid.

Model of PV generation system. Solar energy is cheap and easy to make and install. It is made up of a set of connected PV cells, either in parallel or series. These cells turn sunlight into electricity. This can be expressed as [24–27]:

$$TF_{PV} = \frac{\Delta P_{PV}}{\Delta \phi} = \frac{K_{PV}}{1 + S \cdot T_{PV}}, \quad (5)$$

where TF_{PV} is the transfer function of the PV system; ΔP_{PV} is the change in output power; $\Delta \phi$ is the change in solar irradiance; K_{PV} is the gain constant of the PV; T_{PV} is the time constant.

Model of the wind energy. Wind energy involves converting kinetic energy into electrical energy through the rotation of large turbines directly connected to the rotor of the electrical generator. It can be expressed mathematically as [25–27]:

$$TF_{WTG} = \frac{K_{WTG}}{1 + S \cdot T_{WTG}}, \quad (6)$$

where TF_{WTG} is the transfer function; K_{WTG} is the gain constant of the WTG; T_{WTG} is the time constant.

DEG model. DEG is a traditional source of power production and is used in cases of renewable energy system failure and energy storage systems to supply power to the load. It represents a reliable source for providing energy to the microgrid and can be expressed as [24, 25]:

$$TF_{DEG} = \frac{K_{DEG}}{1 + S \cdot T_{DEG}}, \quad (7)$$

where TF_{DEG} is the transfer function of the DEG; K_{DEG} is the gain constant of the DEG; T_{DEG} is the time constant.

PHEV model. Electric vehicles are considered an important element in this work as they serve two functions: acting as a load and serving as a source for energy storage and load financing in case renewable energy sources fail. They represent an alternative for energy storage to meet needs in controlling frequency deviations in the microgrid. The energy present in electric vehicles can be expressed based on frequency deviation as [28]:

$$\Delta P_{PHEV} = \begin{cases} -\Delta P_{\max} \cdot U_C < -\Delta P_{\max}; \\ -\Delta P_{\max} \cdot U_C > -\Delta P_{\max}; \\ U_C \cdot |U_C| \le \Delta P_{\max}. \end{cases} \quad (8)$$

where U_C is the output signal determines whether the ΔP_{PHEV} will be employed for either charging or discharging purposes [28]; $P_{\max}$ is the maximum power that can be obtained from an individual electric vehicle.

The battery's state of charge (SOC) influences the value of K_{EV} (Fig. 2) depicting the relationship between K_{EV} and SOC for PHEV [29, 30].

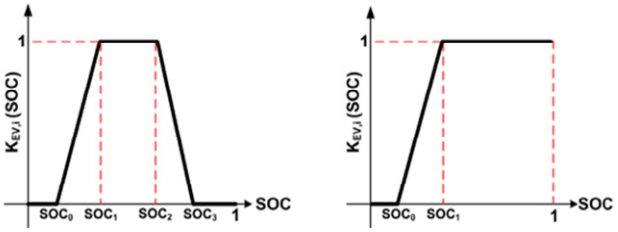

Fig. 2. Representing the charging and discharging PHEV

Following analysis and simplification, the ultimate mathematical expression can be represented in the format of a first-order simplifier:

$$\Delta P_{PHEV} = \frac{N_{EV}\left[\Delta U_C - \Delta f \cdot \frac{K_{EV}}{R_{av}}\right]}{1 + S \cdot T_{EV}}, \quad (9)$$

where ΔP_{PHEV} is the energy generated by a single PHEV; N_{EV} is the total number of electric vehicles; ΔU_C is the controller's output signal; Δf is the frequency deviation; K_{EV} is the gain constant of the PHEV; R_{av} is the droop characteristics of the PHEV; T_{EV} is the battery time constant [28].

MPID controller and objective function. MPID controller is a controller that has the same general concept as a classical controller PID controller in that it adjusts or corrects deviations between the measured variable and the desired set point [16]. It consists of two units PD and PI connected in series (Fig. 3).

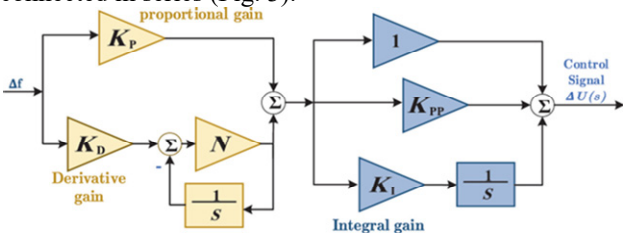

Fig. 3. Block diagram of MPID controller

The unit PD is the first one, and its input is the distortion ratio at the frequency Δf and its output is the

input to unit PI. The output of unit PI serves as an enhanced signal for the frequency using ΔU_C. One of the advantages of unit MPID is that all controller parameters in all stages of frequency variation for the microgrid system can be maximally utilized [13].

MPID controller has an advantage over the classic controller, as it can use the best features of both controllers PD and PI controllers. In the PI controller, the integral term must exist during steady state and the output is constant to the PD controller. This means that the integrated output will be zero during the transient, avoiding the limitation of classical PID. This controller has been successfully applied to many engineering problems [13]. MPID controller is connected to the microgrid and can be implemented as shown in Fig. 4. The mathematical model of the MPID controller can be expressed as:

$$\frac{\Delta U_C}{\Delta f} = \left(K_p + K_d \cdot S\right) \cdot \left(1 + K_{pp} + \frac{K_i}{S}\right), \qquad (10)$$

where ΔU_c is the control signal; K_i is the integral gain; K_p is the proportional gain; K_d is the derivative gain; K_{pp} is the additional proportional gain.

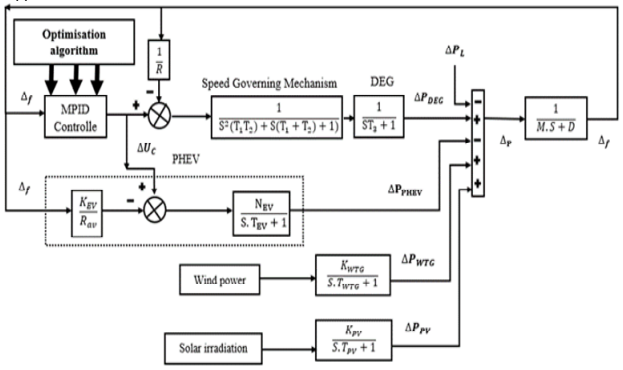

Fig. 4. Dynamic model of the proposed isolated microgrid

Table 1 represents list of all microgrid constants.

Table 1

List of all microgrid constants

Parameter	Value	Parameter	Value
$M(S)$	0.1667	T_1	0.025
D(MW)	0.015	T_2	2
$T_{PI}(S)$	1.8	T_3	3
T_{WTG}	2	K_{PV}	1
T_{EV}	0.1	K_{WTG}	1
R_{av}(Hz/MW)	2.4	N_{EV}	600

Objective function and optimization of MPID controller. The disturbances that cause deviations in the frequency of the microgrid system are a result of random fluctuations in the production of energy, especially from renewable energy sources [19]. Addressing this issue requires precise and quick adjustments in the controller parameters. To tackle this problem, we have studied the following two algorithms:

Overview of KHA. KHA is an optimization algorithm inspired by the natural behavior of a krill swarm, where it relies on collective behavior in searching for nesting areas, food and encounter and move away from predators. The main components of the KHA include [31–33]: krill individuals; krill swarm leader; interaction among swarm individuals; selection and adaptation.

In the KHA each solution can be represented by the foraging space or the distance between it and the predators, and the solutions can be expressed in the following mathematical form [32]:

- To determine the optimal location for food abundance we use the following relationship:

$$\Delta x_i^a = a \sum_{j=1}^{N} \frac{f(x_j) - f(x_i)}{\left\| x_j - x_i \right\|}. \qquad (11)$$

- To determine the distance of a hard krill herd from enemies, we use the following mathematical relationship:

$$\Delta x_i^r = B \sum_{j=1}^{N} \frac{1}{\left\| x_j - x_i \right\|}. \qquad (12)$$

- Finally, to determine the safe space for swarm stability, which is the ideal and best solution, we use the following mathematical relationship:

$$x_j(t+1) = x_j(t) + \Delta x_i^a + \Delta x_j^r, \qquad (13)$$

where Δx^a is the new value of dining space; Δx^r is the new value for the swarm's distance from the enemy; x_j is the new candidate solution that replaces the less-fit solution x_i is the current solution within the search space; N is the number of solutions; a, B are the interaction coefficients for attraction and repulsion; $f(x_j)$ and $f(x_i)$ are the objective function values for solutions j and i, respectively.

Application of KHA to optimize the MPID controller. At this stage we explain how to improve the MPID controller using the algorithm:

Step 1 – initialization. Choose random search spaces using (12) and (13). Since the proposed controller contains (K_p, K_d, K_{pp}, K_i) as 4 basic control parameters, start by searching for random solutions of the parameters.

Step 2 – evaluate solutions. At this stage we evaluate the solutions using (15).

Step 3 – selection. We mark the best solution and update the parameters MPID controller of the KHA.

Step 4 – algorithm termination. At the end of the iterations number, the algorithm chooses the best solution.

Cuckoo search algorithm. CSA was proposed in [17], inspired by the natural life of the cuckoo bird. The strategy relies on the reproductive behavior of the female cuckoo, which lays its eggs in the nests of other bird species to avoid the effort of building nests and caring for the eggs and chicks. This algorithm focuses on two main conditions for its success [34–36]:

- the female cuckoo randomly selects the best nests built by other birds;
- the female cuckoo disposes of the eggs far away from the nest and lays her own eggs at each stage. She repeats this process until only one egg from the other species remains.

Eggs are the primary problem in this algorithm, with the cuckoo's egg being the new solution generated. This solution is calculated using the Levy Flight distribution as follows [33]:

$$x_j(t+1) = x_i(t) + a \cdot levy(\lambda); \qquad (14)$$

$$levy(\lambda) = s \cdot \left(x_i(t) - x_{best}\right); \qquad (15)$$

where x_j is *the* new candidate solution that replaces the less-fit solution; x_i is the current solution in the search space; λ is the Levy exponent; a is the constant; X_{best} is the best current solution; i = 1, 2, 3,..., N:

$$s = \sigma_u \cdot u \cdot \left|V\right|^{-1/\beta}. \qquad (16)$$

where s is the step size used to update solutions in the algorithm, σ_u is the scaling factor or coefficient that determines the overall impact of the step size; u is a random variable generated from a Levy distribution; V is the distance between the current solution and the best existing solution; β is the parameter that controls the behavior of the power-law of the system

If the host bird detects the cuckoo egg, it means that the condition $x_j<x_i$ is true, the host bird discards this cuckoo egg (the new solution is modified) and it is replaced with a new solution calculated as follows:

$$x_j(t+1) = x_i(t) + \text{rand}(n_1 - n_2) \text{ for } n_1, n_2, ..., N . \quad (17)$$

Application of CSA algorithm to optimize the MPID controller.

Step 1 – initialization. Proposing a number of random solutions within the nest search area, we then evaluate each solution using the objective function.

Step 2 – MPID controller initialization. Initialize K_p, K_i, K_d, K_{pp} parameters and error conditions (current error, cumulative error, and previous error).

Step 3. At each iteration, we adjust the MPID controller parameters using Levy trips.

Step 4. Repeat the above steps until convergence or the maximum number of iterations is reached.

Step 5 – best solution. We select the best set of parameters found during the search for the MPID controller.

Begin
Define the objective function
Define the maximum number (n) of iterations and other parameters
while (x < MaxGeneration):
Obtain a cuckoo randomly via Levi's flights and then we determine the MPID parameters
Evaluate its fitness F_i
Choose a nest among n (say j) randomly
if $x_i>x_j$
Replace F_j with the new parameters
End if
End while
A group of bad nests is abandoned, and one nest is chosen as the best solution, which expresses the values of the constants for MPID controller.
End.

Results and discussions. We evaluated the performance of the isolated microgrid system using a MATLAB/Simulink in a time domain of 250 s (Fig. 2). We applied KHA and CSA to improve the parameters of MPID controller for good control of the frequency deviation of the system. In addition to comparing them, we conducted a set of operating scenarios for the microgrid, which are as follows.

Scenario I. Evaluation of technical response KHA-PID compared to PSO-PID and CSA-PID against disturbance load ΔP_L. In this scenario, we simulated the microgrid using the PID controller optimized with KHA, CSA and PSO. As Table 2 shows the values for PID controller optimized with these algorithms, we also compared these results in Fig. 5 showed the superiority of the KHA in terms of speed in stability time, as well as a decrease in unwanted frequency changes. Then followed by the CSA, which also showed its superiority over PSO algorithm. Given these results obtained, they are considered undesirable. Therefore, it has become necessary to search for another approach and work on it.

Table 2

Optimal parameters of the PID controller based on PSO, KHA and CSA

Methods	Optimized gains			
	K_p	K_i	K_d	N
PSO–PID	1.032	1.624	1.1992	100.226
CSA–PID	1.395	1.4281	1.9078	59.26
KHA–PID	2.4702	2.670	1.01	78.3

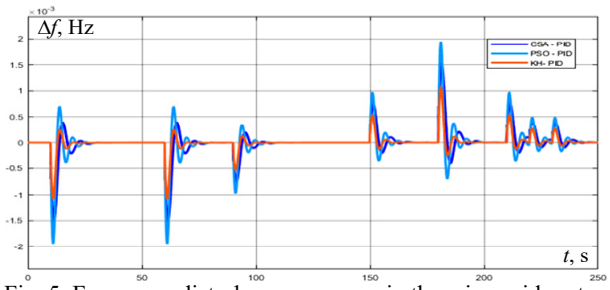

Fig. 5. Frequency disturbance response in the microgrid system using PSO–PID, CSA–PID, KHA–PID

Scenario II. Evaluating the response of the MPID controller and comparing it with the PID controller using the KHA and CSA against disturbance load ΔP_L. In this scenario, we performed frequency deviation simulations using PID and MPID controllers with an optimization algorithm. Table 3 shows the numerical values for each parameter of these controllers. The results (Fig. 6) showed the extent of the superiority of the MPID controller in reducing unwanted frequency deviations compared to PID controller despite using 2 different types of optimization algorithms.

Table 3

Optimal parameters of the MPID controllers based KHA and CSA

Methods	Optimized gains				
	K_p	K_i	K_d	K_{pp}	N
KHA-MPID	4.9736	4.3943	4.5787	0.490	36.753
CSA-MPID	4.650	2.05	2.980	0.297	28.962

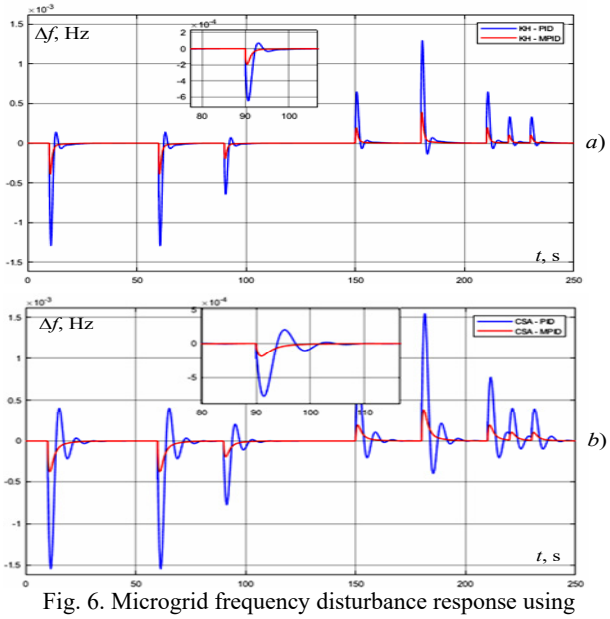

Fig. 6. Microgrid frequency disturbance response using KHA-PID (*a*) and CSA-PID (*b*)

Scenario III. In this scenario, we compared the two approaches proposed in this research MPID-KHA and MPID-CSA under different possible operating conditions (ΔP_L, ΔP_{PV}, ΔP_{WTG}) in the microgrid. In this scenario, we tested frequency drift under a different set of influences and obstacles to the microgrid, namely stochastic changes in climate. We implemented a number of simulation cases as follows.

Case 1. In this case, we place the microgrid under ΔP_L, which represents the energy change in the batteries (Fig. 7,*a*). Figure 7,*b* represents the frequency deviation response Δf in the microgrid.

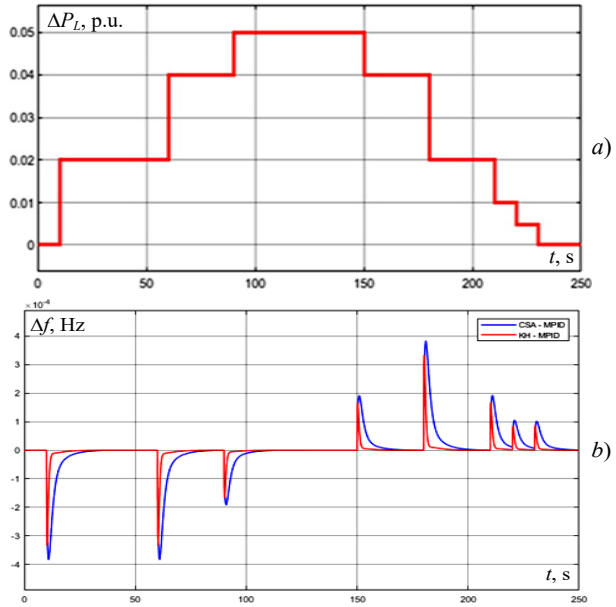

Fig. 7. Frequency disturbance response of KHA-MPID and CSA-MPID under load disturbances ΔP_L

Case 2. In this case, we disconnected the battery source and the solar energy source, and connected only the wind energy ΔP_{WTG} (Fig. 8,*a*). Figure 8,*b* represents the frequency deviation Δf in this case.

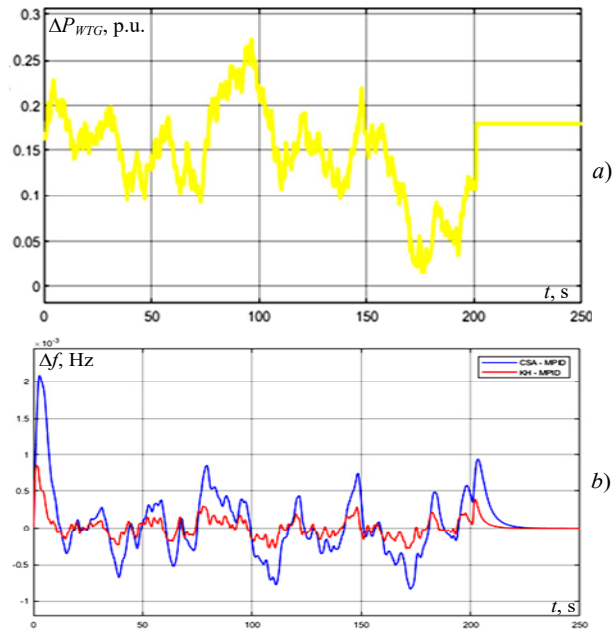

Fig. 8. Frequency disturbance response of KHA-MPID and CSA-MPID under wind energy ΔP_{WTG}

Case 3. In this case, we also disconnected the battery source as well as the wind power source, and connected only the solar power ΔP_{pv} (Fig. 9,*a*). Figure 9,*b* represents the frequency deviation Δf in this case.

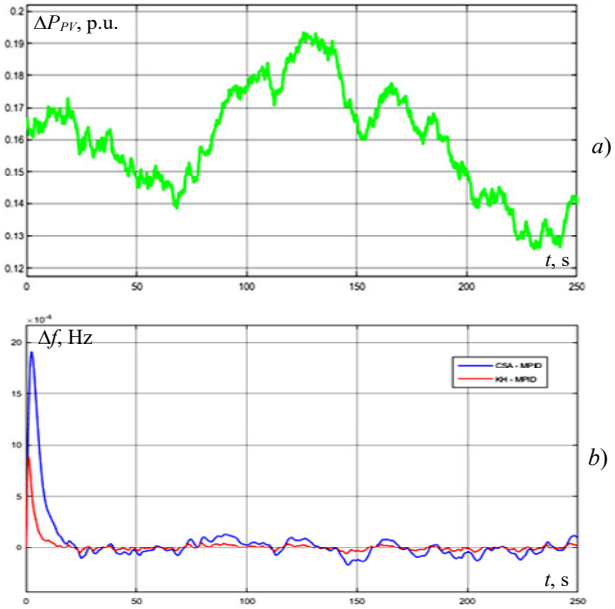

Fig. 9. Frequency disturbance response of KHA-MPID and CSA-MPID under ΔP_{pv}

The objective of these 3 cases is to demonstrate the superiority of the proposed approaches in controlling frequency deviation under various factors affecting the microgrid. Through these results, we observe the significant superiority of KHA-MPID over CSA-MPID in terms of greatly reducing the frequency distortion percentage as well as the speed in reaching the stability state or the settling time.

Scenario IV. In this scenario, we pointed out the role and effectiveness of PHEV in improving and controlling frequency deviation in microgrid. Table 4 represents the percentage of change in electric car batteries (charge rate) as we connect the batteries to the microgrid system. The results in Fig. 10 show that batteries play a major role in reducing and improving frequency deviation, and therefore we say that the storage system has great effectiveness in improving the performance of the microgrid system.

Table 4

Percentage variation in PHEV

Percentage variation, %	Parameters PHEVs			
	R_{av}	T_{EV}	K_{EV}	N_{EV}
±30	0.72	0.03	0.54	180
±50	1.2	0.05	0.9	300
±70	1.68	0.07	1.26	420

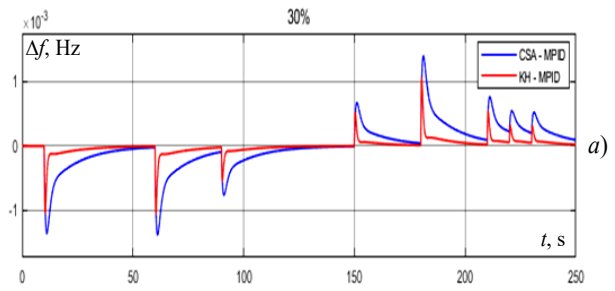

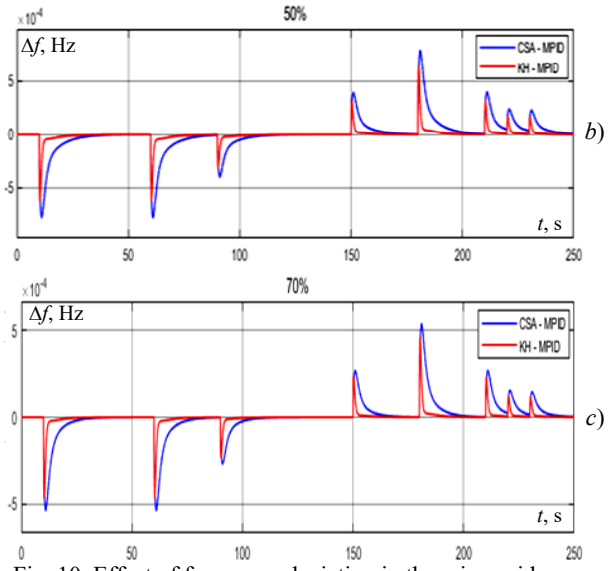

Fig. 10. Effect of frequency deviation in the microgrid versus a difference in battery charge percentage of ±30 % (*a*); ±50 % (*b*); ±70 % (*c*)

Conclusions. In this research we proposed a study to propose an approach to control the frequency deviation of the microgrid system caused by random climate changes. Therefore, we used the MPID controller with two optimization algorithms (KHA and CSA) to adjust the parameters of the controller.

To verify the effectiveness of this approach, we initially compared it with the PID controller based on the same two algorithms. The obtained results demonstrated the superiority of the proposed approach in terms of system stability in terms of faster settling time and lower distortion ratio in the deviation. In the second phase, we confirmed the robustness of this approach in controlling the frequency deviation by conducting several potential impact scenarios. We also demonstrated the superiority of the KHA over CSA using the MPID controller. Finally, based on previous studies and the results obtained in this study, we can confirm that the MPID controller based on the KHA can be relied upon to solve these types of problems, such as controlling frequency deviation in a microgrid.

Conflict of interest. The authors of the article declare that there is no conflict of interest.

REFERENCES

1. Leroutier M., Quirion P. Air pollution and CO2 from daily mobility: Who emits and Why? Evidence from Paris. *Energy Economics*, 2022, vol. 109, art. no. 105941. doi: https://doi.org/10.1016/j.eneco.2022.105941.

2. Alhamrouni I., Wahab W., Salem M., Rahman N.H.A., Awalin L. Modeling of micro-grid with the consideration of total harmonic distortion analysis. *Indonesian Journal of Electrical Engineering and Computer Science*, 2019, vol. 15, no. 2, pp. 581-592. doi: https://doi.org/10.11591/ijeecs.v15.i2.pp581-592.

3. Sathish C., Chidambaram I.A., Manikandan M. Intelligent cascaded adaptive neuro fuzzy interface system controller fed KY converter for hybrid energy based microgrid applications. *Electrical Engineering & Electromechanics*, 2023, no. 1, pp. 63-70. doi: https://doi.org/10.20998/2074-272X.2023.1.09.

4. Manikandan K., Sasikumar S., Arulraj R. A novelty approach to solve an economic dispatch problem for a renewable integrated micro-grid using optimization techniques. *Electrical Engineering & Electromechanics*, 2023, no. 4, pp. 83-89. doi: https://doi.org/10.20998/2074-272X.2023.4.12.

5. Belbachir N., Zellagui M., Settoul S., El-Bayeh C.Z., Bekkouche B. Simultaneous optimal integration of photovoltaic distributed generation and battery energy storage system in active distribution network using chaotic grey wolf optimization. *Electrical Engineering & Electromechanics*, 2021, no. 3, pp. 52-61. doi: https://doi.org/10.20998/2074-272X.2021.3.09.

6. Das D.C., Roy A.K., Sinha N. GA based frequency controller for solar thermal–diesel–wind hybrid energy generation/energy storage system. *International Journal of Electrical Power & Energy Systems*, 2012, vol. 43, no. 1, pp. 262-279. doi: https://doi.org/10.1016/j.ijepes.2012.05.025.

7. Srinivasarathnam C., Yammani C., Maheswarapu S. Load Frequency Control of Multi-microgrid System considering Renewable Energy Sources Using Grey Wolf Optimization. *Smart Science*, 2019, vol. 7, no. 3, pp. 198-217. doi: https://doi.org/10.1080/23080477.2019.1630057.

8. Shankar R., Kumar A., Raj U., Chatterjee K. Fruit fly algorithm-based automatic generation control of multiarea interconnected power system with FACTS and AC/DC links in deregulated power environment. *International Transactions on Electrical Energy Systems*, 2019, vol. 29, no. 1, art. no. e2690. doi: https://doi.org/10.1002/etep.2690.

9. Kalyan C.N.S., Goud B.S., Kumar M.K., Bajaj M., Rubanenko O., Danylchenko D. Fruit Fly Optimization Algorithm Tuned 2DOFPID Controller for Frequency Regulation of Dual Area Power System With AC-DC Lines. *2022 IEEE 3rd KhPI Week on Advanced Technology (KhPIWeek)*, 2022, pp. 1-6. doi: https://doi.org/10.1109/KhPIWeek57572.2022.9916505.

10. Regad M., Helaimi M., Taleb R., Toubal Maamar A.E. Optimum Synthesis of the PID Controller Parameters for Frequency Control in Microgrid Based Renewable Generations. *Lecture Notes in Networks and Systems*, 2020, vol. 102, pp. 546-556. doi: https://doi.org/10.1007/978-3-030-37207-1_58.

11. Yang C., Yao W., Fang J., Ai X., Chen Z., Wen J., He H. Dynamic event-triggered robust secondary frequency control for islanded AC microgrid. *Applied Energy*, 2019, vol. 242, pp. 821-836. doi: https://doi.org/10.1016/j.apenergy.2019.03.139.

12. Regad M., Helaimi M., Taleb R., Othman A.M., Gabbar H.A. Frequency Control in Microgrid Power System with Renewable Power Generation Using PID Controller Based on Particle Swarm Optimization. *Lecture Notes in Networks and Systems*, 2020, vol. 102, pp. 3-13. doi: https://doi.org/10.1007/978-3-030-37207-1_1.

13. Annamraju A., Nandiraju S. A novel fuzzy tuned multistage PID approach for frequency dynamics control in an islanded microgrid. *International Transactions on Electrical Energy Systems*, 2020, vol. 30, no. 12, art. no. e12674. doi: https://doi.org/10.1002/2050-7038.12674.

14. Khadanga R.K., Padhy S., Panda S., Kumar A. Design and analysis of multi-stage PID controller for frequency control in an islanded micro-grid using a novel hybrid whale optimization-pattern search algorithm. *International Journal of Numerical Modelling: Electronic Networks, Devices and Fields*, 2018, vol. 31, no. 5, art. no. e2349. doi: https://doi.org/10.1002/jnm.2349.

15. Louarem S., Kebbab F.Z., Salhi H., Nouri H. A comparative study of maximum power point tracking techniques for a photovoltaic grid-connected system. *Electrical Engineering & Electromechanics*, 2022, no. 4, pp. 27-33. doi: https://doi.org/10.20998/2074-272X.2022.4.04.

16. Sahu P.C., Prusty R.C., Panda S. Optimal design of a robust FO-Multistage controller for the frequency awareness of an islanded AC microgrid under i -SCA algorithm. *International Journal of Ambient Energy*, 2022, vol. 43, no. 1, pp. 2681-2693. doi: https://doi.org/10.1080/01430750.2020.1758783.

17. Ali Moussa M., Derrouazin A., Latroch M., Aillerie M. A hybrid renewable energy production system using a smart controller based on fuzzy logic. *Electrical Engineering & Electromechanics*, 2022, no. 3, pp. 46-50. doi: https://doi.org/10.20998/2074-272X.2022.3.07.

18. Gandomi A.H., Talatahari S., Tadbiri F., Alavi A.H. Krill herd algorithm for optimum design of truss structures. *International Journal of Bio-Inspired Computation*, 2013, vol. 5, no. 5, art. no. 281-288. doi: https://doi.org/10.1504/IJBIC.2013.057191.

19. Yaghoobi S., Mojallali H. Tuning of a PID controller using improved chaotic Krill Herd algorithm. *Optik*, 2016, vol. 127, no. 11, pp. 4803-4807. doi: https://doi.org/10.1016/j.ijleo.2016.01.055.

20. Bolaji A.L., Al-Betar M.A., Awadallah M.A., Khader A.T., Abualigah L.M. A comprehensive review: Krill Herd algorithm (KH) and its applications. *Applied Soft Computing*, 2016, vol. 49, pp. 437-446. doi: https://doi.org/10.1016/j.asoc.2016.08.041.

21. Sarda J., Pandya K., Lee K.Y. Hybrid cross entropy – cuckoo search algorithm for solving optimal power flow with renewable generators and

controllable loads. *Optimal Control Applications and Methods*, 2023, vol. 44, no. 2, pp. 508-532. doi: https://doi.org/10.1002/oca.2759.
22. Barrat J.-L., Del Gado E., Egelhaaf S.U., Mao X., Dijkstra M., Pine D.J., Kumar S.K., (…), Kwon J. Soft matter roadmap. *Journal of Physics: Materials*, 2024, vol. 7, no. 1, art. no. 012501. doi: https://doi.org/10.1088/2515-7639/ad06cc.
23. Abdellah A., Larbi M., Toumi D. Open circuit fault diagnosis for a five-level neutral point clamped inverter in a grid-connected photovoltaic system with hybrid energy storage system. *Electrical Engineering & Electromechanics*, 2023, no. 6, pp. 33-40. doi: https://doi.org/10.20998/2074-272X.2023.6.06.
24. Ayat Y., Badoud A.E., Mekhilef S., Gassab S. Energy management based on a fuzzy controller of a photovoltaic/fuel cell/Li-ion battery/supercapacitor for unpredictable, fluctuating, high-dynamic three-phase AC load. *Electrical Engineering & Electromechanics*, 2023, no. 3, pp. 66-75. doi: https://doi.org/10.20998/2074-272X.2023.3.10.
25. Mohamed R., Helaimi M., Taleb R., Gabbar H.A., Othman A.M. Frequency control of microgrid system based renewable generation using fractional PID controller. *Indonesian Journal of Electrical Engineering and Computer Science*, 2020, vol. 19, no. 2, pp. 745-755. doi: https://doi.org/10.11591/ijeecs.v19.i2.pp745-755.
26. Khan S.A., Mahmood T., Awan K.S. A nature based novel maximum power point tracking algorithm for partial shading conditions. *Electrical Engineering & Electromechanics*, 2021, no. 6, pp. 54-63. doi: https://doi.org/10.20998/2074-272X.2021.6.08.
27. Kumar R.S., Reddy C.S.R., Chandra B.M. Optimal performance assessment of intelligent controllers used in solar-powered electric vehicle. *Electrical Engineering & Electromechanics*, 2023, no. 2, pp. 20-26. doi: https://doi.org/10.20998/2074-272X.2023.2.04.
28. Latif A., Pramanik A., Das D.C., Hussain I., Ranjan S. Plug in hybrid vehicle-wind-diesel autonomous hybrid power system: frequency control using FA and CSA optimized controller. *International Journal of System Assurance Engineering and Management*, 2018, vol. 9, no. 5, pp. 1147-1158. doi: https://doi.org/10.1007/s13198-018-0721-1.
29. Zerzouri N., Ben Si Ali N., Benalia N. A maximum power point tracking of a photovoltaic system connected to a three-phase grid using a variable step size perturb and observe algorithm. *Electrical Engineering & Electromechanics*, 2023, no. 5, pp. 37-46. doi: https://doi.org/10.20998/2074-272X.2023.5.06.
30. Khemis A., Boutabba T., Drid S. Model reference adaptive system speed estimator based on type-1 and type-2 fuzzy logic sensorless control of electrical vehicle with electrical differential. *Electrical Engineering & Electromechanics*, 2023, no. 4, pp. 19-25. doi: https://doi.org/10.20998/2074-272X.2023.4.03.
31. Laifa A., Ayachi B. Application of whale algorithm optimizer for unified power flow controller optimization with consideration of renewable energy sources uncertainty. *Electrical Engineering & Electromechanics*, 2023, no. 2, pp. 69-78. doi: https://doi.org/10.20998/2074-272X.2023.2.11.
32. Mahdad B., Srairi K. Interactive artificial ecosystem algorithm for solving power management optimizations. *Electrical Engineering & Electromechanics*, 2022, no. 6, pp. 53-66. doi: https://doi.org/10.20998/2074-272X.2022.6.09.
33. Tebbakh N., Labed D., Labed M.A. Optimal size and location of distributed generations in distribution networks using bald eagle search algorithm. *Electrical Engineering & Electromechanics*, 2022, no. 6, pp. 75-80. doi: https://doi.org/10.20998/2074-272X.2022.6.11.
34. Mezhoud N., Ayachi B., Amarouayache M. Multi-objective optimal power flow based gray wolf optimization method. *Electrical Engineering & Electromechanics*, 2022, no. 4, pp. 57-62. doi: https://doi.org/10.20998/2074-272X.2022.4.08.
35. Vo D.N., Schegner P., Ongsakul W. Cuckoo search algorithm for non-convex economic dispatch. *IET Generation, Transmission & Distribution*, 2013, vol. 7, no. 6, pp. 645-654. doi: https://doi.org/10.1049/iet-gtd.2012.0142.
36. Thao N.T.P., Thang N.T. Environmental Economic Load Dispatch with Quadratic Fuel Cost Function Using Cuckoo Search Algorithm. *International Journal of U- and e-Service, Science and Technology*, 2014, vol. 7, no. 2, pp. 199-210. doi: https://doi.org/10.14257/ijunesst.2014.7.2.19.

Received 19.06.2024
Accepted 15.08.2024
Published 02.01.2025

B. Alouache [1]*, PhD Student,*
M. Helaimi [1]*, PhD, Associate Professor,*
A.B. Djilali [1]*, Doctor of Electrical Engineering,*
H.A. Gabbar [2]*, Full Professor,*
H. Allouache [1]*, Doctor of Electrical Engineering,*
A. Yahdou [1]*, Doctor of Electrical Engineering,*
[1] Electrical Engineering Department,
Laboratoire Génie Electrique et Energies Renouvelables
(LGEER), Hassiba Benbouali University, Chlef, Algeria,
e-mail: b.alouache@univ-chlef.dz (Corresponding Author);
[2] Department of Energy and Nuclear Engineering,
Faculty of Engineering and Applied Science,
University of Ontario Institute of Technology (UOIT), Canada.

How to cite this article:
Alouache B., Helaimi M., Djilali A.B., Gabbar H.A., Allouache H., Yahdou A. Optimal tuning of multi-stage PID controller for dynamic frequency control of microgrid system under climate change scenarios. *Electrical Engineering & Electromechanics*, 2025, no. 1, pp. 8-15. doi: https://doi.org/10.20998/2074-272X.2025.1.02

UDC 621.3 https://doi.org/10.20998/2074-272X.2025.1.03

A. Boudia, S. Messalti, S. Zeghlache, A. Harrag

Type-2 fuzzy logic controller-based maximum power point tracking for photovoltaic system

Introduction. *Photovoltaic (PV) systems play a crucial role in converting solar energy into electricity, but their efficiency is highly influenced by environmental factors such as irradiance and temperature. To optimize power output, Maximum Power Point Tracking (MPPT) techniques are used. This paper introduces a novel approach utilizing a Type-2 Fuzzy Logic Controller (T2FLC) for MPPT in PV systems. The* ***novelty*** *of the proposed work lies in the development of a T2FLC that offers enhanced adaptability by managing a higher degree of uncertainty, we introduce an original method that calculates the error between the output voltage and a dynamically derived reference voltage, which is obtained using a mathematical equation. This reference voltage adjusts in real-time based on changes in environmental conditions, allowing for more precise and stable MPPT performance. The* ***purpose*** *of this paper is to design and validate the effectiveness of a T2FLC-based MPPT technique for PV systems. This approach seeks to enhance power extraction efficiency in response to dynamic environmental factors such as changing irradiance and temperature. The* ***methods*** *used in this study involve the implementation of T2FLC to adjust the duty cycle of a DC-DC converter for continuous and precise MPPT. The system was simulated under various environmental conditions, comparing the performance of T2FLC against T1FLC. The* ***results*** *show that the T2FLC MPPT system significantly outperforms traditional methods in terms of tracking speed, stability, and power efficiency. T2FLC demonstrated faster convergence to the MPP, reduced oscillations, and higher accuracy in rapidly changing environmental conditions. The findings of this study confirm the* ***practical value*** *of T2FLC logic in improving the efficiency and stability of PV systems, making it a promising solution for enhancing renewable energy technologies.* References 33, tables 4, figures 10.
Key words: **fuzzy logic controller, DC-DC boost converter**, **maximum power point tracking, photovoltaic system.**

Вступ. *Фотоелектричні (PV) системи відіграють вирішальну роль у перетворенні сонячної енергії в електрику, але їхня ефективність сильно залежить від факторів навколишнього середовища, таких як освітленість та температура. Для оптимізації вихідної потужності використовують методи відстеження точки максимальної потужності (MPPT). У цій статті наведено новий підхід з використанням контролера нечіткої логіки типу 2 (T2FLC) для MPPT у PV системах.* ***Новизна*** *запропонованої роботи полягає у розробці T2FLC, який забезпечує покращену адаптивність за рахунок управління вищим ступенем невизначеності; ми представляємо оригінальний метод, який обчислює помилку між вихідною напругою та динамічно отриманою опорною напругою, яка виходить за допомогою математичного рівняння. Ця опорна напруга регулюється в режимі реального часу на основі змін умов довкілля, що дозволяє забезпечити більш точну та стабільну роботу MPPT.* ***Метою*** *статті є розробка та перевірка ефективності методу MPPT на основі T2FLC для PV систем. Цей підхід спрямований на підвищення ефективності отримання енергії у відповідь на динамічні фактори навколишнього середовища, такі як зміна освітленості та температури.* ***Методи****, що використовуються у цьому дослідженні, включають реалізацію T2FLC для регулювання робочого циклу DC-DC-перетворювача для безперервного та точного MPPT. Система була змодельована у різних умовах навколишнього середовища, порівнюючи продуктивність T2FLC та T1FLC.* ***Результати*** *показують, що система MPPT T2FLC значно перевершує традиційні методи з погляду швидкості відстеження, стабільності та енергоефективності. T2FLC продемонструвала більш швидку збіжність до MPP, знижені коливання та більш високу точність у швидко мінливих умовах довкілля. Результати цього дослідження підтверджують* ***практичну цінність*** *логіки T2FLC для підвищення ефективності та стабільності PV систем, що робить її перспективним рішенням для покращення технологій відновлюваної енергії.* Бібл. 33, табл. 4, рис. 10.
Ключові слова: **контролер нечіткої логіки, DC-DC підвищувальний перетворювач, відстеження точки максимальної потужності, фотоелектрична система.**

Introduction. Photovoltaic (PV) systems have garnered considerable interest as a viable and renewable energy source. The efficiency of these systems largely depends on the ability to maximize the extraction of electrical power from solar panels, a process known as Maximum Power Point Tracking (MPPT). The PV module output power is highly sensitive to environmental conditions changes, making the MPPT a critical component in PV systems [1–4].

Traditional MPPT methods, including Incremental Conductance (IC), Perturb and Observe (P&O) [3, 5, 6] have been extensively utilized due to their straightforwardness and effortless integration. However, these methods often exhibit limitations in dynamic environments [7]. For instance, the P&O method may exhibit oscillations around the Maximum Power Point (MPP) under stable conditions and fail to track the MPP accurately during rapidly changing conditions. The IC method, while more accurate, can be computationally intensive and slow in response [8–10].

Advanced MPPT techniques have been developed to address these challenges [11, 12], among which are Fuzzy Logic Controllers (FLCs) [13], which have shown promise. Based on fuzzy logic theory, FLC can handle the nonlinear and uncertain nature of PV systems more effectively than traditional methods. By mimicking human reasoning and decision-making processes, FLC can provide a more robust and adaptive approach to MPPT [14].

Type-1 FLCs (T1FLCs) have been successfully applied to MPPT [15], demonstrating improved performance over conventional methods [16]. However, T1FLCs have limitations in dealing with uncertainties and imprecise information, which are inherent in PV systems. This has led to the development of Type-2 FLCs (T2FLCs), which offer an enhanced capability to manage uncertainties by introducing a higher degree of fuzziness.

The implementation of T2FLCs in MPPT for PV systems has emerged as a promising approach to enhance the efficiency and reliability of solar energy systems [17]. The inherent nonlinear characteristics of PV systems, influenced by environmental factors such as temperature and irradiance, necessitate advanced control strategies that can adapt to these variations. Type-2 fuzzy logic, an extension of traditional fuzzy logic, provides a robust framework for handling uncertainty and imprecision in the control process, making it particularly suitable for MPPT applications. T2FLCs are designed to manage the complexities associated with the nonlinear output of PV systems. As highlighted by the application of Type-2 fuzzy logic in MPPT allows for improved performance in environments with high uncertainty, such as varying

weather conditions [18, 19]. This is crucial since the output power of PV systems is not only dependent on solar irradiance but also on temperature fluctuations, which can affect the efficiency of energy conversion. The ability of Type-2 fuzzy logic to incorporate degrees of uncertainty in its decision-making process enables it to adapt more effectively to these dynamic changes compared to traditional T1FLCs [18].

The performance of T2FLCs in MPPT has been demonstrated through various studies. For instance, a novel algorithm utilizing a T2FLC in conjunction with a push-pull converter developed, showing significant improvements in tracking efficiency and total harmonic distortion reduction [20]. This aligns with findings from who proposed an asymmetrical fuzzy logic control-based MPPT algorithm that simplified calculations while enhancing both dynamic and steady-state performance [21]. The results indicate that Type-2 fuzzy logic not only improves the tracking speed but also stabilizes the output power under fluctuating conditions, which is essential for maximizing energy yield from PV systems.

Moreover, the integration of T2FLCs with dual-axis solar tracking systems further enhances the effectiveness of MPPT strategies. It is demonstrated that combining Type-2 fuzzy logic with a photo-resistive tracking method significantly improved the power output of solar trackers, showcasing the synergy between advanced control strategies and tracking technologies [18]. This combination allows for continuous adjustment of the PV panels' orientation, ensuring optimal exposure to sunlight throughout the day, thereby maximizing energy capture.

Furthermore, the integration of Type-2 fuzzy logic with other control strategies, such as ANFIS, has shown promising results in enhancing MPPT performance. compared fuzzy logic and ANFIS-based MPPT controllers, revealing that the hybrid approach could leverage the strengths of both methodologies to improve tracking accuracy and efficiency [19]. This suggests that the future of MPPT in PV systems may lie in the combination of multiple intelligent control strategies to address the challenges posed by environmental variability.

The ongoing research into T2FLCs for MPPT continues to yield innovative solutions that enhance the efficiency and reliability of PV [20]. As the demand for renewable energy sources grows, the development of advanced control strategies that can adapt to changing conditions will be crucial in maximizing the potential of solar energy. The findings from various studies underscore the importance of Type-2 fuzzy logic in achieving optimal performance in MPPT applications, paving the way for more efficient and sustainable energy systems.

The aim of the paper is to develop and demonstrate the effectiveness of a T2FLC-based MPPT technique for PV systems. The goal is to improve power extraction efficiency under varying environmental conditions, such as fluctuating irradiance and temperature, by addressing the limitations of in T1FLCs. The paper seeks to highlight how the adaptive capabilities of the T2FLC can enhance tracking speed, reduce oscillations, and improve overall accuracy, ultimately contributing to the optimization of PV system performance and efficiency.

The primary distinction between our work and previous studies lies in the method used to implement the fuzzy logic control for MPPT in PV systems. In our approach, we introduce an original method that calculates the error between the output voltage and a reference voltage. Which is calculated by mathematic equation, this equation provides a precise value that dynamically adjusts according to variations in irradiance and temperature. By employing this mathematical model, the system is capable of calculating an accurate reference voltage, ensuring more precise and stable MPPT performance even under fluctuating environmental conditions. In contrast, many previous studies employ a more conventional approach to fuzzy logic control, often modifying the P&O algorithm by replacing its decision-making process with fuzzy logic [17, 21–24]. These approaches, which are commonly applied in both Type-1 and Type-2 fuzzy logic control, focus primarily on improving the efficiency of P&O by mitigating oscillations and improving response times [25–27]. However, these methods are limited by their reliance on fixed reference points or simplified control rules, which can reduce their effectiveness in highly dynamic environments. Our method's ability to generate a real-time, dynamically adjusted reference voltage offers a significant improvement in tracking accuracy and system stability.

PV system modelling. PV cell, also known as a solar cell, is the basic unit in a PV that converts sunlight directly into electrical energy through the PV effect. When sunlight (photons) hits the PV cell, it can excite electrons in the semiconductor material, creating free electrons (negative charge) and holes (positive charge).

The electric field at the P-N junction separates these charges, causing them to move in opposite directions and generate an electric current when connected to a load [5]. The single-diode model of a PV cell is expressed as:

$$I = I_{ph} - \frac{I_0}{e^{(V+IR_S)/nV_t} - 1} - \frac{V + IR_S}{nV_t}, \qquad (1)$$

where I is the output current; I_{ph} is the photocurrent; I_0 is the reverse saturation current; V is the terminal voltage; R_s is the series resistance; R_{sh} is the shunt resistance; n is the ideality factor; V_t is the thermal voltage.

Figure 1 illustrates the performance of a PV BP SX 60 system under varying temperature and irradiance conditions, with fuzzy logic Type-2 employed for MPPT, it demonstrates the influence of irradiation on the cell at a constant temperature (*a*) and the impact of temperature on the cell with a set level of irradiation (*b*).

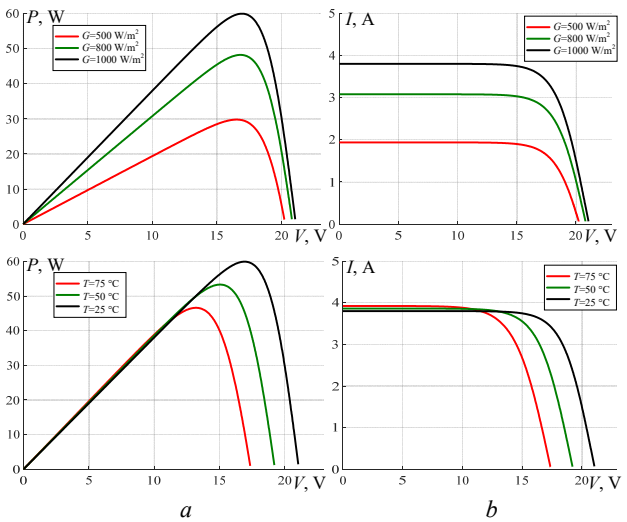

Fig. 1. The characteristics of $P(V)$ (*a*) and $I(V)$ (*b*) fluctuate with variations in environmental factors such as irradiation G and temperature T

Temperature impact.

- *I-V* curve: The *I-V* relationship at different temperatures: 25 °C, 50 °C, 75 °C demonstrates that as the temperature increases , the voltage decreases significantly which is typical behavior for PV cells. The current slightly increases with higher temperatures, but the overall power decreases due to the reduction in voltage.
- *P-V* curve: The P-V relationship shows that with increasing temperature (moving from black to red), the MPP shifts to a lower voltage and reduces in magnitude. The PV system loses efficiency as temperature increases, which is evident in the shift and reduction of the power output at 75 °C compared to 25 °C.

Irradiance impact.

- *I-V* curve: the *I-V* curve illustrates the effect of irradiance levels (500 W/m², 800 W/m², 1000 W/m²). As irradiance increases, both the current and voltage increase, improving the power output. The *I-V* curve shows that at higher irradiance (black line), the current significantly increases, which leads to a larger area under the curve, indicating more power generation.
- *P-V* curve: The *P-V* curve demonstrates the relationship between power and voltage under different irradiance conditions. As irradiance increases, the power output increases significantly, and the MPP shifts upwards. The PV system performs better at higher irradiance levels, with the MPP for 1000 W/m² being much higher than that for 500 W/m².

Type-2 fuzzy logic control. Fuzzy logic Type-2 and Type-1 display notable resemblances. However, there are two basic differences between them, specifically, the forms of the function membership and the output of the processor. The interval of Type-2 fuzzy logic control comprises multiple components, including a fuzzifier, an inference engine, type reduction, rule bases and a defuzzifier. This section offers a concise summary of the main characteristics of T2FLC and introduces important ideas associated with them [28].

Functions membership. T2FLC is distinguished by the configuration of their function membership. Figure 2 shows two distinct functions of membership: *a* – standard T1FLC membership function; *b* – fuzzy Type-1 functions membership that depicts a blurred representation Type-2 functions membership refers to a specific type of mathematical function used in fuzzy logic systems [29].

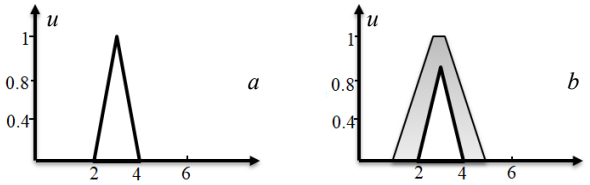

Fig. 2. Type-1 functions membership (*a*) and uncertainty footprint (*b*)

Definition 1. T2FLC system, represented as $\widetilde{A}$, is defined by a functions membership Type-2 $\mu_{\widetilde{A}} = (x, \mu)$, with $x \in X$ and $\mu \in J_x \subseteq [0, 1]$:

$$\widetilde{A} = \left\{\left((x,u), \mu_{\widetilde{A}}(x,u)\right)\right) \mid \forall x \in X, \forall u \in J_x \subseteq [0, 1]. \quad (2)$$

Type-2 function membership is a bivariate function that is contingent upon two variables, x and u. It is important to mention that $\mu_{\widetilde{A}} = (x, \mu)$ is a value that falls within the range of 0 to 1 [30]:

$$\widetilde{A} = \int_{x \in X} \int_{u \in J_x} \mu_{\widetilde{A}}(x,u) / (x,u) J_x \subseteq [0, 1], \quad (3)$$

where the symbol $\iint$ represents the union of all x and u.

Definition 2. $\widetilde{A}$ is an interval T2FLC system where the function membership $\mu_{\widetilde{A}}(x, \mu)$ is equal to 1 for all values of x and u [31].

Definition 3. The primary function membership of x refers to the scope of a secondary function membership. Thus, J_x represents the main membership of x. By employing this notation, the equation (3) can be restated as:

$$\widetilde{A} = \left\{\left((x,u), \mu_{\widetilde{A}}(x,u)\right)\right) \mid \forall x \in X. \quad (4)$$

Footprint of Uncertainty is the crucial parameter in T2FLC and is commonly employed in this paper. This term represents the ambiguity inside the system, providing a practical way to describe the complete range of the secondary function membership.

Definition 4. The uncertainty in the primary memberships of T2FLC is represented by a confined region referred to as the Fuzzy Output Universe (FOU). This region is the primary union of all function memberships [31], i.e.:

$$FOU\left(\widetilde{A}\right) = U_{x \in X} / J_x. \quad (5)$$

Definition 5. When the FOU of a T2FLC is constrained by two Type-1 functions membership, the upper function membership corresponds to the upper bound, denoted by $\overline{\mu}_{\widetilde{A}}(x), \forall x \in X$, and the lower function membership corresponds to the lower bound, noted by $\underline{\mu}_{\widetilde{A}}(x), \forall x \in X$. This relationship can be expressed as [32]:

$$\begin{aligned} \overline{\mu}_{\widetilde{A}} &= \overline{FOU\left(\widetilde{A}\right)}, \forall x \in X \\ \underline{\mu}_{\widetilde{A}} &= \underline{FOU\left(\widetilde{A}\right)}, \forall x \in X. \end{aligned} \quad (6)$$

Definition 6. An embedded Type-2 set $\widetilde{A}_e$ is provided for a continuous universe of discourse X and U [31]:

$$\widetilde{A} = \int_{x \in X} \left[f_x(\theta / \theta)\right] / x \ldots \ldots \theta \in J_x \subseteq [0, 1]. \quad (7)$$

The set $\widetilde{A}_e$ is a subset of set $\widetilde{A}$, and there exist an unlimited number of Type-2 sets.

T2FLC structure. Figure 3 illustrates the structure general of a T2FLC. This structure resembles that of a T1FLC, with the primary difference being the output processor. The output processor comprises two processes: type-reduction and defuzzification. The following sections will explain each component of Fig. 3 in detail.

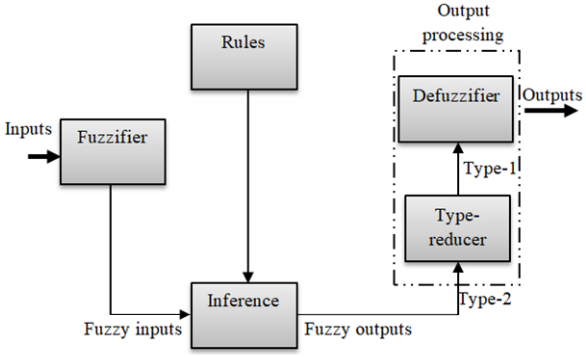

Fig. 3. Structure of T2FLC [31]

Fuzzifier. The initial block in Fig. 3 is the Fuzzifier, which converts the precise inputs into fuzzy values. The fuzzifier transforms the precise input vector $x^T = (x_1, x_2,...,x_n)^T$ into a Type-2 fuzzy system $\tilde{A}_x$, using a similar process as in a Type-1 fuzzy logic system.

Rules. The *i*-th rule in a Type-2 fuzzy logic system can be represented in the following generic form:

$$\text{If } x_1 \text{ is } \tilde{F}_1^i \text{ and } x_2 \text{ is } \tilde{F}_2^i \text{ and } \dots x_n \text{ is } \tilde{F}_n^i .$$

Than:

$$y^i = \tilde{G}^i , \tag{8}$$

where $i = 1,\dots, M$; $\tilde{F}_j^i$ represents the T2FLC for the input state j of the i-th rule, $x_1, x_2, \dots, x_n$ are the inputs, $\tilde{G}^i$ is the output of Type-2 fuzzy system for rule i, and M is the total number of rules. As can be seen, the rule structure of a T2FLC is almost identical to that of a Type-1, with the only difference being the replacement of Type-1 functions membership with their Type-2 equivalents.

Inference engine. In fuzzy system interval Type-2 using the minimum or product *t*-norm operations, the *i*-th activated rule is processed $F^i = (x_1,...,x_n)$ gives us the interval that is determined by two extreme:

$$\begin{aligned} &\underline{f}^i = (x_1, \dots, x_n) \quad \text{and} \quad \overline{f}^i = (x_1, \dots, x_n) \text{ [33];} \\ &F^i = (x_1, \dots, x_n) = \\ &= \left[\underline{f}^i = (x_1, \dots, x_n), \overline{f}^i = (x_1, \dots, x_n) \right] \equiv \left[\underline{f}^i, \overline{f}^i \right], \end{aligned} \tag{9}$$

where $\underline{f}^i$ and $\overline{f}^i$ are:

$$\begin{aligned} \underline{f}^i &= \underline{\mu}_{F_1^i}(x_1) \times \dots \times \underline{\mu}_{F_n^i}(x_n); \\ \overline{f}^i &= \overline{\mu}_{F_1^i}(x_1) \times \dots \times \overline{\mu}_{F_n^i}(x_n). \end{aligned} \tag{10}$$

Type reducer. T2FLC is calculated after the rules are triggered and inference is performed, resulting in a Type-1 fuzzy system. This section explores the techniques for calculating the centroid of a T2FLC using the extension concept [31]. The centroid of a Type-1 fuzzy system A can be mathematically represented as:

$$C_A = \sum_{i=1}^{n} z_i w_i \Big/ \sum_{i=1}^{n} w_i , \tag{11}$$

where n is the number of discretized domains of A, $z_i \in R$ and $W_i \in [0, 1]$.

If each z_i and w_i are replaced with a Type-1 fuzzy systems, Z_i and W_i, having associated functions membership of $\mu_Z(z_i)$ and $\mu_W(W_i)$ respectively, then by applying the extension principle, the generalized centroid for the Type-2 fuzzy $\tilde{A}$ is given by:

$$GC_{\tilde{A}} = \int_{z_1 \in Z_1} \dots \int_{z_n \in Z_n} \int_{w_1 \in W_1} \dots \int_{w_n \in W_n} \frac{\left[T_{i=1}^n \mu_Z(z_i) \cdot T_{i=1}^n \mu_W(z_i) \right]}{\sum_{i=1}^{n} z_i w_i \Big/ \sum_{i=1}^{n} w_i}, \tag{12}$$

where T is the *t*-norm; note that $GC_{\tilde{A}}$ is T1FLC. For interval of T2FLC:

$$GC_{\tilde{A}} = \int_{z_1 \in Z_1} \dots \int_{z_n \in Z_n} \int_{w_1 \in W_1} \dots \int_{w_n \in W_n} 1 \Big/ \frac{\sum_{i=1}^{n} z_i w_i}{\sum_{i=1}^{n} w_i} = [y_l, y_r]. \tag{13}$$

Karnik–Mendel algorithms. The well-known Karnik–Mendel techniques are used to determine the centroid of interval T2FLC, the most widely used Type-2 system. Initially, the expression (13) is written as:

$$\int_{f^M \in \left[\underline{f}^M, \overline{f}^M \right]} 1 \Big/ \frac{\sum_{i=1}^{M} f^i y^i}{\sum_{i=1}^{M} f^i} . \tag{14}$$

Iterative techniques are provided by the algorithms of Karnik–Mendel to calculate y_l, y_r in (14) as follows.

To calculate y_r:

1. For the sake of simplicity, let's assume that the values of y_{ri} are sorted in ascending order; i.e. $y_r^1 \le y_r^2 \le \dots \le y_r^M$

2. Compute y_r as $y_r = \sum_{i=1}^{M} f_r^i y_r^i \Big/ \sum_{i=1}^{M} f_r^i$ by initially setting $f_r^i = \frac{\underline{f}^i + \overline{f}^i}{2}$ for $i = 1,...,M$ and let $y_r' \equiv y_r$.

3. Locate R ($1 \le R \le M$–1r) such that $y_r^R \le y_r' \le y_r^{R+1}$

4. Compute $y_r = \sum_{i=1}^{M} f_r^i y_r^i \Big/ \sum_{i=1}^{M} f_r^i$ with $f_r^i = \underline{f}^i$ for $I \le R$ and $f_r^i = \overline{f}^i$ for $i > R$ and let $y_r'' \equiv y_r$.

5. If $y_r'' \ne y_r'$ then go to step 6. If $y_r'' = y_r'$, then stop and set $y_r'' \ne y_r$.

6. Return to step 3 after setting equal to y_r''.

The process of calculating y_l is highly analogous to that of computing y_r. Simply substitute y_r^i with y_l^i in step 3, find $L (1 \le L \le M$–1) such that In step 2, calculate y_l as $y_l = \sum_{i=1}^{M} f_l^i y_l^i \Big/ \sum_{i=1}^{M} f_l^i$ by initially setting $f_l^i = \frac{\underline{f}^i + \overline{f}^i}{2}$ for $i = 1,..,M$ and in step 4, calculate $y_l = \sum_{i=1}^{M} f_l^i y_l^i \Big/ \sum_{i=1}^{M} f_l^i$ with $f_l^i = \overline{f}^i$ for $i \le L$ and $f_l^i = \underline{f}^i$ for $i \ge L$.

Deffuzzifier. In order to achieve a clear and precise output from a T1FLC, it is necessary to defuzzify the type-reduced set. A widely used approach is to determine the centroid of the set after reducing its type. The centroid of the discretized set Y, consisting of m points, is determined as follows:

$$y_{output}(x) = \sum_{i=1}^{m} y^i \mu(y^i) \Big/ \sum_{i=1}^{m} \mu(y^i) . \tag{15}$$

The output is calculated using the algorithms of iterative Karnik–Mendel, which leads to the defuzzified output of an interval T2FLC:

$$y_{output}(x) = \frac{y_1(x) + y_r(x)}{2} . \tag{16}$$

Simulation studies. The fundamental structure of the system depicted in Fig. 4 is outlined as follows. To optimize the power output, a mathematical model is employed to calculate the reference voltage V_{ref}, which is dynamically adjusted based on environmental factors such as irradiance G and temperature T:

$$V_{ref} = \frac{N_S \cdot n \cdot k \cdot T}{q} \log\left(\frac{I_{ph} - I_{ref} + I_0}{I_0}\right), \qquad (17)$$

where N_S is the number of cells in series; n is the diode's ideality factor; k is the Boltzmann constant; q is the charge of the electron; T is the absolute temperature of the p-n junction; I_{ref} is the reference current.

MPPT is implemented using a T2FLC, which determines the optimal operating point of the PV system. The boost converter then adjusts the output voltage to match the calculated V_{ref}, ensuring that the system operates at maximum efficiency.

Simulation results are conducted utilizing the BP SX 60 PV module, which is widely recognized for its reliability in solar energy applications. Figure 4 illustrates the overall PV system architecture employing the T2FLC for MPPT, showcasing the integration of the PV module, the FLC and the DC-DC boost converter.

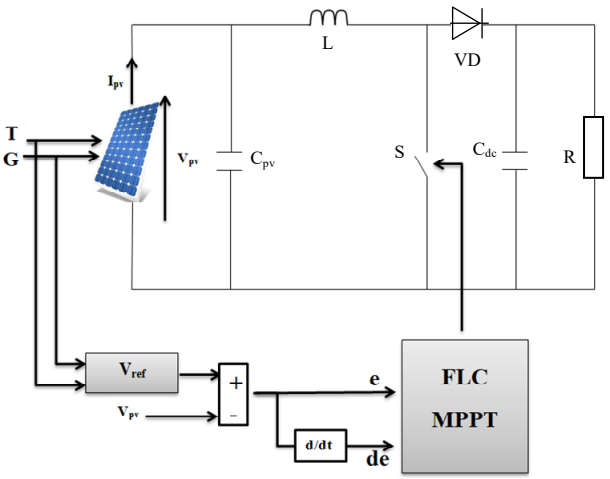

Fig. 4. PV system with FLC MPPT

The detailed parameters of the DC-DC boost converter are provided in Table 1. The simulation results were conducted using the BP SX 60 module and a boost converter.

Table 1

DC-DC boost parameters

Parameters	Values
C_{dc}, mF	$2 \cdot 10^{-4}$
C_{pv}, mF	$3 \cdot 10^{-4}$
L, H	$2 \cdot 10^{-2}$

Tables 2, 3 show the T2FLC membership function of output.

Table 2

T2FLC parameters

Controller	Parameters	Values
T2FLC	k_1	3
	k_2	4
	k_3	5

Table 3

T2FLC outputs membership function

ZE	S	M	B
0	0.3	0.7	1

Table 4 presents the T2FLC fuzzy rules, while Figure 5 illustrates the Type-2 fuzzy membership functions for the inputs. Figure 6 depicts the surface of the Type-2 fuzzy logic interval.

Table 4

T2FLC fuzzy rules

de/e	NB	NM	NS	ZE	PS	PM	PB
NB	B	M	S	ZE	S	M	B
NM	B	M	M	S	M	M	B
NS	B	B	M	M	M	B	B
ZE	B	B	B	B	B	B	B
PS	B	B	M	M	M	B	B
PM	B	M	M	S	M	M	B
PB	B	M	S	ZE	S	M	B

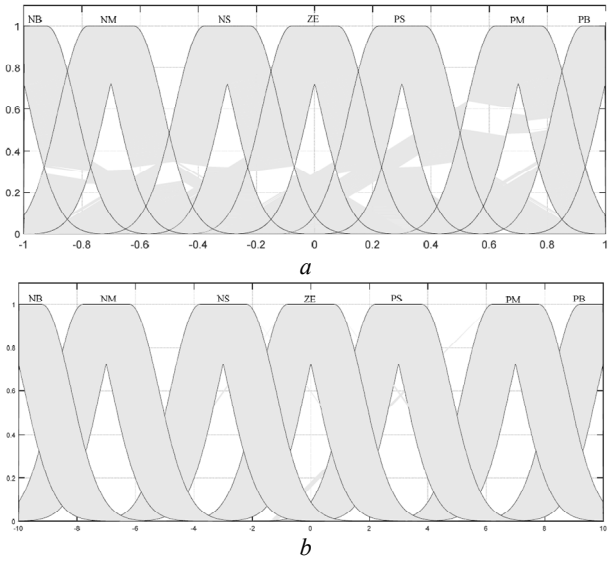

Fig. 5. Type-2 fuzzy function membership of inputs: a – error e; b – error variation de

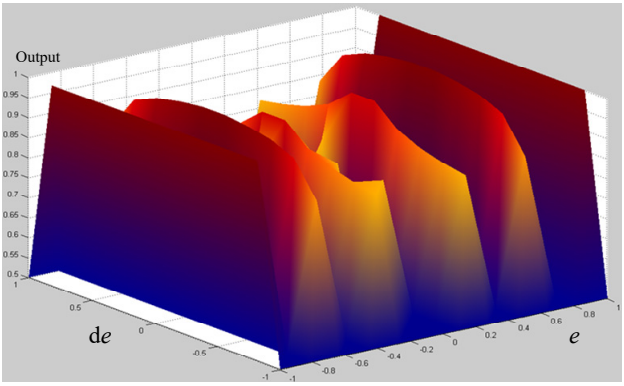

Fig. 6. Surface of the Type-2 fuzzy logic interval

Simulation results are conducted to analyze the effects of different levels of solar irradiation and normal conditions. Figure 7 shows the power and voltage outputs of the PV module under two different steps of irradiation G = 800 W/m^2 and G = 1000 W/m^2. The results depicted in Fig. 7 demonstrate that both fuzzy logic approaches (fuzzy Type-2 and fuzzy Type-1) successfully achieve MPP under varying irradiation levels. Specifically, at an irradiation level of 1000 W/m^2, both methods attain an MPP of 60 W, while at 800 W/m^2, they achieve an MPP of 48 W. These findings indicate the effectiveness of both fuzzy logic approaches in tracking MPP across different irradiation conditions, ensuring optimal power output.

Figure 8 shows the performance comparison between T2FLC and T1FLC-based MPPT methods, along with the reference voltage V_{ref}. The reference voltage was precisely calculated using a mathematical equation, which dynamically adjusts to these conditions.

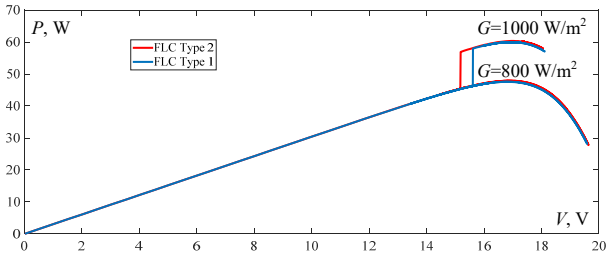

Fig. 7. *P-V* curves with T1FLC and T2FLC MPPT under two irradiation changes and fixed temperature $T = 25$ °C

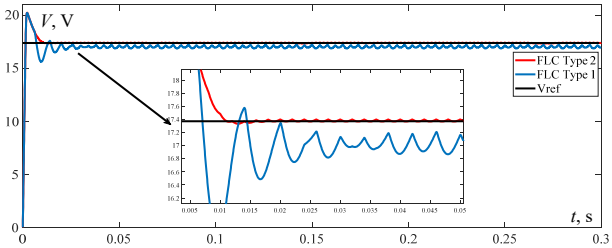

Fig. 8. Output voltage and the voltage reference with T1FLC and T2FLC MPPT under irradiation $G = 1000$ W/m^2 and $T = 25$ °C

Figure 9 shows a comparative analysis of T1FLC and T2FLC MPPT in the fixed step of irradiation $G = 1000$ W/m^2 and temperature $T = 25$ °C.

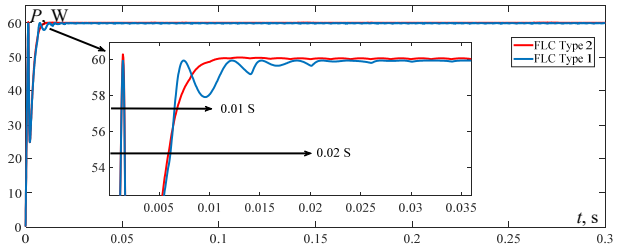

Fig. 9. Output power with T1FLC and T2FLC MPPT under irradiation $G = 1000$ W/m^2 and $T = 25$ °C

Figure 10 shows a comparative analysis of T1FLC and T2FLC MPPT in two variations of the steps of irradiation $G = 800$ W/m^2 and $G = 1000$ W/m^2 and $T = 25$ °C. Each change in irradiation level lasted for 0.01 s.

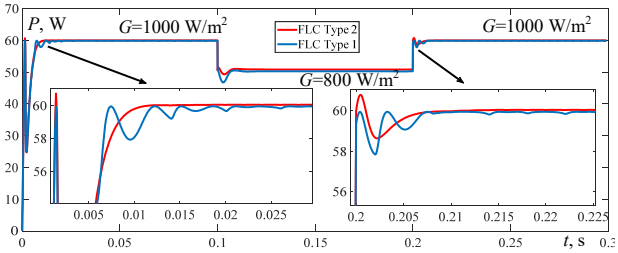

Fig. 10. Output power with T1FLC and T2FLC MPPT under two irradiation changes and fixed temperature $T = 25$ °C

In Fig. 9, 10 both controllers show an initial surge in power before stabilizing around 60 W. The surge happens quickly, within the first 0.01 s, as both controllers attempt to track the MPP. However, the T2FLC shows a smoother and quicker approach to the MPP compared to the T1FLC. It stabilizes almost 0.01 s before the T1FLC, indicating a faster dynamic response. This is crucial in PV systems, as faster MPPT leads to improved energy efficiency under rapidly changing environmental conditions.

Which is remains steady without any oscillations or error, highlighting the effectiveness of the mathematical equation in providing a highly accurate and stable target voltage. This accuracy is crucial for optimal MPPT performance, as it allows the system to converge to the correct operating point.

T2FLC quickly converges to the reference voltage with minimal oscillations, showcasing its superior performance in tracking the MPP with high precision and stability.

In contrast, the T1FLC exhibits more oscillations around the MPP and a slower convergence to the reference voltage, indicating less precision and stability in comparison to the T2FLC.

The inset zooms in on the initial response period, clearly showing the smooth tracking behavior of the T2FLC and the effectiveness of the reference voltage calculation. The mathematical equation provides a reference voltage that is precise, free from oscillations, and highly reliable, ensuring optimal MPPT performance with no error.

T1FLC exhibits more oscillations during the transient period compared to the T2FLC. These oscillations indicate that the T1FLC is slightly less stable than the T2FLC during the initial phase, which suggests improved stability and reduced power losses due to fluctuations. This could be attributed to the higher flexibility and adaptability of Type-2 fuzzy logic systems, which account for uncertainties better than Type-1 systems.

T2FLC outperforms T1FLC in terms of:

- faster settling time (0.01 s vs. 0.02 s);
- smoother power curve with fewer oscillations.

While both controllers eventually reach a similar steady-state power, the T2FLC demonstrates superior performance, especially in the transient period, which is critical for real-time PV applications where irradiance and temperature can change rapidly.

In summary, T2FLC provides better MPPT performance by reaching the MPP faster and with more stability than T1FLC. This makes it a preferable choice for optimizing PV system efficiency.

Conclusions. The proposed T2FLC-based MPPT system demonstrates significant improvements in the performance of PV systems under dynamic environmental conditions. The enhanced adaptability of the T2FLC, with its ability to manage higher levels of uncertainty through flexible membership functions, allows it to outperform traditional MPPT techniques such as P&O, IC and T1FLCs.

Simulation results validate the achievement of the paper's purpose by showing that the T2FLC-based MPPT system achieves faster response times, reduces power losses caused by oscillations around the MPP, and maintains high accuracy even under rapidly changing irradiance and temperature scenarios. These results confirm the system's ability to optimize energy extraction and improve the overall efficiency and reliability of PV systems.

This research successfully demonstrates the validity of the T2FLC as a robust and efficient control technique for renewable energy applications. By ensuring stable operation and optimizing power output, the T2FLC-based MPPT system offers a promising solution for advancing PV system performance in real-world conditions, thereby fulfilling the objective of enhancing power extraction efficiency under varying environmental conditions.

Conflict of interest. The authors declare that there is no conflict of interest.

REFERENCES

1. Sahraoui H., Mellah H., Drid S., Chrifi-Alaoui L. Adaptive maximum power point tracking using neural networks for a photovoltaic systems according grid. *Electrical Engineering & Electromechanics*, 2021, no. 5, pp. 57-66. doi: https://doi.org/10.20998/2074-272X.2021.5.08.

2. Lahiouel Y., Latreche S., Khemliche M., Boulemzaoud L. Photovoltaic fault diagnosis algorithm using fuzzy logic controller based on calculating distortion ratio of values. *Electrical Engineering & Electromechanics*, 2023, no. 4, pp. 40-46. doi: https://doi.org/10.20998/2074-272X.2023.4.06.
3. Boudia A., Messalti S., Harrag A., Boukhnifer M. New hybrid photovoltaic system connected to superconducting magnetic energy storage controlled by PID-fuzzy controller. *Energy Conversion and Management*, 2021, vol. 244, art. no. 114435. doi: https://doi.org/10.1016/j.enconman.2021.114435.
4. Li X., Wang Q., Wen H., Xiao W. Comprehensive Studies on Operational Principles for Maximum Power Point Tracking in Photovoltaic Systems. *IEEE Access*, 2019, vol. 7, pp. 121407-121420. doi: https://doi.org/10.1109/ACCESS.2019.2937100.
5. Assam B., Abderahim Z., Sabir M., Abdelghani H., Boukhnifer M. Modeling and Control Of Grid-PV-SMES System. *2022 International Conference of Advanced Technology in Electronic and Electrical Engineering (ICATEEE)*, 2022, pp. 1-4. doi: https://doi.org/10.1109/ICATEEE57445.2022.10093729.
6. Zerzouri N., Ben Si Ali N., Benalia N. A maximum power point tracking of a photovoltaic system connected to a three-phase grid using a variable step size perturb and observe algorithm. *Electrical Engineering & Electromechanics*, 2023, no. 5, pp. 37-46. doi: https://doi.org/10.20998/2074-272X.2023.5.06.
7. Mao M., Cui L., Zhang Q., Guo K., Zhou L., Huang H. Classification and summarization of solar photovoltaic MPPT techniques: A review based on traditional and intelligent control strategies. *Energy Reports*, 2020, vol. 6, pp. 1312-1327. doi: https://doi.org/10.1016/j.egyr.2020.05.013.
8. Sarvi M., Azadian A. A comprehensive review and classified comparison of MPPT algorithms in PV systems. *Energy Systems*, 2022, vol. 13, no. 2, pp. 281-320. doi: https://doi.org/10.1007/s12667-021-00427-x.
9. Sharma A.K., Pachauri R.K., Choudhury S., Minai A.F., Alotaibi M.A., Malik H., Marquez F.P.G. Role of Metaheuristic Approaches for Implementation of Integrated MPPT-PV Systems: A Comprehensive Study. *Mathematics*, 2023, vol. 11, no. 2, art. no. 269. doi: https://doi.org/10.3390/math11020269.
10. Gonzalez-Castano C., Restrepo C., Kouro S., Rodriguez J. MPPT Algorithm Based on Artificial Bee Colony for PV System. *IEEE Access*, 2021, vol. 9, pp. 43121-43133. doi: https://doi.org/10.1109/ACCESS.2021.3066281.
11. Pathak P.K., Yadav A.K. Design of battery charging circuit through intelligent MPPT using SPV system. *Solar Energy*, 2019, vol. 178, pp. 79-89. doi: https://doi.org/10.1016/j.solener.2018.12.018.
12. Al-Majidi S.D., Abbod M.F., Al-Raweshidy H.S. A particle swarm optimisation-trained feedforward neural network for predicting the maximum power point of a photovoltaic array. *Engineering Applications of Artificial Intelligence*, 2020, vol. 92, art. no. 103688. doi: https://doi.org/10.1016/j.engappai.2020.103688.
13. Ullah K., Ishaq M., Tchier F., Ahmad H., Ahmad Z. Fuzzy-based maximum power point tracking (MPPT) control system for photovoltaic power generation system. *Results in Engineering*, 2023, vol. 20, art. no. 101466. doi: https://doi.org/10.1016/j.rineng.2023.101466.
14. Loukil K., Abbes H., Abid H., Abid M., Toumi A. Design and implementation of reconfigurable MPPT fuzzy controller for photovoltaic systems. *Ain Shams Engineering Journal*, 2020, vol. 11, no. 2, pp. 319-328. doi: https://doi.org/10.1016/j.asej.2019.10.002.
15. Muthubalaji S., Devadasu G., Srinivasan S., Soundiraraj N. Development and validation of enhanced fuzzy logic controller and boost converter topologies for a single phase grid system. *Electrical Engineering & Electromechanics*, 2022, no. 5, pp. 60-66. doi: https://doi.org/10.20998/2074-272X.2022.5.10.
16. Ali M.N., Mahmoud K., Lehtonen M., Darwish M.M.F. Promising MPPT Methods Combining Metaheuristic, Fuzzy-Logic and ANN Techniques for Grid-Connected Photovoltaic. *Sensors*, 2021, vol. 21, no. 4, art. no. 1244. doi: https://doi.org/10.3390/s21041244.
17. Verma P., Garg R., Mahajan P. Asymmetrical interval type-2 fuzzy logic control based MPPT tuning for PV system under partial shading condition. *ISA Transactions*, 2020, vol. 100, pp. 251-263. doi: https://doi.org/10.1016/j.isatra.2020.01.009.
18. Abadi I., Uyuniyah Q., Nur Fitriyanah D., Jani Y., Abdullah K. Performance Study of Maximum Power Point Tracking (MPPT) Based on Type-2 Fuzzy Logic Controller on Active Dual Axis Solar Tracker. *E3S Web of Conferences*, 2020, vol. 190, art. no. 00016. doi: https://doi.org/10.1051/e3sconf/202019000016.
19. Pratama D.A., Damsi F., Zarkasih M.S. Simulation of Maximum Power Point Tracking with Fuzzy Logic Control Method on Solar Panels Using MATLAB. *Jurnal Teknologi Informasi Dan Pendidikan*, 2024, vol. 17, no. 1, pp. 138-148 doi: https://doi.org/10.24036/jtip.v17i1.731.
20. Li I.-H. Design for a Fluidic Muscle Active Suspension Using Parallel-Type Interval Type-2 Fuzzy Sliding Control to improve Ride Comfort. *International Journal of Fuzzy Systems*, 2022, vol. 24, no. 3, pp. 1719-1734. doi: https://doi.org/10.1007/s40815-021-01229-0.
21. Rahman A.F.S., Fattah A., Asni A., Waruni M., Kasrani, Ardiansyah W. Fuzzy Logic Control System for Optimizing Dual-Axis Solar Panel Tracking. *E3S Web of Conferences*, 2024, vol. 500, art. no. 03021. doi: https://doi.org/10.1051/e3sconf/202450003021.
22. Magaji N., Mustafa M.W. Bin, Lawan A.U., Tukur A., Abdullahi I., Marwan M. Application of Type 2 Fuzzy for Maximum Power Point Tracker for Photovoltaic System. *Processes*, 2022, vol. 10, no. 8, art. no. 1530. doi: https://doi.org/10.3390/pr10081530.
23. Kececioglu O.F., Gani A., Sekkeli M. Design and Hardware Implementation Based on Hybrid Structure for MPPT of PV System Using an Interval Type-2 TSK Fuzzy Logic Controller. *Energies*, 2020, vol. 13, no. 7, art. no. 1842. doi: https://doi.org/10.3390/en13071842.
24. Bakkar M., Aboelhassan A., Abdelgeliel M., Galea M. PV Systems Control Using Fuzzy Logic Controller Employing Dynamic Safety Margin under Normal and Partial Shading Conditions. *Energies*, 2021, vol. 14, no. 4, art. no. 841. doi: https://doi.org/10.3390/en14040841.
25. Merchaoui M., Hamouda M., Sakly A., Mimouni M.F. Fuzzy logic adaptive particle swarm optimisation based MPPT controller for photovoltaic systems. *IET Renewable Power Generation*, 2020, vol. 14, no. 15, pp. 2933-2945. doi: https://doi.org/10.1049/iet-rpg.2019.1207.
26. Subramanian V., Indragandhi V., Kuppusamy R., Teekaraman Y. Modeling and Analysis of PV System with Fuzzy Logic MPPT Technique for a DC Microgrid under Variable Atmospheric Conditions. *Electronics*, 2021, vol. 10, no. 20, art. no. 2541. doi: https://doi.org/10.3390/electronics10202541.
27. Hong Y.-Y., Buay P.M.P. Robust design of type-2 fuzzy logic-based maximum power point tracking for photovoltaics. *Sustainable Energy Technologies and Assessments*, 2020, vol. 38, art. no. 100669. doi: https://doi.org/10.1016/j.seta.2020.100669.
28. Sajan C., Satish Kumar P., Virtic P. Enhancing grid stability and low voltage ride through capability using type 2 fuzzy controlled dynamic voltage restorer. *Electrical Engineering & Electromechanics*, 2024, no. 4, pp. 31-41. doi: https://doi.org/10.20998/2074-272X.2024.4.04.
29. Zeghlache S., Djerioui A., Benyettou L., Benslimane T., Mekki H., Bouguerra A. Fault tolerant control for modified quadrotor via adaptive type-2 fuzzy backstepping subject to actuator faults. *ISA Transactions*, 2019, vol. 95, pp. 330-345. doi: https://doi.org/10.1016/j.isatra.2019.04.034.
30. Tan W.W., Chua T.W. Uncertain Rule-Based Fuzzy Logic Systems: Introduction and New Directions (Mendel, J.M.; 2001) [book review]. *IEEE Computational Intelligence Magazine*, 2007, vol. 2, no. 1, pp. 72-73. doi: https://doi.org/10.1109/MCI.2007.357196.
31. Mendel J.M., John R.I., Liu F. Interval Type-2 Fuzzy Logic Systems Made Simple. *IEEE Transactions on Fuzzy Systems*, 2006, vol. 14, no. 6, pp. 808-821. doi: https://doi.org/10.1109/TFUZZ.2006.879986.
32. Qilian Liang, Mendel J.M. Interval type-2 fuzzy logic systems: theory and design. *IEEE Transactions on Fuzzy Systems*, 2000, vol. 8, no. 5, pp. 535-550. doi: https://doi.org/10.1109/91.873577.
33. Mendel J.M. On answering the question "Where do I start in order to solve a new problem involving interval type-2 fuzzy sets?" *Information Sciences*, 2009, vol. 179, no. 19, pp. 3418-3431. doi: https://doi.org/10.1016/j.ins.2009.05.008.

Received 11.08.2024
Accepted 02.10.2024
Published 02.01.2025

A. Boudia[1], *Associate Professor,*
S. Messalti[1], *Professor,*
S. Zeghlache[1], *Professor,*
A. Harrag[2], *Professor,*
[1] University of M'sila, Algeria,
e-mail: assam.boudia@univ-msila.dz (Corresponding Author).
[2] Ferhat Abbas University Setif 1, Algeria.

How to cite this article:
Boudia A., Messalti S., Zeghlache S., Harrag A. Type-2 fuzzy logic controller-based maximum power point tracking for photovoltaic system. *Electrical Engineering & Electromechanics*, 2025, no. 1, pp. 16-22. doi: https://doi.org/10.20998/2074-272X.2025.1.03

UDC 621.314 https://doi.org/10.20998/2074-272X.2025.1.04

F. Laouafi

Improved grey wolf optimizer for optimal reactive power dispatch with integration of wind and solar energy

*The **aim** of this paper is to present a new improved grey wolf optimizer (IGWO) to solve the optimal reactive power dispatch (ORPD) problem with and without penetration of renewable energy resources (RERs). It is a nonlinear multivariable problem of optimization, with multiconstraints. The purpose is to minimize real power losses and improve the voltage profile of a given electric system by adjusting control variables, such as generator voltages, tap ratios of a transformer, switching VAr sources, without violating technical constraints that are presented as equalities and inequalities. **Methodology**. Metaheuristics are stochastic algorithms that can be applied to solve a wide variety of optimization problems without needing specific problem structure information. The penetration of RERs into electric power networks has been increased considerably to reduce the dependence of conventional energy resources, reducing the generation cost and greenhouse emissions. It is essential to include these sources in power flow studies. The wind and photovoltaic based systems are the most applied technologies in electrical systems compared to other technologies of RERs. Moreover, grey wolf optimizer (GWO) is a powerful metaheuristic algorithm that can be used to solve optimization problems. It is inspired from the social hierarchy and hunting behavior of grey wolves in the wild. **The novelty.** This paper presents an IGWO to solve the ORPD problem in presence of RERs. **Methods.** The IGWO based on enhancing the exploitation phase of the conventional GWO. The robustness of the method is tested on the IEEE 30 bus test system. For the control variables, a mixed representation (continuous/discrete), is proposed. The obtained **results** demonstrate the effectiveness of the introduced improvement and ability of the proposed algorithm for finding better solutions compared to other presented methods.* References 40, tables 3, figures 9.

Key words: **optimal reactive power dispatch, renewable energy resources, wind energy, solar energy, improved grey wolf optimizer.**

***Метою** статті є представлення нового покращеного оптимізатора сірого вовка (IGWO) для вирішення задачі оптимального розподілу реактивної потужності (ORPD) із застосуванням відновлюваних джерел енергії (RERs) та без них. Це нелінійне багатовимірне завдання оптимізації з безліччю обмежень. Мета полягає в тому, щоб мінімізувати реальні втрати потужності і покращити профіль напруги заданої електричної системи шляхом регулювання змінних керуючих, таких як напруги генератора, коефіцієнти відгалужень трансформатора, перемикання джерел реактивної потужності, не порушуючи технічних обмежень, які представлені у вигляді рівностей і нерівностей. **Методологія**. Метаевристика – це стохастичні алгоритми, які можна застосовувати для вирішення широкого спектра задач оптимізації без необхідності конкретної інформації про структуру проблеми. Проникнення RER в електромережі значно зросла задля зниження залежності від традиційних джерел енергії, зниження вартості генерації та викидів парникових газів. Вкрай важливо включити ці джерела до дослідження потоків потужності. Системи на основі вітру та фотоелектрики є найбільш застосовуваними технологіями в електричних системах порівняно з іншими технологіями RERs. Більш того, оптимізатор сірого вовка (GWO) – це потужний метаевристичний алгоритм, який можна використовувати для розв'язання оптимізації задач. Він натхненний соціальною ієрархією та мисливською поведінкою сірих вовків у дикій природі. **Новизна**. У цій статті представлено IGWO для вирішення проблеми ORPD при наявності RERs. **Методи**. IGWO, заснований на покращенні фази експлуатації звичайного GWO. Надійність методу перевірена на тестовій системі шини IEEE 30. Для керуючих змінних запропоновано змішане уявлення (безперервне/дискретне). **Отримані результати** демонструють ефективність введеного покращення та здатність запропонованого алгоритму знаходити кращі рішення порівняно з іншими методами.* Бібл. 40, табл. 3, рис. 9.

Ключові слова: **оптимальний розподіл реактивної потужності, відновлювані джерела енергії, енергія вітру, сонячна енергія, покращений оптимізатор сірого вовка.**

Introduction. The development of an optimal solution for the operation and management of electrical networks was initiated in 1958 by L.K. Kirchmayer [1], with the goal of minimizing the operational cost of supplying electrical energy to a given load. Thus, the problem evolved into a dispatch problem. At that time, significant progress had been made in the ordinary power flow, and the use of computers showed promising potential. Consequently, analysts tried to incorporate this success into the field of optimal power flow (OPF). In 1962, J. Carpentier introduced for the first time the OPF problem [2], which was further developed by H. Dommel and W. Tinney [3]. Since then, the OPF has generated significant interest among researchers focused on power system operation and planning.

The optimal reactive power dispatch (ORPD) problem is a specific case of the OPF problem and has an increasingly important role in enhancing the reliability, security, and economic efficiency of power systems [4, 5]. It is a multi-constraints nonlinear multivariable problem of optimization that aims to get the best profile of the voltage and reduction of power losses by adjusting a set of control variable values including the voltages of generator, shunt VAR reactive compensators and the tap changing of the transformers. Meanwhile, optimization constraints generator reactive power capabilities, voltages of load bus and power balance must be satisfied.

In the past few decades, numerous optimization techniques have been studied to solve this kind of problems after using some simplifications and special treatments [6, 7]: gradient-based approach, linear programming, interior point, quadratic programming and non-linear programming. However, all these techniques have some of difficulties to solve the intricated problem of ORPD such as:

- trapping into the local minima;
- premature convergence;
- the algorithmic complexity;
- large iteration number;
- sensitivity to an initial search point;
- limited modeling capabilities (in handling nonlinear, discontinuous functions and constraints, etc.).

With the advancement of soft computing during the last years, these problems can be overcome by the introduction of many new stochastic search methods developed for global optimization problems.

Metaheuristics are stochastic algorithms for solving a wide range of problems for which there is no known effective conventional methods. These techniques are often inspired from biology (evolutionary algorithms [8–13], differential evolution [14–18]), physics (simulated annealing [19, 20], Archimedes optimization algorithm [21]) and ethnology (ant colony optimization [22], particle swarm optimization (PSO) [23, 24], honey bee mating optimization [25], firefly algorithm [26], grey wolf optimizer (GWO) [27–30]). In order to improve the performance of optimization algorithms, some authors have proposed hybrid algorithms [31–34].

Nowadays, the contribution of renewable energy resources (RERs) in electric power system is intensively considered [35–40]. This integration leads to reducing greenhouse emissions, generation fuel cost, and enhancing the system operation. The most applied technologies for RERs are the wind and photovoltaic (PV) energy generation systems.

On the other side, GWO is a powerful metaheuristic method that has few parameters to be set, and it is easy to use it for solving ORPD problem.

The **aim** of this paper is to present a new improved grey wolf optimizer (IGWO) to solve ORPD problem with and without penetration of RERs. The IGWO is used to increase the diversity of solutions and resist premature convergence. The proposed algorithm is tested on the IEEE 30 bus test system.

Problem formulation. Minimization problems with constraints are generally expressed in the following form:

$$\begin{aligned} &\text{Minimize}: f(x), \\ &\text{Subject to}: h_i(x)=0, \quad i=0,...,m; \\ &\qquad\qquad g_j(x)\le 0, \quad j=0,...,n, \end{aligned} \tag{1}$$

where m is the number of equality constraints; n is the number of inequality constraints; $f(x)$ is the objective function; $h_i(x)$ is the equality constraint; $g_j(x)$ is the inequality constraint;

The number of variables is equal to the dimension of the vector $\boldsymbol{x}$.

The main objectives of the ORPD are to reduce transmission losses and improve the voltage profile in a power system. The total losses are represented as:

$$f(x)=p=\sum_{k\in N_B}P_{kLoss}=\sum_{k\in N_B}g_{ij}\left(V_i^2+V_j^2-2V_iV_j\cos\theta_{ij}\right), \tag{2}$$

where k is the branch between buses i and j; N_B is the set of branch numbers; P_{kLoss} is the active power loss of branch k; g_{ij} is the conductance of the branch existing between the buses i and j; V_i, V_j are the voltage profiles at bus i and j respectively; θ_{ij} is the phase angle of voltage between buses i and j.

The objective function $f(x)$ is constrained by a number of equality constraints (real and reactive power balance at each node) which are associated with the load flow:

$$P_{gi}-P_{di}-V_i\sum_{j\in N_i}V_j\left(G_{ij}\cos\theta_{ij}+B_{ij}\sin\theta_{ij}\right)=0, i\in N_0, \tag{3}$$

$$Q_{gi}-Q_{di}-V_i\sum_{j\in N_i}V_j\left(G_{ij}\sin\theta_{ij}-B_{ij}\cos\theta_{ij}\right)=0, i\in N_{PQ}, \tag{4}$$

Inequality constraints of control variables are given as:

$$T_{i\min}\le T_i\le T_{i\max}, \quad i\in N_T; \tag{5}$$

$$Q_{gi\min}\le Q_{gi}\le Q_{gi\max}, \quad i\in N_{cap}; \tag{6}$$

$$V_{i\min}\le V_i\le V_{i\max}, \quad i\in N_{PV}. \tag{7}$$

Inequality constraints of state variables are written as:

$$V_{i\min}\le V_i\le V_{i\max}, \quad i\in N_{PQ}; \tag{8}$$

$$Q_{gi\min}\le Q_{gi}\le Q_{gi\max}, \quad i\in N_{PV}, \tag{9}$$

where P_{gi} is the generated active power at bus i; Q_{gi} is the generated reactive power at bus i; P_{di} is the active power load at bus i; Q_{di} is the reactive power load at bus i; G_{ij} is the transfer conductance between buses i and j; B_{ij} is the transfer susceptance between buses i and j; N_i is the set of the bus numbers adjacent to bus i including bus i; N_0 is the set of the bus numbers except the swing bus; N_{PQ} is the set of PQ bus (load bus) numbers; N_{PV} is the set of PV bus (generator bus) numbers containing swing bus; T_i is the tap-setting of the transformer i; N_T is the set containing the numbers of tap-setting transformer branches; N_{cap} is the set of bus numbers containing shunt compensator banks.

Control variables, including generator bus voltage, transformer tap settings, and switchable shunt capacitor banks, are inherently constrained. Meanwhile, load bus voltages and reactive power generation are state variables; with their limitations incorporated into the objective function as quadratic penalty terms, forming a penalty function:

$$\begin{aligned} \min F(x)=p+&\sum_{i\in N_{PQ}}\lambda_{V_i}(V_i-V_i^{\lim})^2+\\ &+\sum_{i\in N_{PV}}\lambda_{Q_{gi}}(Q_{gi}-Q_{gi}^{\lim})^2. \end{aligned} \tag{10}$$

This new formulation of the objective function is constrained by the equality constraints (3) – (4) and inequality constraints of control variables (5) – (7). The coefficients λ_{V_i} and $\lambda_{Q_{gi}}$ serve as penalty factors:

$$V_i^{\lim}=\begin{cases} V_{i\min} & \text{if} \quad V_i<V_{i\min}; \\ V_{i\max} & \text{if} \quad V_i>V_{i\max}; \\ V_i & \text{if} \quad V_{i\min}\le V_i\le V_{i\max}; \end{cases} \tag{11}$$

$$Q_{gi}^{\lim}=\begin{cases} Q_{gi\min} & \text{if} \quad Q_{gi}<Q_{gi\min}; \\ Q_{gi\max} & \text{if} \quad Q_{gi}>Q_{gi\max}; \\ Q_{gi} & \text{if} \quad Q_{gi\min}\le Q_{gi}\le Q_{gi\max}. \end{cases} \tag{12}$$

Mathematical modelling of RERs.

1) *Model of wind power.* A wind turbine generates power output according to the wind speed it encounters. The relationship between output power and wind speed (v_w) is expressed as [36, 37]:

$$P_{wt}(v_w)=\begin{cases} 0 & \text{for} \quad v_w\le v_{w,in} \text{ and } v_{w,out}\le v_w; \\ P_{wr}\left(\dfrac{v_w-v_{w,in}}{v_{w,r}-v_{w,in}}\right) & \text{for} \quad v_{w,in}\le v_w\le v_{w,r}; \\ P_{wr} & \text{for} \quad v_{w,r}\le v_w\le v_{w,out}, \end{cases} \tag{13}$$

where P_{wr} is the rated power generated by the wind turbine while $v_{w,in}$, $v_{w,r}$ and $v_{w,out}$, denote the cut-in, rated, and cut-out wind speed, respectively.

The active and reactive generated powers of the wind farm are depicted as [37]:

$$P_{wf}=P_{wt}\cdot N_{wt}; \quad Q_{wf}=\frac{P_{wf}}{\cos\phi}\sqrt{1-\cos\varphi}, \tag{14}$$

where P_{wf} , Q_{wf} are the active and reactive power respectively generated by the wind farm; N_{wt} is the number of the wind turbines connected in a wind farm; $\cos\varphi$ is the power factor.

2) *Model of solar power*. The output of the solar PV units also fluctuates due to daily and seasonally variation in solar irradiation, which causes a change in the power system. The solar irradiance G_s to energy conversion is given by following relationship with maximum output power limited to the PV unit rated power P_{sr}:

$$P_s(G_s)=\begin{cases} P_{sr}\left(\dfrac{G_s^2}{G_{std}\cdot R_c}\right) & \text{for} \quad 0\le G_s\le R_c; \\ P_{sr}\left(\dfrac{G_s}{G_{std}}\right) & \text{for} \quad G_s\ge R_c, \end{cases} \tag{15}$$

where P_{sr} is the equivalent rated power output of the PV generator; R_c, is the certain irradiance point set as 120 W/m^2; G_{std} is the solar irradiation in standard environment, set as 1000 W/m^2.

3) *Effect of the wind and solar powers in ORPD*. Wind and solar power significantly influence the dispatch solution of the ORPD problem. The integrated mathematical formulation of ORPD, which includes wind farms and PV systems, is presented in (16). It's important to note that this equation describes a balanced power flow in the system, taking into account RERs:

$$\begin{cases} P_{gi}+P_{wf}+P_s=P_{di}+V_i\sum\limits_{j\in N_i}V_j\left(G_{ij}\cos\theta_{ij}+B_{ij}\sin\theta_{ij}\right); \\ Q_{gi}+Q_{wf}+Q_s=Q_{di}+V_i\sum\limits_{j\in N_i}V_j\left(G_{ij}\sin\theta_{ij}-B_{ij}\cos\theta_{ij}\right). \end{cases} \tag{16}$$

Today, PV inverters operate with a very small amount of reactive power, resulting in a power factor that is very close to the unit. As a result, PV installations only inject active power into the grid.

Grey wolf optimizer. GWO is a metaheuristic optimization method that mimics the social hierarchy and hunting mechanism of grey wolves. This algorithm was first introduced in [27]. Wolves are classified into 4 main groups:

- Alpha (α) – the leader of the pack;
- Beta (β) – the second in command;
- Delta (δ) – the third in command;
- the remaining wolves are considered Omegas (ω).

The positions of the wolves are updated based on the positions of the 3 best wolves (Alpha, Beta and Delta). The GWO search algorithm begins with a group of search agents, also known as design solutions (X).

The reproduction process involves the following 3 main operators: *social hierarchy*, *encircling prey* and *hunting*.

1) *Social hierarchy*. The social hierarchy of grey wolves classifies them into 4 groups based on their objective function values. The groups are Alpha (α) for the best, Beta (β) for the second best, and Delta (δ) for the third best, while the remaining wolves are assigned to the Omega (ω) group.

2) *Encircling prey*. The process of encircling prey by grey wolves for hunting can be mathematically defined as:

$$D=\left|\, C\cdot X_p(t)-X(t)\,\right|; \tag{17}$$

$$X(t+1)=X_p(t)-A\cdot D, \tag{18}$$

where:

$$A=2\cdot a\cdot r_1-a; \tag{19}$$

$$C=2\cdot r_2, \tag{20}$$

where t is the current iteration; A, C are the coefficient vectors; X_p is the position vector of the prey; X is the position vector of a grey wolf; r_1, r_2 are the uniform random vectors whose elements are generated randomly within the range [0, 1] [27]. The magnitude of A is allowed to be large initially to encourage exploration and it is gradually reduced to get good exploitation in later iterations.

The components of a are linearly decreased from 2 to 0 throughout the optimization process. It can be formulated as:

$$a=2-\frac{2\cdot t}{\text{maximum number of iterations}}. \tag{21}$$

3) *Hunting*. In the hunting phase, the positions of the grey wolves Alpha (X_α), Beta (X_β) and Delta (X_δ), as defined in the social hierarchy play a crucial role. These 3 agents collectively influence a new search at iteration t, which is referred to as the hunting operator as:

$$D_\alpha=\left|\, C_1\cdot X_\alpha(t)-X(t)\,\right|; \tag{22}$$

$$D_\beta=\left|\, C_2\cdot X_\beta(t)-X(t)\,\right|; \tag{23}$$

$$D_\delta=\left|\, C_3\cdot X_\delta(t)-X(t)\,\right|; \tag{24}$$

$$X_1=X_\alpha(t)-A_1\cdot D_\alpha; \tag{25}$$

$$X_2=X_\beta(t)-A_2\cdot D_\beta; \tag{26}$$

$$X_3=X_\delta(t)-A_3\cdot D_\delta. \tag{27}$$

A new grey wolf position, or the next generation, can then be determined as:

$$X(t+1)=\frac{X_1+X_2+X_3}{3}. \tag{28}$$

Once all new agents or design solutions are generated, the function evaluations of these agents are carried out. The process is repeated until a termination condition is met. A pseudo-code for the GWO algorithm applied to ORPD is illustrated in Fig. 1.

Initial system data, Number of search agent, Number of iterations,
Initialize the grey wolf population X_i within the limits of their control variables.
Initialize a, A, C.
Evaluate the fitness of each search agent (run Newton–Raphson load flow)
Determine:
X_α = the best search agent
X_β = the second best search agent
X_δ = the third best search agent
while (t<max number of iterations)
for each search agent
Update the position of the current search agent by equation (28) (within their limits of control variables)
end for
Update a, A, C.
Calculate the fitness of all search agents (using Newton–Raphson load flow)
Update X_α, X_β, X_δ
$t = t + 1$
end while
return X_α.

Fig. 1. Pseudo code of the GWO algorithm for ORPD

Improved grey wolf optimizer. In this work, the reproduction process of the original GWO is modified. Rather than averaging the positions of X_1, X_2 and X_3 as with (28), the reproduced solution $X(t + 1)$ has 2 possible

choices to be modified as shown in (29). Those choices have equal probability to take place. The modification of this step is expected to provide better population diversity.

$$X(t+1)=\begin{cases}\dfrac{X_1+X_2}{2} & \text{if} \quad p<0.5\,;\\ \dfrac{X_1+X_2+X_3}{3} & \text{if} \quad p\geq 0.5\,,\end{cases} \tag{29}$$

where $p\in[0, 1]$ is the uniform random number generated a new for each agent.

Simulation and results.

1) *Data of the studied network*. In this section, we evaluate the IGWO algorithm for solving the ORPD problem with and without integration of RERs: wind and solar energy. This assessment utilizes the IEEE 30-bus test system, which includes 30 buses, 41 branches, 6 generators, 4 tap-setting transformers, and 9 VAR switching sources. Bus 1 is the swing bus, while buses 2, 5, 8, 11, and 13 are designated as PV buses. The possible locations for reactive power installations are buses 10, 12, 15, 17, 20, 21, 23, 24, and 29. The tap-setting transformers are located on branches (6–9), (6–10), (4–12) and (28–27). System data is referenced from sources [17, 24]. The used base of power is S_B = 100 MVA.

2) *Load flow calculation*. At the beginning, the load flow calculation is done without consideration of the powers of RERs. The Newton–Raphson method results, shown in Table 1, indicate a total transmission loss of 5.8223 MW. Voltages exceeding the acceptable limits are observed at buses $V_{19} - V_{27}$, V_{29} and V_{30}. It is crucial to adjust the control variables to minimize transmission losses and enhance the voltage profile in the network. It should be noted that constraints for control and state variables are shown in Table 2, 3 respectively.

Table 1

Load flow results

Bus	Voltage		Load		Generation	
	V, pu	θ, °	P_d, pu	Q_d, pu	P_g, pu	Q_g, pu
1	1.0500	0	0	0	0.9922	–0.0153
2	1.0400	–1.7623	0.217	0.127	0.8000	0.1564
3	1.0279	–3.9323	0.024	0.012	0	0
4	1.0222	–4.6963	0.076	0.016	0	0
5	1.0100	–6.4824	0.942	0.190	0.5000	0.1641
6	1.0166	–5.4355	0	0	0	0
7	1.0059	–6.3969	0.228	0.109	0	0
8	1.0100	–5.6272	0.300	0.300	0.2000	0.1354
9	0.9755	–7.0162	0	0	0	0
10	0.9547	–9.1959	0.058	0.020	0	0
11	1.0500	–4.6886	0	0	0.2000	0.3800
12	0.9976	–8.7884	0.112	0.075	0	0
13	1.0500	–7.2567	0	0	0.2000	0.3954
14	0.9773	–9.7952	0.062	0.016	0	0
15	0.9680	–9.7932	0.082	0.025	0	0
16	0.9718	–9.2538	0.035	0.018	0	0
17	0.9540	–9.4522	0.090	0.058	0	0
18	0.9501	–10.3964	0.032	0.009	0	0
19	0.9429	–10.5331	0.095	0.034	0	0
20	0.9450	–10.2636	0.022	0.007	0	0
21	0.9408	–9.7516	0.175	0.112	0	0
22	0.9413	–9.7419	0	0	0	0
23	0.9467	–10.1714	0.032	0.016	0	0
24	0.9274	–10.2804	0.087	0.067	0	0
25	0.9204	–10.3073	0	0	0	0
26	0.9008	–10.8220	0.035	0.023	0	0
27	0.9257	–10.0102	0	0	0	0
28	1.0116	–5.8711	0	0	0	0
29	0.9035	–11.5199	0.024	0.009	0	0
30	0.8907	–12.6115	0.106	0.019	0	0
Total real losses: 5.8223 MW						

Table 2

Control variables and losses obtained from execution of GWO and IGWO with and without integration of RERs, CPVEIHBMO [25] and PSOGWO [34]

Control variables	Min	Max	Initial	GWO without RERs	IGWO without RERs	GWO with RERs	IGWO with RERs	CPVEIHBMO [25]	PSOGWO [34]
V_1, pu	0.95	1.1	1.05	1.0701	1.0714	1.0638	1.0624	1.0254	0.9615
V_2, pu	0.95	1.1	1.04	1.0615	1.0616	1.0605	1.0578	1.0352	1.0020
V_5, pu	0.95	1.1	1.01	1.0378	1.0389	1.0444	1.0407	1.0563	0.9437
V_8, pu	0.95	1.1	1.01	1.0390	1.0394	1.0442	1.0429	1.0273	0.9623
V_{11}, pu	0.95	1.1	1.05	1.0939	1.0799	1.0807	1.0640	1.0287	0.9476
V_{13}, pu	0.95	1.1	1.05	1.0378	1.0599	1.0401	1.0630	1.0756	1.0464
T6–9	0.9	1.1	1.078	0.9813	1.0375	0.9875	1.0188	0.9983	0.9746
T6–10	0.9	1.1	1.069	1.0875	0.9313	1.0438	0.9063	0.9748	1.0105
T4–12	0.9	1.1	1.032	1.0063	0.9875	0.9938	1.0000	0.9726	0.9776
T28–27	0.9	1.1	1.068	1.0063	0.9688	0.9813	0.9750	1.0817	0.9392
Q_{gc10}, pu	0	0.05	0	0.0160	0.0250	0.0250	0.0135	0.0482	0.0040
Q_{gc12}, pu	0	0.05	0	0.0260	0.0295	0.0025	0.0465	0.0483	0.0580
Q_{gc15}, pu	0	0.05	0	0.0255	0.0370	0.0490	0.0280	0.0476	0.0342
Q_{gc17}, pu	0	0.05	0	0.0500	0.0370	0.0215	0.0150	0.0485	0.0272
Q_{gc20}, pu	0	0.05	0	0.0475	0.0200	0.0005	0.0115	0.0498	0.0016
Q_{gc21}, pu	0	0.05	0	0.0215	0.0285	0.0385	0.0350	0.0499	0.0720
Q_{gc23}, pu	0	0.05	0	0.0035	0.0035	0.0035	0.0110	0.0489	0.0347
Q_{gc24}, pu	0	0.05	0	0.0475	0.0460	0.0490	0.0330	0.0499	0.0111
Q_{gc29}, pu	0	0.05	0	0.0425	0.0185	0.0105	0.0365	0.0499	0.0157
Total real losses, MW			5.8223	4.9496	4.9015	2.5374	2.5193	5.3243	5.0903

3) *Treatment of control variables, initiation and evaluation steps*. Each potential solution (search agent) is represented by a vector $\boldsymbol{X}$ that includes the values of control parameters such as generator voltages V_{gi}, transformer taps T_i and the reactive power of switchable shunt capacitors Q_{gci}. This vector is expressed as:

$$\boldsymbol{X}=\left[V_{g_1}\ldots V_{g_{N_{PV}}}\middle|T_1\ldots T_{N_T}\middle|Q_{gc1}\ldots Q_{gcN_{cap}}\right]. \tag{30}$$

Generator voltages are treated as continuous variables, whereas transformer taps and reactive power settings are considered discrete. During the initialization phase of both the GWO and IGWO approaches, initial solutions are generated using uniform random variables:

$$X_i = X_{i\min} + rnd \cdot \left(X_{i\max} - X_{i\min}\right), \qquad (31)$$

where $0 < rnd < 1$ is the random value.

To handle discrete variables, we adjust the variable value using the following formulation:

$$X_i = X_{i\min} + NX_i \cdot \Delta X_i, \qquad (32)$$

where N is the set of the total number of buses; NX_i is the integer number represents the variation number of the variable X_i; ΔX_i is the step size of the variable X_i.

In this paper, each transformer has 32 discrete settings, while each of the nine shunt compensator banks offers 100 possible configurations. To evaluate any solution, the fitness function value is determined by running a load-flow analysis using the Newton–Raphson method.

Table 3

Dependent variables obtained from execution of GWO and IGWO with and without integration of RERs

Dependent variables, pu	Min	Max	Initial	GWO without RERs	IGWO without RERs	GWO with RERs	IGWO with RERs
V_3	0.95	1.05	1.0279	1.0495	1.0498	1.0500	1.0500
V_4	0.95	1.05	1.0222	1.0441	1.0441	1.0463	1.0465
V_6	0.95	1.05	1.0166	1.0408	1.0403	1.0454	1.0430
V_7	0.95	1.05	1.0059	1.0319	1.0320	1.0473	1.0443
V_9	0.95	1.05	0.9755	1.0499	1.0408	1.0491	1.0448
V_{10}	0.95	1.05	0.9547	1.0221	1.0413	1.0282	1.0467
V_{12}	0.95	1.05	0.9976	1.0286	1.0497	1.0339	1.0499
V_{14}	0.95	1.05	0.9773	1.0164	1.0378	1.0231	1.0389
V_{15}	0.95	1.05	0.9680	1.0143	1.0357	1.0234	1.0389
V_{16}	0.95	1.05	0.9718	1.0202	1.0402	1.0249	1.0419
V_{17}	0.95	1.05	0.9540	1.0190	1.0377	1.0231	1.0408
V_{18}	0.95	1.05	0.9501	1.0081	1.0269	1.0194	1.0368
V_{19}	0.95	1.05	0.9429	1.0076	1.0249	1.0201	1.0386
V_{20}	0.95	1.05	0.9450	1.0129	1.0292	1.0213	1.0403
V_{21}	0.95	1.05	0.9408	1.0115	1.0315	1.0189	1.0368
V_{22}	0.95	1.05	0.9413	1.0121	1.0322	1.0196	1.0373
V_{23}	0.95	1.05	0.9467	1.0064	1.0280	1.0156	1.0320
V_{24}	0.95	1.05	0.9274	1.0035	1.0252	1.0127	1.0283
V_{25}	0.95	1.05	0.9204	1.0079	1.0327	1.0195	1.0352
V_{26}	0.95	1.05	0.9008	0.9900	1.0152	1.0018	1.0178
V_{27}	0.95	1.05	0.9257	1.0194	1.0458	1.0324	1.0480
V_{28}	0.95	1.05	1.0116	1.0378	1.0360	1.0407	1.0397
V_{29}	0.95	1.05	0.9035	1.0120	1.0318	1.0159	1.0392
V_{30}	0.95	1.05	0.8907	0.9952	1.0184	1.0032	1.0236
Q_{g1}	–0.2	0.25	–0.0153	–0.0447	–0.0158	–0.0521	–0.0360
Q_{g2}	–0.2	1	0.1564	0.1286	0.1055	0.0974	0.0589
Q_{g5}	–0.15	0.8	0.1640	0.2084	0.2218	0.1786	0.1678
Q_{g8}	–0.15	0.6	0.1353	0.2618	0.2951	0.2877	0.3155
Q_{g11}	–0.1	0.5	0.3800	0.2350	0.2067	0.1678	0.1017
Q_{g13}	–0.15	0.6	0.3954	0.0710	0.0797	0.0488	0.1016

4) *System without integration of RERs*.

4.1) *Application of GWO*. The GWO results are presented in Table 2, 3. The obtained results are based on:

- grey wolf population size: 100;
- maximum number of iterations: 500.

The optimization led to a significant reduction in total real losses, improving by 14.98 % from 5.8223 MW (initial case of load flow calculation) to 4.9496 MW. The voltage profile has been enhanced, and all constraints have been respected. The convergence characteristics of the algorithm are illustrated in Fig. 2, 3.

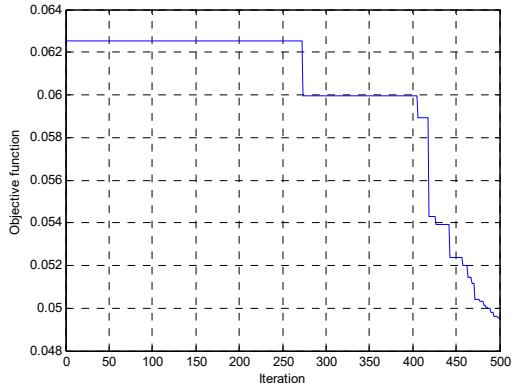

Fig. 2. Convergence of the objective function using GWO without RERs

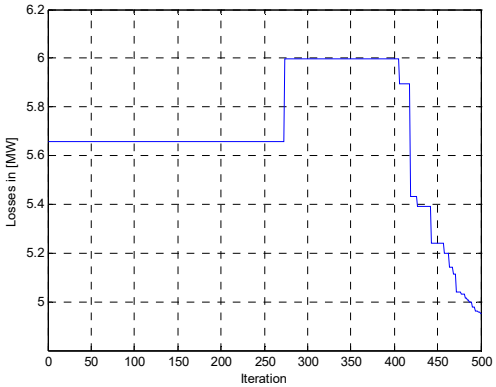

Fig. 3. Convergence of active losses using GWO without RERs

4.2) *Application of IGWO*. The IGWO without integration of RERs results are given in Table 2, 3 and Fig. 4, 5. Hence, we can clearly perceive the superiority of IGWO over GWO, where all the constraints are also respected and the losses are moved from 4.9496 MW to 4.9015 MW, with a minimization in total active losses of 15.81 % compared to the initial load flow case.

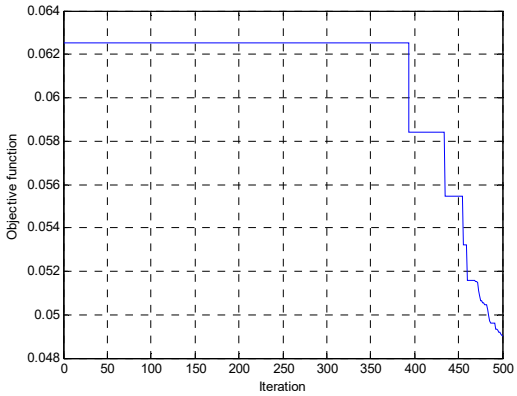

Fig. 4. Convergence of the objective function using IGWO without RERs

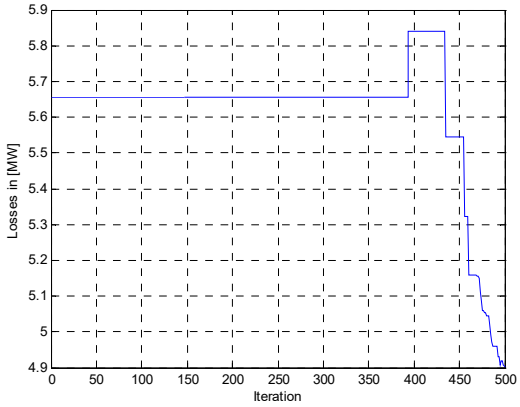

Fig. 5. Convergence of active losses using IGWO without RERs

5) *System with integration of RERs*. In this paper, RERs are added on buses 7 and 19. Wind speed and solar radiation data are taken from [35]. In bus 7, there is a wind farm, which consists of 30 wind turbines with a rated power of 3 MW for each one. The wind turbine cut-in, cut-out, and the rated speeds respectively are: $v_{w,in}$ = 3 m/s; $v_{w,out}$ = 25 m/s; $v_{w,r}$ = 16 m/s. The annual average wind speed from the location of this wind farm is taken as 7.536 m/s, which leads to an overall power output of 31.41 MW according to (13) and (14). In this work a power factor of 0.95 is considered for this wind farm.

The solar power plant is added on bus 19, where the PV array output power P_{sr} is assumed to be 30 MW, R_c is set as 120 W/m^2 and the annual average radiation from this location is taken as G_s = 471.76 W/m^2. Using (15) the total power generation for this plant in this location is 14.153 MW. Unity power factor is considered for the solar farm.

5.1) *Application of GWO*. The convergence characteristics of the GWO algorithm with integration of RERs are shown in Fig. 6, 7. The simulation results are resumed in Table 2, 3. The penetration of RERs has reduced the active power loss in the system largely to 2.5374 MW, with a minimization of 56.41 % compared to the initial load flow case. All the constraints are respected again.

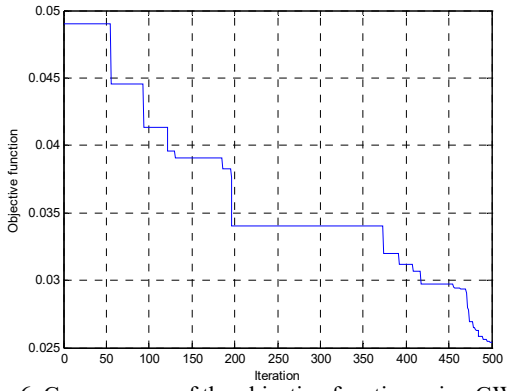

Fig. 6. Convergence of the objective function using GWO with RERs

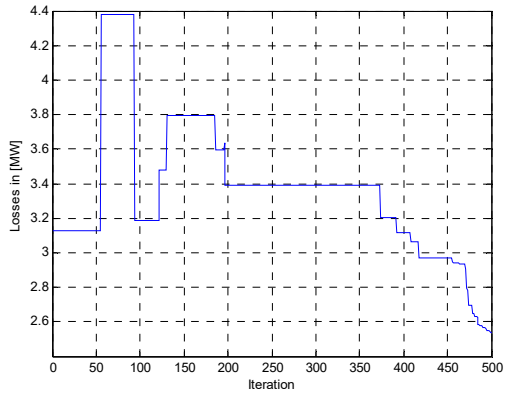

Fig. 7. Convergence of active losses using GWO with RERs

5.2) *Application of IGWO*. The IGWO results are presented in Table 2, 3, with addition of convergence characteristics in Fig. 8, 9. Power losses have continued to decrease. One can clearly perceive an important improvement of 56.73 % in total real losses, ranging also from 5.8223 MW in the case of load flow calculation to 2.5193 MW in our current case. The voltage profile has been improved and all the constraints have been respected.

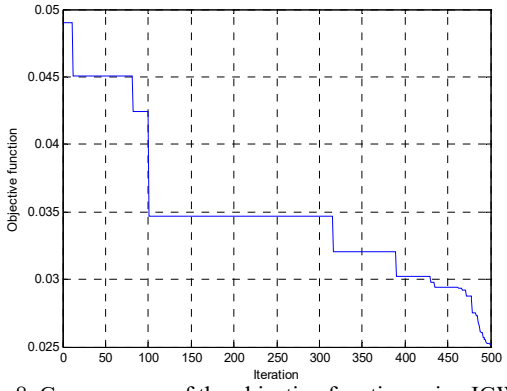

Fig. 8. Convergence of the objective function using IGWO with RERs

Table 2 presents a comparison of our applied algorithms with results obtained from:

- the new multi-objective strategy (Case IV) based on the Chaotic Parallel Vector Evaluated Interactive Honey Bee Mating Optimization (CPVEIHBMO) technique, as described in [25];
- the hybrid GWO-PSO optimization technique (Case I) discussed in [34].

The comparison highlights the effectiveness and superiority of the IGWO approach.

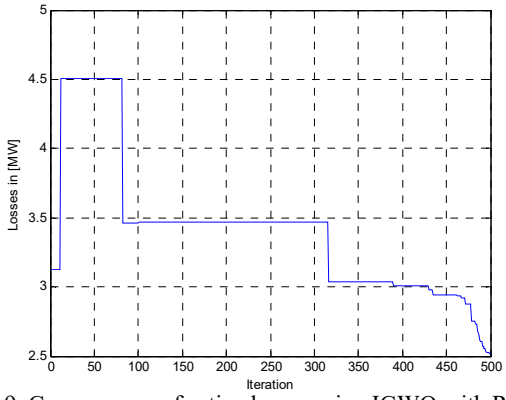

Fig. 9. Convergence of active losses using IGWO with RERs

Conclusions. The ORPD problem is a nonlinear multivariable optimization problem with both equality and inequality constrains. To solve this problem, the paper has proposed GWO and a new IGWO with and without incorporating of wind and solar energy systems.

In this work, the modification in the reproduction process step of IGWO is expected to provide better population diversity.

To make the ORPD problem more practical, control variables are represented in a mixed format, combining continuous and discrete values. Specifically, generator voltages are treated as continuous, while reactive power installations and transformer taps are considered discrete. The robustness of the proposed methods is evaluated using the standard IEEE 30-bus test system. The results demonstrate that IGWO offers notable advantages over GWO. The results also show that the introduction of RERs into the network, combined with control variable adjustments through the algorithm, leads to a more significant reduction in active power loss and voltage deviation compared to scenarios without RERs.

Conflict of interest. The author declares that there is no conflict of interest.

REFERENCES

1. Kirchmayer L.K. *Economic operation of power systems.* New York, John Wiley & Sons Inc., 1958. 260 p.

2. Carpentier J. Contribution á l'étude du dispatching économique. *Bulletin de la Société Francaise des électriciens*, 1962, vol. 3, ser. 8, pp. 431-447. (Fra).

3. Dommel H., Tinney W. Optimal Power Flow Solutions. *IEEE Transactions on Power Apparatus and Systems*, 1968, vol. PAS-87, no. 10, pp. 1866-1876. doi: https://doi.org/10.1109/TPAS.1968.292150.

4. Shaheen M.A.M., Ullah Z., Hasanien H.M., Tostado-Véliz M., Ji H., Qais M.H., Alghuwainem S., Jurado F. Enhanced transient search optimization algorithm-based optimal reactive power dispatch including electric vehicles. *Energy*, 2023, vol. 277, art. no. 127711. doi: https://doi.org/10.1016/j.energy.2023.127711.

5. Jamal R., Zhang J., Men B., Khan N.H., Ebeed M., Kamel S. Solution to the deterministic and stochastic Optimal Reactive Power Dispatch by integration of solar, wind-hydro powers using Modified Artificial Hummingbird Algorithm. *Energy Reports*, 2023, vol. 9, pp. 4157-4173. doi: https://doi.org/10.1016/j.egyr.2023.03.036.

6. Chamba A., Barrera-Singaña C., Arcos H. Optimal Reactive Power Dispatch in Electric Transmission Systems Using the Multi-Agent Model with Volt-VAR Control. *Energies*, 2023, vol. 16, no. 13, art. no. 5004. doi: https://doi.org/10.3390/en16135004.

7. Shaik M., Gaonkar D.N., Nuvvula R.S.S., Kumar P.P., Khan B. Probabilistic Optimal Active and Reactive Power Dispatch including Load and Wind Uncertainties considering Correlation. *International Transactions on Electrical Energy Systems*, 2023, vol. 2023, art. no. 2759073. doi: https://doi.org/10.1155/2023/2759073.

8. Ali A., Abbas G., Keerio M.U., Touti E., Ahmed Z., Alsalman O., Kim Y.-S. A Bi-Level Techno-Economic Optimal Reactive Power Dispatch Considering Wind and Solar Power Integration. *IEEE Access*, 2023, vol. 11, pp. 62799-62819. doi: https://doi.org/10.1109/ACCESS.2023.3286930.

9. Granados J.F.L., Uturbey W., Valadão R.L., Vasconcelos J.A. Many-objective optimization of real and reactive power dispatch problems. *International Journal of Electrical Power & Energy Systems*, 2023, vol. 146, art. no. 108725. doi: https://doi.org/10.1016/j.ijepes.2022.108725.

10. Pattanaik J.K., Basu M., Dash D.P. Improved Real-Coded Genetic Algorithm for Reactive Power Dispatch. *IETE Journal of Research*, 2022, vol. 68, no. 2, pp. 1462-1474. doi: https://doi.org/10.1080/03772063.2019.1654933.

11. Bhurt F., Ali A., Keerio M.U., Abbas G., Ahmed Z., Mugheri N.H., Kim Y.-S. Stochastic Multi-Objective Optimal Reactive Power Dispatch with the Integration of Wind and Solar Generation. *Energies*, 2023, vol. 16, no. 13, art. no. 4896. doi: https://doi.org/10.3390/en16134896.

12. Zhang M., Li Y. Multi-Objective Optimal Reactive Power Dispatch of Power Systems by Combining Classification-Based Multi-Objective Evolutionary Algorithm and Integrated Decision Making. *IEEE Access*, 2020, vol. 8, pp. 38198-38209. doi: https://doi.org/10.1109/ACCESS.2020.2974961.

13. Candra O., Alghamdi M.I., Hammid A.T., Alvarez J.R.N., Staroverova O.V., Hussien Alawadi A., Marhoon H.A., Shafieezadeh M.M. Optimal distribution grid allocation of reactive power with a focus on the particle swarm optimization technique and voltage stability. *Scientific Reports*, 2024, vol. 14, no. 1, art. no. 10889. doi: https://doi.org/10.1038/s41598-024-61412-9.

14. Biswas P.P., Suganthan P.N., Mallipeddi R., Amaratunga G.A.J. Optimal reactive power dispatch with uncertainties in load demand and renewable energy sources adopting scenario-based approach. *Applied Soft Computing*, 2019, vol. 75, pp. 616-632. doi: https://doi.org/10.1016/j.asoc.2018.11.042.

15. Kumar P.G.A, Jeyanthy P.A., Devaraj D. Hybrid CAC-DE in optimal reactive power dispatch (ORPD) for renewable energy cost reduction. *Sustainable Computing: Informatics and Systems*, 2022, vol. 35, art. no. 100688. doi: https://doi.org/10.1016/j.suscom.2022.100688.

16. Kar M.K., Kumar S., Singh A.K., Panigrahi S. Reactive power management by using a modified differential evolution algorithm. *Optimal Control Applications and Methods*, 2023, vol. 44, no. 2, pp. 967-986. doi: https://doi.org/10.1002/oca.2815.

17. Abou El Ela A.A., Abido M.A., Spea S.R. Differential evolution algorithm for optimal reactive power dispatch. *Electric Power Systems Research*, 2011, vol. 81, no. 2, pp. 458-464. doi: https://doi.org/10.1016/j.epsr.2010.10.005.

18. Naderi E., Mirzaei L., Pourakbari-Kasmaei M., Cerna F.V., Lehtonen M. Optimization of active power dispatch considering unified power flow controller: application of evolutionary algorithms in a fuzzy framework. *Evolutionary Intelligence*, 2024, vol. 17, no. 3, pp. 1357-1387. doi: https://doi.org/10.1007/s12065-023-00826-2.

19. Saddique M.S., Bhatti A.R., Haroon S.S., Sattar M.K., Amin S., Sajjad I.A., Ul Haq S.S., Awan A.B., Rasheed N. Solution to optimal reactive power dispatch in transmission system using meta-heuristic techniques – Status and technological review. *Electric Power Systems Research*, 2020, vol. 178, art. no. 106031. doi: https://doi.org/10.1016/j.epsr.2019.106031.

20. Li C., Lu Q., He H., Zhao J., Jiang Y., Xu B., Yan Y., Bian J., Du W. Reactive Power Optimization of Active Distribution Networks Based on Simulated Annealing Algorithm. *2023 IEEE*

7th Information Technology and Mechatronics Engineering Conference (ITOEC), 2023, pp. 1022-1026. doi: https://doi.org/10.1109/ITOEC57671.2023.10291951.
21. Srinivasan G., Mahesh Kumar Reddy V., Venkatesh P., Parimalasundar E. Reactive power optimization in distribution systems considering load levels for economic benefit maximization. *Electrical Engineering & Electromechanics*, 2023, no. 3, pp. 83-89. doi: https://doi.org/10.20998/2074-272X.2023.3.12.
22. Wu X., Yan J., Zhao J. Comparative Research on Reactive Power Optimization of Distribution Network Based on Ant Colony and Bee Colony Algorithm. *2022 IEEE 6th Information Technology and Mechatronics Engineering Conference (ITOEC)*, 2022, pp. 247-251. doi: https://doi.org/10.1109/ITOEC53115.2022.9734469.
23. Vishnu M., Sunil Kumar T.K. An Improved Solution for Reactive Power Dispatch Problem Using Diversity-Enhanced Particle Swarm Optimization. *Energies*, 2020, vol. 13, no. 11, art. no. 2862. doi: https://doi.org/10.3390/en13112862.
24. Jimenez-Nunez J.J., Cedeno-Maldonado J.R. A particle swarm optimization approach for reactive power dispatch. *Proceedings of the 37th Annual North American Power Symposium*, 2005, pp. 198-205. doi: https://doi.org/10.1109/NAPS.2005.1560524.
25. Ghasemi A., Valipour K., Tohidi A. Multi objective optimal reactive power dispatch using a new multi objective strategy. *International Journal of Electrical Power & Energy Systems*, 2014, vol. 57, pp. 318-334. doi: https://doi.org/10.1016/j.ijepes.2013.11.049.
26. Jaisiva S., Prabaakaran K., Kumar C., Lakshmanan M., Alwabli A., Jaffar A., Alharbi A., Miyajan A. A novel solution for the optimal reactive power dispatch problem using an artificial neural network integrated with the firefly optimization algorithm. *Frontiers in Energy Research*, 2023, vol. 11, art. no. 1310010. doi: https://doi.org/10.3389/fenrg.2023.1310010.
27. Mirjalili S., Mirjalili S.M., Lewis A. Grey Wolf Optimizer. *Advances in Engineering Software*, 2014, vol. 69, pp. 46-61. doi: https://doi.org/10.1016/j.advengsoft.2013.12.007.
28. Varan M., Erduman A., Menevşeoğlu F. A Grey Wolf Optimization Algorithm-Based Optimal Reactive Power Dispatch with Wind-Integrated Power Systems. *Energies*, 2023, vol. 16, no. 13, art. no. 5021. doi: https://doi.org/10.3390/en16135021.
29. Jamal R., Men B., Khan N.H. A Novel Nature Inspired Meta-Heuristic Optimization Approach of GWO Optimizer for Optimal Reactive Power Dispatch Problems. *IEEE Access*, 2020, vol. 8, pp. 202596-202610. doi: https://doi.org/10.1109/ACCESS.2020.3031640.
30. Hosseini-Hemati S., Sheisi G.H., Karimi S. Allocation-Based Optimal Reactive Power Dispatch Considering Polynomial Load Model Using Improved Grey Wolf Optimizer. *Iranian Journal of Science and Technology, Transactions of Electrical Engineering*, 2021, vol. 45, no. 3, pp. 921-944. doi: https://doi.org/10.1007/s40998-021-00419-8.
31. Hasanien H.M., Alsaleh I., Tostado-Véliz M., Zhang M., Alateeq A., Jurado F., Alassaf A. Hybrid particle swarm and sea horse optimization algorithm-based optimal reactive power dispatch of power systems comprising electric vehicles. *Energy*, 2024, vol. 286, art. no. 129583. doi: https://doi.org/10.1016/j.energy.2023.129583.
32. Abd-El Wahab A.M., Kamel S., Hassan H.M., Domínguez-García J.L., Nasrat L. Jaya-AEO: An Innovative Hybrid Optimizer for Reactive Power Dispatch Optimization in Power Systems. *Electric Power Components and Systems*, 2024, vol. 52, no. 4, pp. 509-531. doi: https://doi.org/10.1080/15325008.2023.2227176.
33. Abd-El Wahab A.M., Kamel S., Sultan H.M., Hassan M.H., Ruiz-Rodríguez F.J. Optimizing reactive power dispatch in electrical networks using a hybrid artificial rabbits and gradient-based optimization. *Electrical Engineering*, 2024, vol. 106, no. 4, pp. 3823-3851. doi: https://doi.org/10.1007/s00202-023-02188-5.
34. Shaheen M.A.M., Hasanien H.M., Alkuhayli A. A novel hybrid GWO-PSO optimization technique for optimal reactive power dispatch problem solution. *Ain Shams Engineering Journal*, 2021, vol. 12, no. 1, pp. 621-630. doi: https://doi.org/10.1016/j.asej.2020.07.011.
35. Ahmed M.K., Osman M.H., Korovkin N.V. Optimal reactive power dispatch in power system comprising renewable energy sources by means of a multi-objective particle swarm algorithm. *Materials Science. Power Engineering*, 2021, vol. 27, no. 1, pp. 5-20. doi: https://doi.org/10.18721/JEST.27101.
36. Hassan M.H., Kamel S., El-Dabah M.A., Khurshaid T., Dominguez-Garcia J.L. Optimal Reactive Power Dispatch With Time-Varying Demand and Renewable Energy Uncertainty Using Rao-3 Algorithm. *IEEE Access*, 2021, vol. 9, pp. 23264-23283. doi: https://doi.org/10.1109/ACCESS.2021.3056423.
37. Khan N.H., Wang Y., Tian D., Jamal R., Ebeed M., Deng Q. Fractional PSOGSA Algorithm Approach to Solve Optimal Reactive Power Dispatch Problems With Uncertainty of Renewable Energy Resources. *IEEE Access*, 2020, vol. 8, pp. 215399-215413. doi: https://doi.org/10.1109/ACCESS.2020.3039571.
38. Manikandan K., Sasikumar S., Arulraj R. A novelty approach to solve an economic dispatch problem for a renewable integrated micro-grid using optimization techniques. *Electrical Engineering & Electromechanics*, 2023, no. 4, pp. 83-89. doi: https://doi.org/10.20998/2074-272X.2023.4.12.
39. Nid A., Sayah S., Zebar A. Power fluctuation suppression for grid connected permanent magnet synchronous generator type wind power generation system. *Electrical Engineering & Electromechanics*, 2024, no. 5, pp. 70-76. doi: https://doi.org/10.20998/2074-272X.2024.5.10.
40. Bounechba H., Boussaid A., Bouzid A. Experimental validation of fuzzy logic controller based on voltage perturbation algorithm in battery storage photovoltaic system. *Electrical Engineering & Electromechanics*, 2024, no. 5, pp. 20-27. doi: https://doi.org/10.20998/2074-272X.2024.5.03.

Received 30.07.2024
Accepted 22.09.2024
Published 02.01.2025

F. Laouafi [1]*, PhD, Lecturer,*
Department of Electrical Engineering, LES Laboratory,
University 20 Août 1955 - Skikda, Algeria,
e-mail: laouafi_f@yahoo.fr (Corresponding Author)

How to cite this article:
Laouafi F. Improved grey wolf optimizer for optimal reactive power dispatch with integration of wind and solar energy. *Electrical Engineering & Electromechanics*, 2025, no. 1, pp. 23-30. doi: https://doi.org/10.20998/2074-272X.2025.1.04

UDC 621.3.013 https://doi.org/10.20998/2074-272X.2025.1.05

H. Rahali, S. Zeghlache, B.D.E. Cherif, L. Benyettou, A. Djerioui

Robust adaptive fuzzy type-2 fast terminal sliding mode control of robot manipulators in attendance of actuator faults and payload variation

Introduction. *This study presents a robust control method for the path following problem of the PUMA560 robot. The technique is based on the Adaptive Fuzzy Type-2 Fast Terminal Sliding Mode Control (AFT2FTSMC) algorithm and is designed to handle actuator faults, uncertainties (such as payload change), and external disturbances. The* ***aim*** *of this study is to utilize the Fast Terminal Sliding Mode Control (FTSMC) approach in order to ensure effective compensation for faults and uncertainties, minimize tracking error, reduce the occurrence of chattering phenomena, and achieve rapid transient response. A novel adaptive fault tolerant Sliding Mode Control (SMC) approach is developed to address the challenges provided by uncertainties and actuator defects in real robotics tasks.* ***Originality.*** *The present work combined the AFT2FTSMC algorithm in order to give robust controllers for trajectory tracking of manipulator's robot in presence parameters uncertainties, external disturbance, and faults. We use an adaptive fuzzy logic system to estimate the robot's time-varying, nonlinear, and unfamiliar dynamics. A strong adaptive term is created to counteract actuator defects and approximation errors while also guaranteeing the convergence and stability of the entire robot control system.* ***Novelty.*** *The implemented controller effectively mitigates the chattering problem while maintaining the tracking precision and robustness of the system. The stability analysis has been conducted using the Lyapunov approach.* ***Results.*** *Numerical simulation and capability comparison with other control strategies show the effectiveness of the developed control algorithm.* References 53, table 1, figures 8.
Key words: **robot manipulator, type-2 fuzzy system, fast terminal sliding mode control, adaptive control.**

Вступ. *У роботі представлено надійний метод керування для проблеми слідування шляху робота PUMA560. Методика базується на алгоритмі адаптивного нечіткого типу 2 швидкого ковзного керування терміналом (AFT2FTSMC) і призначена для обробки несправностей приводу, невизначеностей (таких як зміна корисного навантаження) та зовнішніх завад.* ***Метою*** *статті є використання підходу швидкого ковзного режиму керування терміналом (FTSMC) для забезпечення ефективної компенсації помилок і невизначеностей, мінімізації помилок відстеження, зменшення виникнення явищ деренчання та досягання швидкої реакції на перехідні процеси. Розроблено новий адаптивний відмовостійкий підхід до керування ковзним режимом для вирішення проблеми, що пов'язана з невизначеністю та дефектами приводу в реальних роботах.* ***Оригінальність***. *Ця робота об'єднала алгоритм адаптивного нечіткого типу 2 і швидкого кінцевого ковзного режиму керування з метою створення надійних контролерів для відстеження траєкторії робота-маніпулятора в умовах невизначеності параметрів присутності, зовнішніх завад і несправностей. Використано систему адаптивної нечіткої логіки для оцінки змінної в часі нелінійної та невідомої динаміки робота. Створено сильний адаптивний термін для протидії дефектам приводу та помилкам апроксимації, а також для гарантії конвергенції та стабільності усієї системи керування роботом.* ***Новизна***. *Реалізований контролер ефективно пом'якшує проблему тріскання, зберігаючи при цьому точність відстеження та надійність системи. Аналіз стабільності проведено за підходом Ляпунова.* ***Результати***. *Чисельне моделювання та порівняння можливостей з іншими стратегіями керування показують ефективність розробленого алгоритму керування.* Бібл. 53, табл. 1, рис. 8.
Ключові слова: **робот-маніпулятор, нечітка система типу 2, швидке керування ковзним режимом терміналу, адаптивне керування.**

1. Introduction. After the beginning of robotics, robotic manipulators have been extensively utilized in industrial automation containing the medical and nuclear domains. Manipulator robot system control is a very hard mission, principally in reason to the existence of high nonlinearities, very strong coupling effects, uncertainties parameters, and external disturbances in this type of system [1]. Recently, a significant scientific endeavor has been dedicated to develop an efficient controller of robot manipulators. For example, PID controller [2, 3], intelligent control [4, 5], optimal control [6, 7]. In [8], a feedback linearization technique was employed to create an inverse dynamics control system for precise motion control of a manipulator robot and computed torque control has been also proposed in [9, 10], where this approach is performed by using feedback linearization method.

Several studies have suggested different approaches to develop robust controllers for accurately following a desired trajectory of a manipulator robot, even when there are external disturbances, uncertainties in the parameters, and defects [11, 12]. Sliding Mode Control (SMC) is a highly reliable control technique that has been widely employed in the motion control of robot manipulators due to its exceptional ability to handle uncertainty and external disturbances [13, 14]. This good property of SMC has been utilized in the Fault Tolerant Control (FTC) design [15, 16].

Numerous articles have proposed multiple alternatives to preserve the benefits and reduce or eliminate the drawbacks of the conventional SMC. The adoption of terminal SMC in [17, 18] aims to achieve finite-time convergence. Nevertheless, the conventional terminal SMC exhibits a singularity issue and provides a sluggish rate of convergence. To address the issue of SMC, researchers have devised two control methods: Fast Terminal SMC (FTSMC) and nonsingular terminal SMC [19–22]. The authors in [20, 23, 24] devised a method called Nonsingular Fast Terminal SMC (NFTSMC) to achieve both cancellation of singularities and rapid finite-time convergence. Two control methods PID based SMC (PID-SMC) and integral SMC, were introduced in [25, 26]. A second-order sliding mode controller is implemented based on a super twisting algorithm for higher performance and stability in dealing with parameter changes and external disturbances for a three-level inverter-fed permanent magnet synchronous motor proposed in [27]. To enhance the transient response of the conventional SMC, the utilization of the integral action within the PID controller is employed to enhance the transient responsiveness [28].

Several techniques have been suggested to reduce the chattering effect. In [29–31], a SMC has been developed utilizing a saturation function to address this issue. But this approach compromises the system's robustness to external disturbances, a high-order sliding mode controller is employed, with super-twisting algorithm tested for effectiveness and robustness [32]. A High-Order SMC

(HOSMC) approach proposed in [33, 34], effectively reduces chattering effect, but requires understanding the temporal derivative of sliding surfaces, which is not always accessible. The fuzzy logic control is chosen for its simplicity and reliability, demonstrating its ability to handle complex, nonlinear systems effectively through linguistic variables and heuristic reasoning [35].

To summarize, numerous approaches have been developed to address the shortcomings of classic SMC, but no literature exists that proposes a controller synthesis method that can collectively overcome all disadvantages of SMC. To achieve a reliable FTC system, SMC design must satisfy 4 essential requirements: chattering reduction, fast transient response, finite-time convergence, and compensation of uncertainties, external perturbations and faults.

Aim and objectives of the article. Motivated by the precedent problems, this work proposes a FTC to overcome the external perturbations effects, uncertainties and actuator faults for 3 Degrees of Freedom (3-DOF) manipulators robot utilizing Adaptive Fuzzy Type-2 Fast Terminal SMC (AFT2FTSMC). The main contribution of this study is the development of a single, resilient controller that starts with selecting a rapid nonlinear terminal sliding surface, this controller aims to minimize tracking errors, best performances and chattering reducing. In addition, an adaptive type-2 fuzzy system has been utilized in the synthesized controller, to identify the unknown nonlinear model of robots due to actuator faults and external disturbances.

The primary objective of this work is to assess the effectiveness of modern control techniques in regulating the joint positions of a manipulator robot. Secondly, implement and validate the proposed command.

The Lyapunov approach was utilized for stability demonstration, with the work's contributions being highlighted by:

1) The design utilizes a fast nonlinear terminal sliding surface for improved control precision, finite-time convergence and fast transient response.

2) Stability analysis was proved according to the Lyapunov criterion, in which all adaptive laws were generated.

3) Compared to other control strategies suggested in the literature, such as computed torque control [9, 10], PID [2, 3], PID-SMC [25, 26], and conventional NFTSMC proposed in [20, 23, 24]. The proposed control strategy demonstrates the best performance when there is a defective.

In comparison with control strategies developed in [33–44] the following points encapsulate the work's contributions.

A complicated internal model based on passive FTC has been developed in [36, 37]. This control approach does not provide accurate trajectory tracking in the event of significant faults. The objective of this work is to use robust AFT2FTSMC for robot manipulators in the presence of payload changes.

The developed fast nonlinear terminal sliding surface outperforms studies in [38, 39] of best performances and exhibits robustness against actuator fault effects.

In contrast to [38–40], the controller synthesis in the work that is being described is independent of the robot manipulators' dynamic model. In our case, we supposed that the inertia matrix, Coriolis matrix, centrifugal forces, gravity terms are unknown.

In contrast to the control approach described in [41, 42], where the time delay identification it is adopted to estimate the unknown dynamics model. This study employs type-2 fuzzy systems to detect the uncertainties and nonlinear functions included in the model of robot manipulators. It also utilizes the FTSMC concept to develop a FTC controller that does not rely on time delay detection.

In [43] a complicated FTC strategy based on the association of SMC and nonlinear observer has been developed. Regrettably, this control technique requires a nonlinear observer, which will increase the intricacy and computing time. In this work, a robust FTC control has been developed without requiring a complex observer and can give good faults tolerance.

The authors in [33–35] proposed a HOSMC; this control algorithm has shown to be efficient to minimize the chattering effect, but requires the acquaintance of temporal derivative of sliding surfaces and it is sensible to actuator faults.

However, the suggested control technique effectively addresses the issue of chattering and successfully achieves optimal trajectory tracking even in the presence of external disturbances, uncertainties and actuator defects.

In [44], an adaptive fuzzy sliding control strategy has been proposed for 3-DOF manipulator robot, the results proved a favorable tracking performance with chattering phenomenon elimination, but this work did not deal the fault effects, but the proposed control strategy can give the best trajectory tracking in faulty operation.

The originality of our work was to combine the performance of fuzzy logic, the flexibility of adaptive control, and the robustness of sliding mode for the definition of a robust control structure tolerant to faults, achieving the best stability/performance ratios and speed/performance in the context of controlling a robot manipulator.

A novel adaptive fault tolerant SMC approach is developed to address the challenges provided by uncertainties and actuator defects in real robotics tasks. This method does not rely on prior knowledge of uncertainties and external disturbances unlike most of the methods known from the literature.

2. Robot manipulator dynamic modeling.

2.1 Robot manipulator dynamic modeling in healthy condition. The PUMA 560 robots are a 3-DOF robot arm, this type of robot is extensively utilized in industrial application. The configuration of PUMA 560 robots is presented in Fig. 1.

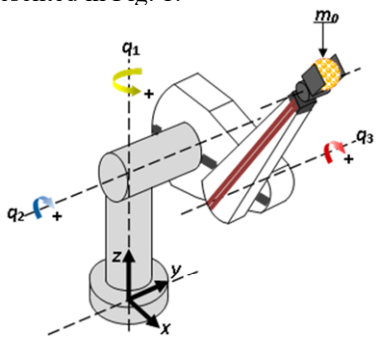

Fig. 1. PUMA 560 robot [45]

Using Lagrange formalism, the dynamic model of PUMA 560 robot is given as:

$$M(q)\,q'' + V_m(q,q')q' + G(q) + u_{m0} = u + \tau_d\,, \quad (1)$$

where $q = [q_1,\ q_2,\ q_3]^T$ is the joint position vector; $q' = [q_1',\ q_2',\ q_3']^T$ is the joint velocity vector; $q'' = [q_1'',\ q_2'',\ q_3'']^T$ is the joint acceleration vector; $u = [u_1,\ u_2,\ u_3]^T$ is the joint input torque vector; $M(q)$ is the symmetric positive definite matrix of inertial accelerations; $V_m(q,\ q')$ is the matrix of Coriolis and centrifugal forces; $G(q)$ is the state varying vector of gravity terms; u is the motor torques; τ_d is the external disturbances; u_{m0} is the vector of torque due to the payload m_0 obtained by [45]:

$$u_{m0} = m_0 J^T(q)\left[J(q)q'' + J'(q,q')q' + g\right], \quad (2)$$

with $g = [0\ 0\ 9.81]^T$ and J is the Jacobian matrix, equation (1) can be rewritten as:

$$M(q)\,q'' + V_m(q,q')q' + G(q) = u + E(q,q',q'')\,, \quad (3)$$

with $E(q,q',q'') = \tau_d - u_{m0}$.

2.2 Robot manipulator dynamic modeling in faulty condition. In robotic manipulators, defeat in the actuators can be generated by various reasons such as defeat in power supply systems. The dynamic model of robot manipulator in faulty condition is given by:

$$M(q)\,q'' + V_m(q,q')q' + G(q) = u_f + E(q,q',q'')\,, \quad (4)$$

where:

$$u_f = u + U_0, \quad (5)$$

where u_f is the motor torques in faulty condition; u is the motor torques; U_0 is the actuator fault component.

Substituting (5) in (4), the dynamic model in (3) is rearranged as:

$$q'' = \left[M\right]^{-1}[u - V_m(q,q')q' - G(q)] + \vartheta(q,q',q'')\,, \quad (6)$$

with:

$$\vartheta(q,q',q'') = [M]^{-1}[U_0 + E(q,q',q'')]\,,$$

where $\vartheta(q,\ q',\ q'')$ is the uncertainties component, which include payload variations and actuator faults effects.

3. Robust FTC using AFT2FTSMC. The dynamic model (6) can be expressed in the state space form by:

$$\begin{cases} x_1' = x_2; \\ x_2' = \left[M\right]^{-1}\left[u - V_m(q,q',q'') - G(q)\right] + \vartheta(q,q',q''); \\ y = x_1, \end{cases} \quad (7)$$

where $x_1 = [q_1\ q_2\ q_3]^T$ is the state vector; $x_2 = (q'_1\ q'_2\ q'_3)^T$.

The tracking error variable e_1 is defined by:

$$e_1 = q_d - x_1, \quad (8)$$

where $q_d = [q_{1d}\ q_{2d}\ q_{3d}]^T$ is desired signal.

The time derivative of (8) is computed by:

$$e_1' = q_d' - x_2\,.$$

The global fast dynamic terminal sliding surface is given by [46–48]:

$$s = e_1' + \lambda e_1 + \beta e_1^{m_1/n_1} = q_d' - x_2 + \lambda e_1 + \beta e_1^{m_1/n_1}\,, \quad (9)$$

where s is the global fast dynamic terminal sliding surface; λ, β, m_1, n_1 are the positive constants ($m_1 < n_1$).

The time derivative of (9) is given as:

$$s' = q_d'' + \left(\lambda + \beta\frac{m_1}{n_1}e_1^{(m_1-n_1)/n_1}\right)e_1' + \\ + \left[M(q)\right]^{-1}\left[V_m(q,q')q' + G(q)\right] - \left[M(q)\right]^{-1}u - \vartheta(q,q',q''), \quad (10)$$

where s' is the time derivative of s.

Define the following Lyapunov function as:

$$V = \frac{1}{2}[M(q)]s^2\,, \quad (11)$$

where V is the Lyapunov's function.

The time derivative of (11) is calculated by:

$$V' = [M(q)]ss' - \frac{1}{2}[M'(q)]^{-1}[M(q)]^2 s^2\,, \quad (12)$$

where V' is the time derivative of Lyapunov's function.

Substituting (10) in (12) yields:

$$V' = s\left(\begin{array}{l} q_d'' + \left(\lambda + \beta\frac{m_1}{n_1}e_1^{(m_1-n_1)/n_1}\right)e_1' + \\ + \frac{\left[M(q)\right]^{-1}\left[V_m(q,q')q' + G(q)\right] - \vartheta(q,q',q'')}{\left[M(q)\right]^{-1}} - \\ -\frac{1}{2}\left[M'(q)\right]^{-1}\left[M(q)\right]^2 s - u \end{array}\right). \quad (13)$$

The control law u is extracted by:

$$u = \frac{1}{\left[M(q)\right]^{-1}}\left(\begin{array}{l} q_d'' + \left(\lambda + \beta\frac{m_1}{n_1}e_1^{(m_1-n_1)/n_1}\right)e_1' + \\ + \left[M(q)\right]^{-1}\left[V_m(q,q')q' + G(q)\right] - \\ -\frac{1}{2}\left[M'(q)\right]^{-1}\left[M(q)\right]^2 s - \vartheta(q,q',q'') \end{array}\right) + \alpha s\,, \quad (14)$$

where $\alpha = \mathrm{diag}[\alpha_1\ \alpha_2\ \alpha_3] > 0$.

Using (14), it can be checked that:

$$V' \le -\alpha s^2 < 0\,. \quad (15)$$

If we considered a free of payload variations and without actuator defects, i.e., $\vartheta(q,\ q',\ q'') = 0$, the ideal control law is written as:

$$u = \frac{1}{[M(q)]^{-1}}(q_d'' + (\lambda + \beta\frac{m_1}{n_1}e_1^{(m_1-n_1)/n_1})e_1' + \\ + [M(q)]^{-1}[V_m(q,q')q' + G(q)] - \frac{1}{2}[M'(q)]^{-1}[M(q)]^2 s) + \alpha s. \quad (16)$$

The functions $M(q)$, $V_m(q,\ q')$ and $G(q)$ are unknown and $\vartheta(q,\ q',\ q'')$ expression which include actuator faults effects and payload variations are different to zero ($\vartheta(q,\ q',\ q'') \neq 0$), in this work an adaptive type fuzzy-2 system has been utilized to treat this problematic. The developed method concern the online identification of the ideal control law given by global fast dynamic terminal sliding mode control using fuzzy type-2 inference system where the fuzzy parameters are adapted.

The ideal control law presented in (16) can be rewritten as [49]:

$$u = u_b + \alpha s, \quad (17)$$

where u_b is the real control law:

$$u_b = \frac{1}{[M(q)]^{-1}}(q_d'' + (\lambda + \beta\frac{m_1}{n_1}e_1^{(m_1-n_1)/n_1})e_1' + \\ + [M(q)]^{-1}[V_m(q,q')q' + G(q)] - \frac{1}{2}[M'(q)]^{-1}[M(q)]^2 s). \quad (18)$$

To synthesis an adaptive control law, we suppose that each component of the control law $u_b = [u_{b1}\ u_{b2}\ u_{b3}]^T$ can be identified by a type-2 fuzzy as:

$$\hat{u}_{bj} = W_j^T(e_1(j), e_1'(j))\Theta_j\,. \quad (19)$$

Let us denote: $\Theta = [\Theta_1^T\ \Theta_2^T\ \Theta_3^T]^T$ and

$(e_1, e_1') = diag[W_1(e_1(1), e_1'(1))W_2(e_1(2), e_1'(2))W_3(e_1(3), e_1'(3))]$, therefore, we can write:

$$\hat{u}_b = W^T(e_1, e_1')\Theta, \tag{20}$$

where Θ denotes adapted vector parameters; $W(X)$ is the average basis functions obtained by fuzzy type-2 system where each basis function is obtained by the average of corresponded left and right basis functions.

The real control law u_b is expressed by:

$$u_b = W^T(e_1, e_1')\Theta^* + \varepsilon, \tag{21}$$

where Θ^* is the optimal parameter; $\varepsilon = [\varepsilon_1\ \varepsilon_2\ \varepsilon_3]^T$ is the identification error that guaranty that $|\varepsilon| \le \bar{\varepsilon}$, where $\bar{\varepsilon}$ is positive constant.

The adaptive control law applied to the robot is expressed as [49]:

$$u = u_a + u_r + u_p, \tag{22}$$

where:

1) $u_{a,j}$ is the fuzzy type-2 adaptive control term which is designed in order to identified the ideal global fast dynamic terminal sliding mode control law u_b in (21) given as:

$$u_a = \hat{u}_b = W^T(e_1, e_1')\Theta, \tag{23}$$

where $W^T(e_1, e'_1)$ is the average basis functions obtained by fuzzy type-2 system where each basis function is given by the average of corresponded left and right basis functions and Θ is the adjusted vector parameters given by:

$$\Theta' = \gamma \cdot s \cdot W^T(e_1, e_1') - \sigma_1\Theta, \tag{24}$$

where $\gamma = diag[\gamma_1\ \gamma_2\ \gamma_3] > 0$, $\sigma_1 = diag[\sigma_{1,1}\ \sigma_{1,2}\ \sigma_{1,3}] > 0$, $s = q_d' - x_2 + \lambda e_1 + \beta e_1^{m_1/n_1}$ and $\Theta(0) = 0$.

2) u_r is the robust control term are added to minimize both the effects of fuzzy type-2 identification error and uncertainties expressed as [50]:

$$u_r = \hat{\varepsilon}\tanh(s/\chi), \tag{25}$$

with $\hat{\varepsilon} = diag[\hat{\varepsilon}_1\ \hat{\varepsilon}_2\ \hat{\varepsilon}_3]$,

$$\hat{\varepsilon}' = \eta s\tanh(s/\chi) - \sigma_2\hat{\varepsilon}, \tag{26}$$

with $\eta = diag[\eta_1\ \eta_2\ \eta_3] > 0$, $\sigma_2 = diag[\sigma_{2,1}\ \sigma_{2,2}\ \sigma_{2,3}] > 0$, $\chi > 0$ and $\hat{\varepsilon}_j(0) = 0$.

3) $u_{p,j}$ is given by:

$$u_p = \alpha s, \tag{22}$$

where $\alpha = diag[\alpha_1\ \alpha_2\ \alpha_3] > 0$.

3.1 Stability demonstration. The Lyapunov function is given by:

$$V = \frac{1}{2}M^{-1}(q)s^2 + \frac{1}{2\gamma}\tilde{\Theta}^T\tilde{\Theta} + \frac{1}{2\eta_j}\tilde{\varepsilon}^T\tilde{\varepsilon}, \tag{28}$$

where $\tilde{\varepsilon}$ and $\tilde{\Theta}$ are the identification errors given as:

$$\tilde{\varepsilon} = \varepsilon^* - \hat{\varepsilon}, \tag{29}$$

where $\hat{\varepsilon}$ is the estimate of ε^*;

$$\tilde{\Theta} = \Theta^* - \Theta. \tag{30}$$

The time derivative of (28) yields:

$$V' = s(u_b - u) + \frac{1}{\gamma}\tilde{\Theta}^T\tilde{\Theta}' + \frac{1}{\eta}\tilde{\varepsilon}^T\tilde{\varepsilon}'. \tag{31}$$

Substituting (21), (22), (23) and (27) in (31) yields:

$$V' \le s\left(W^T(e_1, e_1')\Theta^* + \varepsilon - W^T(e_1, e_1')\Theta - u_r - \alpha s\right) + \frac{1}{\gamma}\tilde{\Theta}^T\tilde{\Theta}' + \frac{1}{\eta}\tilde{\varepsilon}^T\tilde{\varepsilon}'. \tag{32}$$

The optimal parameters vector Θ^* and ε^* are slowly time varying, therefore the time derivative of estimation error will be:

$$\tilde{\varepsilon}' = -\hat{\varepsilon}' \quad \text{and} \quad \tilde{\Theta}' = -\Theta'. \tag{33}$$

Substituting (33) in (32) and taking account (30) we obtain:

$$V' \le -\alpha s^2 + sW^T(e_1, e_1')\tilde{\Theta} + s(\varepsilon - u_r) - \frac{1}{\gamma}\tilde{\Theta}^T\tilde{\Theta}' - \frac{1}{\eta}\tilde{\varepsilon}^T\tilde{\varepsilon}'. \tag{34}$$

By introducing (24) and (26) into (34), yield:

$$V' \le -\alpha s^2 + s(\varepsilon - u_r) + \frac{\sigma_1}{\gamma}\tilde{\Theta}^T\Theta - \frac{1}{\eta}\tilde{\varepsilon}\eta s\tanh\left(\frac{s}{\chi}\right) + \frac{\sigma_2}{\eta}\tilde{\varepsilon}\hat{\varepsilon}. \tag{35}$$

Substituting (29) in (35) we obtain:

$$V' \le -\alpha s^2 + s(\varepsilon - u_r) + \frac{\sigma_1}{\gamma}\tilde{\Theta}^T\Theta - \varepsilon^* s\tanh\left(\frac{s}{\chi}\right) + \varepsilon_j^* s\tanh\left(\frac{s}{\chi}\right) + \frac{\sigma_2}{\eta}\tilde{\varepsilon}\hat{\varepsilon}. \tag{36}$$

Or equivalently:

$$V' \le -\alpha s^2 + \frac{\sigma_1}{\gamma}\tilde{\Theta}^T\Theta - \varepsilon^* s\tanh\left(\frac{s}{\chi}\right) + \hat{\varepsilon}\, s\tanh\left(\frac{s}{\chi}\right) + \frac{\sigma_2}{\eta}\tilde{\varepsilon}\hat{\varepsilon} - su_{r,j} + |s|\varepsilon^*. \tag{37}$$

By introducing (25) into (37), yields:

$$V' \le -\alpha s^2 + \frac{\sigma_1}{\gamma}\tilde{\Theta}^T\Theta + |s|\varepsilon_j^* - \varepsilon^* s\tanh\left(\frac{s}{\chi}\right) + \frac{\sigma_2}{\eta}\tilde{\varepsilon}\hat{\varepsilon}. \tag{38}$$

Let the inequality given as follows for any value of $\zeta > 0$ [50]:

$$|s| - s\tanh\left(\frac{s}{\chi}\right) \le \zeta\chi = \varsigma, \tag{39}$$

with ζ is the constant that confirms $\zeta = e^{-(\zeta+1)}$, i.e. $\zeta = 0.2785$.

Equation (39) is changed as:

$$V' \le -\alpha s^2 + \varepsilon^*\varsigma + \frac{\sigma_1}{\gamma}\tilde{\Theta}^T\Theta + \frac{\sigma_2}{\eta}\tilde{\varepsilon}\hat{\varepsilon}. \tag{40}$$

By using young's inequality, we obtain:

$$\frac{\sigma_1}{\gamma}\tilde{\Theta}^T\Theta \le -\frac{\sigma_1}{2\gamma}\tilde{\Theta}^T\Theta + \frac{\sigma_1}{2\gamma}\tilde{\Theta}^{*T}\Theta^*. \tag{41}$$

$$\frac{\sigma_2}{\eta}\tilde{\varepsilon}^T\hat{\varepsilon} \le -\frac{\sigma_2}{2\eta}\tilde{\varepsilon}^2 + \frac{\sigma_2}{2\eta}\left|\varepsilon^*\right|^2. \tag{42}$$

By introducing (41) and (42) into (40), yields:

$$V' \le -\alpha s^2 + \varepsilon^*\varsigma - \frac{\sigma_1}{2\gamma}\tilde{\Theta}^T\Theta + \frac{\sigma_1}{2\gamma}\tilde{\Theta}^{*T}\Theta^* - \frac{\sigma_2}{2\eta}\tilde{\varepsilon}^2 + \frac{\sigma_2}{2\eta}\left|\varepsilon^*\right|^2. \tag{43}$$

Let's specify:

$$c = \min\{\sigma_1,\ \sigma_2,\ 2\alpha\}. \tag{44}$$

So (43) becomes:

$$V' \le -cV + \rho, \tag{45}$$

with:

$$\rho = \varepsilon^*\varsigma + \frac{\sigma_1}{2\gamma}\tilde{\Theta}^{*T}\Theta^* + \frac{\sigma_2}{2\eta}\left|\varepsilon^*\right|^2. \tag{46}$$

By integrating (46), we find that:

$$V(t) \le V(0)e^{-ct} + \rho/c. \quad (47)$$

Using (45) it can be demonstrated that the developed control algorithm of PUMA 560 robot presented in (22) is stable despite the existence of payload uncertainties and actuator faults consequently the tracking errors converge to zero. The proposed control scheme is showed in Fig. 2.

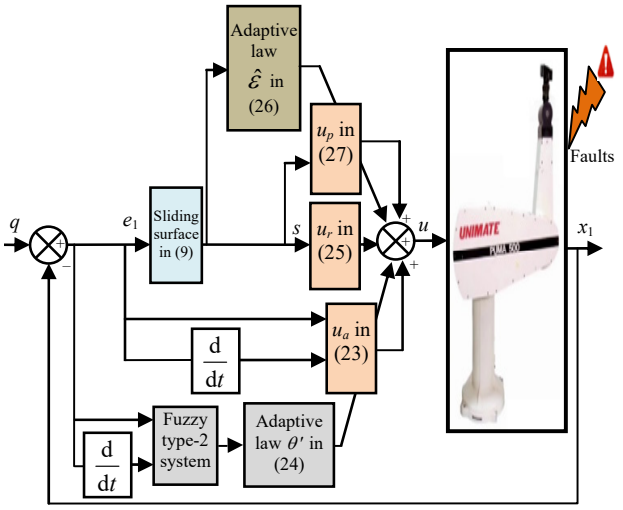

Fig. 2. Proposed adaptive control algorithm

4. Simulation results. The developed control method has been carried out by numerical simulation using MATLAB/Simulink environment in order to prove the efficiency of tracking capability of the three joints (q_1, q_2, q_3), where payload uncertainties and actuator faults are taken into account.

Cycloidal desired trajectories are considered to the three joints of PUMA 560 robot defined as:

$$q_{dj}(t) = \begin{cases} q_{dj}(0) + \dfrac{D_j}{2\pi}\left[2\pi\dfrac{t}{t_f} - \sin\left(2\pi\dfrac{t}{t_f}\right)\right] \text{for } 0 \le t \le t_f; \\ q_{dj}(t_f) \text{ for } t > t_f, \end{cases} \quad (48)$$

where $q_{dj}(t)$ is the cycloidal desired trajectory, j = 1,..., 3; $D_j = q_{dj}(t_f) - q_{dj}(0)$, and t_f is the final time of robot motion.

In addition, a comparative study with other state-of-the-art control methodology has been carried out, the input variables (e_1, e'_1) of the fuzzy type-2 system in (23) are decomposed into five linguistic variables on the normalized intervals [–1, 1] with five type-2 Gaussian membership functions. In order to verify the efficiency of the proposed control to versus actuator faults, we supply the following abrupt faults:

$$U_0 = \begin{cases} 150 \text{ N}\cdot\text{m} & t = 2 \text{ s}; \\ 120 \text{ N}\cdot\text{m} & t = 2 \text{ s}; \\ 230 \text{ N}\cdot\text{m} & t = 3 \text{ s}. \end{cases}$$

In addition, the payload mass m_0 varies in the interval from 10 kg to 2 kg, where it is showed in Fig. 3, and additional external disturbances τ_d are supposed varied in the time as:

$$\tau_d = \begin{cases} 10\sin(t) + 5\sin(200\pi t); \\ 5\cos(2t) + 5\sin(200\pi t); \\ 5\cos(2t) + 5\sin(200\pi t). \end{cases}$$

The initial conditions of the three joints are $q(0)$ = [–45 –130 125]^T deg. Three joints trajectory tracking are showed in Fig. 4, where it is remarked that, the positions for joints 1, 2, and 3 given by the control method proposed in [38, 51, 52] are deviated from their desired trajectory as depicted in Fig. 4, which show the insufficiency of this control strategy in faulty condition.

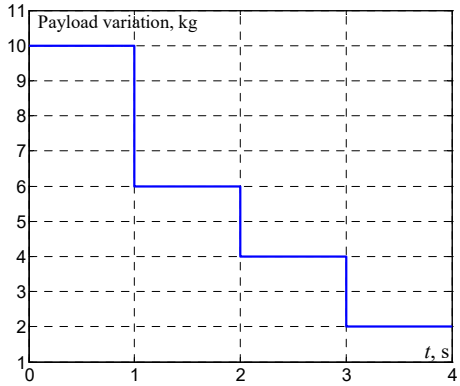

Fig. 3. Payload variation

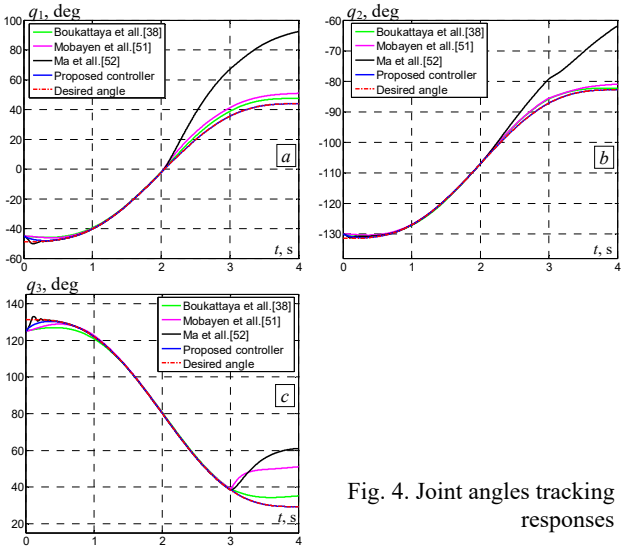

Fig. 4. Joint angles tracking responses

Figure 5 presents the joint tracking error for joints 1, 2, and 3, respectively. In Fig. 5, it is noted that in faulty operation, the proposed control give a smallest tracking error in compared to the proposed control in [38, 51, 52].

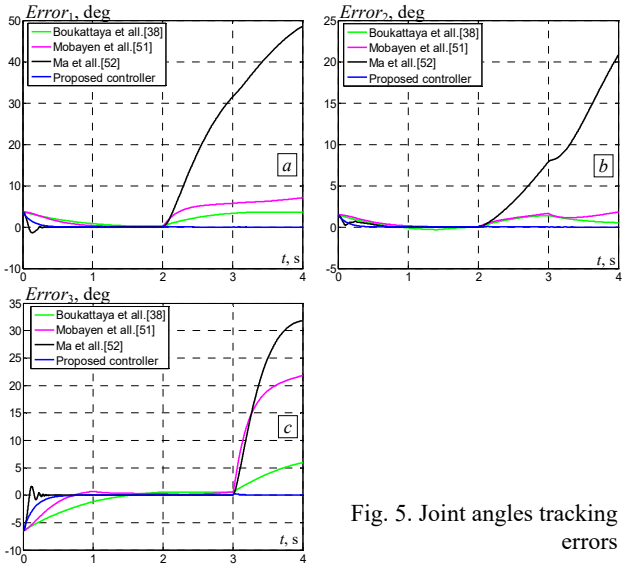

Fig. 5. Joint angles tracking errors

It is noted also from Fig. 6, that the proposed control strategy give lower control efforts with smooth signal, this

can be checked by the integral square of control input values (ISV) in Table 1. The trajectory tracking of the robot in Cartesian space under the proposed controller and the proposed control in [38, 51, 52], are indicated in Fig. 7. It is remarked that the proposed control achieved a good tracking in compared to other controllers.

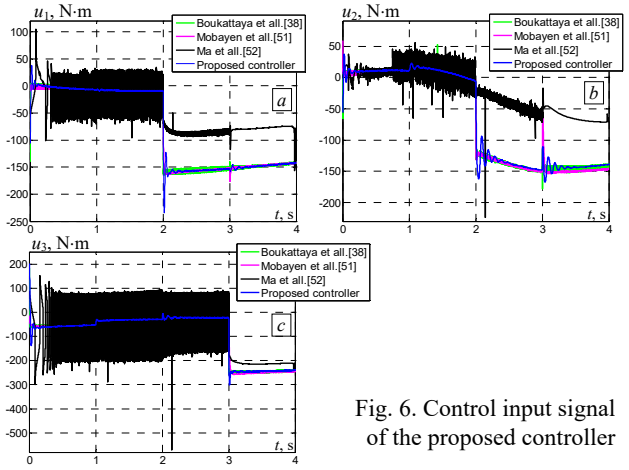

Fig. 6. Control input signal of the proposed controller

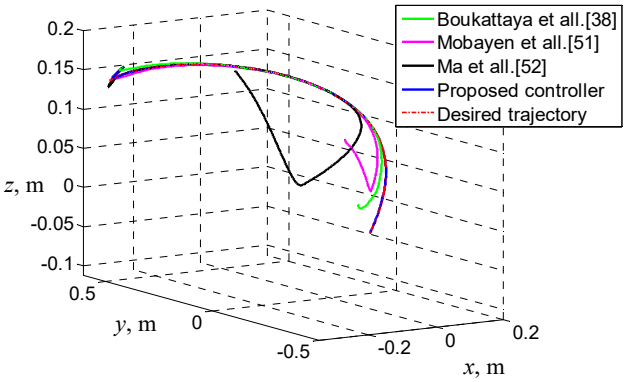

Fig. 7. Performed trajectory in Cartesian space

5. Quantitative comparison. In this section a quantitative comparison will be addressed in order to well illustrate the comparison between 4 control strategies, for this purpose an integral absolute error (IAE), integral square error (ISE), integral time absolute error (IATE) and ISV. The IAE, ISE and IATE are utilized as error tracking measured and ISV denotes energy consumption [53]. The IAE, ISE, IATE and ISV criteria are defined as:

$$IAE = \int_0^{t_f} |e_1(t)| \mathrm{d}t ; \quad (50) \qquad ISE = \int_0^{t_f} e_1^2(t) \mathrm{d}t ; \quad (51)$$

$$IATE = \int_0^{t_f} t|e_1(t)| \mathrm{d}t ; \quad (52) \qquad ISV = \int_0^{t_f} u_1^2(t) \mathrm{d}t . \quad (53)$$

From the quantitative comparison results presented in Table 1 and Fig. 8, it is confirmed that performance indices (IAE, ISE, IATE) values of the proposed controller are lower compared with the existing control [38, 51, 52]. In addition, comparing the control inputs (energy consumption), it is remarked that the proposed control strategy also give superior control input performance as shown in Table 1 and Fig. 8.

Table 1

Quantitative comparison under external disturbances, payload variation and actuator

Control scheme	IAE			ISE		
	Joint 1	Joint 2	Joint 3	Joint 1	Joint 2	Joint 3
Ref. [38]	8.16	2.45	8.15	23.14	2.27	30.95
Ref. [51]	12.61	3.14	19.55	65.93	3.83	318.87
Ref. [52]	57.99	16.94	21.85	2.07	210.51	558.25
Proposed controller	0.5323	0.2155	1.016	0.9763	0.1484	3.233
Control scheme	IATE			ISV		
	Joint 1	Joint 2	Joint 3	Joint 1	Joint 2	Joint 3
Ref. [38]	19.53	5.61	16.61	277	1447.5	5067.1
Ref. [51]	34.41	7.76	61.75	202.28	1301.6	5587.9
Ref. [52]	189.31	56.78	77.59	4455.1	2439	7870
Proposed controller	0.122	0.08	0.26	189.76	1122.4	4926.1

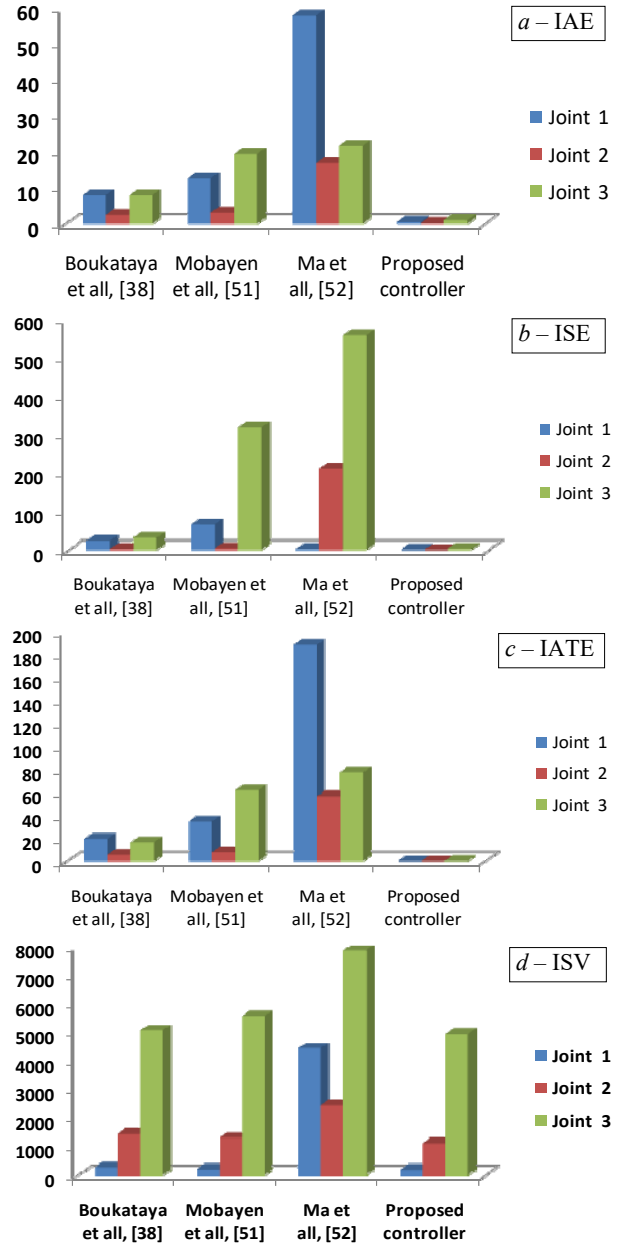

Fig. 8. Histogram of performance indices (IAE, ISE, IATE, ISV)

6. Conclusions. This work proposed a novel adaptive control strategy for path following of 3 degrees of freedom robot manipulators in the existence of uncertainties (payload variation), external disturbances, and actuator faults.

The developed approach associates an adaptive fuzzy type-2 control and FTSMC. The proposed control

algorithm is characterized by the integration of advantages of SMC, adaptive fuzzy type-2 control, and FTSMC. By utilizing only one powerful controller can supply several benefits such as faults and uncertainties compensation, small tracking error, chattering phenomenon reducing, and fast transient response. In addition, the proposed controller can supply globally asymptotic stability, where it has been demonstrated by the Lyapunov theory.

The proposed control law in this paper has been applied to the PUMA560 robot and compared with other developed controllers. The numerical simulation results demonstrate the upper tracking capability of the developed control methodology in the attendance of external perturbations, uncertainties, and actuator faults. Finally, as future work, the measurement noises and sensor defects effects will be taken into account. In addition, an optimization algorithm will be addressed in order to give the optimal values of the developed controller.

Conflict of interest. The authors declare that there is no conflict of interest.

REFERENCES

1. Capisani L.M., Ferrara A., Magnani L. Second order sliding mode motion control of rigid robot manipulators. *2007 46th IEEE Conference on Decision and Control*, 2007, pp. 3691-3696. doi: https://doi.org/10.1109/CDC.2007.4434473.

2. Wen Yu, Rosen J. Neural PID Control of Robot Manipulators With Application to an Upper Limb Exoskeleton. *IEEE Transactions on Cybernetics*, 2013, vol. 43, no. 2, pp. 673-684. doi: https://doi.org/10.1109/TSMCB.2012.2214381.

3. Su Y., Muller P.C., Zheng C. Global asymptotic saturated PID control for robot manipulators. *IEEE Transactions on Control Systems Technology*, 2010, vol. 18, no. 6, pp. 1280-1288. doi: https://doi.org/10.1109/TCST.2009.2035924.

4. Tayebi A., Abdul S., Zaremba M.B., Ye Y. Robust Iterative Learning Control Design: Application to a Robot Manipulator. *IEEE/ASME Transactions on Mechatronics*, 2008, vol. 13, no. 5, pp. 608-613. doi: https://doi.org/10.1109/TMECH.2008.2004627.

5. Wang M., Yang A. Dynamic Learning From Adaptive Neural Control of Robot Manipulators With Prescribed Performance. *IEEE Transactions on Systems, Man, and Cybernetics: Systems*, 2017, vol. 47, no. 8, pp. 2244-2255. doi: https://doi.org/10.1109/TSMC.2016.2645942.

6. Duchaine V., Bouchard S., Gosselin C.M. Computationally Efficient Predictive Robot Control. *IEEE/ASME Transactions on Mechatronics*, 2007, vol. 12, no. 5, pp. 570-578. doi: https://doi.org/10.1109/TMECH.2007.905722.

7. Feng Lin, Brandt R.D. An optimal control approach to robust control of robot manipulators. *IEEE Transactions on Robotics and Automation*, 1998, vol. 14, no. 1, pp. 69-77. doi: https://doi.org/10.1109/70.660845.

8. Morecki A., Knapczyk J. *Basics of Robotics: Theory and Components of Manipulators and Robots*. Springer, 1999. 580 p.

9. Vidyasagar M. *Robot Dynamics and Control*. Wiley, 1989. 336 p.

10. Jansen H.V., Tas N.R., Berenschot J.W. *Encyclopedia of Nanoscience and Nanotechnology*. Addison-Wisley, 1989.

11. Ferrara A., Incremona G.P. Design of an Integral Suboptimal Second-Order Sliding Mode Controller for the Robust Motion Control of Robot Manipulators. *IEEE Transactions on Control Systems Technology*, 2015, vol. 23, no. 6, pp. 2316-2325. doi: https://doi.org/10.1109/TCST.2015.2420624.

12. Jin M., Kang S.H., Chang P.H., Lee J. Robust Control of Robot Manipulators Using Inclusive and Enhanced Time Delay Control. *IEEE/ASME Transactions on Mechatronics*, 2017, vol. 22, no. 5, pp. 2141-2152. doi: https://doi.org/10.1109/TMECH.2017.2718108.

13. Utkin V. *Sliding Modes on Control and Optimization*. Springer, 1992. 286 p.

14. Abed K., Zine H.K.E. Intelligent fuzzy back-stepping observer design based induction motor robust nonlinear sensorless control. *Electrical Engineering & Electromechanics*, 2024, no. 2, pp. 10-15. doi: https://doi.org/10.20998/2074-272X.2024.2.02.

15. Xiao B., Hu Q., Zhang Y. Adaptive Sliding Mode Fault Tolerant Attitude Tracking Control for Flexible Spacecraft Under Actuator Saturation. *IEEE Transactions on Control Systems Technology*, 2012, vol. 20, no. 6, pp. 1605-1612. doi: https://doi.org/10.1109/TCST.2011.2169796.

16. Liang Y.-W., Xu S.-D., Liaw D.-C., Chen C.-C. A Study of T–S Model-Based SMC Scheme With Application to Robot Control. *IEEE Transactions on Industrial Electronics*, 2008, vol. 55, no. 11, pp. 3964-3971. doi: https://doi.org/10.1109/TIE.2008.2005138.

17. Chen G., Song Y., Guan Y. Terminal Sliding Mode-Based Consensus Tracking Control for Networked Uncertain Mechanical Systems on Digraphs. *IEEE Transactions on Neural Networks and Learning Systems*, 2018, vol. 29, no. 3, pp. 749-756. doi: https://doi.org/10.1109/TNNLS.2016.2636323.

18. Xu Q. Piezoelectric Nanopositioning Control Using Second-Order Discrete-Time Terminal Sliding-Mode Strategy. *IEEE Transactions on Industrial Electronics*, 2015, vol. 62, no. 12, pp. 7738-7748. doi: https://doi.org/10.1109/TIE.2015.2449772.

19. Wang H., Man Z., Kong H., Zhao Y., Yu M., Cao Z., Zheng J., Do M.T. Design and Implementation of Adaptive Terminal Sliding-Mode Control on a Steer-by-Wire Equipped Road Vehicle. *IEEE Transactions on Industrial Electronics*, 2016, vol. 63, no. 9, pp. 5774-5785. doi: https://doi.org/10.1109/TIE.2016.2573239.

20. Zheng J., Wang H., Man Z., Jin J., Fu M. Robust Motion Control of a Linear Motor Positioner Using Fast Nonsingular Terminal Sliding Mode. *IEEE/ASME Transactions on Mechatronics*, 2015, vol. 20, no. 4, pp. 1743-1752. doi: https://doi.org/10.1109/TMECH.2014.2352647.

21. Madani T., Daachi B., Djouani K. Modular-Controller-Design-Based Fast Terminal Sliding Mode for Articulated Exoskeleton Systems. *IEEE Transactions on Control Systems Technology*, 2017, vol. 25, no. 3, pp. 1133-1140. doi: https://doi.org/10.1109/TCST.2016.2579603.

22. Solis C.U., Clempner J.B., Poznyak A.S. Fast Terminal Sliding-Mode Control With an Integral Filter Applied to a Van Der Pol Oscillator. *IEEE Transactions on Industrial Electronics*, 2017, vol. 64, no. 7, pp. 5622-5628. doi: https://doi.org/10.1109/TIE.2017.2677299.

23. Van M., Ge S.S., Ren H. Finite Time Fault Tolerant Control for Robot Manipulators Using Time Delay Estimation and Continuous Nonsingular Fast Terminal Sliding Mode Control. *IEEE Transactions on Cybernetics*, 2017, vol. 47, no. 7, pp. 1681-1693. doi: https://doi.org/10.1109/TCYB.2016.2555307.

24. Xu S.S.-D., Chen C.-C., Wu Z.-L. Study of Nonsingular Fast Terminal Sliding-Mode Fault-Tolerant Control. *IEEE Transactions on Industrial Electronics*, 2015, vol. 62, no. 6, pp. 3906-3913. doi: https://doi.org/10.1109/TIE.2015.2399397.

25. Parra-Vega V., Arimoto S., Yun-Hui Liu, Hirzinger G., Akella P. Dynamic sliding PID control for tracking of robot manipulators: theory and experiments. *IEEE Transactions on Robotics and Automation*, 2003, vol. 19, no. 6, pp. 967-976. doi: https://doi.org/10.1109/TRA.2003.819600.

26. Incremona G.P., Ferrara A., Magni L. MPC for Robot Manipulators With Integral Sliding Modes Generation. *IEEE/ASME Transactions on Mechatronics*, 2017, vol. 22, no. 3, pp. 1299-1307. doi: https://doi.org/10.1109/TMECH.2017.2674701.

27. Oualah O., Kerdoun D., Boumassata A. Super-twisting sliding mode control for brushless doubly fed reluctance generator based on wind energy conversion system. *Electrical Engineering & Electromechanics*, 2023, no. 2, pp. 86-92. doi: https://doi.org/10.20998/2074-272X.2023.2.13.

28. Van M., Ge S.S., Ren H. Robust Fault-Tolerant Control for a Class of Second-Order Nonlinear Systems Using an Adaptive

Third-Order Sliding Mode Control. *IEEE Transactions on Systems, Man, and Cybernetics: Systems*, 2016, vol. 47, no. 2, pp. 221-228. doi: https://doi.org/10.1109/TSMC.2016.2557220.
29. Lilly J.H., Liang Yang. Sliding mode tracking for pneumatic muscle actuators in opposing pair configuration. *IEEE Transactions on Control Systems Technology*, 2005, vol. 13, no. 4, pp. 550-558. doi: https://doi.org/10.1109/TCST.2005.847333.
30. Chen J.-Y. Expert SMC-based fuzzy control with genetic algorithms. *Journal of the Franklin Institute*, 1999, vol. 336, no. 4, pp. 589-610. doi: https://doi.org/10.1016/S0016-0032(97)00077-X.
31. Tondu B. *Artificial Muscles for Humanoid Robots, Humanoid Robots: Human-like Machines*, 2007. Book edited by Matthias Hackel, pp. 89-122, Itech, Vienna, Austria.
32. Braikia K., Chettouh M., Tondu B., Acco P., Hamerlain M. Improved Control Strategy of 2-Sliding Controls Applied to a Flexible Robot Arm. *Advanced Robotics*, 2011, vol. 25, no. 11-12, pp. 1515-1538. doi: https://doi.org/10.1163/016918611X579510.
33. Van M., Kang H.-J., Suh Y.-S. Second Order Sliding Mode-Based Output Feedback Tracking Control for Uncertain Robot Manipulators. *International Journal of Advanced Robotic Systems*, 2013, vol. 10, no. 1, pp. 1-9. doi: https://doi.org/10.5772/55060.
34. Guezi A., Bendaikha A., Dendouga A. Direct torque control based on second order sliding mode controller for three-level inverter-fed permanent magnet synchronous motor: comparative study. *Electrical Engineering & Electromechanics*, 2022, no. 5, pp. 10-13. doi: https://doi.org/10.20998/2074-272X.2022.5.02.
35. Aissaoui M., Bouzeria H., Benidir M., Labed M.A. Harmonics suppression in high-speed railway via single-phase traction converter with an LCL filter using fuzzy logic control strategy. *Electrical Engineering & Electromechanics*, 2024, no. 2, pp. 16-22. doi: https://doi.org/10.20998/2074-272X.2024.2.03.
36. Bonivento C., Gentili L., Paoli A. Internal model based fault tolerant control of a robot manipulator. *2004 43rd IEEE Conference on Decision and Control (CDC)*, 2004, vol. 5, pp. 5260-5265. doi: https://doi.org/10.1109/CDC.2004.1429643.
37. Bonivento C., Gentili L., Paoli A. Fault Tolerant Tracking of a Robot Manipulator: An Internal Model Based Approach. *Systems and Control: Foundations and Applications*, 2006, no. 9780817643836, pp. 271-287. doi: https://doi.org/10.1007/0-8176-4470-9_15.
38. Boukattaya M., Mezghani N., Damak T. Adaptive nonsingular fast terminal sliding-mode control for the tracking problem of uncertain dynamical systems. *ISA Transactions*, 2018, vol. 77, pp. 1-19. doi: https://doi.org/10.1016/j.isatra.2018.04.007.
39. Yi S., Zhai J. Adaptive second-order fast nonsingular terminal sliding mode control for robotic manipulators. *ISA Transactions*, 2019, vol. 90, pp. 41-51. doi: https://doi.org/10.1016/j.isatra.2018.12.046.
40. Mondal S., Mahanta C. Adaptive second order terminal sliding mode controller for robotic manipulators. *Journal of the Franklin Institute*, 2014, vol. 351, no. 4, pp. 2356-2377. doi: https://doi.org/10.1016/j.jfranklin.2013.08.027.
41. Van M., Ge S.S., Ren H. Finite Time Fault Tolerant Control for Robot Manipulators Using Time Delay Estimation and Continuous Nonsingular Fast Terminal Sliding Mode Control. *IEEE Transactions on Cybernetics*, 2017, vol. 47, no. 7, pp. 1681-1693. doi: https://doi.org/10.1109/TCYB.2016.2555307.
42. Van M., Do X.P., Mavrovouniotis M. Self-tuning fuzzy PID-nonsingular fast terminal sliding mode control for robust fault tolerant control of robot manipulators. *ISA Transactions*, 2020, vol. 96, pp. 60-68. doi: https://doi.org/10.1016/j.isatra.2019.06.017.
43. Xiao B., Yin S., Gao H. Reconfigurable Tolerant Control of Uncertain Mechanical Systems With Actuator Faults: A Sliding Mode Observer-Based Approach. *IEEE Transactions on Control Systems Technology*, 2018, vol. 26, no. 4, pp. 1249-1258. doi: https://doi.org/10.1109/TCST.2017.2707333.
44. Amer A.F., Sallam E.A., Elawady W.M. Adaptive fuzzy sliding mode control using supervisory fuzzy control for 3 DOF planar robot manipulators. *Applied Soft Computing*, 2011, vol. 11, no. 8, pp. 4943-4953. doi: https://doi.org/10.1016/j.asoc.2011.06.005.
45. Guendouzi A., Boubakir A., Hamerlain M. Higher order sliding mode control of robot manipulator. *The Ninth International Conference on Autonomic and Autonomous Systems (ICAS 2013)*, 2013, pp. 61-66.
46. Xinghuo Yu, Man Zhihong. Fast terminal sliding-mode control design for nonlinear dynamical systems. *IEEE Transactions on Circuits and Systems I: Fundamental Theory and Applications*, 2002, vol. 49, no. 2, pp. 261-264. doi: https://doi.org/10.1109/81.983876.
47. Chen M., Wu Q.-X., Cui R.-X. Terminal sliding mode tracking control for a class of SISO uncertain nonlinear systems. *ISA Transactions*, 2013, vol. 52, no. 2, pp. 198-206. doi: https://doi.org/10.1016/j.isatra.2012.09.009.
48. Xiong J.-J., Zhang G.-B. Global fast dynamic terminal sliding mode control for a quadrotor UAV. *ISA Transactions*, 2017, vol. 66, pp. 233-240. doi: https://doi.org/10.1016/j.isatra.2016.09.019.
49. Yacef F., Bouhali O., Hamerlain M., Rizoug N. Observer-based Adaptive Fuzzy Backstepping Tracking Control of Quadrotor Unmanned Aerial Vehicle Powered by Li-ion Battery. *Journal of Intelligent & Robotic Systems*, 2016, vol. 84, no. 1-4, pp. 179-197. doi: https://doi.org/10.1007/s10846-016-0345-0.
50. Bounar N., Boulkroune A., Boudjema F., M'Saad, M., Farza M. Adaptive fuzzy vector control for a doubly-fed induction motor. *Neurocomputing*, 2015, vol. 151, part 2, pp. 756-769. doi: https://doi.org/10.1016/j.neucom.2014.10.026.
51. Mobayen S., Tchier F., Ragoub L. Design of an adaptive tracker for n -link rigid robotic manipulators based on super-twisting global nonlinear sliding mode control. *International Journal of Systems Science*, 2017, vol. 48, no. 9, pp. 1990-2002. doi: https://doi.org/10.1080/00207721.2017.1299812.
52. Ma Z., Sun G. Dual terminal sliding mode control design for rigid robotic manipulator. *Journal of the Franklin Institute*, 2018, vol. 355, no. 18, pp. 9127-9149. doi: https://doi.org/10.1016/j.jfranklin.2017.01.034.
53. Li T.-H.S., Huang Y.-C. MIMO adaptive fuzzy terminal sliding-mode controller for robotic manipulators. *Information Sciences*, 2010, vol. 180, no. 23, pp. 4641-4660. doi: https://doi.org/10.1016/j.ins.2010.08.009.

Received 27.06.2024
Accepted 18.08.2024
Published 02.01.2025

H. Rahali [1], *Doctor of Electrotechnical,*
S. Zeghlache [2], *Doctor of Electrotechnical, Professor,*
B.D.E. Cherif [1], *Doctor of Electrotechnical,*
L. Benyettou [1], *Doctor of Electrotechnical, Professor,*
A. Djerioui[1], *Doctor of Electrotechnical, Professor,*
[1] Laboratory of Electrical Engineering,
Faculty of Technology, University of M'Sila, Algeria,
e-mail: hilal.rahali@univ-msila.dz (Corresponding Author);
[2] Laboratory of Signals and Systems Analysis,
Faculty of Technology, University of M'Sila, Algeria.

How to cite this article:
Rahali H., Zeghlache S., Cherif B.D.E., Benyettou L., Djerioui A. Robust adaptive fuzzy type-2 fast terminal sliding mode control of robot manipulators in attendance of actuator faults and payload variation. *Electrical Engineering & Electromechanics*, 2025, no. 1, pp. 31-38. doi: https://doi.org/10.20998/2074-272X.2025.1.05

UDC 620.179.147:519.853.6 https://doi.org/10.20998/2074-272X.2025.1.06

V.Ya. Halchenko, R.V. Trembovetska, V.V. Tychkov

Computer-economical optimization method for solving inverse problems of determining electrophysical properties of objects in eddy current structroscopy

Introduction. *The problems of determining the profiles of electrophysical material properties are among the inverse problems of electrodynamics. In these studies, the focus is on the creation of a computer-economical method for reconstructing the profiles of electrical conductivity and magnetic permeability of metal planar objects under testing. These parameters can include the information about the results and quality of the production process or the effects of exposure to an aggressive environment. Registration of changes in electrophysical properties by means of eddy current testing allows for prompt adoption of effective management decisions regarding controlled processes. The simultaneous determination of these parameters because of non-contact indirect measurements of the electromotive force (EMF) by surface eddy current probes over the surface object with the subsequent restoration of the parameter distributions along its thickness by numerical methods is an urgent task.* ***Objective.*** *To create a computer-economical method for determining the electrophysical properties of objects by means of surrogate optimization with the accumulation of additional apriori knowledge about them in neural network metamodels with nonlinearly reduced dimensionality to improve the accuracy of simultaneous profile determination.* ***Methodology.*** *The method for determining the electrophysical properties of objects is based on homogeneous designs of experiments, surrogate optimization with the accumulation of apriori knowledge about them in metamodels with nonlinearly reduced dimensionality.* ***Originality.*** *Integration of multiple capabilities in the surrogate model that combine the advantages of high-performance computing and optimization algorithms in the factor space reduced by the Kernel PCA (Principal Component Analysis) method. The accumulated additional apriori knowledge about objects is incorporated into the neural network metamodel. This makes it possible to implicitly identify complex patterns hidden in the data that are characteristic of the eddy current measuring process and take them into account during reconstruction.* ***Results.*** *The reduction of the search space is a considerable result. It was possible due to the nonlinear Kernel-PCA transformations with the analysis of the eigenvalues of the kernel matrix and the restriction on the number of PCA principal components. The results confirmed the validity of a significant reduction in space without major loss of information. Another indicator of the effectiveness of the method is a high precision of the created surrogate models. The accuracy of the reduced dimensional metamodels was achieved by using a homogeneous computer design of experiment and deep learning networks. The adequacy and informativeness of the constructed surrogate models have been proved by numerical indicators. The efficiency of the method is demonstrated on model examples.* References 36, table 5, figures 6.

Key words: **inverse problems, optimization method, eddy current measurings, reconstruction, material electrophysical properties, surrogate neural network models of reduced dimensionality, apriori information, global extremum.**

Вступ. *Серед обернених задач електродинаміки певну частину складають задачі визначення профілів електрофізичних властивостей матеріалів. В цих дослідженнях акцентується увага на створенні обчислювально-економного методу реконструкції профілів електричної провідності та магнітної проникності металевих пласких об'єктів контролю. Ці параметри можуть нести інформацію щодо результатів та якості виробничого процесу або наслідків впливу на об'єкт агресивного середовища. Реєстрація змін електрофізичних властивостей засобами вихрострумового контролю дозволяє здійснювати оперативне прийняття ефективних управлінських рішень щодо контрольованих процесів. Одночасне визначення вказаних параметрів у результаті безконтактних непрямих вимірювань електрорушійної сили (ЕРС) накладними вихрострумовими перетворювачами над поверхнею об'єкту із наступним відновленням розподілів параметрів вздовж його товщі чисельними методами є актуальним завданням.* ***Мета.*** *Створення обчислювально-економного методу визначення електрофізичних властивостей об'єктів засобами сурогатної оптимізації із накопиченням додаткових апріорних знань щодо них у нейромережевих метамоделях із нелінійно-скороченою розмірністю для підвищення точності одночасного визначення профілів.* ***Методологія.*** *Метод визначення електрофізичних властивостей об'єктів створюється на основі однорідних планів експериментів, сурогатної оптимізації із накопиченням апріорних знань щодо них у метамоделях із нелінійно-скороченою розмірністю.* ***Оригінальність.*** *Інтеграція у сурогатній моделі комбінованих можливостей, які поєднують одночасно переваги високопродуктивних обчислень та виконання оптимізаційних алгоритмів у скороченому за допомогою методу Kernel PCA-просторі факторів. Виконано інкорпорацію акумульованих додаткових апріорних знань щодо об'єктів у нейромережеву метамодель. Це дозволяє неявно визначати складні приховані в даних закономірності, котрі характерні для процесу вихрострумових вимірювань, та врахувати їх під час реконструкції.* ***Результати.*** *Суттєвим результатом є скорочення простору пошуку. Це вдалося завдяки нелінійним перетворенням Kernel-PCA з аналізом власних значень ядерної матриці і обмеженням на кількість головних компонент PCA. Отримані результати підтвердили обґрунтованість істотного скорочення простору без суттєвої втрати інформації. Іншим показником ефективності методу є висока точність створених сурогатних моделей. Точності метамоделей скороченої розмірності вдалося досягти використанням однорідного комп'ютерного плану експерименту та мереж глибокого навчання. Числовими показниками доведені адекватність та інформативність побудованих сурогатних моделей. На модельних прикладах продемонстрована ефективність методу.* Бібл. 36, табл. 5, рис. 6.

Ключові слова: **обернені задачі, оптимізаційний метод, вихрострумові вимірювання, реконструкція, електрофізичні властивості матеріалу, сурогатні нейромережеві моделі скороченої розмірності, апріорна інформація, глобальний екстремум.**

Introduction. The inverse problems of determining the material electrophysical properties of metal planar testing objects (TO) make up a rather certain part among the varieties of computational electromagnetism problems [1–3]. This is due to their considerable practical importance for industry, where they help solve different problems related to production and technology. In particular, these studies focus on the tasks of inverse identification of the electrophysical properties of metal planar test objects (TO). The typical parameters to be measured indirectly are usually the electrical conductivity (EC) and magnetic permeability (MP). In many cases, they can provide information on the results and quality of the production process or the effects of exposure to aggressive environments on the TO. Registration of changes in the electrophysical properties of the TO by means of eddy current nondestructive testing allows for the prompt adoption of effective management decisions regarding controlled processes. Therefore, the

simultaneous determination of these parameters as a result of noncontact measurements of the electromotive force (EMF) by surface eddy current probes (ECP) over the surface of the TO with the subsequent reconstruction of the distributions of EC and MP (i.e., parameter profiles) along its thickness by numerical methods is an urgent task that needs to be solved.

The problem is not trivial, since it belongs to the mathematically incorrectly posed ones [4], which are characterized by instability of the solution in the presence of noise and uncontrolled variations of the complex-valued signal generated by the ECP. The peculiarity of determining the profiles of the EC and MP is the combination of measurement procedures and numerical solution of the inverse problem on the space of the set of complex numbers, each of which introduces a corresponding specificity into their overall interaction. Although some attempts to solve this problem have been made, as, for example, in [5], they are not yet sufficiently perfect and require further progress, including on the basis of intelligent technologies.

The analysis of scientific publications on this topic shows a deep interest in this issue.

A fairly thorough analytical review of current research on the problem under consideration was made by the authors in publication [6], where they reviewed publications [7–16]. It summarizes the latest trends in the development of approaches to determining the profiles of electrophysical properties of TO materials and their inherent shortcomings. In particular, we considered optimization and data-driven methods [17] that use the achievements of artificial intelligence techniques, measurements at many fixed and swept-frequencies.

This group of papers also includes the article [13], which proposes a method of inverse identification for the experimental characterization of elastic-plastic contact in indentation problems. The second group of publications consists of studies [14–17], which differ from the achievements of the previous one by the general concept of building reverse identification procedures, which constitutes a certain alternative to the identification methods from the first group.

Thus, there is a clear trend towards the widespread use of optimization and machine learning-based methods.

When using optimization methods, researchers are focused on solving inverse problems by means of gradient-free metaheuristic algorithms for finding a global extremum, in particular Simulated Annealing, Harmony Search, Genetic Algorithms (GA), Particle Swarm Optimization (PSO), etc. and their hybrids, which minimize each other's weaknesses and add to the development of their respective strengths, ensuring efficient organization of research coverage of the multidimensional search space. In addition, it is proposed to replace resource-intensive target functions with their high-performance surrogate models, which guarantee fast and reliable computations when they are repeatedly executed. It should also be noted that the method is quite dependent on the dimensionality of the search space, i.e., the number of variables searched. This is due to the effect of the «curse of dimensionality» and requires additional special actions to reduce the dimensionality of the space.

Machine learning-based methods have their advantages and disadvantages. They are more flexible, provide better generalization capability even for data that was not used during training, and have a greater potential for processing complex data with significantly nonlinear dependencies. These methods are robust to noise and random variations in data during measurements, which has a positive impact on their reliability. Researchers consider various approaches to the implementation of intelligent technologies, including deep-learning algorithms of neural networks (artificial neural network – ANN), transfer learning, various types of ANNs from physics-informed neural networks (PINN) to generative ones, in particular variational autoencoders (VAE). However, machine learning methods often require a significant amount of data for their implementation.

To summarize, it is worth noting that hybrid optimization strategies that integrate all the advantages of the analyzed methods, should be used for further research. Thus, it is promising to use surrogate optimization with the use of proxy models (metamodels, i.e., surrogate models) of reduced dimensionality to determine the profiles of electrophysical properties of TO materials, provided that they are created on the basis of deep fully connected neural networks. Furthermore, when analyzing existing studies, the authors did not find any known approaches to incorporating additional redundant knowledge about TO into neural network metamodels, which would be useful to be included directly in them. This makes it possible to implicitly establish complex nonlinear patterns of signal formation hidden in the data during experimental measurements of the ECP, to expect a more clear reflection of the physics of the eddy current testing process by the metamodel and, accordingly, a higher identification accuracy, since the degree of transparency increases with the availability of apriori information.

The feasibility of the approach to solving the problem proposed by the authors has already been proven by their previous research [6], where they compared the results of the corresponding calculations by the classical method of surrogate optimization and an alternative method using surrogate models of reduced dimensionality. However, this reduction was carried out by linear PCA (Principal Component Analysis) transformations, which led to a reduction in the dimensionality of the metamodels by almost half. However, the use of nonlinear Kernel PCA-transformations for this purpose allows us to hope for even more convincing results.

Thus, the **aim of the paper** is to develop a computationally efficient method for determining the electrophysical properties of planar metal objects by means of surrogate optimization with the accumulation of additional apriori knowledge about them in neural network metamodels with a nonlinearly reduced dimensionality to improve the accuracy of simultaneous determination of electrical conductivity and magnetic permeability profiles in eddy current measurements when establishing their microstructural features.

Research methodology. The reconstruction of the profiles of ECs and MPs is performed by an experimental and numerical method, the sequence of stages of which

largely coincides with those proposed in [1], but with certain changes concerning the accumulation of a priori information in the neural network metamodel.

The first stage involves a single measurement with an surface ECP over a planar metal TO with the registration of a sinusoidal EMF signal e_{mes}, mathematically represented by a complex number in the exponential form of recording, i.e., with the fixation of its amplitude and phase. This completes the experimental part of the method, and all subsequent stages relate exclusively to its numerical implementation.

At the next stage, the key basic and additional parameters of the electrodynamic model that describes the measurement process and reflects the result of the interaction of the electromagnetic field with the conductive medium of the TO are determined. Hence, the main ones are the discretized profiles of the EC $\sigma_i(z)$ and MP $\mu_i(z)$, $i = 1, ..., L$, where L is the number of conditional layers of the breakdown of the zone of penetration of the electromagnetic field into the TO; and additional useful ones are the frequency f of excitation of the sensing electromagnetic field and the diameter $2 \cdot r$ of the pick-up coil of the ECP; while the lift-off distance is an additional interference. It is possible to enter all these parameters into the metamodel. The a priori information, which is also accumulated in the metamodel, also includes the laws of distribution of EC and MP. At this stage, a computerized uniform design of experiment (DOE) is also created with the mandatory input of the main model parameters, but the incorporation of certain additional parameters may take place depending on the requirements for calculation accuracy. Their addition increases the time and computing resources required to form a training sample at the points of the generated design. The accuracy of the approximation of the multidimensional nonlinear response hypersurface by the neural network metamodel depends on the properties of the design. Therefore, the design should have high homogeneity rates both in the entire search space and especially in two-dimensional projections. The organization of a detailed study of the response surface topography depends on the rational arrangement of the design points [18]. Since it is not possible to visualize the topography of the response hypersurface, it is advisable to have a uniform arrangement of points in the search space. The design is based on modified LP_τ-quasi-Sobol's sequences, the advantages and features of which are described in detail in the authors' publications [6, 19], which illustrate the method of its creation in a unit hyperspace, which provides low weighted symmetrized centered discrepancy (WSCD). After scaling to the specified dimensions of the design space, the design can be used for modeling.

At the third stage, a high-cost electrodynamic model of the eddy current testing process is used to generate a training sample and to calculate the model value of the EMF e_{mod} of the probe at the design points.

So, here we will use the solution of the corresponding forward problem of field theory, the geometric model of which is shown in Fig. 1.

A cylindrical ECP excitation coil is placed above the magnetic and conductive half-space associated with the TO. It has a rectangular cross-section of finite dimensions. The electromagnetic field is excited by a sinusoidal current I, which varies with an angular frequency $\omega = 2 \cdot \pi \cdot f$. The field is quasi-stationary, i.e., wave processes in the air are neglected. The bias currents in the TO are ignored due to their negligible values compared to the conduction currents. The excitation coil is characterized by a homogeneous current density across the cross-section i_0 and has a number of turns W. The TO is considered to be conditionally multilayer, which makes it possible to simplify the representation of continuous distributions $\sigma(z)$ and $\mu(z)$ by their piecewise constant approximation analogs of L discrete samples. The laws of distribution of the electrophysical properties of the TO are assumed to be known and determined experimentally [21]. The mathematical model was created under the assumptions of linearity, isotropy, and homogeneity of the environment. For further studies, due to its versatility and ease of use for any number of conditional layers, we chose the most popular analytical electrodynamic model Uzal-Cheng-Dodd-Deeds [21–24] in the matrix formulation in the modified Theodoulidis form [25].

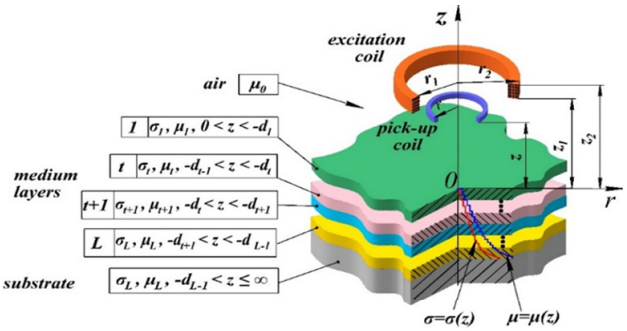

Fig. 1. Geometric model of the forward problem [20]

The magnetic vector potential in the lift-off below the ECP excitation coil is formed by summing its two components, namely, the primary potential $A^{(s)}$ of the coil itself in free space without the presence of the TO and the secondary potential $A^{(ec)}$ created by eddy currents induced in the object:

$$A_0 = A^{(s)} + A^{(ec)}. \quad (1)$$

The primary field of the excitation coil is calculated according to the expression:

$$A^{(s)} = \int_0^\infty J_1(\kappa r) \cdot C_S \cdot e^{\kappa z} \mathrm{d}\kappa, \quad (2)$$

where

$$C_S = \frac{\mu_0 \cdot i_0}{2} \cdot \frac{\chi(\kappa r_1, \kappa r_2)}{\kappa^3} \cdot \left(e^{-\kappa z_1} - e^{-\kappa z_2}\right),$$

$$\chi(x_1, x_2) = \left\{ x_1 \cdot J_0(x_1) - 2 \cdot \sum_{m=0}^{\infty} J_{2m+1}(x_1) \right\} -$$

$$- \left\{ x_2 \cdot J_0(x_2) - 2 \cdot \sum_{m=0}^{\infty} J_{2m+1}(x_2) \right\},$$

$i_0 = W \cdot I \cdot (r_2 - r_1)^{-1} \cdot (z_2 - z_1)^{-1}$, $\mu_0 = 4 \cdot \pi \cdot 10^{-7}$ H/m is a magnetic constant.

The secondary field is calculated according to the solution of the boundary value problem in the form of a second-order partial differential equation for the

azimuthal component of the magnetic vector potential A in the cylindrical coordinate system, which is valid for axially symmetric systems:

$$A\frac{\partial^2 A}{\partial r^2}+\frac{1}{r}\cdot\frac{\partial A}{\partial r}-\frac{A}{r^2}+\frac{\partial^2 A}{\partial z^2}=k^2\cdot A, \quad (3)$$

where $k^2=j\cdot\omega\cdot\mu_r\cdot\mu_0\cdot\sigma$, $j=\sqrt{-1}$; under the given boundary conditions

$$\left[\begin{array}{c} A_0=A_1 \\ \frac{\partial A_0}{\partial z}=\frac{1}{\mu_{r1}}\cdot\frac{\partial A_1}{\partial z}\end{array}\right]_{z=0} \text{and} \left[\begin{array}{c} A_{t+1}=A_t \\ \frac{1}{\mu_{t+1}}\cdot\frac{\partial A_{t+1}}{\partial z}=\frac{1}{\mu_t}\cdot\frac{\partial A_t}{\partial z}\end{array}\right]_{z=-d_t}. \quad (4)$$

The solution of the boundary value problem is represented by the following expression for an arbitrary number of conditional layers of the TO:

$$A^{(ec)}=\int_0^\infty J_1(\kappa r)\cdot D_{ec}\cdot e^{-\kappa z}\mathrm{d}\kappa, \quad (5)$$

$$\boldsymbol{V}=\boldsymbol{T}(1,2)\cdot\boldsymbol{T}(2,3)...\boldsymbol{T}(L-2,L-1)\cdot\boldsymbol{T}(L-1,L);$$

$$T_{11}(t,t+1)=\frac{1}{2}\cdot e^{(-\lambda_{t+1}+\lambda_t)dt}\cdot\left(1+\frac{\mu_t}{\mu_{t+1}}\cdot\frac{\lambda_{t+1}}{\lambda_t}\right),$$

$$D_{ec}=\frac{(\kappa\cdot\mu_{t+1}-\lambda_1)\cdot V_{11}(1)+(\kappa\cdot\mu_{t+1}+\lambda_1)\cdot V_{21}(1)}{(\kappa\cdot\mu_{t+1}+\lambda_1)\cdot V_{11}(1)+(\kappa\cdot\mu_{t+1}-\lambda_1)\cdot V_{21}(1)}\cdot C_s,$$

$$T_{12}(t,t+1)=\frac{1}{2}\cdot e^{(\lambda_{t+1}+\lambda_t)dt}\cdot\left(1-\frac{\mu_t}{\mu_{t+1}}\cdot\frac{\lambda_{t+1}}{\lambda_t}\right),$$

$$T_{21}(t,t+1)=\frac{1}{2}\cdot e^{(-\lambda_{t+1}-\lambda_t)dt}\cdot\left(1-\frac{\mu_t}{\mu_{t+1}}\cdot\frac{\lambda_{t+1}}{\lambda_t}\right),$$

$$T_{22}(t,t+1)=\frac{1}{2}\cdot e^{(\lambda_{t+1}-\lambda_t)dt}\cdot\left(1+\frac{\mu_t}{\mu_{t+1}}\cdot\frac{\lambda_{t+1}}{\lambda_t}\right),$$

$$\lambda_t=\left(\kappa^2+j\cdot\omega\cdot\mu_0\cdot\mu_t\cdot\sigma_t\right)^{1/2},$$

where $\boldsymbol{V}$ is a matrix with elements V_{11}, V_{21}; $\boldsymbol{T}()$ is a matrix with elements $T_{11}()$, $T_{12}()$, $T_{21}()$, $T_{22}()$; $J_0()$, $J_1()$, $J_m()$ are cylindrical Bessel functions of the first kind of zero, first, and m-th orders; (r_2-r_1) is the width of the cross-section of the ECP excitation coil, m; (z_2-z_1) is the height of the cross-section of the ECP excitation coil, m.

Thus, the output signal of the surface ECP induced in the pick-up coil can be calculated according to the formula:

$$e_{mod}=-j\cdot\omega\cdot w_{mes}\cdot\oint_{Lc}A_0(P)dl_p, \quad (6)$$

where w_{mes} is the number of turns of the pick-up coil; P is the observation point with coordinates (r, z) belonging to the contour L_c of the pick-up coil.

Thus, we finally obtain the EMF induced in the pick-up coil of the probe with a radius r:

$$e_{mod}=-j\cdot 2\cdot\pi\cdot r\cdot\omega\cdot w_{mes}\cdot A_0(P). \quad (7)$$

The verification of calculations based on the «exact» model was performed in the works of the authors [20, 26], where the results of calculations using the created software in the cases of two- and three-layer conditional representation of the TO were compared with numerical calculations by the finite element method and analytical expressions obtained for these simple idealizations. In addition, the verification was carried out by comparing the results of experimental studies conducted in [27], which recorded a sufficient level of accuracy.

The next step of the framework is to reduce the dimensionality of the search space. The purpose of these transformations is to simplify the architecture of the neural network surrogate model while simplifying it's training and increasing computational capacity and improving the conditions for the optimization algorithm. The reduction is performed by the Kernel PCA method [28, 29] with standard nonlinear transformations using the Gaussian kernel function. First, the data from the DOE are projected into a space of much higher dimensionality to obtain a kernel matrix, where linearly inseparable in the original space, significantly nonlinear data have much greater opportunities to determine independent variables with little loss of information due to the use of linear PCA. This ensures the transition to a significantly reduced dimensional PCA space with its characteristic advantages.

The fifth step is to create a neural network surrogate model. This is necessary because solving the inverse problem using an optimization implementation requires a computational model of the target function that can be used repeatedly with different parameter profiles. In this sense, model (7) creates a bottleneck in optimization, since the calculation of the non-proprietary integral of the first kind, integrals of special functions, and cumbersome combinations of special functions require quite significant expenditures of machine resources. On the other hand, a neural network metamodel also allows accumulating apriori information about the TO in advance. The metamodel is created using deep ANN techniques. The peculiarities of this stage include the need to use a CVNN (complex-valued neural network). However, in these studies, we used SCVNN (splitable complex-valued neural networks) instead of CVNN, i.e., a network split into two classical real-valued networks. They were constructed separately for the real and imaginary parts of the ECP output signal, and not for its amplitude and phase, which is essential, with subsequent combination into a common complex output. At the same time, the ANN inputs were really significant and subject to scaling. It is important for this stage to verify the adequacy and informativeness of the created metamodels according to the relevant statistical criteria and indicators.

After the necessary experimental measurements are performed and computational models are prepared, it is important to implement a productive strategy for the optimization process in the reduced search space. At this stage, a stochastic metaheuristic hybrid particle swarm global optimization algorithm PSO with evolutionary swarm composition formation, which is a low-level hybridization with the genetic algorithm GA, was used to find the extremum of the target function. The hybrid has proven its effectiveness in solving many practical problems, for example, in [31–33]. To reconstruct the profiles, the target function was compiled on the basis of the least squares method, which was minimized by comparing the simulated ECP signal with its experimental measured value when varying the EC and MP profiles:

$$F(\boldsymbol{\sigma},\boldsymbol{\mu},f...)=\left(\mathrm{Re}(e_{mes})-\mathrm{Re}(e_{metamod})\right)^2+\left(\mathrm{Im}(e_{mes})-\mathrm{Im}(e_{metamod})\right)^2\rightarrow\min, \quad (8)$$

where $\boldsymbol{\sigma}$, $\boldsymbol{\mu}$ are the corresponding vectors of electrophysical properties of the TO that determine the desired profiles; $e_{metamod}$ is the EMF probe was calculated by the surrogate model.

The final stage of the framework involves projecting the found profiles of the electrophysical parameters of the TO from the reduced space to the original one. The inverse transformation is performed by an iterative process [31], which embodies the corresponding reproduction and is possible when using the Gaussian kernel function.

Numerical experiments. Let us demonstrate the main stages of the proposed methodology through numerical experiments. These experiments do not require any measurements of the ECP. Therefore, the first stage will be implemented with synthesized data, which will be obtained later at the stage of creating a surrogate model.

At the second stage to apply the electrodynamic model, we consider its parameters to be set: discretized profiles of the EC $\sigma_i(z)$ and MP $\mu_i(z)$, i = 1, ... , L, where L = 60; f = 2 kHz, r_1 = 32 mm, r_2 = 50 mm, z_1 = 1 mm, z_2 = 18 mm, I = 1 A, W = 100, r = 25 mm, z = 1 mm, w_{mes} = 50.

Since the modeling was limited to only two main factors, a combination of LP$_\tau$-sequences ξ_1, ξ_6 was used to implement a homogeneous quasi-design of the experiment. The creation of discretized profiles based on this design will be presented later. The number of samples was N = 2820. The homogeneity of DOE in a unit square is demonstrated in Fig. 2,*b* a bivariate histogram and Voronoi diagram. Only a limited number of points, namely 256, are shown for the convenience of visualizing the DOE homogeneity in Fig. 2,*b*. The quality of this design is estimated by the numerical index WSCD = $3.157 \cdot 10^{-7}$.

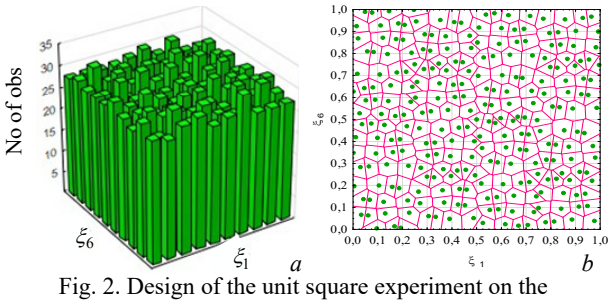

Fig. 2. Design of the unit square experiment on the LP$_\tau$-quasi Sobol's sequences ξ_1, ξ_6:
a – bivariate histogram; *b* – Voronoi diagram

Later on, the scaling was used to move to the dimensions of real space. Let us dwell on this in more detail. The zone of penetration of the electromagnetic field inside the TO is determined by the parameter $D = 3 \cdot 10^{-4}$ m. Before the microstructure changes, the TO is characterized by constant values of EC σ_{deep} and MP μ_{deep}. When the TO is exposed to any of the electrophysical factors (temperature, deformation, etc.), the values of the EC and MP change to the maximum on the surface to σ_{surf} and μ_{surf}, remaining unchanged at some depth of the zone. Due to the influence of uncontrollable physical factors, we assume that the values of σ_{surf} and μ_{surf} can vary within some apriori defined limits, for example, within ±15 %. In this case, the profiles are characterized by the values of EC $\sigma_{deep} = 2 \cdot 10^6$ S/m, $\sigma_{surf} = 9.2 \cdot 10^6$ S/m and MP – μ_{deep} = 10, μ_{surf} = 29.78, within which they vary in accordance with the established patterns determined previously.

Table 1 shows the numerical values of the electrophysical properties μ_{surf} and σ_{surf} on the surface of the TO at the DOE points (Fig. 2,*b*) projected by scaling into the real factor space. Then, taking into account the specified limits, the ranges of change in the EC parameters on the surface of the TO will be $7.82 \cdot 10^6 \le \sigma_{surf} \le 10.1 \cdot 10^6$ S/m, and the MP will be $24.531 \le \mu_{surf} \le 35.028$, with σ_{deep} and μ_{deep} being unchanged at the depth of the field penetration zone for any profiles.

During the modeling, we consider the laws of distribution of the electrophysical properties of the TO to be known and previously determined [21], namely, the EC is «exponential», the MP is «gaussian». Then, within the specified boundary limits of changes in electrophysical properties in the real design space (Table 1), we calculated the distributions of EC and MP for all DOE samples with discretization into a specified number of conditional As a result, we obtained a data set in the full factor space of size $N \times 2L$, i.e., the dimension of the factor space is 120, which is quite significant layers.

Table 1

Scaled design of the experiment

Parameters	Design of experiment samples							
	1	2	3	…	2817	2818	2819	2820
$\sigma_{surf} \times 10^6$, S/m	9.2	9.89	8.51	…	7.952756	8.642756	1.002276	9.677756
μ_{surf}	29.78	27.155	32.405	…	29.813	27.188	32.438	25.876

Some of the obtained profiles are shown in Fig. 3, and their numerical values are given in Table 2 to present the laws of distribution of the EC and MP, which are inherent in changes in the field penetration zone.

The third stage involves the calculations of the model value of the EMF e_{mod} of the probe, which are also included in Table 2, at the points of the formed design using a high-cost electrodynamic model [7].

At the fourth stage, the Kernel PCA method was used to reduce the dimensionality of the search space. To implement it, a number of mathematical transformations were performed: first, the transition from the original feature space to the auxiliary high-dimensional one was performed by projecting the DOE from dimension D to dimension N using a Gaussian kernel [31]. As a result, the kernel similarity matrix $\boldsymbol{K}$ of dimension $N \times N$ is obtained. Secondly, we apply the centering operation [31] to the kernel matrix and obtain the Gram matrix.

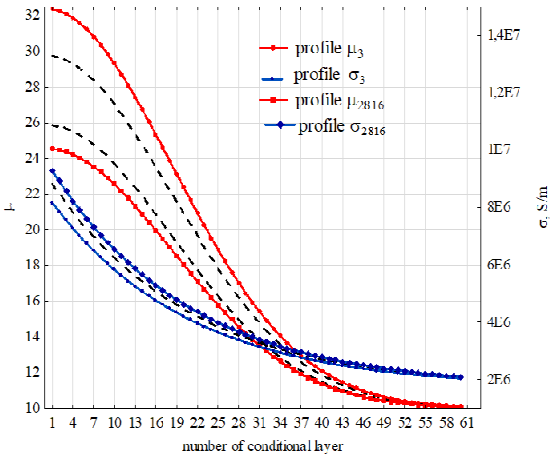

Fig. 3. Some profiles of MP and EC in the field penetration zone in the TO

Table 2

Array of initial data in the full factor space 2820×120

Profiles	Parameter	Numbers of conditional layers					ECP signal	
		1	2	…	59	60	Re(e_{mod})	Im(e_{mod})
1	μ	29.750	29.663	…	10.115	10.096	–0.737	–1.427
	σ, S/m	8834221	8486281	…	2092548	2073403		
2	μ	27.129	27.054	…	10.0994	10.083	–0.746	–1.389
	σ, S/m	9490569	9110618	…	2128662	2107756		
…	…	…	…	…	…	…	…	…
2818	μ	27.163	27.087	…	10.0997	10.083	–0.742	–1.427
	σ, S/m	8304154	7982065	…	2063382	2045659		
2819	μ	32.405	32.306	…	10.130	10.109	–0.734	–1.419
	σ, S/m	9616850	9230741	…	2135611	2114366		
2820	μ	25.852	25.782	…	10.092	10.077	–0.748	–1.386
	σ, S/m	9288676	8918572		2117553	2097189		

Third, we performed a standard linear PCA on the Gram matrix data, which assumes a singular value decomposition of the SVD [6]. Eventually, we have matrices of eigenvectors and a diagonal matrix containing eigenvalues, or rather singular numbers whose squares are eigenvalues. The ranking of the eigenvalues in the direction of reduction $\lambda_1 \geq \lambda_2 \geq ... \geq \lambda_N \geq 0$, which determines the eigenvectors for the reduced space, is shown in Fig. 4.

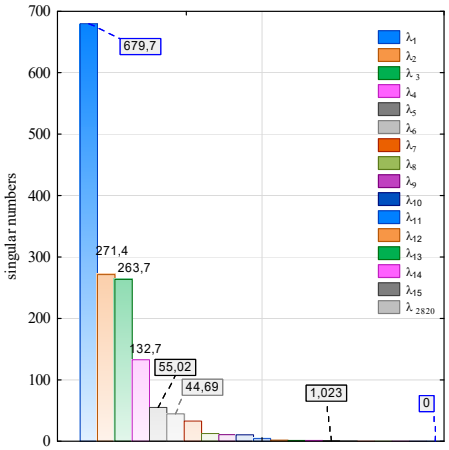

Fig. 4. Diagram of eigenvalues of the matrix

We select the first M eigenvectors under the condition $M<D$. Consequently, the first 15 eigenvectors whose singular values are greater than one, have been chosen. The reduced eigenvector matrix of dimension $N\times M$ is obtained, the elements of which g_{ij} are shown in Table 3.

Thus, the dimensionality reduction is carried out by projecting the original data onto the 15 selected principal components.

Table 3

Reduced design matrix for creating a metamodel with dimension 2820×15

Samples	Elements of a reduced plan matrix				
	$g^{(1)}$	$g^{(2)}$	…	$g^{(14)}$	$g^{(15)}$
1	–0.0128	8.0135	…	0.000046289	0.000075681
2	–14.5184	0.8005	…	–0.0091929	–0.0018594
3	14.5202	–0.0864	…	0.0088841	0.0016829
4	15.1605	–4.2985	…	0.0308	0.0079691
5	–8.9933	5.429	…	0.0348	–0.0182
…	…	…	…	…	…
2817	17.1196	–7.4162	…	–0.0212	–0.0326
2818	12.6383	2.9075	…	–0.0146	0.003627
2819	–15.7642	–2.18	…	–0.0274	–0.00028853
2820	–10.3193	3.5479	…	0.0234	0.0203

The next step is to create neural network surrogate models [18, 19] based on deep ANNs, for which the outputs of each of the two networks are the real and imaginary parts of the probe signal, respectively, and the inputs are samples of the reduced eigenvector matrix (Table 3). The division of samples was performed according to the ratio: 80 % for NN training, 9.5 % for testing and cross-validation. The data from one percent of the samples were not used in training, but later some of them were used as synthesized data to verify the reliability of the solution to the inverse profile reconstruction problem.

Thus, two neural networks were obtained, each of which is characterized by an architecture of four hidden layers Re-MLP-14-9-9-7-1 and Im-MLP-15-13-10-9-1. In each hidden layer, the activation function of the hyperbolic tangent was used, and in the output layer, the linear one. The validity of the obtained metamodels was assessed visually by histograms of residuals, normal probability plots of residuals, scatter plots, and box plots. In addition, their numerical validity is confirmed by the small values of the error $MAPE_{metamod}$, % (Mean Absolute Percentage Error). Figure 5 shows the values of these errors for both metamodels separately for the training, cross-validation, and test samples.

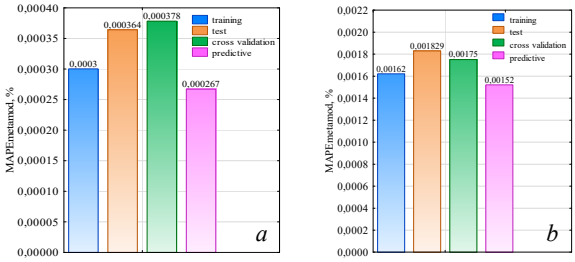

Fig. 5. Statistical assessment of the quality of metamodels by MAPE indicators:
a) Re-MLP-14-9-9-7-1; *b*) Im-MLP-15-13-10-9-1

The final step of this stage is to check the adequacy and informativeness of the created metamodels according to Fisher's criterion at a significance level of 5 % [19, 32]. Both of the created metamodels are adequate, since the estimated model values of the Fisher's criterion for them significantly exceed its critical value. Thus, the Re-MLP-14-9-9-7-1 metamodel has a Fisher's index value of $F^{total}_{15;2804} = 1.5\cdot10^9$, and the critical value of this criterion with a significance level of α = 5 % and the number of degrees of freedom v_R = 2804, v_D = 15 is $F^{table}_{0.05;15;2804} = 1.67$, which complies with the adequacy terms. For the metamodel Im-MLP-15-

13-10-9-1, the condition of adequacy according to this criterion is also met, since $F_{15;2804}^{total} = 2.39 \cdot 10^8$. The coefficient of determination for both metamodels is $R^2 = 0.98$, which indicates their high informativeness.

Consequently, computational models can be involved in the optimization process in a reduced search space, due to which the next stage is implemented. To verify the reliability of the solution to the inverse problem of profile reconstruction, the synthesized data reserved at the stage of building the metamodel were used. Table 4 shows three examples for testing.

Due to their properties, it is advisable to use metaheuristic algorithms for optimization [33–36]. Therefore, the inverse problem for the three test samples was solved by means of a stochastic metaheuristic hybrid global optimization algorithm [6, 30]. The target function is minimized by comparing the theoretical and synthesized signals of the ECP (Table 4). In other words, a series of starts of the optimization algorithm was carried out and solution vectors were obtained in the reduced space, the results of which were averaged. In essence, the application of the multistart technique improved the accuracy of the solution.

Table 4

Test samples for verification of the procedure for determining the profiles of electrophysical property of TO

Test samples		Conditional layers					ECP signals	
		1	2	…	59	60	Re(e_{mes})	Im(e_{mes})
1	μ_{test}	26.446	26.373	…	10.095	10.080	–0.748	–0.7482
	σ_{test}, S/m	9529687	9147829	…	2130815	2109804		
2	μ_{test}	25.791	25.721	…	10.092	10.077	–0.751	–0.752
	σ_{test}, S/m	10021950	9616082	…	2157900	2135568		
3	μ_{test}	34.964	34.854	…	10.145	10.122	–0.726	–0.726
	σ_{test}, S/m	9037426	8679576	…	2103729	2084039		

The final stage is the projection of the found profiles of the electrophysical properties of the OC into the original space using the iterative inverse transformation of Kernel PCA. Thus, we have an actual solution to the inverse problem of finding electrophysical properties in the original space. The accuracy of this solution is assessed by the values of the absolute error in determining the components of the vectors of the desired parameters, given the known solution vectors μtest and σ_{test} (Table 4). Table 5 shows the values of these errors for the EC and MP profiles for each conditional layer, respectively, for three test cases.

Table 5

Values of absolute errors of profile reconstruction

Test samples		Conditional layers					
		1	2	3	…	59	60
1	$\Delta_\mu \cdot 10^{-3}$	–9.09	–9.05	–8.98	…	–0.0543	–0.0449
	Δ_σ	–2789	–2653	–2524	…	–153.47	–145.98
2	$\Delta_\mu \cdot 10^{-3}$	–6.559	–6.53	–6.482	…	–0.0379	–0.0312
	Δ_σ	–1938	–1844	–1754	…	–106.79	–101.59
3	$\Delta_\mu \cdot 10^{-3}$	–11.45	–11.4	–11.31	…	–0.0662	–0.0546
	Δ_σ	–3441	–3273	–3113	…	–189.295	–180.055

Figure 6 contains a graphical representation of the relative errors and, additionally, values of the error MAPE, % reconstruction of each of the corresponding profiles.

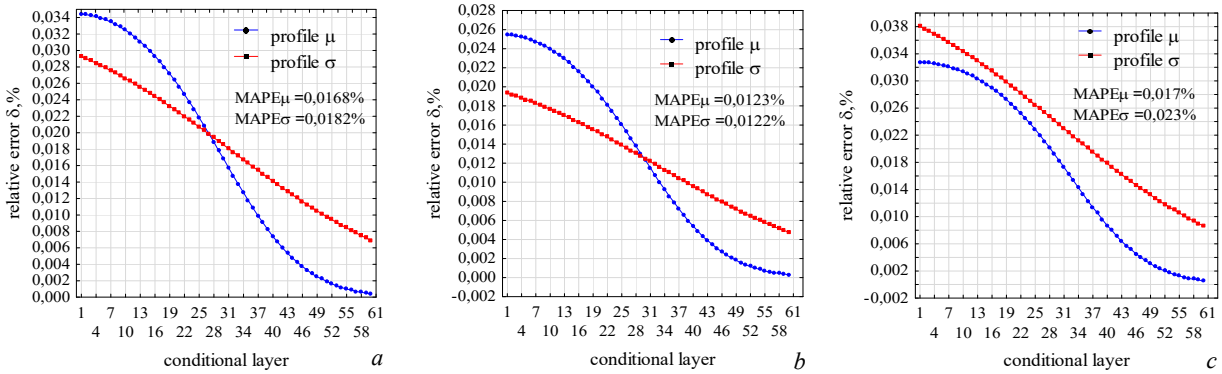

Fig. 6. Graphs of relative error distributions for EC and MP profiles: *a* – test 1; *b* – test 2; *c* – test 3

Discussions and conclusions. The most interesting result of the numerical experiments is the reduction of the search space by more than 85 %, which allowed us to move from the dimension of the primary space of 120 to the reduced one with dimension 15. It was possible due to nonlinear transformations using the Kernel PCA and the Gaussian kernel function with the analysis of the eigenvalues of the resulting Gram matrix and the limitation on the number of principal components of the linear PCA when its eigenvalues are less than one. This allowed for much more cost-effective implementation of surrogate models and optimization in a significantly reduced search space. The results confirmed the validity of such a significant reduction in space without a substantial loss of information.

Another indicator proving the effectiveness of the proposed method is the high accuracy of the created surrogate models, which is estimated by the errors $MAPE_{metamod}$ and is $0.318 \cdot 10^{-3}$ and $1.65 \cdot 10^{-3}$ %, respectively. This accuracy of the reduced-dimensional metamodels was achieved through the use of homogeneous computer DOE and deep learning networks. The adequacy and informativeness of the constructed surrogate models have been proved by numerical indicators.

Verification of the method for reconstructing the electrophysical properties of the testing object was carried

out on synthetically generated data (test samples) that are known in advance. As a result of the study, it was found that the errors MAPE of profile reconstruction for the test cases in comparison with theoretical solutions do not exceed 0.05 %, i.e., much better than the solution of the problem in the full-factor and PCA spaces, where the maximum errors reached 5.53 % and 0.96 %, respectively. In addition, it should be noted that this error contains a number of essential components: first, the error of reduction of the primary space, second, the error of approximation using surrogate models based on neural networks, third, the error of solving the inverse problem by the global optimization algorithm, and the error of projecting the found profiles of the electrophysical properties of the TO into the primary space.

Thus, the proposed computer-economical method for determining the electrophysical properties of planar metal objects by means of surrogate optimization with the accumulation of additional apriori knowledge about them in neural network metamodels with nonlinearly reduced dimensionality has demonstrated its effectiveness and ability to sufficiently accurately solve the problem of simultaneous determination of the profiles of electrical conductivity and magnetic permeability in eddy current measurements. It can be used to assess the quality of various technological processes, or the effects of uncontrolled exposure to aggressive media on the TO during their monitoring.

Conflict of interest. The authors declare that they have no conflicts of interest.

REFERENCES

1. Sabbagh H.A., Murphy R.K., Sabbagh E.H., Aldrin J.C., Knopp J.S. *Computational Electromagnetics and Model-Based Inversion*. Springer New York, 2013. 448 p. doi: https://doi.org/10.1007/978-1-4419-8429-6.

2. Liu G.R., Han X. *Computational Inverse Techniques in Nondestructive Evaluation*. CRC Press, 2003. 592 p. doi: https://doi.org/10.1201/9780203494486.

3. Di Barba P. *Multiobjective Shape Design in Electricity and Magnetism*. Springer, 2010. 313 p. doi: https://doi.org/10.1007/978-90-481-3080-1.

4. Argoul P. *Overview of Inverse Problems*. DEA. Parameter Identification in Civil Engineering, Ecole Nationale des Ponts et chaussées, 2012. 13 p.

5. Xia Z., Huang R., Chen Z., Yu K., Zhang Z., Salas-Avila J.R., Yin W. Eddy Current Measurement for Planar Structures. *Sensors*, 2022, vol. 22, no. 22, art. no. 8695. doi: https://doi.org/10.3390/s22228695.

6. Halchenko V.Y., Trembovetska R., Tychkov V., Tychkova N. Surrogate methods for determining profiles of material properties of planar test objects with accumulation of apriori information about them. *Archives of Electrical Engineering*, 2024, pp. 183-200. doi: https://doi.org/10.24425/aee.2024.148864.

7. Lu M. *Forward and inverse analysis for non-destructive testing based on electromagnetic computation methods.* PhD Thesis, The University of Manchester, UK, 2018. 224 p.

8. Campbell S.D., Sell D., Jenkins R.P., Whiting E.B., Fan J.A., Werner D.H. Review of numerical optimization techniques for meta-device design [Invited]. *Optical Materials Express*, 2019, vol. 9, no. 4, pp. 1842-1863. doi: https://doi.org/10.1364/OME.9.001842.

9. Tesfalem H., Hampton J., Fletcher A.D., Brown M., Peyton A.J. Electrical Resistivity Reconstruction of Graphite Moderator Bricks From Multi-Frequency Measurements and Artificial Neural Networks. *IEEE Sensors Journal*, 2021, vol. 21, no. 15, pp. 17005-17016. doi: https://doi.org/10.1109/JSEN.2021.3080127.

10. Hampton J., Fletcher A., Tesfalem H., Peyton A., Brown M. A comparison of non-linear optimisation algorithms for recovering the conductivity depth profile of an electrically conductive block using eddy current inspection. *NDT & E International*, 2022, vol. 125, art. no. 102571. doi: https://doi.org/10.1016/j.ndteint.2021.102571.

11. Tesfalem H., Peyton A.J., Fletcher A.D., Brown M., Chapman B. Conductivity Profiling of Graphite Moderator Bricks From Multifrequency Eddy Current Measurements. *IEEE Sensors Journal*, 2020, vol. 20, no. 9, pp. 4840-4849. doi: https://doi.org/10.1109/JSEN.2020.2965201.

12. Xu J., Wu J., Xin W., Ge Z. Measuring Ultrathin Metallic Coating Properties Using Swept-Frequency Eddy-Current Technique. *IEEE Transactions on Instrumentation and Measurement*, 2020, vol. 69, no. 8, pp. 5772-5781. doi: https://doi.org/10.1109/TIM.2020.2966359.

13. Xu J., Wu J., Xin W., Ge Z. Fast measurement of the coating thickness and conductivity using eddy currents and plane wave approximation. *IEEE Sensors Journal*, 2021, vol. 21, no. 1, pp. 306-314. doi: https://doi.org/10.1109/JSEN.2020.3014677.

14. Huang P., Zhao J., Li Z., Pu H., Ding Y., Xu L., Xie Y. Decoupling Conductivity and Permeability Using Sweep-Frequency Eddy Current Method. *IEEE Transactions on Instrumentation and Measurement*, 2023, vol. 72, pp. 1-11. doi: https://doi.org/10.1109/TIM.2023.3242017.

15. Hampton J., Tesfalem H., Fletcher A., Peyton A., Brown M. Reconstructing the conductivity profile of a graphite block using inductance spectroscopy with data-driven techniques. *Insight - Non-Destructive Testing and Condition Monitoring*, 2021, vol. 63, no. 2, pp. 82-87. doi: https://doi.org/10.1784/insi.2021.63.2.82.

16. Yi Q., Tian G.Y., Malekmohammadi H., Laureti S., Ricci M., Gao S. Inverse reconstruction of fibre orientation in multilayer CFRP using forward FEM and eddy current pulsed thermography. *NDT & E International*, 2021, vol. 122, art. no. 102474. doi: https://doi.org/10.1016/j.ndteint.2021.102474.

17. Arridge S., Maass P., Öktem O., Schönlieb C.-B. Solving inverse problems using data-driven models. *Acta Numerica*, 2019, vol. 28, pp. 1-174. doi: https://doi.org/10.1017/S0962492919000059.

18. Halchenko V.Ya., Trembovetska R.V., Tychkov V.V., Sapogov M.M., Gromaszek K., Smailova S., Luganskaya S. Additive neural network approximation of multidimensional response surfaces for surrogate synthesis of eddy-current probes. *Przegląd Elektrotechniczny*. 2021, no. 9, pp. 46-49. doi: https://doi.org/10.15199/48.2021.09.10.

19. Halchenko V.Y., Trembovetska R.V., Tychkov V.V. Development of excitation structure rbf-metamodels of moving concentric eddy current probe. *Electrical Engineering & Electromechanics*, 2019, no. 2, pp. 28-38. doi: https://doi.org/10.20998/2074-272X.2019.2.05.

20. Trembovetska R., Halchenko V., Bazilo C. Inverse Multi-parameter Identification of Plane Objects Electrophysical Parameters Profiles by Eddy-Current Method. *Lecture Notes in Networks and Systems*, 2023, vol. 536 LNNS, pp. 202-212. doi: https://doi.org/10.1007/978-3-031-20141-7_19.

21. Uzal E. *Theory of eddy current inspection of layered metals*. PhD Dissertation. Iowa State University, 1992. 190 p. doi: https://doi.org/10.31274/rtd-180813-9635.

22. Bowler N. *Eddy-current nondestructive evaluation*. Springer, New York. 2019, 217 p. doi: https://doi.org/10.1007/978-1-4939-9629-2.

23. Lei Y.-Z. General series expression of eddy-current impedance for coil placed above multi-layer plate conductor. *Chinese Physics B*, 2018, vol. 27, no. 6, art. no. 060308. doi: https://doi.org/10.1088/1674-1056/27/6/060308.

24. Zhang J., Yuan M., Xu Z., Kim H.-J., Song S.-J. Analytical approaches to eddy current nondestructive evaluation for stratified conductive structures. *Journal of Mechanical Science and Technology*, 2015, vol. 29, no. 10, pp. 4159-4165. doi: https://doi.org/10.1007/s12206-015-0910-7.

25. Theodoulidis T.P., Kriezis E.E. *Eddy current canonical problems (with applications to nondestructive evaluation*). Tech Science Press. 2006, 259 p.
26. Halchenko V., Trembovetska R., Bazilo C., Tychkova N. Computer simulation of the process of profiles measuring of objects electrophysical parameters by surface eddy current probes. *Lecture Notes on Data Engineering and Communications Technologies*, 2023, vol. 178, pp. 411-424. doi: https://doi.org/10.1007/978-3-031-35467-0_25.
27. Dodd C.V., Deeds W.E. *Calculation of magnetic fields from time-varying currents in the presence of conductors*. Technical Report no. ORNL-TM-4958, Oak Ridge National Laboratory, Tennessee, United States, 1975. 35 p.doi: https://doi.org/10.2172/4178400.
28. Raschka S. Mirjalili, V. *Python Machine Learning: Machine Learning and Deep Learning with Python, scikit-learn, and TensorFlow 2, 3rd Ed.* Packt Publ., 2019. 772 p.
29. Schölkopf B., Smola A.J. (2001). *Learning with Kernels: Support Vector Machines, Regularization, Optimization, and Beyond*. The MIT Press, 2001. 626 p. doi: https://doi.org/10.7551/mitpress/4175.001.0001.
30. Halchenko V.Y., Trembovetska R.V., Tychkov V.V. Synthesis of eddy current probes with volumetric structure of the excitation system, implementing homogeneous sensitivity in the testing zone. *Technical Electrodynamics*, 2021, no. 3, pp. 10-18. (Ukr). doi: https://doi.org/10.15407/techned2021.03.010.
31. Wang Q. *Kernel principal component analysis and its applications in face recognition and active shape models*. 2012, doi: https://doi.org/10.48550/arXiv.1207.3538.
32. Montgomery D.C. *Design and Analysis of Experiments. 10th ed.* John Wiley and Sons, 2020. 688 p.
33. Kuznetsov B., Nikitina T., Bovdui I., Voloshko O., Chunikhin K., Dobrodeyev P. Electromagnetic Shielding of Two-Circuit Overhead Power Lines Magnetic Field. *Problems of the Regional Energetics*, 2023, vol. 4, no. 60, pp. 14-29. doi: https://doi.org/10.52254/1857-0070.2023.4-60.02.
34. Kuznetsov B.I., Nikitina T.B., Bovdui I.V., Voloshko O.V., Kolomiets V.V., Kobylianskyi B.B. Optimization of spatial arrangement of magnetic field sensors of closed loop system of overhead power lines magnetic field active silencing. *Electrical Engineering & Electromechanics*, 2023, no. 4, pp. 26-34. doi: https://doi.org/10.20998/2074-272X.2023.4.04.
35. Koshevoy N.D., Muratov V.V., Kirichenko A.L., Borisenko S.A. Application of the "jumping frogs" algorithm for research and optimization of the technological process. *Radio Electronics, Computer Science, Control*, 2021, no. 1, pp. 57-65. doi: https://doi.org/10.15588/1607-3274-2021-1-6.
36. Koshevoy N.D., Kostenko E.M., Muratov V.V. Application of the fish search method for optimization plans of the full factor experiment. *Radio Electronics, Computer Science, Control*, 2020, no. 2, pp. 44-50. doi: https://doi.org/10.15588/1607-3274-2020-2-5.

Received 04.06.2024
Accepted 21.08.2024
Published 02.01.2025

V.Ya. Halchenko[1], *Doctor of Technical Science, Professor,*
R.V. Trembovetska[1], *Doctor of Technical Science, Professor,*
V.V. Tychkov[1], *Candidate of Technical Science, Associate Professor,*
[1] Cherkasy State Technological University,
460, Blvd. Shevchenka, Cherkasy, 18006, Ukraine,
e-mail: v.halchenko@chdtu.edu.ua; r.trembovetska@chdtu.edu.ua;
v.tychkov@chdtu.edu.ua (Corresponding Author)

How to cite this article:
Halchenko V.Ya., Trembovetska R.V., Tychkov V.V. Computer-economical optimization method for solving inverse problems of determining electrophysical properties of objects in eddy current structroscopy. *Electrical Engineering & Electromechanics*, 2025, no. 1, pp. 39-47. doi: https://doi.org/10.20998/2074-272X.2025.1.06

UDC 621.3.013 https://doi.org/10.20998/2074-272X.2025.1.07

B.I. Kuznetsov, T.B. Nikitina, I.V. Bovdui, K.V. Chunikhin, V.V. Kolomiets, B.B. Kobylianskyi

Multispheroidal model of magnetic field of uncertain extended energy-saturated technical object

Problem. *The implementation of strict requirements for magnetic silence of elongated energy-saturated technical objects – such as naval vessel and submarines is largely determined by the adequacy of mathematical models to the signatures of a real magnetic field.* ***Aim***. *Simplification of mathematical modeling of the magnetic field of an uncertain extended energy-saturated object based on the development and application of a multispheroidal model of its magnetic field instead of the well-known multidipole model.* ***Methodology.*** *Coordinates of the geometric location and magnitudes of spatial extended spheroidal harmonics of spheroidal sources of multispheroidal model of magnetic field calculated as magnetostatics geometric inverse problems solution in the form of nonlinear minimax optimization problem based on near field measurements for prediction far extended technical objects magnetic field magnitude. Nonlinear objective function calculated as the weighted sum of squared residuals between the measured and predicted magnetic field COMSOL Multiphysics software package used. Nonlinear minimax optimization problems solutions calculated based on particle swarm nonlinear optimization algorithms.* ***Results.*** *Results of prediction far magnetic field magnitude of extended technical objects based on designed multispheroidal model of the magnetic field in the form of spatial prolate spheroidal harmonics in prolate spheroidal coordinate system using near field measurements with consideration of extended technical objects magnetic characteristics uncertainty.* ***Originality.*** *For the first time the method for design of multispheroidal model of magnetic field of uncertain extended energy-saturated technical object based on magnetostatics geometric inverse problems solution and magnetic field spatial spheroidal harmonics calculated in prolate spheroidal coordinate system taking into account of technical objects magnetic characteristics uncertainties developed.* ***Practical value.*** *It is shown the possibility to reduce the number of spheroidal sources of the magnetic field for adequate modeling of the real magnetic field based on the developed multispheroidal model compared to the number of well-known dipole sources of the magnetic field in the multidipole model of the magnetic field.* References 48, figures 4.

Key words: **energy-saturated extended technical objects, magnetic field, multispheroidal model, magnetic silencing, extended spheroidal coordinate system, spatial extended spheroidal harmonics.**

Проблема. *Реалізація жорстких вимог щодо «магнітної тиші» витягнутих енергонасичених технічних об'єктів – таких як військові кораблі та підводні човни, значною мірою визначається адекватністю математичних моделей сигнатурам реального магнітного поля цих об'єктів.* ***Мета.*** *Спрощення математичного моделювання магнітного поля невизначеного видовженого енергонасиченого об'єкта на основі розробки та застосування мультисфероїдальної моделі його магнітного поля замість відомої мультидипольної моделі.* ***Методологія.*** *Координати геометричного розташування та величини просторових витягнутих сфероїдних гармонік сфероідальних джерел мультисфероїдальної моделі магнітного поля витягнутих технічних об'єктів розраховані як розв'язок обернених геометричних задач магнітостатики в формі нелінійної задачі мінімаксної оптимізації на основі вимірювань ближнього поля для прогнозування величини магнітного поля витягнутих технічних об'єктів. Нелінійна цільова функція розрахована як зважена сума квадратів залишків між виміряним і прогнозованим магнітним полем з використаням програмного пакету COMSOL Multiphysics. Розв'язки задач нелінійної мінімаксної оптимізації розраховані на основі алгоритмів нелінійної оптимізації рою частинок.* ***Результати.*** *Результати прогнозування величини віддаленого магнітного поля витягнутих технічних об'єктів на основі спроектованої мультисфероїдальної моделі магнітного поля в вигляді просторових витягнутих сфероїдальних гармонік в витягнутій сфероїдній системі координат з використанням вимірювань ближнього поля та з врахуванням невизначеності магнітних характеристик витягнутих технічних об'єктів.* ***Оригінальність****. Вперше розроблено метод проектування мультисфероїдальної моделі магнітного поля невизначеного витягнутого енергонасиченого технічного об'єкта на основі розв'язку геометричних обернених задач магнітостатики та обчислення просторових сфероїдальних гармонік магнітного поля в витягнутій сфероїальній системі координат з врахуванням невизначеності магнітних характеристик технічного об'єкта.* ***Практична цінність****. Показана можливість зниження кількості сфероідальних джерел магнітного поля для адекватного моделювання реального магнітного поля на основі розробленої мультісфероідальної моделі в порівнянні із кількістю дипольних джерел магнітного поля в відомій мультідипольній моделі магнітного поля.* Бібл. 48, рис. 4.

Ключові слова: **енергонасичені витягнуті технічні об'єкти, магнітне поле, мультисфероїдальна модель, магнітна тиша, витягнута сфероїдна система координат, просторові витягнуті сфероїдні гармоніки**.

Introduction. Most mathematical models of the magnetic field of energy-saturated technical objects are designed on the basis of multi-dipole models. Such models are widely used to simulate the magnetic field of spacecraft, naval vessel, submarines and other energy-saturated technical objects [1–9]. The number of dipoles in the mathematical model of the magnetic field is determined by the required accuracy of modeling the magnetic field of a real technical object can be 20 dipoles, 39 dipoles, or more dipoles [10–13].

For spacecraft, in addition to the magnitude of the magnetic field at the installation point of the on-board magnetometer, an important technical characteristic is also the magnitude of the magnetic moment of the spacecraft. Therefore, at the stage of design, production of elements and testing of spacecraft, the magnitude of the magnetic moment is compensated, so that the magnitude of the resulting magnetic moment of the spacecraft becomes very small. In this case, the main share of the spacecraft's magnetic field is generated not by dipoles, but by quadrupole, octupole and higher harmonics, and the model of the spacecraft's magnetic field is taken in the form of a multipole model [14].

For extended energy-saturated technical objects, the mathematical model of the magnetic field is most simply considered not in a spherical or rectangular coordinate system, but in an elongated spheroidal coordinate system. Naturally, for such objects it is most appropriate to consider the mathematical model of the magnetic field not in the form of a multidipole model, but in the form of a multispheroidal model of the magnetic field [15–18].

Due to the fact that the characteristics of the magnetic field of a technical object are known inaccurately and change during operation, when designing a mathematical model of the magnetic field, it is necessary to take into account the uncertainties of the magnetic characteristics of the technical object [4].

The goal of the work is simplification of mathematical modeling of the magnetic field of an uncertain extended energy-saturated object based on the development and application of a multispheroidal model of its magnetic field instead of the well-known multidipole model.

Problem statement. The external magnetic field of an elongated energy-saturated technical object is generated by engines, electric generators, electric motors, distribution boards and many other consumers of electrical energy [19–21]. Let's consider the design of a multispheroidal mathematical model that adequately describes the real magnetic field of an elongated energy-saturated technical object in an elongated spheroidal coordinate system associated with the center of the technical object.

In contrast to the multi-dipole model, which is widely used to model the external magnetic field of elongated energy-saturated technical objects [1–13], we assume that at the *i* points of an elongated energy-saturated technical object with coordinates (x_i, y_i, z_i) in the orthogonal system coordinates associated with the center of the technical object are located *I* sources of not a dipole, but a spheroidal magnetic field sources [22, 23]. These *I* sources generate a magnetic field at *J* measurement points with coordinates (x_j, y_j, z_j) in rectangular coordinate systems associated with the center of the technical object.

The layout of spheroidal magnetic field sources at points with the coordinates (x_i, y_i, z_i) and measuring points with the coordinates(x_j, y_j, z_j) in rectangular coordinate systems associated with the center of the extended energy-saturated technical object shown in Fig. 1.

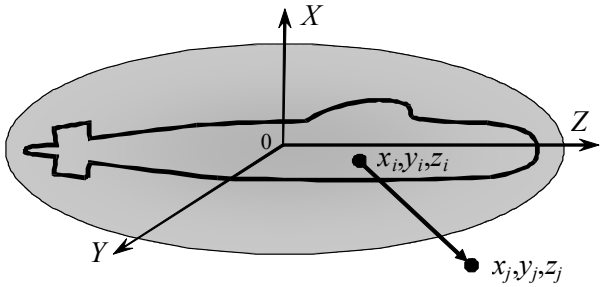

Fig. 1. The extended energy-saturated technical object

Then the components $H_{\xi ij}$, $H_{\eta ij}$, $H_{\varphi ij}$ of the magnetic field generated by these *I* spheroidal sources at *J* measurement points are calculated at points with coordinates ξ_{ij}, η_{ij}, φ_{ij} in elongated spheroidal coordinate systems associated with the centers of these sources, according to the following dependencies [18]:

$$H_{\xi ij} = -\frac{\sqrt{\xi_{ij}^{\,2}-1}}{c_i\sqrt{\xi_{ij}^{\,2}-\eta_{ij}^{2}}}\sum_{n=1}^{\infty}\sum_{m=0}^{n}\frac{\mathrm{d}Q_{ni}^{m}(\xi_{ij})}{\mathrm{d}\xi_{ij}}\left\{c_{ni}^{m}\cos(m\varphi_{ij})+s_{ni}^{m}\sin(m\varphi_{ij})\right\}P_{ni}^{m}\left(\cos(\eta_{ij})\right);$$

$$H_{\eta ij} = -\frac{\sqrt{1-\eta_{ij}^{\,2}}}{c_i\sqrt{\xi_{ij}^{\,2}-\eta_{ij}^{\,2}}}\sum_{n=1}^{\infty}\sum_{m=0}^{n}Q_{ni}^{m}(\xi_{ij})\frac{\mathrm{d}P_{ni}^{m}\left(\cos(\eta_{ij})\right)}{\mathrm{d}\eta_{ij}}\left\{c_{ni}^{m}\cos(m\varphi_{ij})+s_{ni}^{m}\sin(m\varphi_{ij})\right\}; \quad (1)$$

$$H_{\varphi ij} = \frac{m}{c_i\sqrt{\left(\xi_{ij}^{\,2}-1\right)\left(1-\eta_{ij}^{\,2}\right)}}\sum_{n=1}^{\infty}\sum_{m=0}^{n}Q_{ni}^{m}(\xi)P_{ni}^{m}\left(\cos(\eta_{ij})\right)\left\{c_{ni}^{m}\sin(m\varphi_{ij})-s_{ni}^{m}\cos(m\varphi_{ij})\right\}.$$

Here are the spherical coordinates ξ_{ij}, η_{ij}, φ_{ij} of observation points of the space of a technical object with coordinates (x_j, y_j, z_j) in rectangular coordinate systems associated with the center of the technical object, from the location points of spheroidal magnetic field sources with coordinates (x_i, y_i, z_i) in an orthogonal system coordinates associated with the center of the technical object are related by the relation

$$\begin{aligned} x_j - x_i &= c_i\cdot\sqrt{\xi_{ij}^{\,2}-1}\cdot\sqrt{1-\eta_{ij}^{\,2}}\cos(\varphi_{ij}),\\ y_j - y_i &= c_i\cdot\sqrt{\xi_{ij}^{\,2}-1}\cdot\sqrt{1-\eta_{ij}^{\,2}}\sin(\varphi_{ij}),\\ z_j - z_i &= c_i\cdot\xi_{ij}\cdot\eta_{ij}; \end{aligned} \Rightarrow \begin{aligned} \xi_{ij} &\in [1,\infty[;\\ \eta_{ij} &\in [0,1];\\ \varphi_{ij} &\in [0,2\pi]; \end{aligned} \quad (2)$$

where $P_{ni}^{m}\left(\xi_{ij}\right)$, $Q_{ni}^{m}\left(\xi_{ij}\right)$ associated Legendre functions of the first and second kind, respectively, with degree *n* and order *m*; c_i, c_{ni}^{m}, s_{ni}^{m} – constant coefficients characterizing the amplitudes of external spheroidal harmonics of the magnetic field.

Practical measurements and calculations of magnetic field components it is more convenient to carry out in the orthogonal coordinate system (x_j, y_j, z_j), the transition to which for the components H_{xij}, H_{yij}, H_{zij} is carried out using the formulas [18]:

$$H_{xij} = \xi_{ij}\cdot\frac{\sqrt{1-\eta_{ij}^{\,2}}}{\sqrt{\xi_{ij}^{\,2}-\eta_{ij}^{\,2}}}\cdot\cos(\varphi_{ij})\cdot H_{\xi ij} - \eta_{ij}\cdot\frac{\sqrt{\xi_{ij}^{\,2}-1}}{\sqrt{\xi_{ij}^{\,2}-\eta_{ij}^{\,2}}}\cdot\cos(\varphi_{ij})\cdot H_{\eta ij} - \sin(\varphi_{ij})\cdot H_{\varphi ij};$$

$$H_{yij} = \xi_{ij}\cdot\frac{\sqrt{1-\eta_{ij}^{\,2}}}{\sqrt{\xi_{ij}^{\,2}-\eta_{ij}^{\,2}}}\cdot\sin(\varphi_{ij})\cdot H_{\xi ij} - \eta_{ij}\cdot\frac{\sqrt{\xi_{ij}^{\,2}-1}}{\sqrt{\xi_{ij}^{\,2}-\eta_{ij}^{\,2}}}\cdot\sin(\varphi_{ij})\cdot H_{\eta ij} + \cos(\varphi_{ij})\cdot H_{\varphi ij}; \quad (3)$$

$$H_{zij} = \eta_{ij} \cdot \frac{\sqrt{\xi_{ij}^{\,2} - 1}}{\sqrt{\xi_{ij}^{\,2} - \eta_{ij}^{\,2}}} \cdot H_{\xi ij} + \cdot \xi_{ij} \cdot \frac{\sqrt{1 - \eta_{ij}^{\,2}}}{\sqrt{\xi_{ij}^{\,2} - \eta_{ij}^{\,2}}} \cdot H_{\eta ij} \cdot$$

Practical harmonic analysis in elongated spheroidal coordinate system based on (1) or (3) requires the calculation of associated Legendre polynomials of the first $P_{ni}^{m}(\xi_{ij})$ and second $Q_{ni}^{m}(\xi_{ij})$ kind. Polynomials $Q_{ni}^{m}(\xi_{ij})$ of the second kind calculated using the well-known formula with a limitation on the number of terms of the infinite series [18]

$$Q_{ni}^{m}(\xi_{ij}) = \frac{(-1)^m \cdot (2)^{m-1} \cdot (\xi_{ij}^{\,2} - 1)^{\frac{m}{2}}}{\xi_{ij}^{\,n+m+1}} \times \sum_{k=0}^{\infty} \frac{\Gamma_i\left(\frac{n}{2} + \frac{m}{2} + k + \frac{1}{2}\right)! \cdot \Gamma_i\left(\frac{n}{2} + \frac{m}{2} + k + 1\right)}{\Gamma_i(k+1) \cdot \Gamma_i\left(n + k + \frac{3}{2}\right) \cdot \xi_{ij}^{\,2k}}. \tag{4}$$

The region $\xi \in [\xi_0, 4]$ places strict demands on the accuracy of $Q_{ni}^{m}(\xi_{ij})$ function calculations. Algorithms for direct calculation $Q_{ni}^{m}(\xi_{ij})$ obtained in the form of finite sums [18]

$$Q_{ni}^{m}(\xi_{ij}) = \frac{P_{ni}(\xi_{ij})}{2} \cdot \ln\left(\frac{\xi_{ij}+1}{\xi_{ij}-1}\right) - \sum_{k=1}^{n} \frac{1}{k} \cdot \sum_{\lambda=0}^{m} C_{mi}^{\lambda} \cdot P_{k-1}^{\lambda}(\xi_{ij}) \cdot P_{n-k}^{m-\lambda}(\xi_{ij}) + + \frac{(1-\delta(m,0))}{2} \times \ldots$$

$$\ldots \times \sum_{q=0}^{m-1} C_{mi}^{q} \cdot P_{ni}^{q}(\xi_{ij}) \cdot (m-q-1)! \cdot \frac{(\xi_{ij}-1)^{m-q} - (\xi_{ij}+1)^{m-q}}{(-1)^{m-q-1}\left(\xi_{ij}^{\,2}-1\right)^{\frac{m-q}{2}}};$$

$$Q_{ni}^{m}(\xi_{ij}) = \frac{\left(\xi_{ij}^{\,2}-1\right)^{\frac{m}{2}} n!\, m!}{2^{n+1}} \sum_{k=0}^{m} \frac{(k+n)!\, \Omega(m-k, \xi_{ij})}{k!\,(m-k)!} \sum_{\lambda=k}^{n} \frac{(\xi_{ij}-1)^{n-\lambda}(\xi_{ij}+1)^{\lambda-k}}{\lambda!\,(n+k-\lambda)!\,(\lambda-k)!\,(n-\lambda)!} - \ldots \tag{5}$$

$$\ldots - \sum_{k=1}^{n} \frac{1}{k} \sum_{\lambda=0}^{m} C_{mi}^{\lambda} P_{k-1}^{\lambda}(\xi_{ij}) P_{n-k,i}^{m-\lambda}(\xi_{ij}),$$

where

$$\Omega(\nu, \xi_{ij}) = \begin{cases} \nu = 0 & \ln\left(\frac{\xi_{ij}+1}{\xi_{ij}-1}\right) \\ \nu \neq 0 & (-1)^{\nu-1}(\nu-1)! \frac{(\xi_{ij}-1)^{\nu} - (\xi_{ij}+1)^{\nu}}{\left(\xi_{ij}^{\,2}-1\right)^{\nu}} \end{cases} \qquad C_n^k = \frac{n!}{(n-k)!\,k!}.$$

Note that the calculation of the components $H_{\xi ij}$, $H_{\eta ij}$, $H_{\varphi ij}$ of the magnetic field in spheroidal coordinates ξ_{ij}, η_{ij}, φ_{ij} using (1) or components H_{xij}, H_{yij}, H_{zij} in the orthogonal coordinate system (x_j, y_j, z_j) using (3) generated by spheroidal sources of the magnetic field for given values of parameters c_i and spatial spheroidal harmonics c_{ni}^{m}, s_{ni}^{m} at measurement points with coordinates (x_j, y_j, z_j) is a direct problem of magnetostatics for spheroidal magnetic field sources [24–29].

Solution method. Let us introduce a vector $\boldsymbol{X}$ of the required parameters, the components of which are the coordinates (x_i, y_i, z_i) of the location I of the sources of the spheroidal magnetic field in the space of the technical object, as well as the values of the parameters c_i and spatial spheroidal harmonics c_{ni}^{m}, s_{ni}^{m} of these I spheroidal magnetic field sources [30–32].

Then, for a given vector $\boldsymbol{X}$ and for given vector $\boldsymbol{G}$ the components $H_{\xi ij}$, $H_{\eta ij}$, $H_{\varphi ij}$ of the magnetic field in spheroidal coordinates ξ_{ij}, η_{ij}, φ_{ij} calculated based on (1) and components H_{xij}, H_{yij}, H_{zij} in the orthogonal coordinate system (x_j, y_j, z_j) generated by these I spheroidal sources of magnetic field at measurement points with coordinates (x_j, y_j, z_j) calculated based on (3).

Then, based on this calculated components H_{xij}, H_{yij}, H_{zij} of the magnetic field generated by each element I the components H_{xj}, H_{yj}, H_{zj} of magnetic field generated by all I spheroidal sources of magnetic field at the measurement points J calculated in the orthogonal coordinate system (x_j, y_j, z_j) associated with the center of the technical object.

In this case, the axes of orthogonal coordinate systems of spheroidal magnetic field sources located in the space of a technical object with coordinates (x_i, y_i, z_i) are taken parallel to the orthogonal coordinate systems of magnetic field measurement points with coordinates (x_j, y_j, z_j) and parallel axes of orthogonal coordinate systems of the magnetic field of a technical object with zero coordinates.

With this choice of arrangement of axes of orthogonal coordinate systems, the values of the resulting magnetic field components H_{xj}, H_{yj}, H_{zj} at the measurement points are calculated in the form of sums of the corresponding magnetic field components H_{xij}, H_{yij}, H_{zij} generated by individual spheroidal magnetic field sources. Naturally, to calculate based on (3) the components H_{xij}, H_{yij}, H_{zij} in the orthogonal coordinate system (x_j, y_j, z_j) generated by these I spheroidal sources of magnetic field at measurement points with coordinates (x_j, y_j, z_j) the components $H_{\xi ij}$, $H_{\eta ij}$, $H_{\varphi ij}$ of the magnetic field in spheroidal coordinates ξ_{ij}, η_{ij}, φ_{ij} are first calculated based on (1).

A feature of energy-saturated extended technical objects is the uncertainty of the magnetic characteristics of their elements, as well as changes in their values in different operating modes [33–38]. Let us introduce the uncertainty vector $\boldsymbol{G}$ of parameters of energy-saturated extended technical object [41, 42].

Let us introduce a vector $\boldsymbol{Y_C(X, G)}$ whose components are the components of the calculated values or components H_{xj}, H_{yj}, H_{zj} in the orthogonal coordinate system (x_j, y_j, z_j) of the magnetic field at J measurement points with coordinates (x_j, y_j, z_j).

Let us introduce a vector $\boldsymbol{Y_M(G)}$ whose components are the measured values H_{xj}, H_{yj}, H_{zj} in the orthogonal coordinate system (x_j, y_j, z_j) of the magnetic field at J measurement points with coordinates (x_j, y_j, z_j). Naturally, these measurements depend on the vector $\boldsymbol{G}$ of uncertainty parameters of the magnetic characteristics of the technical object.

Let us introduce the residual vector $\boldsymbol{E(X, G)}$ of the vector $\boldsymbol{Y_M(G)}$ of the measured magnetic field and the vector $\boldsymbol{Y_C(X, G)}$ of the magnetic field calculated according to multispheroidal model (3)

$$\boldsymbol{E(X,G) = Y_M(G) - Y_C(X,G)}. \qquad (6)$$

The nonlinear vector objective function (6) obtained based on (3) relative to the vector $\boldsymbol{X}$ of unknown required parameters, the components of which are the coordinates (x_i, y_i, z_i) of the location I of the sources of the spheroidal magnetic field in the space of the technical object, as well as the values of the parameters c_i and spatial spheroidal harmonics c_{ni}^m, s_{ni}^m of these I spheroidal magnetic field sources and uncertainty vector $\boldsymbol{G}$ of the parameters of the magnetic characteristics of a technical object.

This approach is standard when constructing a robust multispheroidal mathematical model of the magnetic field of an elongated, energy-saturated technical object, when the coordinates of the spatial location and the magnitude of spatial spheroidal harmonics are found from the conditions of minimizing the divergence vector between the vector of the measured magnetic field and the vector of the predicted one model of a magnetic field, but for the «worst» vector of parameters, the uncertainties of the magnetic characteristics of a technical object are found from the conditions of maximizing the same vector of the residual of the vector of the measured magnetic field and the vector of the magnetic field predicted by multispheroidal model.

Note that the calculation of the desired coordinates (x_i, y_i, z_i) of the spatial location I of spheroidal magnetic field sources, as well as the desired values of parameters c_i and spatial spheroidal harmonics c_{ni}^m, s_{ni}^m of these spheroidal magnetic field sources and the uncertainty vector $\boldsymbol{G}$ of the parameters of the magnetic characteristics of a technical object is geometric the inverse problem of magnetostatics for spheroidal magnetic field sources. Based on the obtained spheroidal model (3), it is possible to calculate and predict the magnitude of the magnetic field at any point in the far zone of a technical object and, therefore, prediction problem of the magnetic field of technical object solved.

In the course of solving this geometric inverse problem (6) of magnetostatics for a spheroidal magnetic field model, it is necessary to repeatedly solve the direct problem (3) when iteratively calculating the values of the desired coordinates desired coordinates (x_i, y_i, z_i) of the spatial location I of spheroidal magnetic field sources, as well as the desired values of parameters c_i and spatial spheroidal harmonics c_{ni}^m, s_{ni}^m of these spheroidal magnetic field sources and the uncertainty vector $\boldsymbol{G}$ of the parameters of the magnetic characteristics of a technical object.

The components of the vector game (6) are nonlinear functions of the vector $\boldsymbol{X}$ of required parameters and the vector $\boldsymbol{G}$ of uncertainty parameters of the geometric inverse problem of magnetostatics of predicting the magnetic field of a technical object, taking into account the uncertainties of the direct problem and calculated using COMSOL Multiphysical software.

When solving the geometric inverse problem of magnetostatics of predicting the magnetic field of technical objects, taking into account the uncertainties of the direct problem, a worst-case design approach is used to make the multi-spheroidal magnetic field model robust. In these cases, solving the inverse geometric forecasting problem comes down to solving a game in which the vector $\boldsymbol{X}$ of the required parameters – the first player minimizes the game payoff (6), but the vector $\boldsymbol{G}$ of uncertainties of the direct problem – the second player tries to maximize the same game payoff (6).

A feature of the considered problem of vector minimax optimization is the multi-extremal nature of the game payoff (6), so that the considered region of possible solutions contains local minima and maxima. Therefore, to calculate the solution to the vector game under consideration, stochastic multi-agent optimization algorithms are used [33–36].

The basic approach to multicriteria optimization is to find a Pareto set that includes all solutions that are not dominated by other solutions. To adapt the PSO method in relation to the problem of finding Pareto optimal solutions on the set of possible values of the vector criterion, binary preference relations are used that determine the Pareto dominance of individual solutions.

To calculate one global solution to the vector game (6), individual swarms exchange information with each other in the process of calculating optimal solutions to local games. Information about the global optimum obtained by particles from another swarm is used to calculate the speed of movement of particles from another swarm, which makes it possible to calculate all potential Pareto-optimal solutions [37–40]. To increase the speed of searching for a global solution, a nonlinear stochastic multi-agent optimization algorithm has recently been used, in which the movement of a swarm particle is described by the following expressions

$$v_{ij}(t+1) = w_{1j}v_{ij}(t) + c_{1j}r_{1j}(t)H\left(p_{1ij}(t) - \varepsilon_{1ij}(t)\right)\left[y_{ij}(t) - x_{ij}(t)\right] + c_{2j}r_{2j}(t)H\left(p_{2ij}(t) - \varepsilon_{2ij}(t)\right)\left[y_j^*(t) - x_{ij}(t)\right]; \qquad (7)$$

$$u_{ij}(t+1) = w_{2j}u_{ij}(t) + c_{3j}r_{3j}(t)H\left(p_{3ij}(t) - \varepsilon_{3ij}(t)\right)\left[z_{ij}(t) - \delta_{ij}(t)\right] + c_{4j}r_{4j}(t)H\left(p_{4ij}(t) - \varepsilon_{4ij}(t)\right)\left[z_j^*(t) - \delta_{ij}(t)\right]; \qquad (8)$$

$$x_{ij}(t+1) = x_{ij}(t) + v_{ij}(t+1); \quad g_{ij}(t+1) = \delta_{ij}(t) + u_{ij}(t+1), \qquad (9)$$

where $x_{ij}(t)$, $g_{ij}(t)$ and $v_{ij}(t)$, $u_{ij}(t)$ is the position and velocity of i particle of j swarm. In (7) – (20) $y_{ij}(t)$, $z_{ij}(t)$ and $y_j^*(t)$, $z_j^*(t)$ – the best local and global positions of the i–th particle, found respectively by only one i-th particle and all the particles of j swarm. Moreover, the best local position $y_{ij}(t)$ and the global position $y_j^*(t)$ of the i particle of j swarm are understood in the sense of

the first player strategy $x_{ij}(t)$ for minimum of component of the vector payoff (6). However, the best local position $z_{ij}(t)$ and the global position z_j^* of the i particle of j swarm are understood in the sense of the second player strategy $g_{ij}(t)$ for maximum of the same component of the vector payoff (6). Four independent random numbers $r_{1j}(t)$, $r_{2j}(t)$, $r_{3j}(t)$, $r_{4j}(t)$ are in the range of [0, 1], which determine the stochastic particle velocity components. Positive constants c_{1j}, c_{2j} and c_{3j}, c_{4j} determine the cognitive and social weights of the particle velocity components.

In random search, the motion of the particle is carried out in the direction of the maximum growth of the component of the objective function, found in the process of random search. In general, this direction serves as an estimate of the direction of the gradient in a random search. Naturally, such an increment of the objective function serves as an analogue of the first derivative – the rate of change of the objective function.

To take these constraints into account when searching for solutions special particle swarm optimization method for constrained optimization problems used [43]. To take these binary preference relations into account when searching for solutions special evolutionary algorithms for multiobjective optimizations used [44].

Simulation results. Let's consider the design of a mathematical model of an indefinite elongated energy-saturated object. A many number of studies have been devoted to measuring the actual signatures of the initial magnetic field of naval vessel and submarines [45–48]. Let us consider the initial data of the magnetic field of an energy-saturated elongated technical object [8]. The initial magnetic field generated by 16 dipoles located in the space of a technical object with coordinates $x = \pm 39$ m and ± 13 m with $y = \pm 4$ m and $z = 3.5$ m. These dipoles have different values of the magnetic moment components M_x, M_y and M_z along the three axes of the rectangular coordinate system. Magnetic field levels were calculated in the range from $x = -100$ m to $x = 100$ m for three values $y = 0$ and $y = \pm 20$ m. Thus, the three components of the magnetic field strength were calculated at 303 points, so that the total number of measurements was 909. In this case, the calculations were carried out for values $z = 19$ m.

Let us first consider the design of a mathematical model of a magnetic field in the form of one ellipsoid located in the center of a technical object, taking into account three harmonics. At the same time, in the course of solving the inverse problem of magnetostatics, the following values of the parameter $c = 45.2148$, and three harmonics were calculated

$c_1^0 = -2.975$, $c_1^1 = -0.784038$, $s_1^1 = -1.20929$,

$c_2^0 = -7.61817$, $c_2^1 = 1.02379$, $c_2^2 = -0.0247782$,

$s_2^1 = 0.321446$, $s_2^2 = 0.0175008$, $c_3^0 = 2.30691$,

$c_3^1 = -0.555912$, $c_3^2 = 0.00222368$, $c_3^3 = 0.000110636$,

$s_3^1 = 0.856451$, $s_3^2 = -0.0155754$, $s_3^3 = 0.000037359$.

In Fig. 2 shown signatures of projections of inductions of the original magnetic field of a technical object (solid lines) and models (dashed lines) for three coordinate values: *a*) $Y = -20$ m, $Z = 19$ m, *b*) $Y = 0$ m, $Z = 19$ m, *c*) $Y = 20$ m, $Z = 19$ m, d) induction modules of the original and model magnetic field of the technical object.

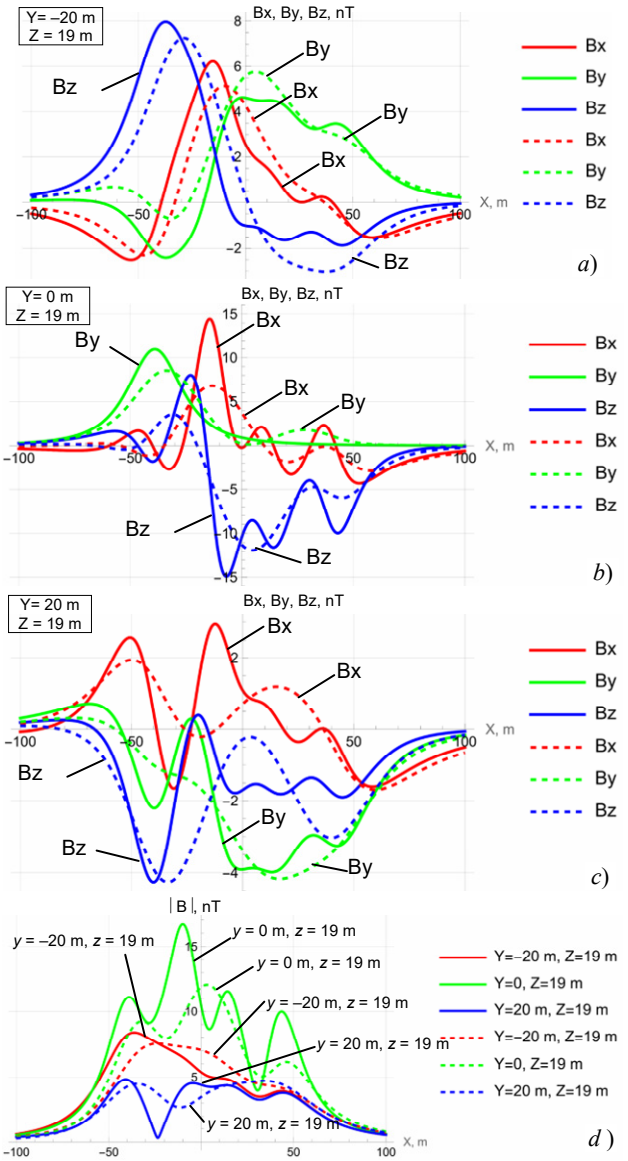

Fig. 2. Signatures of the original magnetic field and the model in the form of a single spheroid

Let us now consider the design of a mathematical model of a magnetic field in the form of three ellipsoids located in the space of a technical object, taking into account only the first spatial harmonics of these ellipsoids.

As a result of solving the geometric inverse problem of magnetostatics, the coordinates of the spatial location and values of the parameters c and first harmonics c_1^0, c_1^1, s_1^1 of these three ellipsoids calculated. Source M_1 – $x = -38.2288$ m, $y = 0.23875$ m, $z = -0.898403$ m, $c = 0.255598$, $c_1^0 = 2150.98$, $c_1^1 = -20787.9$, $s_1^1 = -5998.98$. Source M_2 – $x = -15.1439$ m, $y = 0.851608$ m, $z = 3.27869$ m, $c = 0.288814$, $c_1^0 = -17081.5$, $c_1^1 = 510.902$, $s_1^1 = 107.937$. Source M_3 – $x = 5.13809$ m, $y = 0.455979$ m, $z = -0.342088$ m, $c = 58.0619$, $c_1^0 = -1.63027$, $c_1^1 = 0.0270398$, $s_1^1 = -0.356172$.

In Fig. 3 shown signatures of projections of inductions of the original magnetic field of a technical object (solid lines) and models (dashed lines) for three coordinate values: *a*) $Y = -20$ m, $Z = 19$ m, *b*) $Y = 0$ m, $Z = 19$ m, *c*) $Y = 20$ m, $Z = 19$ m, *d*) induction modules of the original and model magnetic field of the technical object.

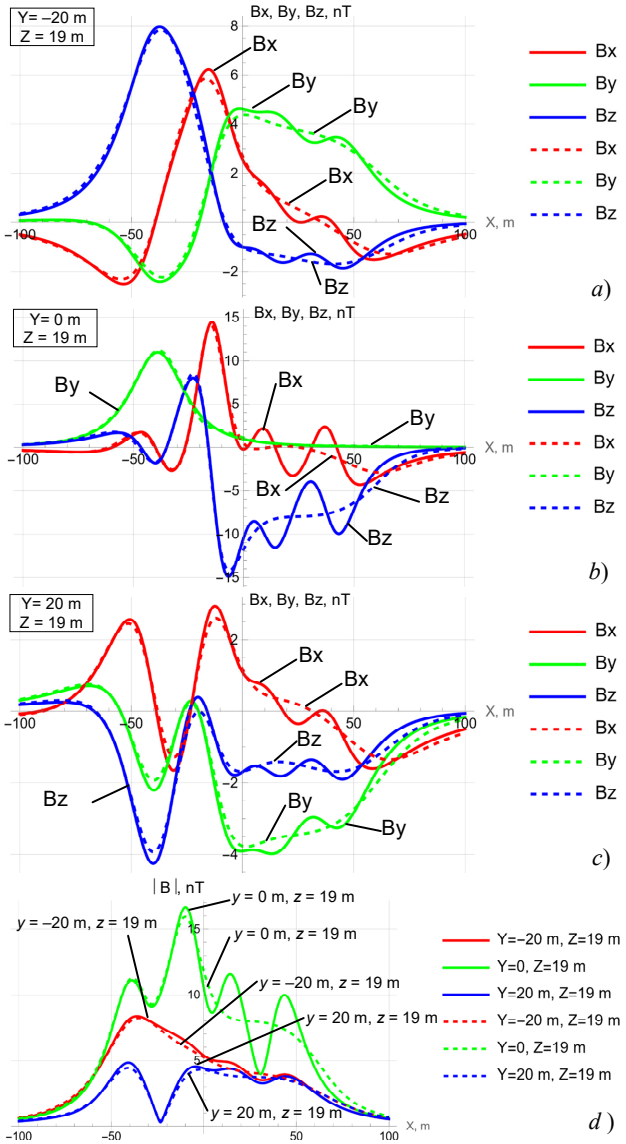

Fig. 3. Signatures of the initial magnetic field and the multispheroidal model in three ellipsoids form

Thus, the multispheroidal model of the magnetic field of an elongated technical object in the form of three spheroids, in which only the first spatial harmonics were taken into account. Describes the initial magnetic field significantly more adequately compared to the single-sphere model, even when taking into account three harmonics, as shown in Fig. 3.

Let us now consider the design of a mathematical model of a magnetic field in the form of four ellipsoids located in the space of a technical object, taking into account only the first spatial harmonics of these ellipsoids. As a result of solving the geometric inverse problem of magnetostatics, the coordinates of the spatial location and values of the parameters c and first harmonics c_1^0, c_1^1, s_1^1 of these four ellipsoids calculated.

1) Source M_1 – x = 24.1775 m, y = 0.203945 m, z = 1.44653 m, c = 17.1245, c_1^0 = –840.073, c_1^1 = 13.9223, s_1^1 = –193.016.

2) Source M_2 – x = –13.2818 m, y = 0.498642 m, z = 0.266331 m, c = 0.232014, c_1^0 = –58875.5, c_1^1 = 1373.1, s_1^1 = –7953.4.

3) Source M_3 – x = –38.496 m, y = 0.276427 m, z = –1.03295 m, c = 0.337585, c_1^0 = –3620.08, c_1^1 = –11852.2, s_1^1 = –3933.69.

4) Source M_4 – x = 24.1911 m, y = 0.203772 m, z = 1.4617 m, c = 16.9606, c_1^0 = 847.093, c_1^1 = –14.0885, s_1^1 = 194.566.

In Fig. 4 shown signatures of projections of inductions of the original magnetic field of a technical object (solid lines) and models (dashed lines) for three coordinate values: *a*) Y = –20 m, Z = 19 m, *b*) Y = 0 m, Z = 19 m, *c*) Y = 20 m, Z = 19 m, *d*) induction modules of the original and model magnetic field of the technical object.

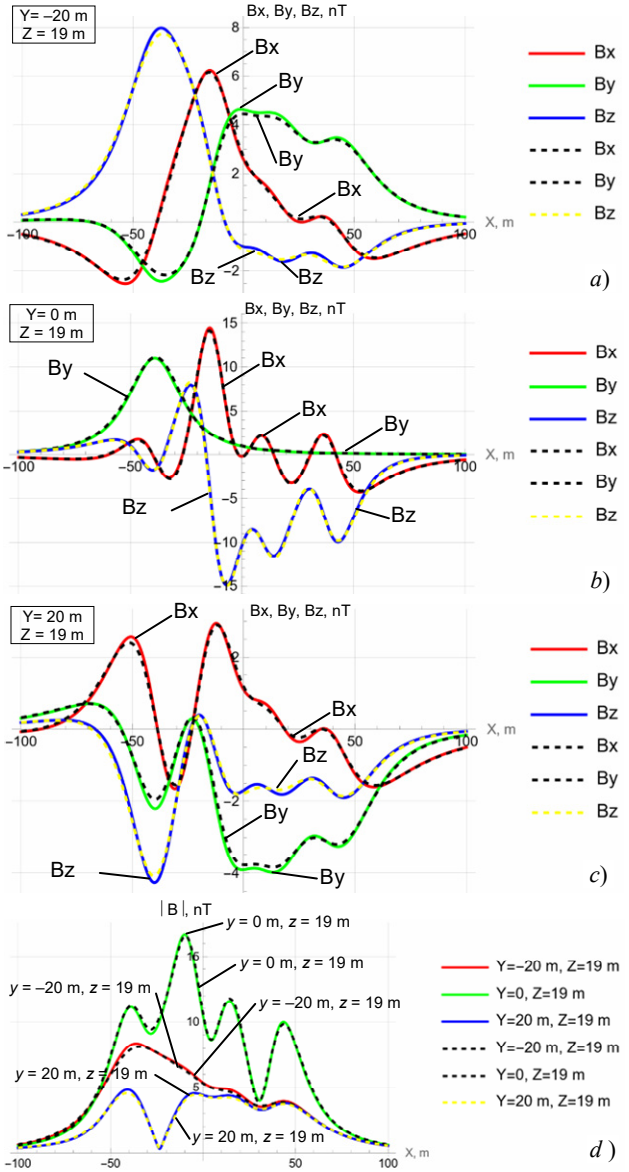

Fig. 4. Signatures of the initial magnetic field and the multispheroidal model in four ellipsoids form

Thus, the multispheroidal model of the magnetic field of an elongated technical object in the form of four spheroids, in which only the first spatial harmonics were taken into account, almost accurately describes the original magnetic field of the technical object, specified in the form of 16 magnetic dipoles located in the space of the technical object.

Conclusions.

1. For the first time the method for design of multispheroidal model of magnetic field of uncertain extended energy-saturated technical object for simplification of mathematical modeling of the magnetic field of an uncertain extended energy-saturated object instead of the well-known multidipole model. Design of multispheroidal model based on magnetostatics geometric inverse problems solution and magnetic field spatial spheroidal harmonics calculated in prolate spheroidal coordinate system taking into account of technical objects magnetic characteristics uncertainties developed.

2. Coordinates of the geometric location and magnitudes of spatial extended spheroidal harmonics of spheroidal sources of multispheroidal model of magnetic field calculated as magnetostatics geometric inverse problems solution in the form of nonlinear minimax optimization problem based on near field measurements for prediction far extended technical objects magnetic field magnitude. Nonlinear objective function calculated as the weighted sum of squared residuals between the measured and predicted magnetic field COMSOL Multiphysics software package used. Nonlinear minimax optimization problems solutions calculated based on particle swarm nonlinear optimization algorithms.

3. Based on the developed multispheroidal model, the signature of extended energy-saturated technical object simulated. The initial magnetic field generated by 16 dipoles located in the space of the object. Using the designed multispheroid model, the initial magnetic field in the form of 4 spheroidal magnetic field sources adequately approximated.

4. Based on the results of using the developed multispheroidal model, it is shown the possibility to reduce the number of spheroidal sources of the magnetic field for adequate modeling of the real magnetic field based on the developed multispheroidal model compared to the number of dipole sources of the magnetic field in the well-known multidipole model of the magnetic field more than 4 times.

Acknowledgments. The authors express their gratitude to the researcher Anatoliy Erisov of the department of magnetism of technical object of Anatolii Pidhornyi Institute of Mechanical Engineering Problems of the National Academy of Sciences of Ukraine for the kindly provided materials on the results of experimental measured magnetic field generated by energy-saturated technical objects and also for numerous discussions that allowed the authors to improve the article manuscript.

REFERENCES

1. Rozov V.Yu., Getman A.V., Petrov S.V., Erisov A.V., Melanchenko A.G., Khoroshilov V.S., Schmidt I.R Spacecraft magnetism. *Technical Electrodynamics. Thematic issue «Problems of modern electrical engineering»*, 2010, part 2, pp. 144-147. (Rus).

2. Rozov V.Yu. Methods for reducing external magnetic fields of energy-saturated objects. *Technical Electrodynamics*, 2001, no. 1, pp. 16-20.

3. Rozov V.Yu. Selective compensation of spatial harmonics of the magnetic field of energy-saturated objects. *Technical Electrodynamics*, 2002, no. 1, pp. 8-13. (Rus).

4. *ECSS-E-HB-20-07A. Space engineering: Electromagnetic compatibility hand-book. ESA-ESTEC. Requirements & Standards Division*. Noordwijk, Netherlands, 2012. 228 p.

5. Droughts S.A., Fedorov O.P. Space project Ionosat-Micro. Monograph. Kyiv, Akademperiodika Publ., 2013. 218 p. (Rus).

6. Holmes J.J. *Exploitation of A Ship's Magnetic Field Signatures*. Springer Cham, 2006. 67 p. doi: https://doi.org/10.1007/978-3-031-01693-6.

7. Woloszyn M., Jankowski P. Simulation of ship's deperming process using Opera 3D. *2017 18th International Symposium on Electromagnetic Fields in Mechatronics, Electrical and Electronic Engineering (ISEF) Book of Abstracts*, 2017, pp. 1-2. doi: https://doi.org/10.1109/ISEF.2017.8090680.

8. Birsan M., Holtham P., Carmen. Using global optimisation techniques to solve the inverse problem for the computation of the static magnetic signature of ships. *Defense Research Establishment Atlantic*, 9 Grove St., PO Box 1012, Dartmouth, Nova Scotia, B2Y 3Z7, Canada.

9. Zuo C., Ma M., Pan Y., Li M., Yan H., Wang J., Geng P., Ouyang J. Multi-objective optimization design method of naval vessels degaussing coils. *Proceedings of SPIE - The International Society for Optical Engineering*, 2022, vol. 12506, art. no. 125060J. doi: https://doi.org/10.1117/12.2662888.

10. Mehlem K., Wiegand A. Magnetostatic cleanliness of spacecraft. *2010 Asia-Pacific International Symposium on Electromagnetic Compatibility*, 2010, pp. 936-944. doi: https://doi.org/10.1109/APEMC.2010.5475692.

11. Messidoro P., Braghin M., Grande M. Magnetic cleanliness verification approach on tethered satellite. *16th Space Simulation Conference: Confirming Spaceworthiness into the Next Millennium*, 1991, pp. 415-434.

12. Mehlem K., Narvaez P. Magnetostatic cleanliness of the radioisotope thermoelectric generators (RTGs) of Cassini. *1999 IEEE International Symposium on Electromagnetic Compatability*, 1999, vol. 2, pp. 899-904. doi: https://doi.org/10.1109/ISEMC.1999.810175.

13. Eichhorn W.L. *Magnetic dipole moment determination by near-field analysis*. Goddard Space Flight Center. Washington, D.C., National Aeronautics and Space Administration, 1972. NASA technical note, D 6685. 87 p.

14. Rozov V.Yu., Dobrodeev P.N., Volokhov S.A. Multipole model of a technical object and its magnetic center. *Technical Electrodynamics*, 2008, no. 2, pp. 3-8. (Rus).

15. Rozov V.Yu., Getman A.V., Kildishev A.V. Spatial harmonic analysis of the external magnetic field of extended objects in a prolate spheroidal coordinate system. *Technical Electrodynamics*, 1999, no. 1, pp. 7-11. (Rus).

16. Rozov V.Yu. Mathematical model of electrical equipment as a source of external magnetic field. *Technical Electrodynamics*, 1995, no. 2, pp. 3-7. (Rus).

17. Volokhov S.A., Dobrodeev P.N., Ivleva L.F. Spatial harmonic analysis of the external magnetic field of a technical object. *Technical Electrodynamics*, 1996, no. 2, pp. 3-8. (Rus).

18. Getman A.V. *Analysis and synthesis of the magnetic field structure of technical objects on the basis of spatial harmonics*. Dissertation thesis for the degree of Doctor of Technical Sciences. Kharkiv, 2018. 43 p. (Ukr).

19. Xiao C., Xiao C., Li G. Modeling the ship degaussing coil's effect based on magnetization method. *Communications in Computer and Information Science*, 2012, vol. 289, pp. 62-69. doi: https://doi.org/10.1007/978-3-642-31968-6_8.

20. Wołoszyn M., Jankowski P. Ship's de-perming process using coils lying on seabed. *Metrology and Measurement Systems*, 2019, vol. 26, no. 3, pp. 569-579. doi: https://doi.org/10.24425/mms.2019.129582.

21. Fan J., Zhao W., Liu S., Zhu Z. Summary of ship comprehensive degaussing. *Journal of Physics: Conference Series*, 2021, vol. 1827, no. 1, art. no. 012014. doi: https://doi.org/10.1088/1742-6596/1827/1/012014.

22. Getman A.V. Spatial harmonic analysis of the magnetic field of the sensor of the neutral plasma component. *Eastern European Journal of Advanced Technologies*, 2010, vol. 6, no. 5(48), pp. 35-38. doi: https://doi.org/10.15587/1729-4061.2010.3326.

23. Getman A. Ensuring the Magnetic Compatibility of Electronic Components of Small Spacecraft. *2022 IEEE 3rd KhPI Week on Advanced Technology (KhPIWeek)*, 2022, no. 1-4. doi: https://doi.org/10.1109/KhPIWeek57572.2022.9916339.

24. Acuña M.H. *The design, construction and test of magnetically clean spacecraft – a practical guide*. NASA/GSFC internal report. 2004.

25. Junge A., Marliani F. Prediction of DC magnetic fields for magnetic cleanliness on spacecraft. *2011 IEEE International Symposium on Electromagnetic Compatibility*, 2011, pp. 834-839. doi: https://doi.org/10.1109/ISEMC.2011.6038424.

26. Lynn G.E., Hurt J.G., Harriger K.A. Magnetic control of satellite attitude. *IEEE Transactions on Communication and Electronics*, 1964, vol. 83, no. 74, pp. 570-575. doi: https://doi.org/10.1109/TCOME.1964.6539511.

27. Junge A., Trougnou L., Carrubba E. Measurement of Induced Equivalent Magnetic Dipole Moments for Spacecraft Units and Components. *Proceedings ESA Workshop Aerospace EMC 2009 ESA WPP-299*, 2009, vol. 4, no. 2, pp. 131-140.
28. Matsushima M., Tsunakawa H., Iijima Y., Nakazawa S., Matsuoka A., Ikegami S., Ishikawa T., Shibuya H., Shimizu H., Takahashi F. Magnetic Cleanliness Program Under Control of Electromagnetic Compatibility for the SELENE (Kaguya) Spacecraft. *Space Science Reviews*, 2010, vol. 154, no. 1-4, pp. 253-264. doi: https://doi.org/10.1007/s11214-010-9655-x.
29. Boghosian M., Narvaez P., Herman R. Magnetic testing, and modeling, simulation and analysis for space applications. *2013 IEEE International Symposium on Electromagnetic Compatibility*, 2013, pp. 265-270. doi: https://doi.org/10.1109/ISEMC.2013.6670421.
30. Mehlem K. Multiple magnetic dipole modeling and field prediction of satellites. *IEEE Transactions on Magnetics*, 1978, vol. 14, no. 5, pp. 1064-1071. doi: https://doi.org/10.1109/TMAG.1978.1059983.
31. Thomsen P.L., Hansen F. Danish Ørsted Mission In-Orbit Experiences and Status of The Danish Small Satellite Programme. *Annual AIAA/USU Conference on Small Satellites*, 1999, pp. SSC99-I–8.
32. Kapsalis N.C., Kakarakis S.-D.J., Capsalis C.N. Prediction of multiple magnetic dipole model parameters from near field measurements employing stochastic algorithms. *Progress In Electromagnetics Research Letters*, 2012, vol. 34, pp. 111-122. doi: https://doi.org/10.2528/PIERL12030905.
33. Solomentsev O., Zaliskyi M., Averyanova Y., Ostroumov I., Kuzmenko N., Sushchenko O., Kuznetsov B., Nikitina T., Tserne E., Pavlikov V., Zhyla S., Dergachov K., Havrylenko O., Popov A., Volosyuk V., Ruzhentsev N., Shmatko O. Method of Optimal Threshold Calculation in Case of Radio Equipment Maintenance. *Data Science and Security. Lecture Notes in Networks and Systems*, 2022, vol. 462, pp. 69-79. doi: https://doi.org/10.1007/978-981-19-2211-4_6.
34. Ruzhentsev N., Zhyla S., Pavlikov V., Volosyuk V., Tserne E., Popov A., Shmatko O., Ostroumov I., Kuzmenko N., Dergachov K., Sushchenko O., Averyanova Y., Zaliskyi M., Solomentsev O., Havrylenko O., Kuznetsov B., Nikitina T. Radio-Heat Contrasts of UAVs and Their Weather Variability at 12 GHz, 20 GHz, 34 GHz, and 94 GHz Frequencies. *ECTI Transactions on Electrical Engineering, Electronics, and Communications*, 2022, vol. 20, no. 2, pp. 163-173. doi: https://doi.org/10.37936/ecti-eec.2022202.246878.
35. Havrylenko O., Dergachov K., Pavlikov V., Zhyla S., Shmatko O., Ruzhentsev N., Popov A., Volosyuk V., Tserne E., Zaliskyi M., Solomentsev O., Ostroumov I., Sushchenko O., Averyanova Y., Kuzmenko N., Nikitina T., Kuznetsov B. Decision Support System Based on the ELECTRE Method. *Data Science and Security. Lecture Notes in Networks and Systems*, 2022, vol. 462, pp. 295-304. doi: https://doi.org/10.1007/978-981-19-2211-4_26.
36. Shmatko O., Volosyuk V., Zhyla S., Pavlikov V., Ruzhentsev N., Tserne E., Popov A., Ostroumov I., Kuzmenko N., Dergachov K., Sushchenko O., Averyanova Y., Zaliskyi M., Solomentsev O., Havrylenko O., Kuznetsov B., Nikitina T. Synthesis of the optimal algorithm and structure of contactless optical device for estimating the parameters of statistically uneven surfaces. *Radioelectronic and Computer Systems*, 2021, no. 4, pp. 199-213. doi: https://doi.org/10.32620/reks.2021.4.16.
37. Volosyuk V., Zhyla S., Pavlikov V., Ruzhentsev N., Tserne E., Popov A., Shmatko O., Dergachov K., Havrylenko O., Ostroumov I., Kuzmenko N., Sushchenko O., Averyanova Yu., Zaliskyi M., Solomentsev O., Kuznetsov B., Nikitina T. Optimal Method for Polarization Selection of Stationary Objects Against the Background of the Earth's Surface. *International Journal of Electronics and Telecommunications*, 2022, vol. 68, no. 1, pp. 83-89. doi: https://doi.org/10.24425/ijet.2022.139852.
38. Zhyla S., Volosyuk V., Pavlikov V., Ruzhentsev N., Tserne E., Popov A., Shmatko O., Havrylenko O., Kuzmenko N., Dergachov K., Averyanova Y., Sushchenko O., Zaliskyi M., Solomentsev O., Ostroumov I., Kuznetsov B., Nikitina T. Practical imaging algorithms in ultra-wideband radar systems using active aperture synthesis and stochastic probing signals. *Radioelectronic and Computer Systems*, 2023, no. 1, pp. 55-76. doi: https://doi.org/10.32620/reks.2023.1.05.
39. Maksymenko-Sheiko K.V., Sheiko T.I., Lisin D.O., Petrenko N.D. Mathematical and Computer Modeling of the Forms of Multi-Zone Fuel Elements with Plates. *Journal of Mechanical Engineering*, 2022, vol. 25, no. 4, pp. 32-38. doi: https://doi.org/10.15407/pmach2022.04.032.
40. Hontarovskyi P.P., Smetankina N.V., Ugrimov S.V., Garmash N.H., Melezhyk I.I. Computational Studies of the Thermal Stress State of Multilayer Glazing with Electric Heating. *Journal of Mechanical Engineering*, 2022, vol. 25, no. 1, pp. 14-21. doi: https://doi.org/10.15407/pmach2022.02.014.
41. Kostikov A.O., Zevin L.I., Krol H.H., Vorontsova A.L. The Optimal Correcting the Power Value of a Nuclear Power Plant Power Unit Reactor in the Event of Equipment Failures. *Journal of Mechanical Engineering*, 2022, vol. 25, no. 3, pp. 40-45. doi: https://doi.org/10.15407/pmach2022.03.040.
42. Rusanov A.V., Subotin V.H., Khoryev O.M., Bykov Y.A., Korotaiev P.O., Ahibalov Y.S. Effect of 3D Shape of Pump-Turbine Runner Blade on Flow Characteristics in Turbine Mode. *Journal of Mechanical Engineering*, 2022, vol. 25, no. 4, pp. 6-14. doi: https://doi.org/10.15407/pmach2022.04.006.
43. Sushchenko O., Averyanova Y., Ostroumov I., Kuzmenko N., Zaliskyi M., Solomentsev O., Kuznetsov B., Nikitina T., Havrylenko O., Popov A., Volosyuk V., Shmatko O., Ruzhentsev N., Zhyla S., Pavlikov V., Dergachov K., Tserne E. Algorithms for Design of Robust Stabilization Systems. *Computational Science and Its Applications – ICCSA 2022. ICCSA 2022. Lecture Notes in Computer Science*, 2022, vol. 13375, pp. 198-213. doi: https://doi.org/10.1007/978-3-031-10522-7_15.
44. Zhyla S., Volosyuk V., Pavlikov V., Ruzhentsev N., Tserne E., Popov A., Shmatko O., Havrylenko O., Kuzmenko N., Dergachov K., Averyanova Y., Sushchenko O., Zaliskyi M., Solomentsev O., Ostroumov I., Kuznetsov B., Nikitina T. Statistical synthesis of aerospace radars structure with optimal spatio-temporal signal processing, extended observation area and high spatial resolution. *Radioelectronic and Computer Systems*, 2022, no. 1, pp. 178-194. doi: https://doi.org/10.32620/reks.2022.1.14.
45. Wang D., Yu Q. Review on the development of numerical methods for magnetic field calculation of ships. *Ships Science and Technology*, 2014, vol. 36, no. 3, pp. 1-6.
46. Jin H., Wang H., Zhuang Z. A New Simple Method to Design Degaussing Coils Using Magnetic Dipoles. *Journal of Marine Science and Engineering*, 2022, vol. 10, no. 10, art. no. 1495. doi: https://doi.org/10.3390/jmse10101495.
47. Chadebec O., Rouve L.-L., Coulomb J.-L. New methods for a fast and easy computation of stray fields created by wound rods. *IEEE Transactions on Magnetics*, 2002, vol. 38, no. 2, pp. 517-520. doi: https://doi.org/10.1109/20.996136.
48. Baranov M.I., Rozov V.Y., Sokol Y.I. To the 100th anniversary of the National Academy of Sciences of Ukraine – the cradle of domestic science and technology. *Electrical Engineering & Electromechanics*, 2018, no. 5, pp. 3-11. doi: https://doi.org/10.20998/2074-272X.2018.5.01.

Received 10.04.2024
Accepted 30.06.2024
Published 02.01.2025

B.I. Kuznetsov[1], *Doctor of Technical Science, Professor,*
T.B. Nikitina[2], *Doctor of Technical Science, Professor,*
I.V. Bovdui[1], *PhD, Senior Research Scientist,*
K.V. Chunikhin[1], *PhD, Senior Research Scientist,*
V.V. Kolomiets[2], *PhD, Assistant Professor,*
B.B. Kobylianskyi[2], *PhD, Assistant Professor,*
[1] Anatolii Pidhornyi Institute of Power Machines and Systems of the National Academy of Sciences of Ukraine,
2/10, Komunalnykiv Str., Kharkiv, 61046, Ukraine,
e-mail: kuznetsov.boris.i@gmail.com (Corresponding Author)
[2] Bakhmut Education Research and Professional Pedagogical Institute V.N. Karazin Kharkiv National University,
9a, Nosakov Str., Bakhmut, Donetsk Region, 84511, Ukraine.

How to cite this article:
Kuznetsov B.I., Nikitina T.B., Bovdui I.V., Chunikhin K.V., Kolomiets V.V., Kobylianskyi B.B. Multispheroidal model of magnetic field of uncertain extended energy-saturated technical object. *Electrical Engineering & Electromechanics*, 2025, no. 1, pp. 48-55. doi: https://doi.org/10.20998/2074-272X.2025.1.07

UDC 621.3.014 https://doi.org/10.20998/2074-272X.2025.1.08

T. Hamel, S. Bedoui, A. Bayadi

Impact of transmission line lightning performance on an operational substation reliability considering the lightning stroke incidence angle

Introduction. *This study investigates substation failures caused by lightning strikes, which significantly affect operational reliability. Given the random nature of lightning strikes, a robust statistical approach is essential for accurately assessing their effects.* ***Method.*** *The research develops a comprehensive procedure to analyse the random distribution of non-vertical lightning strikes on transmission lines using the Monte Carlo method, a widely recognized statistical simulation technique. The* ***goal*** *of this work is to evaluate the performance of air-insulated substations under various lightning strike scenarios affecting the connected transmission lines. This is assessed in terms of mean time between failures (MTBF), determined by the basic insulation level of the equipment. The study incorporates both vertical and non-vertical strikes to address a critical gap in the literature, offering practical insights to enhance the reliability and safety of air-insulated substations. By considering the angle of lightning strikes, the study improves the accuracy of evaluating lightning performance using precise modelling of system components.* ***Results****. MATLAB and EMTP software were used to simulate and analyse the substation's response to lightning-induced surges at various strike angles. The results are more representative of real-world conditions and reveal that non-vertical lightning strikes significantly reduce MTBF, underscoring the importance of advanced protective measures.* ***Practical value.*** *The findings highlight the necessity of accounting for the angle of lightning strikes when assessing substation reliability.* References 32, table 4, figures 13.
Key words: **lightning, substation, stroke angle, mean time between failure, basic insulation level, Monte Carlo method**.

Вступ. *У цьому дослідженні вивчаються відмови підстанцій, спричинені ударами блискавки, які суттєво впливають на експлуатаційну надійність. Зважаючи на випадковий характер ударів блискавки, надійний статистичний підхід необхідний для точної оцінки їх наслідків.* ***Метод***. *У дослідженні розробляється комплексна процедура для аналізу випадкового розподілу невертикальних ударів блискавки у лінії електропередачі з використанням методу Монте-Карло, широко визнаного методу статистичного моделювання.* ***Метою*** *даної роботи є оцінка продуктивності підстанцій з повітряною ізоляцією при різних сценаріях ударів блискавки, що впливають на підключені лінії електропередачі. Це оцінюється з погляду середнього часу між відмовами (MTBF), що визначається базовим рівнем ізоляції обладнання. Дослідження включає як вертикальні, так і невертикальні удари, щоб заповнити критичну прогалину в літературі, пропонуючи практичні ідеї для підвищення надійності та безпеки підстанцій з повітряною ізоляцією. Розглядаючи кут ударів блискавки, дослідження підвищує точність оцінки продуктивності блискавки з використанням точного моделювання компонентів системи.* ***Результати***. *Для моделювання та аналізу реакції підстанції на стрибки напруги, викликані блискавкою при різних кутах удару, використовувалися програми MATLAB та EMTP. Результати більш репрезентативні для реальних умов і показують, що невертикальні удари блискавки значно скорочують MTBF, що наголошує на важливості розширених заходів захисту.* ***Практична цінність***. *Результати наголошують на необхідності врахування кута удару блискавки при оцінці надійності підстанції.* Бібл. 32, табл. 4, рис. 13.
Ключові слова: **блискавка, підстанція, кут удару, середній час між відмовами, базовий рівень ізоляції, метод Монте-Карло.**

Introduction. Lightning strikes are a major threat to the electrical power system, causing power outages, equipment damage, and even fires. Overhead transmission lines are particularly vulnerable to lightning strikes, as they present a tall and exposed target to the lightning discharge [1, 2]. The random nature of lightning strikes makes difficult to predict the exact form, location, time and lightning strike angle. To address this challenge, engineers and scientists have developed various models and simulations to evaluate the performance of the power system under lightning strikes [2–7].

A vertical flash is generally assumed for the stroke leader on the shielding analyses of transmission lines recommended by the international standards; however, a previously proposed statistical distribution for the stroke angle is more realistic [8, 9].

The majority of lightning strikes on overhead transmission lines are not vertically downward, but instead are inclined at some angle relative to the vertical. Non-vertical lightning strikes can have different impacts on the transmission line compared to vertically downward strikes [10]. The electric and magnetic fields produced by non-vertical lightning strikes can be much higher in magnitude and longer in duration, causing more severe damage to the transmission line and consequently the substation connected [11].

One approach to evaluate the performance of transmission lines under non-vertical lightning strikes is the use of random sampling techniques. These techniques randomly generate the lightning strikes parameters, then use numerical models to simulate deferent phenomenon produced by lightning strikes. This process is repeated many times to generate a large sample of possible lightning strikes, and the results are used to estimate the probability of damage or failure of studied system [12].

In [13], the authors conducted a simulation study to calculate lightning flashover rates of transmission lines using the Monte Carlo method. The authors have done some parametric calculations to analyze the influence of stroke parameters and determine the range of values that may be concerning. Note that the study has been done only for the case of vertical lightning strikes. In [14] the authors investigate how a non-vertical channel of the stroke leader influences the lightning flashover rate of overhead transmission lines. They emphasize that the stroke angle is a critical factor in lightning analysis for overhead lines. The findings of this study indicate that assuming a non-vertical path for the stroke leader may impact the lightning flashover rate of transmission lines.

In [15] the authors assessed how incorporating a cumulative probability distribution of the stroke angle affects the shielding failure flashover rate (SFFOR) of three-phase overhead transmission lines using a modified electric geometric model (EGM). The authors also confirmed the necessity of evaluating the stroke angle distribution in

lightning analyses of transmission lines, but this analysis has not been sufficiently applied to substations.

In 2014, the same authors published a conference paper [16] in which they investigated the effects of considering vertical and non-vertical strokes on the SFFOR estimated in IEEE Flash program together with the effects of the various EGMs. They state that the assumption of a particularly vertical leader reduces conductors' exposure area and therefore leads to shielding outage rates underestimated in around 20 %.

Very few studies [17, 18] have been published with the objective of evaluating the performance of air-insulated substations considering the statistical nature of lightning strikes. The authors have conducted parametric calculations to analyse the influence of certain line and stroke parameters and to determine their applicable range of values. Despite the high number of parameters involved in lightning calculations, the authors have only used some of them. Specifically, they only consider lightning strikes with a vertical angle, which can affect the accuracy of the results obtained.

From the above, it is clear that most of the work has focused on the performance of transmission lines subjected to lightning strikes based on their angle of incidence. However, to the authors' knowledge, there remains a significant gap regarding the influence of lightning strike angles on the performance of high-voltage substations, whether they are air-insulated or gas-insulated. Future studies should consider these factors to enhance the accuracy and reliability of lightning risk assessments in high-voltage substations. The necessary modifications have been incorporated in the original procedure to account stroke leader angle distribution [17, 18].

The **aim** of this work is to evaluate the performance of air-insulated substations under various lightning strike scenarios affecting the connected transmission lines.

This paper summarizes findings of simulation investigations showing the critical importance of considering the incidence angle of lightning strikes in the reliability assessment of a 220 kV substation. The paper examines the impact of the lightning strikes with different incidence angles on the Mean Time Between Failures (MTBF) on which the Basic Insulation Level (BIL) (insulation strength) of substation equipment is usually selected.

MATLAB procedure employs a statistical Monte Carlo method, utilizing the EMTP/ATP program to estimate lightning overvoltages.

By addressing these aspects, our study offers a more precise and realistic evaluation of substation reliability under lightning strike conditions, filling the gaps left by previous models.

Modeling of electrical system components. The studied system is a 220 kV substation equipped with conductors, towers, insulators, measuring and protection devices, breakers, bus bars, arresters and power transformers. The modeling of each of these components is essential to carry out this study [19].

Transmission line model. To represent the transmission line, multiple distributed parameter line spans are required. This representation is achieved by utilizing a frequency-dependent or a constant parameter model, as described in [20]. ATP-EMTP provides several models that have been applied in transmission line systems. The J. Marti model, is a suitable choice for that purpose, this model accounts for frequency attenuation, conductor geometry and material (Fig. 1,*a*). Electrical data is calculated by the EMTP program.

It is worth noting that the J. Marti model assumes an infinite line length in both directions, which helps prevent wave reflections at both ends of the line.

Transmission tower model. Towers, typically made of metal, are used to elevate electric cables above ground level for the purpose of transmitting electricity over long distances. An example of a transmission tower can be seen in Fig. 1,*b*.

There are several models to represent towers. The model used for this work is based on modeling each metallic part of the tower as a single-phase line section [20]. This model requires the following data:

- the propagation velocity assumed in this case to be 300 m/μs.
- the characteristic impedance, determined according to the following formula:

$$Z = 60\left(\ln\left(\sqrt{2}\,\frac{2h}{r}\right)-1\right), \tag{1}$$

where h is the tower height; r is the arms horizontal distance of the tower.

Insulator modeling. The line insulation flashover model is represented in this work by using voltage-dependent switch that is connected in parallel with the insulator (Fig. 1,*c*). The capacitors simulate the way in which the conductors are coupled to the tower structure [21]. The flashover model, as proposed by CIGRE, is expressed as:

$$v = K \cdot V \cdot \left[\frac{V}{D-L} - E_0\right], \tag{2}$$

where v is the arc velocity, m/s; K is the constant (0.8 $m^2 \cdot kV^{-2} \cdot s^{-1}$) [19]; D is the insulator length or gap length (2.5 m); V is the instantaneous voltage across the insulator or across the gap, kV; L is the leader length, m; E_0 is the critical electric field strength (600 kV/m [19]).

To calculate the leader length L at time, given the leader velocity v at time T, you can use the following formula:

$$L(T + \Delta T) = L(T) + v \cdot \Delta T. \tag{3}$$

The leader propagation stops if the gradient in the unbridged part of the gap falls below E_0.

Grounding modeling. A precise model of grounding impedance must consider a decrease in resistance as the discharge current increases. It is recognized that resistance is higher for low lightning currents, and its variation concerning low current and low frequency values is only significant for soils with high resistivity. When considering the effect of soil ionization, the grounding impedance model can be represented by a nonlinear resistance R_T, as expressed in the provided equation [22–24]

$$R_T = \frac{R_0}{\sqrt{1 + I/I_g}}. \tag{4}$$

The grounding resistance R_0 is around 20 Ω at low current and low frequency. The limiting current I_g that initiates the soil ionization and the stroke current I that

passes through the resistance are also important factors in the grounding impedance calculation (R_T). The formula for calculating the limiting current I_g is [25]:

$$I_g = \frac{E_g \rho}{2\pi R_0^2}. \quad (5)$$

This current is calculated using the soil resistivity ρ, [Ω·m] and the soil ionization gradient E_g = 400 kV/m.

The model used in this study is particularly suitable for soils with a specific resistivity greater than 500 Ω·m. This selection is based on empirical data and established standards that confirm the model's accuracy in such conditions.

This information is used to model the earth electrode of a steel tower as a type-91 nonlinear resistor which is controlled by models, as shown in Fig. 1,*d*.

Surge arrester model. In this work, the surge arrester has been modelled using a modified version of the IEEE-recommended model (Fig. 1,*e*), with parameters optimized using genetic algorithms [26]. This model is referred to as the frequency-dependent model which can accurately represents the dynamic behavior of ZnO surge arresters under steep front surge conditions, which is crucial for ensuring proper insulation coordination in power systems. For this model the non-linear V-I characteristic of the arrester is represented with two sections of nonlinear resistance designated A_0 and A_1. The two non-linear sections A_0 and A_1 are separated by an R-L filter and are represented by the exponential non-linear resistive model available in the ATP-EMTP program [27]:

$$i = p\left(V/V_{ref}\right)^q, \quad (6)$$

where i is the arrester current; V is the arrester voltage; p, q, V_{ref} are the constants of the device.

As stated in the EMTP rule book, the reference voltage V_{ref} is theoretically arbitrary. It is used to normalize the equation, and to prevent numerical overflow during exponentiation. Then constants p and q are unique parameters of the device. The surge arrester installed in the substation is a SIEMENS 3EP2 model, and its technical specifications are summarized in Table 1.

Table1

Technical Data of the SIEMENS surge arrester

3EP2	1/2 µs	8/20 µs				30/60 µs	
I, kA	10	5	10	20	40	1	2
U, kV	491	435	463	519	579	384	403

The optimized parameters using the developed genetic algorithms as part of this work are summarized in Table 2.

Table 2

Optimized parameters of the modified IEEE model

R_0, Ω	R_1, Ω	L_0, µH	L_1, µH	C_0, pF	C_1, pF
318.55	205.55	0.668	4.8	19.70	19.9
p_0, A	q_0	V_{ref0}, kV	p_1, A	q_1	V_{ref1}, kV
4.61	20.93	562.39	204	14.93	548.05

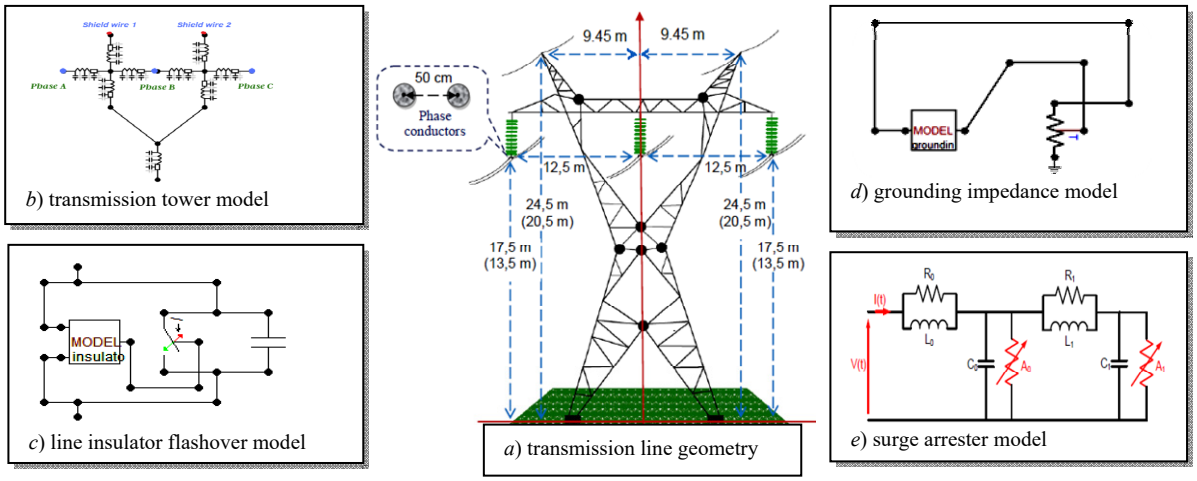

Fig. 1. Modelling of the system elements

Electric geometric model. The EGM is a mathematical model used as a tool to adjust protection and assess the risk of lightning strike on a structure. The model takes into account both the electrical properties and the physical geometry of the structure to determine the probability of an impact and the potential damage that may result. The EGM divides the structure into different zones, each with its own electrical properties, and calculates the risk of impact based on the configuration of the structure and the distance between the zones. Despite the limitations, the EGM is still considered a useful tool for designing an appropriate lightning protection system.

The analysis begins by considering a section of line, and then the study is generalized to the entire line. The first decision made by the EGM is the impact point of the lightning strike if it's directed towards towers, towards conductors or ends on the ground. To make this decision, attraction zones for each point on the line are determined based on the theoretical radius as [28]:

$$r_c = A \cdot I^{\gamma}; \quad r_g = B \cdot I^{\delta}, \quad (7)$$

where $A = B = 8$, $\gamma = \delta = 0.65$ are the constants that depend on the object and the lightning peak current [2]; r_c is the theoretical radius created by the field around the phase conductors and the ground wire in [m]; r_g is the theoretical radius created by the horizontal plane field of the ground in [m]; I is the lightning stroke current amplitude in [kA].

The radius of the sphere used in the EGM was chosen based on established empirical standards. Specifically, the equations presented by Mousa [2] and IEEE-1995 [2] were adopted for this purpose. This approach relies on field data, which demonstrates that using the same radius for both the footing and the wire can yield accurate results within certain limitations. For a

specific value of stroke current, the arcs are drawn, there are two possible situations [17]:

A) the arcs of towers and span center do not intersect;

B) the arcs of towers and span center intersect above the horizontal plane.

Each of these situations is represented in Fig. 2, 3. In addition, a geometric solution is proposed for each case. Since the geometric information is extensive for each case, two ways to solve the problem can be found.

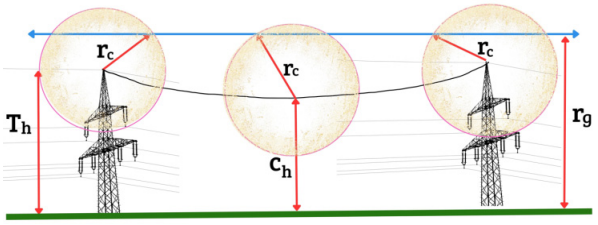

Fig. 2. Representation of EGM with a profile view (case *A*)

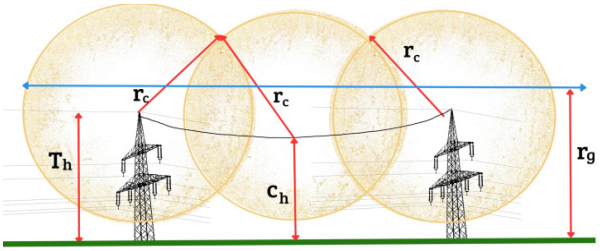

Fig. 3. Representation of EGM with a profile view (case *B*)

Modified electric geometric model (MEGM). MEGM is a refinement of the traditional EGM that has been widely used in the lightning studies. The model provides a more accurate representation of the phenomenon of lightning strikes by taking into account the non-vertical direction of the lightning as well as its random behavior.

In most studies, most significant natural considered to be vertical, when in reality they often hit the ground in a non-vertical manner. MEGM takes this point into account by introducing an angular deviation parameter, denoted by the Greek letter Ψ, which represents the angle between the direction of the lightning strike and the vertical direction. This parameter allows a more accurate description of the lightning path as it makes its way to the ground [15].

Additionally, the angles of lightning display a random behavior that can be modeled using a probability density function described as [10]:

$$p(\Psi)=\begin{cases}0, & \text{if } \Psi<-\pi/2;\\ k\cos^{m}\Psi, & \text{if } -\pi/2<\Psi<\pi/2;\\ 0, & \text{if } \Psi>\pi/2;\end{cases} \quad (8)$$

where Ψ is the angle deviation the direction of a lightning strike and the vertical direction (see Fig. 4).

Figure 5 displays the distribution curves for the stroke angle, and the appropriate distribution function proportional to m values is identified. Specifically, a uniform distribution function is observed for $m = 0$, while m values greater than 2 tend to follow a Gaussian curve. Typically, a value of $m = 2$ is used in computations (in this study, $m = 2$ and $k = 2/\pi$) [28].

The parameters for evaluating lightning impacts are categorized based on the orientation of the lightning strokes. For vertical strokes (Fig. 4) defines the relevant variables, leading to the derivation of (9) – (12), where D_v represents the shielding failure width [28]:

$$\alpha=\tan^{-1}\left(\frac{d}{Y_g-Y_c}\right); \quad (9)$$

$$\varphi=\sin^{-1}\left(\frac{r_g-Y_c}{r_c}\right); \quad (10)$$

$$\beta=\sin^{-1}\frac{(Y_g-Y_c)\cdot\sqrt{1+\tan^2\alpha}}{2\cdot r_c}; \quad (11)$$

$$D_v=r_c\cdot[\cos\varphi-\cos(\alpha+\beta)], \quad (12)$$

in (10) – if $r_g \le Y_c$, then $\varphi = 0$.

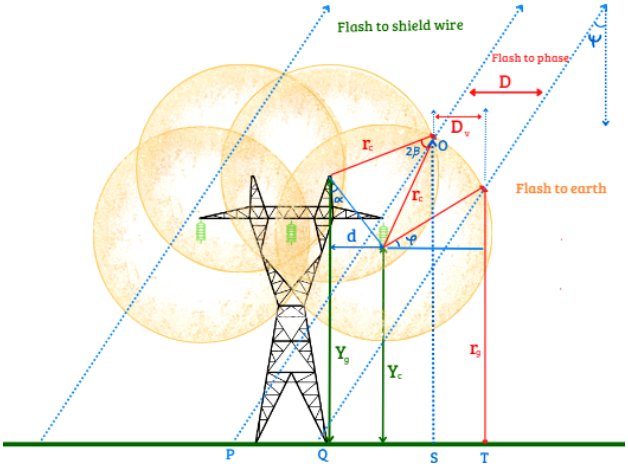

Fig. 4. The scheme of the MEGM

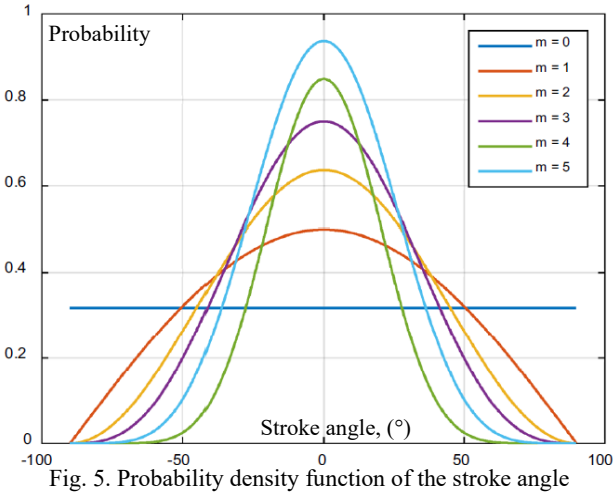

Fig. 5. Probability density function of the stroke angle

For non-vertical strokes in Fig. 4 outlines the associated variables, resulting in equations (13) – (16). In this context, D is the shielding failure distance for a non-vertical flash, with ψ denoting the deviation from the perpendicular direction:

$$SO = Y_c + r_c\cdot\sin(\alpha+\beta); \quad (13)$$

$$PS = SO\cdot\tan\psi; \quad (14)$$

$$QT = r_g\cdot\tan\psi; \quad (15)$$

$$D = PS + D_v - QT. \quad (16)$$

The distance D is critical for determining the strike point – whether it hits the phase conductor, the shield wire, or the ground.

Calculating shielding failure for both vertical and non-vertical lightning strokes involves relatively

straightforward programming, often requiring only a few lines of code in computational software. This distinction is crucial because the angle at which lightning strikes can significantly impact the path and distribution of the electrical discharge.

Traditional EGM primarily focus on the stroke radius on a plane, which works well for vertical strokes. However, incorporating the incidence angle of non-vertical strikes provides a more comprehensive understanding of lightning impact. Non-vertical strokes alter the electric field distribution in ways that vertical strokes do not affecting the shielding effectiveness and overall reliability of electrical substations.

By including these variations, we achieve more precise modeling of lightning impacts, ensuring that our assessments of shielding effectiveness and grounding reliability are accurate and reflective of real-world scenarios. This approach is essential for optimizing the design and protection strategies of electrical infrastructure.

Monte Carlo procedure. The lightning stroke parameters statistical variability has been modeled based on the assumption of a log-normal distribution, utilizing the probability density function as referenced in [29–31]:

$$p(x)=\frac{1}{\sqrt{2\pi}x\sigma_{\ln x}}\exp\left[-\frac{1}{2}\left(\frac{\ln x-\ln x_m}{\sigma_{\ln x}}\right)^2\right]; \quad (17)$$

where $\sigma_{\ln x}$ represents the standard deviation of $\ln x$, and x_m corresponds to the median value of x. Table 3 shows the values used for the lightning parameters.

Table 3

Statistical parameters of lightning strikes [17]

Parameter	x_m	$\sigma_{\ln x}$
I_{100}, kA	34	0.74
t_f, μs	2	0.494
t_h, μs	77.5	0.577

An assumption has been made about a non-zero correlation coefficient between the probability density functions of the peak current magnitude and the rise time. To generate random variables following the joint probability distribution described in (18), the process relies on the conditional probability density function of the rise time (t_f) for a given peak current magnitude (I_p), as shown in (20) [13, 28, 32]:

$$f(I_p,t_f)=\frac{1}{2\pi\cdot I_p\cdot t_f\cdot\sigma_{\ln I_p}\cdot\sigma_{\ln t_f}\cdot\sqrt{1-\rho_c^2}}\cdot\exp(-A); \quad (18)$$

where:

$$A=\frac{1}{2(1-\rho_c^2)}\left[\left(\frac{\ln I_p-\ln\bar{I}_p}{\sigma_{\ln I_p}}\right)^2+\left(\frac{\ln t_f-\ln\bar{t}_f}{\sigma_{\ln t_f}}\right)^2-2\sigma_c\left(\frac{\ln I_p-\ln\bar{I}_p}{\sigma_{\ln I_p}}\right)\left(\frac{\ln t_f-\ln\bar{t}_f}{\sigma_{\ln t_f}}\right)\right]; \quad (19)$$

where ρ_c = 0.47 is the correlation coefficient; $\ln\bar{I}_p$ is the mean value of $\ln I_p$, where $\bar{I}_p$ is the median value of I_p; $\sigma_{\ln Ip}$ is the standard deviation of $\ln I_p$; $\ln\bar{t}_f$ is the mean value of $\ln t_f$, where $\bar{t}_f$ is the median value of t_f; $\sigma_{\ln tf}$ is the standard deviation of $\ln t_f$:

$$p(t_f/I_p=I_{p0})=\frac{p(I_p,t_f)}{p(I_p)}=\frac{\exp\left(-\frac{(\ln t_f-b)^2}{2\sigma^2}\right)}{t_f\sigma\sqrt{2\pi}}; \quad (20)$$

where

$$b=\ln\bar{t}_f+\rho_c\frac{\sigma_{\ln t_f}}{\sigma_{\ln I_p}}(\ln I_{p0}-\ln\bar{I}_p); \quad \sigma=\sigma_{\ln t_f}\sqrt{1-\rho_c^2}.$$

Simulation results. By employing statistical approximations, engineers can enhance their understanding of the system of lightning performance and design more reliable systems. Therefore, in this research we use statistical approximations based on multiple conditions which makes the data of the study very accurate and close-to-reality. Figure 6 illustrates the ATPDraw circuit used to evaluate the lightning performance of the tested system. As reliability is the opposite of failure, and when failures occur randomly, probabilistic studies can be determined to be the most suitable in this case.

Furthermore, it is important to understand how lightning strikes may affect the power system parts in order to analyze the lightning performance of the tested system, here the EGM is applied. Particularly, this model is used to determine the random variables associated with lightning strikes, such as the location of the strike and the current that is generated.

In this work, a developed approach is proposed to assess the lightning performance of a transmission line by generating 10000 combinations of random numbers to obtain the lightning surges incoming to the substation. These cases are analyzed and filtered using the EGM. This means that the model is used to determine which strikes would hit the ground wire, the phase conductor or the ground.

After applying the filtering process, the total number of lightning strikes is reduced to 4514 strikes that hit the line, considering the non-vertical strike case. For the case when only the vertical strikes are considered, we obtained only 3621 case which strikes the transmission line. It is important to note that cases where the lightning strike ends on the ground are ignored in this analysis.

It should also be noted that this study focuses on lightning strikes affecting phase conductors and shield wires. Lightning strikes to footings, which account for approximately 30 % of all strikes on overhead lines, have not been considered in this analysis. These strikes can significantly influence back flashover and substation reliability, and warrant further investigation. Future research will address the distribution and impact of lightning strikes on footings to provide a more comprehensive understanding of lightning performance.

The transmission line is modeled by taking 7 spans from the substation, each span with a length of 300 m. This means that the model focuses on the behavior of the transmission line over a distance of approximately 2.1 km. By using this approach, researchers can gain a better understanding of how lightning strikes may affect the transmission line over a significant distance.

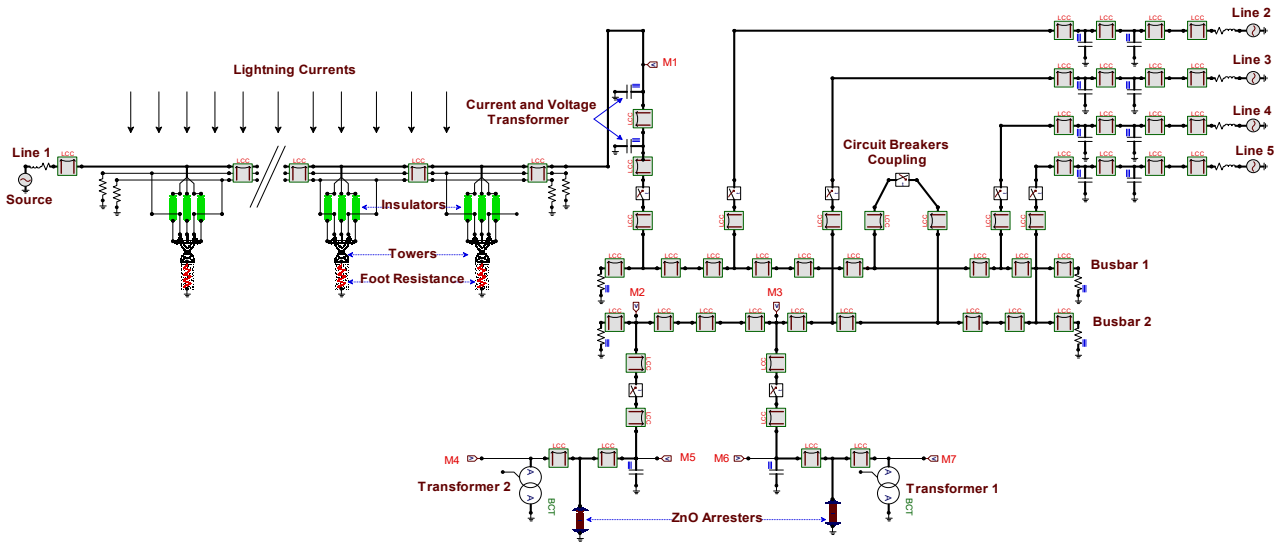

Fig. 6. Complete model of the substation (220 kV) implemented in ATPDraw

In our comprehensive study, we initially analyzed the overall distribution of lightning currents along the transmission line. Figures 7, 8 serve to illustrate the statistical distribution of vertical and non-vertical lightning strikes, respectively. In Fig. 7 the currents most likely to occur (probability of 0.0054) fall within the amplitude range of 26.07 to 41.15 kA, accounting for 813 of the 3569 strokes impacting the shield wire. Similarly, Fig. 8 shows that 4179 strokes impacted the transmission line, with the highest probability (0.0062) occurring for currents ranging from 26.07 to 41.15 kA, representing 935 strokes. This analysis indicates that the probability of lightning currents from non-vertical strikes is higher than that from vertical strikes. Additionally, it is important to note that the probability of vertical lightning currents striking the phase conductor is nearly non-existent as well as occurrences of lightning currents exceeding 500 kA are very rare. These findings underscore the necessity of modeling the transmission line with consideration to lightning angles to enhance the accuracy of our results and ensure the robustness of the electrical infrastructure against variable types of lightning strikes.

This information is very important to understand the lightning damage rate on the transmission line and for developing a strategy to reduce this risk. For example, if non-vertical lightning strikes are more common, it may be necessary to take additional precautions to protect the line from direct lightning damage, such as installing a surge arrester or improving the line's grounding system.

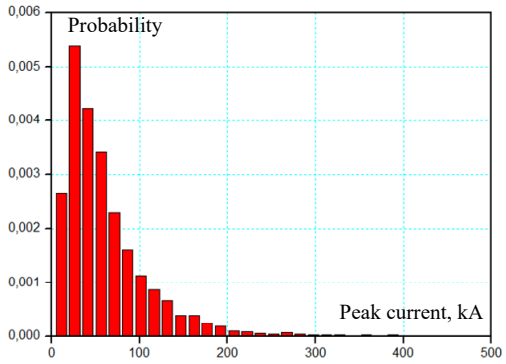

Fig. 7. Statistical distribution of vertical lightning strikes on the transmission line

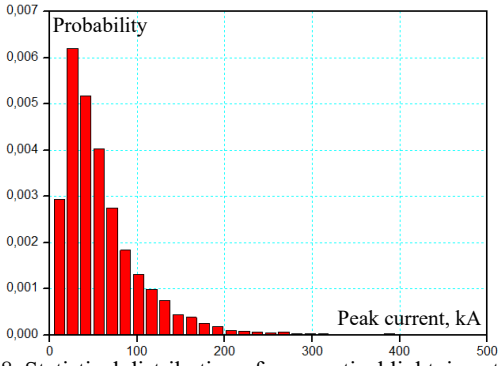

Fig. 8. Statistical distribution of non-vertical lightning strikes on the transmission line

Figure 9 shows the statistical distribution of non-vertical lightning strikes on the shield wire. In this case, the currents having the highest probability (0.0054) have an amplitude ranging from 26.07 to 41.15, it's corresponding to 815 among 3569 strokes impacting the shield wire.

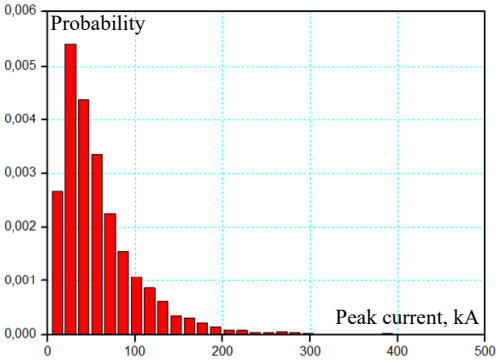

Fig. 9. Statistical distribution of non-vertical lightning strikes on the shield wire

Influence of the lightning stroke incidence angle. In order to improve the assessment of lightning performance of the substation, the influence of the lightning strike angle is investigated in this section.

Figure 10 represents the statistical distribution of non-vertical lightning strikes on phase conductors (610 strokes) where the highest probability (0.00088) occurring for currents ranging from 28.14 to 45.93 kA, representing 158 strokes.

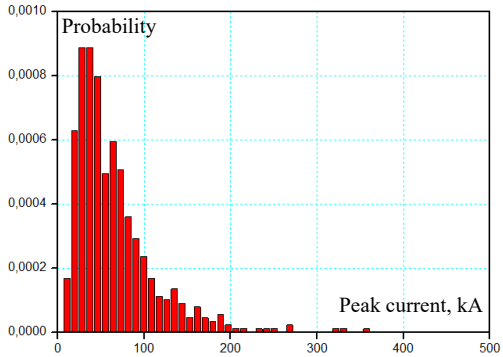

Fig. 10. Statistical distribution of non-vertical lightning strikes on phase conductors

The obtained results for the statistical distribution of lightning strikes on transmission line L_1 as a function of the incidence angle are shown in Fig. 11. As can be seen, the plot reveals the lightning strikes in this case range between –90° and 90°, with a highest probability for those having an angle equals to 20°. In addition to that, the majority of these strikes are concentrated around 0°. Figure 12 shows the distribution of lightning strikes on the shield wire as a function of incidence angle. It is easy to observe that the distribution presents a similar trend as in Fig. 11 indicating that the lightning strikes impacting the shield wire are mostly near-vertical strikes. Distribution of lightning strikes on the phase conductors as a function of incidence angle is shown in Fig. 13. The plot exhibits symmetry around 0° (vertical strike) indicating that phase *B* is not impacted at all independently from the incidence angle. These findings suggest that non-vertical lightning strikes are also important to take into account underscoring the need for enhanced protective strategies against such strikes. The analysis of lightning stroke angles on electrical transmission systems reveals that the distributions on transmission lines, shield wires, and phase conductors follow Gaussian curves. Improving grounding systems and installing surge arresters can significantly contribute to safeguarding electrical infrastructure from potential lightning damage. Additionally, while the use of a common radius for the footing and wire in our model simplifies the calculations, it may introduce some limitations in terms of accuracy. We discuss these limitations in the context of our results and suggest that further refinement of these parameters could lead to more precise modeling outcomes. The assumptions made are based on well-established empirical practices but should be considered with caution in future studies.

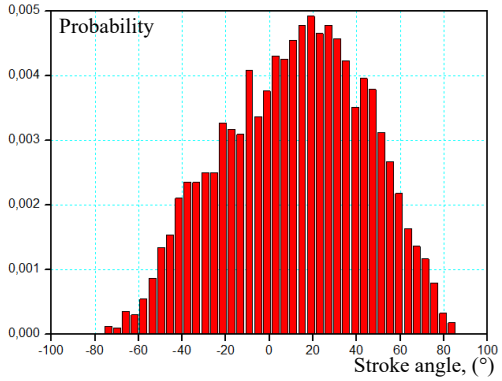

Fig. 11. Statistical distribution of lightning strikes on the transmission line as a function of stroke angle

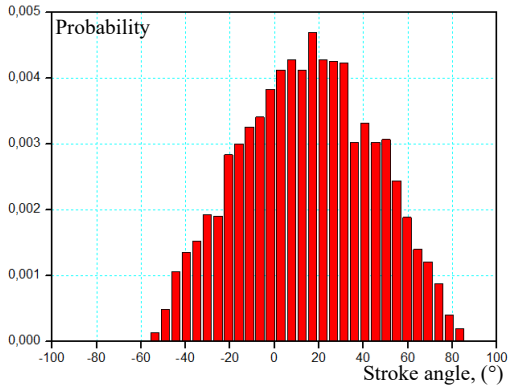

Fig. 12. Statistical distribution of lightning strikes on the shield wire as a function of stroke angle

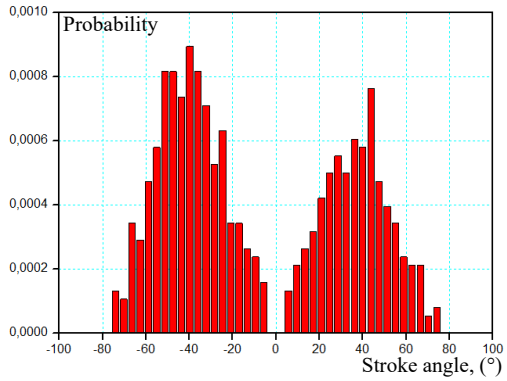

Fig. 13. Statistical distribution of lightning strikes on the phase conductors as a function of stroke angle

The MTBF of the substation. In engineering, reliability is a critical factor in system design and implementation. Generally, reliability refers to the ability of a system to operate without disturbance or failure. To evaluate the reliability of a system, engineers use several methods, one of which is the MTBF that represents the average expected time that elapses between inherent failures of a system during operation. This process is widely used in engineering to assess the systems reliability, such as electronic devices, machines, and other complex systems.

A low MTBF value indicates a high frequency of overvoltages exceeding the equipment's insulation strength, which consequently leads to a higher probability of equipment failure. This measure is used to compare the reliability of systems and to assess the effectiveness of any improvements made to them.

The aim of this part is to evaluate the MTBF for a whole substation. The presented results derived when all the transmission lines are connected to the test substation (line 1 is stroked in this case).

The following expression is used to obtain the MTBF:

$$\text{MTBF} = Y_s / n_f. \quad (21)$$

Taking into account the incoming surges to the substation, the distribution of overvoltages in several basic measuring points in the substation (entrance, circuit breaker, bus bar, surge arrester, auto-transformer) were firstly recorded and compared to the insulation strength. Table 4 presents a summary of the obtained results where the MTBF (years) is determined using the number of faults recorded at the substation equipment (n_f) (overvoltage's number that exceed the equipment BIL value) and the number of years being simulated (Y_s).

The results presented in Table 4 indicate that the higher the selected BIL is, the higher the MTBF will be.

As can be seen, the MTBF values range from 9 years for non-vertical strikes at 850 kV BIL to 12.25 years for non-vertical strikes at 1175 kV BIL. For vertical strikes, MTBF increases substantially, with values starting from 24.48 years at 850 kV BIL.

These findings underscore the critical influence of strike angle and insulation strength on substation reliability. Non-vertical strikes generally result in lower MTBFs, indicating more deleterious effects compared to vertical strikes. This emphasizes the need for accurate modeling in order to improve the system reliability based on adequate technical measures.

Table 4

Simulation results – substation

	BIL, kV	MTBF, years
Non-vertical lightning strikes	850	9.01
	950	9.99
	1050	11.33
	1175	12.25
Vertical lightning strikes	850	24.48
	950	26.75
	1050	28.77
	1175	31.12

Conclusions. This work highlights the critical importance of considering the incidence angle of lightning strikes in the reliability assessment of a 220 kV substation. This work had evaluated the performance of air-insulated substations under various lightning strike scenarios affecting the connected transmission lines. This was assessed in terms of MTBF, determined by the BIL of the equipment. The study has incorporated both vertical and non-vertical strikes to address a critical gap in the literature, offering practical insights to enhance the reliability and safety of air-insulated substations. By considering the angle of lightning strikes, the study improves the accuracy of evaluating lightning performance using precise modelling of system components. Our analysis reveals that the MTBF decreases significantly when lightning strikes occur with non-vertical angles. Specifically, the MTBF values for non-vertical strikes range from 9 years at 850 kV BIL to 12 years at 1175 kV BIL. In contrast, vertical strikes yield higher MTBF values, starting from 24 years at 850 kV BIL. This stark difference underscores the more deleterious effects of non-vertical strikes on substation reliability. Our study utilized an electric geometric model to simulate 10000 random combinations of lightning surges, ultimately reducing the total number of relevant strikes to 4514 when considering non-vertical strikes case and 3621 considering vertical strikes one. The analysis focused on a connected transmission line spanning of about 2.1 km from the substation, revealing that non-vertical strikes have a higher probability of generating damaging currents. For instance, the most likely current amplitude for non-vertical strikes ranges from 26 to 41 kA, occurring with a probability of 0.0062 and representing 935 out of 4179 strokes. Conversely, vertical strikes within the same current range have a probability of 0.0054 representing 813 out of 3569 strokes. These findings demonstrate that non-vertical strikes present a significant risk and are frequent enough to necessitate serious consideration in protective strategy planning. Therefore, instead of recommending the installation of new surge arresters, the study suggests enhancing existing systems by strategically adding surge arresters at critical points, such as the substation entrance or in parallel with line insulators. This optimization would better protect against the risks posed by non-vertical lightning strikes. Future research should focus on assessing the performance of these enhanced systems against non-vertical strikes to better mitigate the associated risks.

Acknowledgment. This work is a part of a research project approved under the number: A01L07UN190120220008. The authors gratefully acknowledge the contributions of the technical staff of SONELGAZ for their help in providing and gathering all the necessary real data to achieve in the best conditions of the present work.

Conflict of interest. The authors of the article declare that there is no conflict of interest.

REFERENCES

1. Wang Q., Ge C., Xue Z., Sun F., Wu S., Li Z., Shi D., Ren H., Li J., Ma H., Cao F. Lightning on transmission lines hazards and prevention measures. *2015 International Conference on Intelligent Systems Research and Mechatronics Engineering*, 2015, pp. 2023-2026. doi: https://doi.org/10.2991/isrme-15.2015.418.

2. Hileman A.R. *Insulation Coordination for Power Systems*. CRC Press, 2018. 767 p. doi: https://doi.org/10.1201/9781420052015.

3. Alto P. *Transmission Line Reference Book – 345 kV and Above. 2nd Edition*. Electric Power Research Institute, California, 1982.

4. *BS EN 60071-2. Insulation Coordination Part 2. Application Guide*. 1997.

5. *IEEE Std 1313.2-1999. IEEE Guide for the Application of Insulation Coordination*, 1999. 68 p. doi: https://doi.org/10.1109/IEEESTD.1999.90576.

6. Savic M.S., Savic A.M. Substation Lightning Performance Estimation Due to Strikes Into Connected Overhead Lines. *IEEE Transactions on Power Delivery*, 2015, vol. 30, no. 4, pp. 1752-1760. doi: https://doi.org/10.1109/TPWRD.2015.2404771.

7. *IEC TR 60071-4:2004. Insulation co-ordination – Part 4: Computational guide to insulation co-ordination and modelling of electrical networks*. 2004. 118 p.

8. Natsui M., Ametani A., Mahseredjian J., Sekioka S., Yamamoto K. FDTD analysis of distribution line voltages induced by non-vertical lightning. *Electric Power Systems Research*, 2020, vol. 189, art. no. 106598. doi: https://doi.org/10.1016/j.epsr.2020.106598.

9. Matsubara I., Sekioka S. Analytical Formulas for Induced Surges on a Long Overhead Line Caused by Lightning With an Arbitrary Channel Inclination. *IEEE Transactions on Electromagnetic Compatibility*, 2009, vol. 51, no. 3, pp. 733-740. doi: https://doi.org/10.1109/TEMC.2009.2025901.

10. Shafaei A., Gholami A., Shariatinasab R. Probabilistic evaluation of lightning performance of overhead transmission lines, considering non-vertical strokes. *Scientia Iranica*, 2012, vol. 19, no. 3, pp. 812-819. doi: https://doi.org/10.1016/j.scient.2011.06.014.

11. Sargent M. Monte Carlo Simulation of the Lightning Performance of Overhead Shielding Networks of High Voltage Stations. *IEEE Transactions on Power Apparatus and Systems*, 1972, vol. PAS-91, no. 4, pp. 1651-1656. doi: https://doi.org/10.1109/TPAS.1972.293342.

12. Karami E., Khalilinia A., Bali A., Rouzbehi K. Monte-Carlo-based simulation and investigation of 230 kV transmission lines outage due to lightning. *High Voltage*, 2020, vol. 5, no. 1, pp. 83-91. doi: https://doi.org/10.1049/hve.2019.0147.

13. Martinez J.A., Castro-Aranda F. Lightning Performance Analysis of Overhead Transmission Lines Using the EMTP. *IEEE Transactions on Power Delivery*, 2005, vol. 20, no. 3, pp. 2200-2210. doi: https://doi.org/10.1109/TPWRD.2005.848454.

14. Martinez J. A., Castro-Aranda F. Influence of the stroke angle on the flashover rate of an overhead transmission line. *2006 IEEE Power Engineering Society General Meeting*, 2006, art. no. 1708911. doi: https://doi.org/10.1109/PES.2006.1708911.

15. Lobato A.T., Schroeder M.A.O., Cruz D.E., Reis M.R., Moura R.A.R., Sales W.S., Nascimento L.C., Assis S.C. Analysis of the cumulative probability distribution of the stroke angle in lightning incidence to three-phase overhead transmission lines. *2013 International Symposium on Lightning Protection (XII SIPDA)*, 2013, pp. 128-133. doi: https://doi.org/10.1109/SIPDA.2013.6729236.
16. Lobato A.T., Schroeder M.A.O., Meireles I.J.W.S., Moura R.A.R., Sales W.S., Nascimento L.C., Assis S.C. Influence of considering a stroke angle distribution on the estimation of the shielding performance of transmission lines: Effects of electrogeometric models. *International Conference on Grounding and Earthing & 6th International Conference on Lightning Physics and Effects.* Manaus, Brazil May, 2014, pp. 1-6.
17. Bedoui S., Bayadi A. Probabilistic evaluation of the substation performance under incoming lightning surges. *Electric Power Systems Research*, 2018, vol. 162, pp. 125-133. doi: https://doi.org/10.1016/j.epsr.2018.05.011.
18. Bedoui S., Bayadi A. Statistical approach for insulation coordination of high voltage substation exposed to lightning strikes. *Electrical Engineering & Electromechanics*, 2024, no. 4, pp. 55-60. doi: https://doi.org/10.20998/2074-272X.2024.4.07.
19. *CIGRE WG 33-01. Guide to Procedures for Estimating the Lightning Performance of Transmission Lines*. CIGRE Brochure 63, 1991.
20. Banjanin M.S. Application possibilities of special lightning protection systems of overhead distribution and transmission lines. *International Journal of Electrical Power & Energy Systems*, 2018, vol. 100, pp. 482-488. doi: https://doi.org/10.1016/j.ijepes.2018.03.006.
21. Martinez-Velasco J.A, Castro-Aranda F. Modeling of Overhead Transmission Lines for Lightning Studies. *International Conference on Power Systems Transients IPST'05*, Montreal, Canada, 2005, pp. 1-6.
22. Abd-Elhady A.M., Sabiha N.A., Izzularab M.A. High-frequency modeling of Zafarana wind farm and reduction of backflow current-overvoltages. *International Transactions on Electrical Energy Systems*, 2014, vol. 24, no. 4, pp. 457-476. doi: https://doi.org/10.1002/etep.1697.
23. Sarajcev P., Vasilj J., Jakus D. Method for estimating backflashover rates on HV transmission lines based on EMTP-ATP and curve of limiting parameters. *International Journal of Electrical Power & Energy Systems*, 2016, vol. 78, pp. 127-137. doi: https://doi.org/10.1016/j.ijepes.2015.11.088.
24. Boumous S., Boumous Z., Anane Z., Nouri H. Comparative study of 220 kV overhead transmission lines models subjected to lightning strike simulation by using electromagnetic and alternative transients program. *Electrical Engineering & Electromechanics*, 2022, no. 4, pp. 68-74. doi: https://doi.org/10.20998/2074-272X.2022.4.10.
25. Martinez J.A., Castro-Aranda F. Lightning Performance Analysis of an Overhead Transmission Line Protected by Surge Arresters. *IEEE Latin America Transactions*, 2009, vol. 7, no. 1, pp. 62-70. doi: https://doi.org/10.1109/TLA.2009.5173466.
26. Bayadi A. Parameter identification of ZnO surge arrester models based on genetic algorithms. *Electric Power Systems Research*, 2008, vol. 78, no. 7, pp. 1204-1209. doi: https://doi.org/10.1016/j.epsr.2007.10.001.
27. *International Standard IEC 60099-4:2014. Surge arresters – Part 4: Metal-oxide surge arresters without gaps for a.c. systems*, 2014. 353 p.
28. De Oliveira Schroeder M.A., Lobato A.T., Do Nascimento L.C., De Sousa Sales W., De Moura R.A.R., De Castro Assis S. Effects of Considering A Stroke Angle Distribution on Estimating the Shielding Performance of Overhead Transmission Lines. *Journal of Control, Automation and Electrical Systems*, 2015, vol. 26, no. 5, pp. 567-578. doi: https://doi.org/10.1007/s40313-015-0198-y.
29. Chowdhuri P., Anderson J.G., Chisholm W.A., Field T.E., Ishii M., Martinez J.A., Marz M.B., McDaniel J., McDermott T.E., Mousa A.M., Narita T., Nichols D.K., Short T.A. Parameters of lightning strokes: a review. *IEEE Transactions on Power Delivery*, 2005, vol. 20, no. 1, pp. 346-358. doi: https://doi.org/10.1109/TPWRD.2004.835039.
30. Martinez Velasco J.A., Corea Araujo J., Bedoui S. Lightning performance analysis of transmission lines using the Monte Carlo method and parallel computing. *Ingeniare. Revista Chilena de Ingeniería*, 2018, vol. 26, no. 3, pp. 398-409. doi: https://doi.org/10.4067/S0718-33052018000300398.
31. Kniaziev V.V. Determination of the probability of a lightning strike in the elements of the object taking into account the statistical distribution of the current value. *Electrical Engineering & Electromechanics*, 2023, no. 5, pp. 57-62. doi: https://doi.org/10.20998/2074-272X.2023.5.08.
32. Borghetti A., Nucci C.A., Paolone M. An Improved Procedure for the Assessment of Overhead Line Indirect Lightning Performance and Its Comparison with the IEEE Std. 1410 Method. *IEEE Transactions on Power Delivery*, 2007, vol. 22, no. 1, pp. 684-692. doi: https://doi.org/10.1109/TPWRD.2006.881463.

Received 02.07.2024
Accepted 04.10.2024
Published 02.01.2025

T. Hamel[1]*, PhD Student,*
S. Bedoui[1]*, Doctor of Science,*
A. Bayadi[2]*, Professor,*
[1] Laboratory of Electrical Engineering and Automatic (LGEA), University of Oum El Bouaghi, Algeria,
e-mail: hameltaher04@gmail.com;
bs_1182@yahoo.fr (Corresponding Author)
[2] Automatic Laboratory of Setif (LAS), University of Setif-1, Algeria,
e-mail: a_bayadi@univ-setif.dz

How to cite this article:
Hamel T., Bedoui S., Bayadi A. Impact of transmission line lightning performance on an operational substation reliability considering the lightning stroke incidence angle. *Electrical Engineering & Electromechanics*, 2025, no. 1, pp. 56-64. doi: https://doi.org/10.20998/2074-272X.2025.1.08

UDC 621.317.727.1 https://doi.org/10.20998/2074-272X.2025.1.09

Y.O. Haran, Y.O. Trotsenko, O.R. Protsenko, M.M. Dixit

The impact of parasitic capacitances on the accuracy of scale transformation of high-voltage dividers

Purpose. *The* ***aim*** *of this work is the determination of the parasitic capacitance's influence on the accuracy of scale transformation of high-voltage dividers. Analyzing the possibilities of reducing such influence is a pressing* ***problem*** *for high voltage measurement, especially at high frequency range of input voltage.* ***Methodology****. Mathematical modeling of the voltage divider equivalent circuit, considering parasitic capacitances and inductances has been performed in the QUCS circuit simulator software under sinusoidal alternating current conditions in the range from 100 Hz to 1 MHz. Using the FEMM software, the finite element method was used to simulate the density distribution of capacitive currents in the module with capacitance graded insulation of the high-voltage arm of the voltage divider.* ***Results****. The results of the calculations show that the percentage of parasitic capacitive currents decreases exponentially depending on the ratio of the outer radii of the shielding disks to the distance between them. However, even with the outer radii of the shielding disks of about 3 m, capacitive currents still make up about 1 % of the total current flowing in the measuring circuit of the voltage divider. Instead of increasing outer radii, it is proposed to use high-voltage capacitance graded insulation between the shielding disks. As a result, a stable error of large-scale voltage transformation was obtained when the values of parasitic capacitances change, and it is proposed to manufacture the high-voltage arm of the voltage divider from the same type of high-voltage modules.* ***Originality****. The results of modeling the dependence of the accuracy of the voltage divider scale transformation on the ratio of the structural elements geometric parameters of its high-voltage arm were obtained. The solution has been proposed that involves changing the design of the high-voltage arm of the voltage divider, which significantly reduces the dependence of its scale transformation error on significant changes in the parasitic capacitances of the structure components on grounded surfaces.* ***Practical value****. The results of mathematical modeling of the characteristics of the voltage divider high-voltage arm make it possible to design, for the purpose of serial production, the same type of high-voltage modules for assembling on-site broadband voltage dividers for any nominal voltage, which will have the possibility of integration into Smart Grid systems.* References 23, tables 1, figures 8.

Key words: **high-voltage divider, parasitic capacitances, scale transformation accuracy.**

В роботі розглянуто вплив будови високовольтного плеча подільника напруги на його характеристики. Для забезпечення зменшення впливу паразитних ємностей конструктивних елементів на зосереджені елементи активної частини та на зовнішні об'єкти досліджено методи екранування зосереджених елементів. Математичним моделюванням визначено вплив співвідношення геометричних параметрів конструкційних елементів високовольтного плеча на похибку масштабного перетворення напруги в області високих частот. В результаті моделювання обрано спосіб екранування зосереджених елементів активної частини подільника напруги з використанням багатошарової ізоляції конденсаторного типу, яка забезпечує стабільність похибки масштабного перетворення напруги в широкому діапазоні частот. Запропоновані зміни в будові високовольтного плеча дозволяють перейти на модульну будову подільника напруги і перейти до його серійного виробництва. Бібл. 23, табл. 1, рис. 8.

Ключові слова: **високовольтний подільник напруги, паразитні ємності, точність масштабного перетворення.**

Problem definition. High-voltage dividers are common large-scale voltage converters used in both microelectronics and high-voltage test and research laboratories. However, these electrical devices are not widely used in the power industry, in particular, in high-voltage electrical installations, since their structure does not allow getting rid of a number of disadvantages that complicate their integration into analog or digital substations as broadband large-scale high-voltage converters [1]. For example, under laboratory conditions, large-scale voltage conversion errors in a wide frequency range of the order of 0.1 are obtained for high-voltage dividers, however, the structure of such a voltage divider is complex and not suitable for wind loads, precipitation, and temperature changes. In open switchgears, the presence of objects near the voltage divider that are at a different potential (or grounded) significantly affect the parasitic capacitances of its high-voltage arm. Parasitic capacitances on such objects significantly affect the accuracy of large-scale voltage conversion at high frequency. Also, the temperature dependence of the complex resistances of the lumped elements of the high-voltage arm affects the scaling factor of the voltage divider. In addition, the production of high-voltage dividers for the specific tasks of the customer complicates the creation of a unified system of mass production of such equipment. This limits the possibility to significantly improve the determination of power quality indicators, safety and automation of processes at high-voltage facilities. For these and other reasons, high-voltage dividers have not yet been used as large-scale high-voltage converters in a wide frequency range. They could not replace, even partially, the existing electromagnetic voltage transformers at high-voltage substations. This applies, in particular, to the determination of power quality indicators, some of which are significantly distorted by the electromagnetic cores of transformers.

Analysis of publications on research topic. The simplest high-voltage divider consists of two serially connected sections of a circle of lumped elements: high-voltage and low-voltage arms. Each of the arms is a section consisting of one or more series-connected lumped elements (the structure of the low-voltage arm can be significantly different, depending on the purpose of the voltage divider) [1, 2]. The principle of voltage division is that the total voltage to be proportionally distributed is applied to the series-connected arms of the voltage divider and is distributed among the lumped elements in proportion to their complex resistances. This principle of voltage distribution is used both for functional voltage distribution (for example, in high-voltage air circuit breakers for ultra-high voltages to divide a long electric arc into a number of short arcs in order to extinguish them more efficiently), and for the purpose of measuring high voltage by connecting measuring devices in parallel to the circuit low-voltage arm.

For measuring high voltage, the high-voltage arm of the voltage divider must consist not only of a link of lumped elements of the active part, but also of high-voltage insulation and armature that holds these lumped elements. High-voltage insulation and armatures

practically do not affect the measurement of constant voltage, accordingly, for measuring high constant voltage, it is sufficient to provide the high-voltage and low-voltage arms of the voltage divider with high-quality precision lumped elements (resistors) that will provide the necessary scaling factor, in accordance with the formula:

$$K_d = \frac{U}{U_{LV}} = \frac{R_{HV} + R_{LV}}{R_{LV}} = 1 + \frac{R_{HV}}{R_{LV}}, \qquad (1)$$

where U is the measured high voltage; U_{LV} is the voltage on the low-voltage arm; R_{HV} is the total active resistance of the area of lumped elements of the high-voltage arm; R_{LV} is the total active resistance of the lumped elements of the low-voltage arm.

However, if the voltage divider is used to measure voltage that changes with time (sinusoidal voltage, transients, etc.), the structure of the arms of the voltage divider becomes significantly more complicated. In AC circuits, especially, with an increase in the frequency or rapidity of transient processes, the influence of reactive component elements of electric circuits increases [2–4]. It is necessary to take into account not only the voltage distribution between the lumped elements of the arms of the voltage divider, but also the parasitic capacitances and inductances, which are integral components of any lumped elements of the electric circuit, as well as the components of the structural elements of its arms. In modern high-voltage dividers designed for measuring alternating voltage and transients (broadband voltage dividers), the structure of high-voltage insulation and armature form complex systems of parasitic capacitances on nearby lumped elements, on grounded structural elements and nearby objects that are under a different potential. In modern designs of voltage dividers, the method of shielding the lumped elements of the high-voltage and low-voltage arms is used in order to reduce the influence of parasitic capacitances on the voltage distribution between different sections of the general electric circuit of the active part. Large-sized capacitive screens are also used, designed to regulate the distribution of the electric field. In works [4–10], various design solutions for the structure of the high-voltage arm of the voltage divider are proposed, which allow to partially reduce the influence of parasitic capacitances (up to a certain level of input voltage frequencies). As a rule, parallel shielding conductive disks are used for this purpose, which between them form a distribution of the electric field that is close to uniform, and between the planes of these disks, sections of the circle of lumped elements of the active part of the voltage divider are placed, thus dividing the high-voltage circuit into a number of shielded sections. Shielding disks and support insulators form the armature that keeps the lumped elements of the high-voltage arm of the voltage divider in a certain spatial position. The consequence of such a structure is the appearance of additional parasitic capacitances (between the shielding disks), which form a high-voltage capacitive (shielding) circuit, which is parallel to the circuit of lumped elements of the high-voltage arm. The lumped circuit elements of the high-voltage arm will have parasitic capacitances on the shielding disks. The greater will be the differences in the potential distribution between the lumped elements and the shielding disks, the greater will be the parasitic capacitive currents between the lumped elements and these disks (especially at a high frequency of the applied voltage).

To analyze the influence of the structure of the high-voltage arm of the voltage divider on its frequency characteristics, researchers offer both direct measurement methods [10–15] using high-precision and reference measuring devices, as well as analytical methods or numerical modeling [15–22], which allow predicting the characteristics of designed voltage dividers or to explain the actual measured parameters for further improvement of the structure of voltage dividers.

In all the publications reviewed, the influence of parasitic capacitances of both the lumped elements of the active part and the structural components of the voltage divider structure, both on external objects and among themselves, is recognized as significant. However, recognizing the significance of the influence of parasitic capacitances on the accuracy of large-scale transformation of voltage dividers at high frequency, in the reviewed publications, researchers propose various schemes and spatial arrangement of lumped elements of the active part, without paying much attention to the structure of the shielding areas of the high-voltage arm (mainly, such studies consider the structure and spatial arrangement of high-voltage large-sized screens). Since the structure of the high-voltage arm of the voltage divider has a significant effect on the distribution of voltage on lumped elements of the active part, it is important to find design solutions that would allow combining mechanical and shielding functions in a wide frequency range.

The goal of the work is to analyze the structure of the high-voltage arm of the voltage divider and to identify the factors that affect the accuracy of large-scale voltage conversion in a wide frequency range in the presence of parasitic capacitances in the circuit of the high-voltage arm.

Analysis of the structure of the high-voltage arm of the voltage divider. To overcome the above-described consequences of the presence of parasitic capacitances between the lumped elements of the high-voltage arm and the surfaces under a different potential, there are several options for the structure of the high-voltage arm. In addition to the above-mentioned method of shielding the sections of the lumped elements of the high-voltage arm of the voltage divider with the help of conductive shielding disks, parallel circuits of lumped shielding elements are used, which are additionally placed between the shielding disks in order to increase the conductivity between them and, as a result, reduce the impact of leakage of capacitive currents from these disks on surfaces under a different potential. Both shunting with resistors and shunting with capacitors or a mixed *RC* connection of shielding disks are used. You can reduce the value of the active resistances of the shielding circuit only to certain limits: if the total resistance of the shielding circuit of the high-voltage arm of the voltage divider is too small, significant currents will flow through it and significant energy will be released in the form of heat, which will affect the stability of the circuit characteristics. In addition to creating an excess load on the source, such energy can cause heating not only of the lumped elements of the shielding circuit, but also of the elements of the measuring circuit, reducing the stability of these resistances.

Figure 1 shows a simplified substitution circuit of a high-voltage divider, in which the low-voltage arm is represented by one, and the high-voltage arm is represented by three series-connected high-voltage, high-resistance, low-inductance resistors of the same rating (R1 – R4).

Parasitic inductances of these resistors are represented by elements L1 – L4. The high voltage from the source V1 is applied to the entire voltage divider, and is measured on the low-voltage arm by the meter U_VN, the internal resistance of which is considered infinite in the simulation. In the absence of parasitic capacitances and the identity of resistors R1 - R4, the voltage on the low-voltage arm should, in accordance with (1), be equal to 25 % of the input voltage of the high-voltage source V1. Capacitances C1 –C4 in Fig. 1 are parasitic capacitances that occur between the shielding disks forming the sections of the voltage divider and the parallel shielding capacitive circuit. Parasitic inductances L5 – L8 are also added to these capacitors in series, which refer to the shielding capacitive circuit, if capacitors are additionally installed in this circuit between the shielding disks to increase the capacitance in this circuit. Parasitic capacitances C5 – C6 occur between the shielding disks and the high-voltage electrode (as a rule, these capacitances have very small values); parasitic capacitances C7 – C8 occur between the shielding disks and the grounded surfaces and, as a rule, have values up to units of picofarads (rarely larger). Parasitic capacitances C9 – C11 occur between the lumped elements of the measuring circuit of the voltage divider and the shielding disks of the shielding circuit. The circuit according to Fig. 1 does not take into account all the parasitic capacitances and inductances of the high-voltage divider and considers a small number of sections, but allows considering the principle relationships between the main and parasitic characteristics of both lumped and structural elements in its composition.

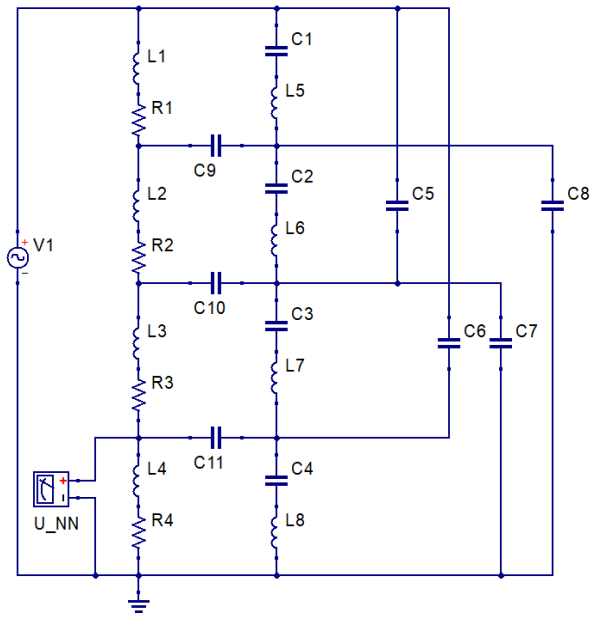

Fig. 1. Schematic substitution circuit of voltage divider taking into account parasitic capacitances and inductances

For the numerical evaluation of the characteristics of lumped and parasitic elements of the circuit in Fig. 1, the possibility of using low-power high-voltage resistors in the active part of the voltage divider is considered. As a rule, when using low-power resistors, the current in the active part is limited to the order of 1 mA. Suppose that the amplitude of the applied voltage of the source V1 is 10 kV. Accordingly, the total input resistance of the voltage divider according to Ohm law (neglecting the insignificant inductive resistances) can be roughly estimated as 10 MΩ. Accordingly, resistors R1 – R4 will have a nominal resistance of 2.5 MΩ. Parasitic capacitances that arise between the shielding disks of the shielding part of the voltage divider circuit can be estimated approximately by formula for parallel plate capacitor:

$$C = \frac{\varepsilon_0 \cdot \varepsilon \cdot \pi \cdot \left(R_2^2 - R_1^2\right)}{d}, \qquad (2)$$

where ε_0 is the electrical constant; ε is the relative permittivity of the dielectric (if the dielectric is air, $\varepsilon = 1$ can be considered as an approximation); d is the distance between parallel disks; R_2 is the outer radius of the shielding disk; R_1 is the radius of the inner hole in the shielding disk (intended for the location of the measuring circle of lumped elements).

According to (2), if we take R_1 = 3 cm, R_2 = 10 cm, d = 1 cm, we obtain $C \approx 25$ pF. Parasitic inductances of resistors L1 - L4 can be taken as equal to 10 nH (for low-inductance resistors). The parasitic capacitances of the lumped elements of the measuring circuit C9 – C11 can be approximately equal to 1 pF (these capacitances are insignificant and depend on the dimensions of the resistors). Parasitic inductances L5 – L8 can be shorted in the absence of shunt capacitors between the shielding disks, or will have very little value when using pulsed capacitors (for example, PHE-450 type or similar), therefore, as a first approximation, these inductances in the circuit can be taken as 1 nH. Parasitic capacitances C5 – C6 can be determined only by mathematical modeling using numerical methods of the electrostatics problem, taking into account the specific geometry of the shielding disks. This also applies to parasitic capacitances C7 – C8. As a rule, the capacitances for the grounded surfaces are several times larger than the corresponding capacitances for the high-voltage electrode. According to the performed mathematical modeling of the problem of electrostatics in the FEMM software package for the geometry of the shielding disks used for calculations according to (2), it is possible to determine the approximate value of these capacitances: C5 ≈ 3 pF; C6 ≈ 1.5 pF; C8 ≈ 5 pF; C7 ≈ 7 pF (if the thickness of the shielding conductive disks is assumed to be equal to 5 mm).

Mathematical modeling of the electric circuit in Fig. 1 in the QUCS circuit modeling software package in the problem of sinusoidal AC in the range from 100 Hz to 1 MHz with discretization of 5000 points gives a graph of the dependence of the voltage on the low-voltage arm (Fig. 2).

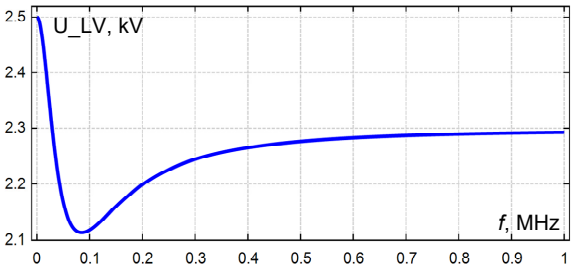

Fig. 2. Dependence of the voltage on the low-voltage arm of the voltage divider on the frequency at the capacitances in the shielding circuit of 25 pF

This graph shows the maximum deviations (in the considered frequency f range) of the output voltage U_LV of the voltage divider from the nominal (2.5 kV) of the order of 15 %, which is unacceptable for large-scale

conversion of high voltage for the purpose of determining power quality indicators. If the capacitance of the shielding circuit is increased to 10 nF, a similar simulation in the QUCS software package gives a graph of the dependence of the output voltage, shown in Fig. 3.

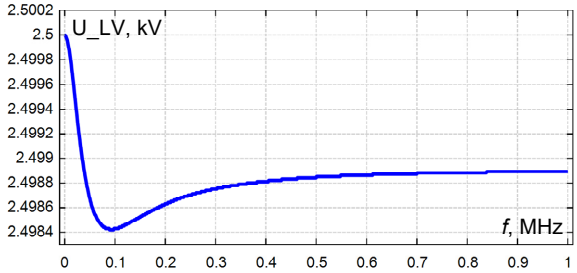

Fig. 3. Dependence of the voltage on the low-voltage arm of the voltage divider on the frequency at the capacitances in the shielding circuit of 10 nF

Analyzing the graph in Fig. 3, it can be seen that the maximum deviations of the output voltage are less than 0.1 % in the frequency f range from 1 Hz to 1 MHz, which can be considered acceptable for the use of such a voltage divider when measuring all power quality indicators at high voltage. When expanding the range of input frequencies to 50 MHz, the result of the analysis gives the graph shown in Fig. 4.

The extended frequency range, in which the high accuracy of the large-scale transformation of the high voltage is preserved, is a consequence of the fact that the capacitances in the shielding circuit significantly shunt the parasitic capacitances of the shielding disks, and, moreover, the parasitic conductances of the shielding circuit and the parasitic conductances of the shielding disks on the surface, which are under a different potential, with increase proportionally in frequency. Accordingly, at high frequencies of the input voltage, parasitic inductances L1 – L4 and parasitic capacitances C9 – C11 remain the biggest factors affecting the accuracy of large-scale voltage conversion.

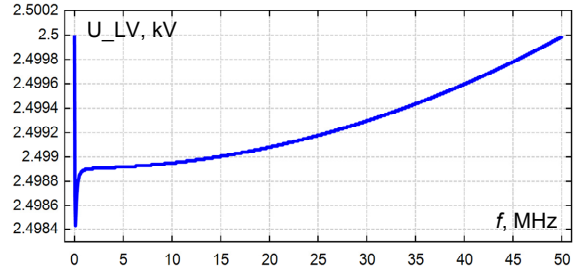

Fig. 4. Dependence of the voltage on the low-voltage arm of the voltage divider on the frequency at the capacitances in the shielding circuit of 10 nF in the range from 100 Hz to 50 MHz

In fact, if the specified parasitic inductances depend solely on the manufacturing technology of high-voltage precision resistors (or other lumped elements of the measuring circuit), the specified parasitic capacitances are dependent on the mutual spatial arrangement of the lumped elements of the measuring circuit and shielding disks. In Fig. 1 lumped elements have practically no parasitic capacitances on grounded surfaces and surfaces under a different potential. This situation is possible only if the ratio between the diameters of the shielding disks and the distance between them in height is significant, when the shielding practically excludes the ingress of external electric fields into the area of the location of the lumped elements of the measuring circle.

If we model mathematically and numerically calculate the spread of currents in the measuring and shielding circuits of a high-voltage divider (in codes using the finite element method) at frequency of 1 MHz (the front shape of a standard full lightning pulse, which is the fastest transient that is determined among the quality indicators of electricity, corresponds to a sinusoid with frequency of about 250 kHz) for the geometry of the electrodes and the nominal values of the lumped elements, according to which the simulation data obtained in the QUCS software package in Fig. 2 (without the use of shunt capacitors), it is possible to obtain results similar to those shown in Fig. 5.

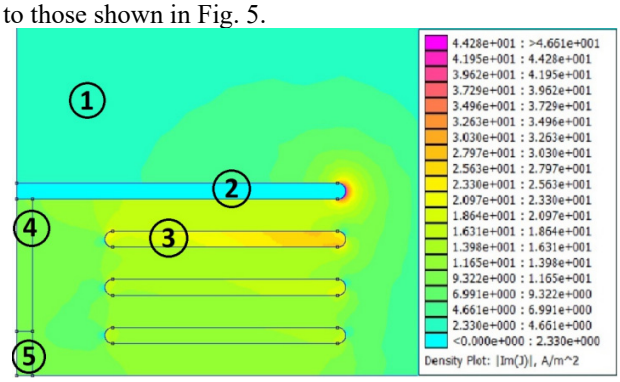

Fig. 5. The result of modeling the current density distribution in the mathematical model of the voltage divider, performed in the FEMM software package

Modeling in the FEMM software package was performed in an axisymmetric coordinate system by solving the equation derived from Maxwell system of equations:

$$-(\sigma + j\omega\varepsilon_0\varepsilon)\cdot\nabla^2 V = 0\,, \qquad (3)$$

where σ is the conductivity of the medium; ε is the relative dielectric permittivity of the medium; ω is the angular frequency of the current; V is the electric potential.

In Fig. 5 the following are marked: 1 – the air region with relative dielectric permittivity ε = 1; 2 – the high-voltage electrode to which sinusoidal voltage with amplitude of 10 kV and frequency of 1 MHz is applied; 3 – the shielding disks; 4 – the active resistance of the high-voltage arm, modeled by a cylinder with geometry and conductivity that provide its resistance at constant voltage of 7.5 MΩ; 5 – the active resistance of the low-voltage arm, modeled by a cylinder with geometry and conductivity that provide its resistance at constant voltage of 2.5 MΩ. The calculation area was limited to a spherical grounded surface with radius 10 times greater than the outer radius of the shielding disks. As a result of the unequal distribution of potentials in the measuring circuit (high-voltage and low-voltage arms) of the voltage divider and vertically along the end surfaces of the shielding disks, between the disks and the side surface of the resistors of the measuring circuit, a potential difference is formed, which, in the presence of parasitic capacitances, leads to the appearance of capacitive currents that increase with frequency of the applied voltage, which can be seen by the color distribution in Fig. 5. The maximum values of the capacitive current density correspond to the rounded end of the high-voltage electrode and are about 110 A/m^2. At the same time, the integral values of the capacitive currents through the side surface of the resistor and through the horizontal surfaces of the shielding disks differ by a factor of ten at a frequency of 1 MHz (the current through the side surface

of the resistor is about 20 mA; the current through the horizontal surfaces of the shielding disks decreases with a decrease in the potential of the disk and, on average is about 400 mA). The presence of leakage of capacitive currents through the side surface of the resistors of the measuring circuit leads to the fact that the current that enters this circuit from the high-voltage electrode is not equal to the current that exits from the resistors of the low-voltage arm of the voltage divider to the grounded electrode. At the same time, the points on the side surface of the resistors of the measuring circuit, which correspond in height to the points closest to them on the surfaces of the shielding disks, have a higher potential for the resistor marked 4 in Fig. 5, and a lower potential for the resistor marked 5 in Fig. 5. As a result, through part of the side surface of the resistors of the measuring circuit, capacitive currents flow out, and through some areas - flow into the resistors. By ensuring the equality of the potentials of the shielding disks and their corresponding points on the side surfaces of the resistors of the active part, it is possible to quantitatively equalize the currents flowing in and out through the side surfaces of the resistors of the active part, in fact, getting rid of the influence of capacitive currents on the processes in the active part of the voltage divider.

Mathematical modeling. Calculation in the FEMM software package of the proposed mathematical model of the voltage divider allows obtaining the numerical values of the currents at the input to the resistor of the high-voltage arm and at the output of the resistor of the low-voltage arm by integrating the current density through the corresponding end surfaces of the resistors. Also, the simulation result allows to estimate the electric potential both on the surfaces of the shielding disks and on the side surfaces of the resistors of the active part.

The model according to Fig. 5 is constructed based on the outer radii of the high-voltage electrode and shielding disks of 100 mm. If the outer radii of the electrodes and disks are increased, leaving the distance between them unchanged, the capacitances of the shielding circle (between the shielding disks) will increase, and the parasitic capacitances of the shielding disks to the high-voltage electrode and to the grounded surfaces will remain almost unchanged. As a result, in the circuit in Fig. 1 capacitances C1 – C4 will increase, in accordance with (2). With significant capacitances in the shielding circuit, the current through this branch of the electric circuit will lead to an almost uniform distribution of potentials between these disks, as a result of which the ends of the shielding disks, which are close to the side surfaces of the resistors of the measuring circuit, will have potentials that are close to the potentials distributed over the surfaces of the resistors measuring circle. The same (or close to the same) distribution of potentials along the adjacent surfaces will lead to the fact that insignificant capacitive currents will flow through the parasitic capacitances formed by these surfaces (or the currents flowing from the side surface will be close to the currents flowing into this surface) due to a small potential differences. Of course, with significant values of the ratio of the outer radii of the shielding disks to the distance between them (R/d), the parasitic capacitances of the side surfaces of the resistors of the measuring circuit to the grounded surfaces are so small, compared to the capacitances between the disks of the shielding circuit, that they can be neglected.

Table 1 shows the results of modeling in which the parameters of the model remained unchanged, in accordance with those specified for Fig. 5, except for the outer radii of the high-voltage electrode and the shielding disks, which were increased. The scale conversion error was indirectly determined through the difference between the currents that enter the active part of the measuring circuit from the end of the resistor, and that exit from it, in accordance with the expression:

$$\Delta = \frac{I_{HV} - I_{LV}}{I_{HV}} \cdot 100\% \cdot \qquad (4)$$

Table 1

Results of modeling the influence of increasing radii of shielding disks on the value of parasitic capacitive currents in the measuring circuit

R/d	I_{HV}, mA	I_{LV}, mA	Δ, %
10	1,456	1,189	18,342
20	1,386	1,25	9,763
30	1,36	1,272	6,45
40	1,348	1,284	4,759
50	1,341	1,288	3,976
60	1,336	1,293	3,233
70	1,333	1,297	2,712
80	1,33	1,3	2,276
90	1,329	1,301	2,137
100	1,328	1,301	2,065
200	1,322	1,303	1,403
300	1,319	1,303	1,158

In Table 1, the current at the input to the high-voltage arm I_{HV}, the current at the output from the low-voltage arm I I_{LV} and the difference Δ between them in percent were determined.

The results of the calculations presented in Table 1 show that the percentage of parasitic capacitive currents decreases exponentially depending on the ratio of the outer radii of the shielding disks to the distances between them. However, it can also be seen that even at outer radii of the shielding disks of about 3 m, capacitive currents still account for about 1 % of the total current flowing in the measuring circuit. However, the manufacture of such sectioned structures of a high-voltage divider is not only unacceptable from the point of view of weight and size, but also practically impossible from the point of view of mechanical strength. In addition, since the shielding disks have a certain thickness that is proportional to the distance between adjacent disks, the end portions of the disks that are close to the side surfaces of the resistors of the measuring circuit have close to the same potential across the thickness of the ends, while the side surface of the resistor that is close to the inner ends of the shielding disks, has a potential distribution close to linear, which varies along the height corresponding to the thickness of the disk. As a result, even an infinite increase in the ratio R/d will not lead to a decrease in the leakage of capacitive currents to zero.

A simple design solution for the high-voltage arm of the voltage divider (this solution can also be applied to the low-voltage arm of the voltage divider) is to simultaneously increase the R/d ratio and reduce the thickness of the shield disks. This solution is described in [23]. The essence of the solution is that instead of sectioning the areas of the high-voltage arm with shielding disks with gas or liquid insulation between them, capacitance graded insulation with thin layers of solid (liquid, gaseous) dielectric and thin layers of

conductive foil between them should be used between the shielding disks. This structure of the insulation of the high-voltage arm of the voltage divider practically makes it impossible for external electric fields to penetrate into the area of the lumped elements of the measuring circuit of the voltage divider, as a result of which such a voltage divider becomes minimally sensitive to the parasitic capacitances of the structural components of the high-voltage arm to external objects and to neighboring sections.

Another advantage of using capacitance graded insulation between shielding disks is that the surface area of the electrodes on which charges are formed (the area of the ends of the electrodes), which create parasitic capacitances on external objects and neighboring structural elements of the high-voltage arm, is reduced. As a result, such capacitances are reduced, and the potential of the voltage applied to the divider is distributed more linearly vertically along the ends of the shielding disks and the ends of the conductive covers of the capacitance graded insulation (both externally and internally, near the lumped elements of the high-voltage arm). If it is necessary to increase the capacitance of the shielding circuit, it is easy to provide through cylindrical holes in the capacitance graded insulation, in which the lumped elements of the shielding circuit (parallel to the lumped elements of the measuring circuit) can be placed, which will also be shielded from the influence of external electric fields.

Since the measuring circuit of lumped elements between two adjacent shielding disks will be shielded by capacitance graded insulation, the distribution of potentials on the inner ends of which will be close to the voltage distribution along, for example, resistive elements of the measuring circuit, it becomes possible to unify individual segments of the high-voltage arm and create them separately manufactured blocks with electrically disconnected measuring and shielding circuits. Such modules can be connected in the future into a high-voltage structure designed for almost any voltage, similar to the arrangement of capacitor columns in capacitive voltage transformers (for example, NDE type). The low-voltage arm of such modular voltage dividers is better performed with a built-in analog-to-digital converter in order to get rid of the electrical connection between the primary and secondary circuits, as well as for convenient integration of such voltage dividers into digital control systems of substations and power facilities (Smart Grid). .

Verification of the mathematical model. In order to verify the above-mentioned assumptions regarding the influence of the structure of the high-voltage arm of the voltage divider on its accuracy of large-scale high-voltage conversion, the mathematical model in Fig. 5 was changed. In the new model (Fig. 6), the distance between the shielding disks was increased, and capacitance graded insulation with copper covers 0.5 mm thick was placed between them (this thickness was chosen for reasons of reducing the volume of finite elements in the problem), as a dielectric material 2 mm thick fiberglass with relative dielectric permittivity of 5.5 was selected for capacitance graded insulation.

Also, the lumped elements of the high-voltage arm were represented by resistors in the form of cylindrical tubes (wall thickness 0.1 mm) with taps located one by one between adjacent shielding disks (film cylindrical resistors with a bifilar shape of the conducting part on the side surface were modeled). The conductivity of the material of the resistors was chosen to ensure that a direct current of 1 mA flows through it.

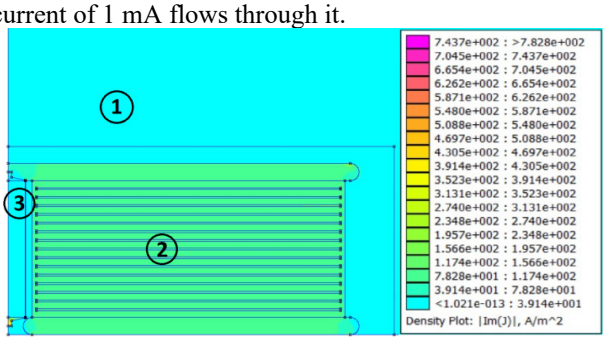

Fig. 6. The result of simulation of the density distribution of capacitive currents in the module with capacitance graded insulation of the high-voltage arm of the voltage divider at frequency of 1 MHz: 1 – area of air; 2 – area of capacitance graded insulation; 3 – resistor of the active part

On the high-voltage electrode of the mathematical model, the limiting condition of the potential of 10 kV was created. Due to the limitation of available computing power, the authors considered only 1 section of the voltage divider (one module) in the calculation. The distance from the side surface of the resistor of the active part to the inner end of the capacitance graded insulation was chosen in such a way as to ensure the smallest difference between the current entering the measuring circuit and the current leaving it. During the simulation, the radius of the hemispherical grounded surface, in the center of which the high-voltage arm of the voltage divider was simulated, was changed – from 3000 mm to 200 mm (in reality, when measuring high voltage, the distance from the voltage divider to grounded objects is much greater than the smallest value of the range). The currents at the input to the resistor of the high-voltage arm and the currents at the output of the resistor were determined by integrating the current density along the corresponding lines of the model based on the results of the numerical calculation, in accordance with (3).

The result of the simulation is a graph (Fig. 7) of the dependence of the current difference Δ at the input and at the output of the high-voltage arm of the voltage divider, which determines the losses in the high-voltage arm, in accordance with expression (4), and which change with the change in the radius r of the grounded surface around the model.

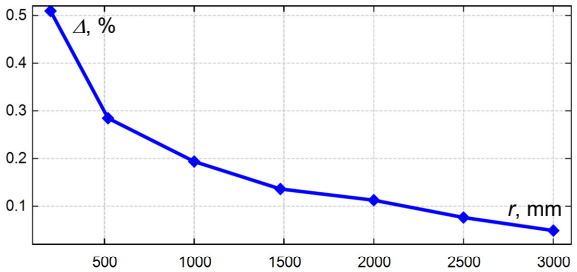

Fig. 7. Dependence of the difference in currents in the high-voltage arm of the voltage divider when the parasitic capacitances change on grounded surfaces (when changing the radius of the grounded surface) for current frequency of 1 MHz

Analysis of results. Analysis of the graph according to Fig. 7 shows the slowly increasing error of the scale transformation of the voltage divider in the range from 3000 mm to 200 mm radius of the grounded hemispherical surface around the model. Such a range can be considered a

very extended range, affecting stray capacitance changes that occur between shielding disks or capacitance graded insulation covers and grounded surfaces (in practice, grounded surfaces are not that close to voltage dividers).

When the radius of the grounded surface decreases, the non-uniform distribution of potentials along the inner ends of the capacitance graded insulation covers changes slowly, and therefore, the leakage currents from the lumped elements (resistors of the measuring circuit) of the active part through parasitic capacitances to the conductive surfaces of the shielding circuit change slightly. It should be noted that different areas of the side surfaces of the lumped elements (resistors) of the active part can be both surfaces of leakage of parasitic capacitive currents, and surfaces through which parasitic capacitive currents flow into these surfaces from the conductive surfaces of the shielding circuit, which are under a higher potential. The integral sum of inflowing and outflowing currents should approach zero with the same distribution of potentials along the surface of the resistor of the measuring circuit and along the inner ends of the capacitance graded insulation between the shielding disks. As an example of such a distribution of capacitive currents the graph (Fig. 8) can be considered, on which you can see the distribution of the density of currents flowing into the side surface of the resistor and currents flowing from this surface.

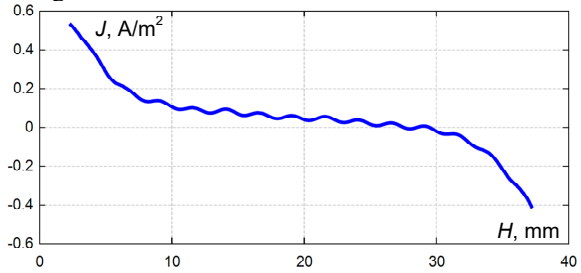

Fig. 8. Dependence of capacitive current density on lateral resistor surface on the height of the capacitance graded insulation covers (current frequency is 1 MHz)

In Fig. 8, it can be seen that the density of capacitive currents J changes non-linearly with an increase in the coordinate H according to the height of the side surface of the resistor, and at a height of about 25-30 mm, it changes its sign to the opposite. This means that in the lower part of the lateral surface of the resistor, capacitive currents flow into this surface, and in the upper part, they flow out (theoretically, it is possible to choose the location of the resistor in the model in such a way that the integrated capacitive currents flowing in and out of the resistor are equal to zero). The wavy shape of the dependence curve corresponds to the coordinates at the extremes of the vertical location of the ends of the capacitance graded insulation covers. Accordingly, an increase in the density of the arrangement of covers will lead to the leveling of such a curve.

However, the structural features of the section structure of the high-voltage arm of the voltage divider with real lumped elements (resistors) never make it possible to equalize such parasitic currents, only allow to reduce the difference between them to an acceptable value. But what is more important is not the reduction to zero of such a difference, but the stabilization of such a difference when changing the values of parasitic capacitances to grounded surfaces and surfaces under a different potential around the voltage divider. Increasing the total capacitance in the shielding circuit due to the arrangement of capacitors parallel to the capacitance graded insulation (for example, in the cylindrical holes of the capacitance graded insulation, with inclusions between the shielding disks) allows to practically proportionally reduce the influence of external parasitic capacitances on the voltage distribution along the high-voltage arm for a wider range of input voltage frequencies. That is, in order for the high-voltage arm of the voltage divider, which consists of a large number of sections segmented by shielding disks (the same type of modules with capacitance graded insulation and an electrically disconnected section of the lumped elements of the measuring circuit), the distribution of potentials on the conductive surfaces close to the elements of the measuring circuit is still preserved more stable and uniform (and to get rid of the need for electrical connection of measuring and shielding electrical circuits on each segment or individual sections, which is characteristic of modern design solutions used in voltage dividers), it is necessary to increase the total capacitance of the sections of the shielding circuit of the corresponding segments (modules), to increase the number of layers of capacitance graded insulation between the shielding disks. Since such an increase in capacitance due to the geometric properties of the structural elements of the high-voltage arm modules, or due to the properties of the relative dielectric constant of the materials, has its limits, it is possible to increase the capacitance in the area of the shielding circuit only by adding lumped elements of a capacitive nature (capacitors) in parallel to the capacitance graded insulation. It is also possible to slightly (several times) increase the capacitance of the shielding circuit of the high-voltage arm of the voltage divider by increasing the outer radius of the shielding disks. An increase in the number of covers (a decrease in the thickness of the insulation between them) has a slight effect on the total capacitance of the high-voltage arm, but it significantly affects the uniformity of the potential distribution near the lumped elements of the measuring circuit (which can be seen by comparing the results of Table 1 and the graph in Fig. 7). It is also possible to reduce the influence of leakage of capacitive currents on the distribution of potentials on the lumped elements of the measuring circuit by reducing their resistance, but this will lead to an increase in heat losses in the active part, as a result of which the structure of the active part will be complicated and the stability of the voltage divider characteristics will deteriorate.

Conclusions.

1. The existing design features of the structure of high-voltage dividers do not allow their use in open switchgears for the purpose of determining all power quality indicators due to the complex distribution of parasitic capacitances and inductances.

2. The division of the electric circuit of the high-voltage arm of the voltage divider into independent electric branches (measuring and shielding) makes sense only in the case when the total conductivity of the shielding branch is much higher and ensures the distribution of electric field potentials along the measuring branch is close to uniform.

3. By means of mathematical modeling, the dependence of the large-scale transformation error of the high-voltage divider on the geometric ratios of the structural elements of the shielding circuit was determined, which allows to vary the structure of the high-voltage arm of the voltage divider to expand the frequency range of the input voltage.

4. The analysis of the proposed mathematical model of the high-voltage divider proves the effectiveness of using the capacitance graded insulation voltage divider in the shielding circuit of the high-voltage arm of the voltage divider. At the same time, even at frequency of 1 MHz of the input voltage, the stability of the coefficient of scale transformation of the applied voltage is ensured with significant changes in the parasitic capacitances of the structural elements to external objects and to each other.

5. The application between the shielding disks of the high-voltage arm of the capacitance graded insulation allows to significantly reduce the effect on the large-scale voltage transformation coefficient of the parasitic capacitors on the grounded surfaces of the structural elements, and in addition, allows to switch to a unified sectioned structure of the high-voltage arm of the voltage divider, as a result of which the manufacture of voltage dividers can to be carried out serially.

Conflict of interest. The authors of the article declare that there is no conflict of interest.

REFERENCES

1. Anokhin Y.L., Brzhezytskyi V.O., Haran Ya.O., Masliuchenko I.M., Protsenko O.P., Trotsenko Ye.O. Application of high voltage dividers for power quality indices measurement. *Electrical Engineering & Electromechanics*, 2017, no. 6, pp. 53-59. doi: https://doi.org/10.20998/2074-272x.2017.6.08.

2. Li D., Liu K., Lei M., Zhou F., Yue C., Yu J. Study on the ratio change measurement of 1000 kV HVDC divider based on improved DC voltage summation method. *High Voltage*, 2020, vol. 5, no. 2, pp. 202-208. doi: https://doi.org/10.1049/hve.2019.0127.

3. Li D., Du B., Zhu K., Yu J., Liang S., Yue C. Optimization of DC Resistance Divider Up to 1200 kV Using Thermal and Electric Field Analysis. *Energy Engineering*, 2023, vol. 120, no. 11, pp. 2611-2628. doi: https://doi.org/10.32604/ee.2023.028282.

4. Xie S., Mu Z., Ding W., Wan Z., Su S., Zhang C., Zhang Y., Xia Y., Luo D. Development of Broadband Resistive–Capacitive Parallel–Connection Voltage Divider for Transient Voltage Monitoring. *Energies*, 2022, vol. 15, no. 2, art. no. 451. doi: https://doi.org/10.3390/en15020451.

5. Zheng J., Li B., Zha K., Guo N., Wang L. Equipotential shielding voltage sensor for contact measurement of transient voltage in EHV/UHV power grids. *High Voltage*, 2021, vol. 6, no. 2, pp. 291-301. doi: https://doi.org/10.1049/hve2.12016.

6. Galliana F., Caria S.E., Roccato P.E. Towards a traceable divider for composite voltage waveforms below 1 kV. *Electrical Engineering*, 2022, vol. 104, no. 2, pp. 1121-1130. doi: https://doi.org/10.1007/s00202-021-01368-5.

7. Kovacevic U.D., Stankovic K.D., Kartalovic N.M., Loncar B.B. Design of capacitive voltage divider for measuring ultrafast voltages. *International Journal of Electrical Power & Energy Systems*, 2018, vol. 99, pp. 426-433. doi: https://doi.org/10.1016/j.ijepes.2018.01.030.

8. Thümmler T., Marx R., Weinheimer C. Precision high voltage divider for the KATRIN experiment. *New Journal of Physics*, 2009, vol. 11, no. 10, art. no. 103007. doi: https://doi.org/10.1088/1367-2630/11/10/103007.

9. Shipu W., Wenlong P., Zhining Y., Kejie Z., Xixiu W. Study on the reliability of new kind of ±1 100 Kv DC voltage divider under the action of impulse voltage. *The Journal of Engineering*, 2019, vol. 2019, no. 16, pp. 2575-2579. doi: https://doi.org/10.1049/joe.2018.8815.

10. Havunen J., Hällström J. Reference switching impulse voltage measuring system based on correcting the voltage divider response with software. *IEEE Transactions on Instrumentation and Measurement*, 2021, vol. 70, pp. 1-8. art. no. 1006008. doi: https://doi.org/10.1109/tim.2021.3063753.

11. Luo Y., Guo B., Qian B., Xu L., Zhang F., Li F., Feng X. Method to Evaluate the Resistance–Capacitance Voltage Divider and Uncertainty Analysis. *Energies*, 2021, vol. 14, no. 22, art. no. 7744. doi: https://doi.org/10.3390/en14227744.

12. Jiang H., Pischler O., Schichler U., Havunen J., Hällström J., Merev A., Dedeoglu S., Özer S., Meisner J., Passon S., Gerdinand F. Prequalification of capacitors for high-precision voltage dividers. *22nd International Symposium on High Voltage Engineering (ISH 2021)*, 2021, pp. 309-314. doi: https://doi.org/10.1049/icp.2022.0031.

13. Abdel Mageed H.M., Salah Eldeen R.S. Adapted Technique for Calibrating Voltage Dividers of AC High-Voltage Measuring Systems. *MAPAN*, 2020, vol. 35, no. 1, pp. 11-17. doi: https://doi.org/10.1007/s12647-019-00334-8.

14. Lee S.H., Yu K.M., Choi J.Y., Jang S.M. Low-Uncertainty Equality Between the Voltage-Dividing and Resistance Ratio of a DC Resistive High Voltage Divider. *Journal of Electrical Engineering & Technology*, 2019, vol. 14, no. 4, pp. 1789-1795. doi: https://doi.org/10.1007/s42835-019-00157-2.

15. Li Q., Wang L., Zhang S., Tang Y., Xu Y. Method to Determine the Ratio Error of DC High-Voltage Dividers. *IEEE Transactions on Instrumentation and Measurement*, 2012, vol. 61, no. 4, pp. 1072-1078. doi: https://doi.org/10.1109/TIM.2011.2178672.

16. Hrbac R., Kolar V., Bartlomiejczyk M., Mlcak T., Orsag P., Vanc J. A development of a capacitive voltage divider for high voltage measurement as part of a combined current and voltage sensor. *Elektronika ir Elektrotechnika*, 2020, vol. 26, no. 4, pp. 25-31. doi: https://doi.org/10.5755/j01.eie.26.4.25888.

17. Havunen J., Passon S., Hällström J., Meisner J., Schlüterbusch T.C. Empirical Characterization of Cable Effects on a Reference Lightning Impulse Voltage Divider. *IEEE Transactions on Instrumentation and Measurement*, 2023, vol. 72, pp. 1-9. doi: https://doi.org/10.1109/TIM.2023.3276028.

18. Li B., He Y., Wang L., Cao M., Fu Z., Zhang H. Calibration Method of a Wideband AC Resistance Voltage Divider Based on an Equivalent Model. *Sensors*, 2023, vol. 23, no. 16, art. no. 7181. doi: https://doi.org/10.3390/s23167181.

19. Pan Feng, Xiao Yong, Lin Guoying, Xiao Xia, Shuai Hang. Analysis of the influencing factors for the 500 kV DC voltage reference divider used for on-site calibration. *2015 12th IEEE International Conference on Electronic Measurement & Instruments (ICEMI)*, 2015, pp. 25-29. doi: https://doi.org/10.1109/ICEMI.2015.7494180.

20. Boyko M.I., Syomkin S.O. Investigation of amplitude-temporal characteristics of a high-voltage resistive voltage divider. *Electrical Engineering & Electromechanics*, 2019, no. 4, pp. 59-68. doi: https://doi.org/10.20998/2074-272X.2019.4.09.

21. Brzhezitsky V.O., Haran Y.O., Trotsenko Y.O., Protsenko O.R., Derzhuk A.O., Dixit M.M. Ultimate effect of non-identity of resistive elements of high-voltage arm on frequency characteristics of broadband voltage divider (analytical research). *Electrical Engineering & Electromechanics*, 2023, no. 3, pp. 52-58. doi: https://doi.org/10.20998/2074-272X.2023.3.08.

22. Brzhezitsky V.O., Haran Y.O., Derzhuk A.O., Protsenko O.R., Trotsenko Y.O., Dixit M.M. Ultimate effect of non-identity of capacitive elements of high-voltage arm on frequency characteristics of voltage divider (analytical research). *Electrical Engineering & Electromechanics*, 2021, no. 4, pp. 46-52. doi: https://doi.org/10.20998/2074-272X.2021.4.06.

23. Haran Y.O., Trotsenko Y.O., Protsenko O.R. *High-voltage wideband divider*. Patent UA, no. 155502, 2024.

Received 01.06.2024
Accepted 22.08.2024
Published 02.01.2025

Y.O. Haran[1], *PhD*,
Y.O. Trotsenko[1], *PhD, Assistant Professor*,
O.R. Protsenko[1], *PhD, Assistant Professor*,
M.M. Dixit[2], *Assistant Professor,*
[1] National Technical University of Ukraine
«Igor Sikorsky Kyiv Polytechnic Institute»,
37, Prospect Beresteiskyi, Kyiv-56, 03056, Ukraine,
e-mail: y.garan@kpi.ua (Corresponding Author)
[2] Vishwaniketan Institute of Management Entrepreneurship and Engineering Technology, India.

How to cite this article:
Haran Y.O., Trotsenko Y.O., Protsenko O.R., Dixit M.M. The impact of parasitic capacitances on the accuracy of scale transformation of high-voltage dividers. *Electrical Engineering & Electromechanics*, 2025, no. 1, pp. 65-72. doi: https://doi.org/10.20998/2074-272X.2025.1.09

UDC 621.3.014.14: 537.528: 533.9.08: 628.16.08: 621.317 https://doi.org/10.20998/2074-272X.2025.1.10

N.A. Shydlovska, S.M. Zakharchenko, M.F. Zakharchenko, M.A. Kulida, S.A. Zakusilo, R.A. Yakovenko

Distribution of volumes of plasma channels components between metal granules in working liquids

Introduction. *Expanding the capabilities of a number of modern technologies and improving quality of their products require detailed spark and plasma erosion processes control in metal granules layers (MGL).* ***Problem.*** *Traditional measurement of exclusively electrical parameters of these processes, even in the case of multi-electrode systems, provides only a general vision, not allowing monitoring processes in individual plasma channels. Optical control methods make it possible to simultaneously have information about almost every plasma channel in the MGL. The* ***aim*** *of the article is to study the characteristic components of plasma channels arising as a result of the flow of discharge currents in the MGL and to establish the laws of distribution of their volumes and their ratios.* ***Methodology****. During the experiments, photographs of plasma channels resulting from the flow of discharge current pulses between Al granules immersed in distilled water were obtained. Using the specialized ToupView program, the volumes of equivalent ellipsoids of rotation, approximating the colored halos and white cores of the plasma channels were determined. Discrete distributions of the volumes of the halo and cores of plasma channels, as well as their ratios were constructed both with and without procedures for screening out «anomalous» results. The efficiency of approximation of discrete distributions obtained in practice by continuous theoretical distributions Weibull, Rosin-Rammler and log-normal was estimated.* ***Results.*** *It is shown that of all the considered theoretical distributions of halo and cores of plasma channels volumes, as well as their ratios, the most adequate is the log-normal one.* ***Originality.*** *For the first time distributions of volumes of halo and cores of plasma channels were studied and their comparative analysis with the size distributions of erosion particles and dimples on the surface of Al granules was given.* ***Practical significance.*** *Taking into account the new obtained results, a technique for constructing distributions of volumes of halo and cores of plasma channels and determining their parameters has been developed.* References 53, figures 7, tables 5.

Key words: **plasma channels, spark, discharge current, statistical distributions, metal granules, erosion particles.**

Вступ. *Розширення можливостей та підвищення якості продукції іскроерозійних технологій потребує залучення не тільки електричних, а і оптичних методів контролю процесів.* ***Проблема.*** *Створення методів керування властивостями іскроерозійних частинок на основі даних оптичних вимірювань потребує вирішення декількох науково-практичних задач.* ***Мета.*** *Визначення законів розподілу об'ємів кольорових гало та білих іскрових ядер плазмових каналів, які виникають у шарі гранул металів в результаті протікання імпульсних розрядних струмів.* ***Методологія.*** *Аналіз якості апроксимації отриманих в ході експериментів розподілів об'ємів складових плазмових каналів низкою теоретичних розподілів.* ***Отримані результати.*** *Найбільш адекватним серед усіх розглянутих теоретичних законів, що описують розподіли об'ємів гало і ядер плазмових каналів, а також їхніх відношень, є логарифмічно-нормальний.* ***Оригінальність.*** *Вперше досліджено розподіли об'ємів гало і ядер плазмових каналів та наведено їх порівняльний аналіз з розподілами розмірів ерозійних частинок і лунок на поверхні гранул Al.* ***Практична значимість.*** *Розроблено методику побудови розподілів об'ємів гало і ядер плазмових каналів.* Бібл. 53, рис. 7, табл. 5.

Ключові слова: **плазмові канали, іскра, розрядний струм, статистичні розподіли, металеві гранули, ерозійні частинки.**

Introduction and research problem definition. The formation of plasma channels as a result of the flow of pulsed discharge currents between the surfaces of adjacent metal and alloy granules in their layers, which are in working fluids, is the electrophysical basis of a number of technological processes. The most common of them can be classified into four main groups.

The first includes the production of microdispersed powders of metals and alloys with special properties: heat-resistant and refractory [1], hard [2], soft magnetic [3], amorphous [4, 5], with shape memory [6], corrosion-resistant [7], etc. [8, 9]. The second includes electric discharge sintering of metal powders under pressure [10]. The third is the production of nanodispersed hydrosols of biocidal metals (*Ag*, *Cu*, *Zn*) for use in veterinary medicine [11] and biogenic metals (*Fe*, *Mg*, *Mn*, *Co*, *Mo*) for use in crop production [12]. The fourth is the production of *Al* and *Fe* hydroxides for purification [13] and disinfection [14] of natural waters, including for the needs of thermal and nuclear power engineering [15].

The key parameters of discharge pulses: their duration [16], number of modes [17], average power over the pulse time [18], amplitude and shape [19, 20] of the discharge current and voltage on the metal granules layers (MGL) together with the technological conditions of the above processes [21] determine the properties of the products obtained [22]. Until now, the basis for controlling the processes described above has been the control and maintenance within certain limits of the values of some parameters of discharge pulses averaged over a certain time: the amplitudes of current and voltage, their duration and repetition frequency, as well as the height of the MGL, the flow rate and the temperature of the working fluid in the discharge chamber [18, 21–23].

Depending on the ratio of the dimensions of the discharge chamber (DC) and the metal granules contained in it, their number in the active zone of the chamber can reach 100 thousand. Under such conditions, it is impossible to control at least one parameter of the discharge pulse in each individual plasma channel by traditional measurements of electrical quantities, even in the case of multi-electrode systems [24]. The large number of places of probable occurrence of plasma channels and the quasi-identity of conditions at each level

of the MGL height [21] are the basis for involving statistical methods for studying these processes [25].

Unlike measuring discharge current parameters, measuring plasma channel parameters by optical methods allows obtaining information about the vast majority of them simultaneously. The number of plasma channels that can be observed simultaneously depends on the number of granules in each observation direction, their packing density in the layer, and the transparency of the working fluid [26].

As is known, the flux of electromagnetic radiation in both the radio frequency and infrared, optical and ultraviolet ranges is proportional to the power of the electric current emitted in the plasma channel [27–33]. Therefore, by studying such components of the radiation flux as the size of the luminous areas, their energy luminosity and the radiation spectrum, it is possible to obtain information about the power emitted in each plasma channel, and knowing the dependence of the radiation flux on time, it is also possible to obtain information about the energy on which the size of the eroded metal particles and the productivity of their production depend [16, 22].

The correlation between the components of the radiation flux of plasma channels and the size of the eroded particles, as well as their dependence on the parameters of the discharge pulses, will form the theoretical basis of the laws of regulating the properties of particles by the parameters of the plasma channels. This is a difficult task, which is solved in several stages. At the first stage, it is necessary to determine the laws of volume distributions of the components of plasma channels in the MGL.

The aim of the work is to study the characteristic sections of plasma channels that arise as a result of the flow of discharge currents in the MGL, to establish the discrete and theoretical continuous laws of their volume distributions and their correlations obtained in practice, and to find the parameters of these laws.

Experimental methodology, equipment, modes and materials. The objects of research were spark cores of plasma channels between *Al* granules in distilled water formed as a result of the action of discharge currents, which had a continuous white emission spectrum and colored halos around them, which had a linear emission spectrum [26]. Halos are caused by streamer and leader channels [34–36] at the early stages of the evolution of plasma channels, and their emission can also be induced by ultraviolet radiation of spark cores. This issue is discussed in more detail in [26]. There is also a functional diagram of the laboratory equipment on which the experiments were conducted and a detailed description of its operation. Here we will give only a brief description of the equipment and its operating modes.

The thyristor discharge pulse generator provided a free aperiodic discharge of a working capacitor with capacitance of C=100 μF with fixed pulse repetition rate f=50 Hz. The inductance of the discharge circuit of the generator was L=2 μH, and the resistance of the resistive shunt R=3 Ω. The shunt was connected in parallel with the DC to reduce the probability of simultaneous current flow in the charging and discharging circuits of the generator due to the delay of the discharge process due to a stochastic increase in the resistance of the MGL. The average values of the amplitudes of the voltage pulses on the MGL were approximately U_m≈220 V, and the current in it I_m≈180 A. The average pulse duration τ was about 100 μs.

The A7E aluminum granules, the surface of which had previously undergone spark discharge treatment, had a quasi-spherical shape with a diameter of approximately 4 mm. The distance between the vertical AD0 grade aluminum electrodes in the DC was 52 mm. The height of the MGL was 30 mm, and its width was 22 mm. The water flow was directed from bottom to top and was approximately 12 ml/s, which ensured the stability of the process and removed erosion particles from the active zone of the DC without significant movement of the aluminum granules in it. To record images of the constituent plasma channels, a household webcam with a matrix of 640×480 pixels was used in video recording mode. The resulting video stream was then decomposed into separate frames, the images of the plasma channels on which were analyzed using the specialized ToupView program [37], which is freely available and is designed to work with digital optical cameras of microscopes and telescopes. The images of the cores and halos were approximated by ellipses of equivalent area, and the sizes of their major *2a* and minor *2b* axes were automatically calculated by the program. Then, the volumes of equivalent ellipsoids of rotation were calculated from them. This procedure is described in more detail in [26].

Optometric analysis of the volumes of the plasma channels components. One of the many frames obtained and processed using the above-described method is shown in Fig. 1. It shows the plasma channels existing during the discharge pulse between aluminum granules immersed in distilled water, which are in the dark, which is necessary to increase the contrast. The ellipses equivalent in area, which were used to approximate the projections of the spark cores of the plasma channels onto the plane of the webcam, are red in color, and their colored halos are blue. In [26] the continuous spectrum of white emission of spark cores and the linear blue-violet spectrum of emission of colored halo plasma channels containing aluminum atoms and their compounds with oxygen and hydrogen were substantiated. This makes it possible to determine the sizes of the corresponding zones in Fig. 1 by their brightness and color, although this process contains a certain element of subjective assessment. In the printed version of the article, the figures are presented in grayscale. Color versions are available on the website of the Journal «Electrical Engineering & Electromechanics».

The ToupView program automatically generates service labels: the designation of the ellipse (capital letter E), its serial number (for spark cores it is odd, starting with 1, and for color halos it is even, starting with 2), the values of the lengths of the major 2*a* and minor 2*b* axes of the ellipses, written through commas and units of measurement (in this case px – pixels). That

is, in a pair of serial numbers, the smaller odd number will correspond to the equivalent in area ellipse projection of the spark core of the plasma channel, and the next even number will correspond to its color halo. Thus, 134 ellipses were obtained with the values of the lengths of their axes, which approximate, respectively, the spark cores and color halos of 67 plasma channels. This number is sufficient to speak about the approximation of the frequency of observation cases to their probability and to construct histograms of discrete distributions of plasma channel volumes obtained during experiments [25, 38, 39].

The width of the image in Fig. 1 corresponds to the width of the MGL in the DC (the electrodes are outside the frame), which is approximately 50 mm. At the same time, the width of the image in the ToupView program is 162 px. This means that one millimeter of a real object corresponds to approximately 3.2 px of the image in the ToupView program. This coefficient was used to convert the sizes of objects from pixels to millimeters in the Microsoft Office Excel 2003 program during further processing of the measurement results.

In [26] it is shown that to determine the volumes of the components of plasma channels under the above conditions, they can be represented by equivalent ellipsoids of rotation, the dimensions of the axes of which are located on their projections onto the plane of the webcam. The camera is located in a plane perpendicular to the planes of the electrode surfaces, i.e. parallel to the planes of flow of the vast majority of discharge currents in the MGL. Therefore, in most cases, from such a perspective, the true size of the axes of the equivalent ellipsoids of rotation is observed without distortion. And in the case of the coincidence of the directions of the corresponding axes of the spark core and color halo ellipsoids, their ratio, as well as the ratio of the volumes of the corresponding ellipsoids, do not depend on the observation perspective [26].

Unfortunately, from the analysis of a 2D image of plasma channels it is impossible to accurately determine which of the two axes of the projection of the equivalent ellipsoid is its axis of rotation or its projection. If the dimensions of the micro-roughness on the surface of the granules are significantly smaller than the distance between adjacent granules, it is more likely that the major axis of the ellipse $2a$ is the axis of rotation of the ellipsoid or its projection and the ellipsoid of rotation is «elongated». The volumes of the equivalent ellipsoids of the plasma channels in this case are denoted by the index a. This situation is more typical for the upper layers of the granules, in which the pressure on the granules is lower.

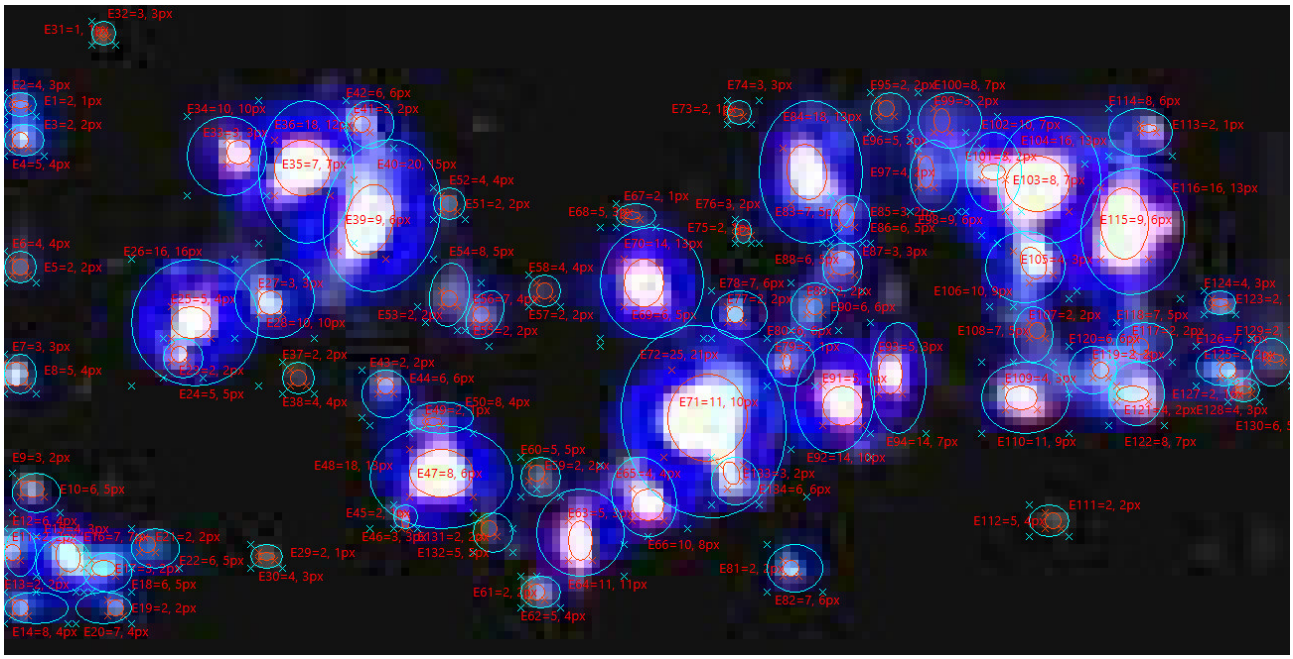

Fig. 1. Plasma channels between aluminum granules in water in the dark

In another case, when the dimensions of micro-roughnesses on the surface of the granules are commensurable to the distance between neighboring granules, with a higher probability the minor axis of the ellipse $2b$ is the axis of rotation of the ellipsoid or its projection and the ellipsoid of rotation is «flattened». In this case, the volumes of equivalent ellipsoids of the constituent plasma channels are denoted by the index b. This situation is more typical for the lower layers of the granules, in which the pressure on the granules is greater.

In real conditions, both options are possible, therefore, when analyzing the volumes of equivalent ellipsoids of rotation of the constituent plasma channels, calculations of their volumes were carried out for both cases (indexes a and b, respectively). The volume of the ellipsoid of rotation, equivalent to the volume of the spark core of the plasma channel (index s) for two cases of the position of the rotation axis (major axis $2a$ or minor axis $2b$) according to the well-known formula [40] was determined:

$$V_s = \begin{cases} V_{sa} = 4\pi a_L b_L^2/3, \text{ if } 2a - \text{axis of rotation;} \\ V_{sb} = 4\pi b_L a_L^2/3, \text{ if } 2b - \text{axis of rotation.} \end{cases} \quad (1)$$

The volumes of colored halos (denoted by the index L) were assumed to be the difference of the total volumes of plasma channels and their spark cores and were calculated for the two cases of the rotation axis position as:

$$V_L = \begin{cases} V_{La} = 4\pi\left(a_L b_L^2 - a_s b_s^2\right)/3, \text{ if } 2a - \text{rotation;} \\ V_{Lb} = 4\pi\left(b_L a_L^2 - b_s a_s^2\right)/3, \text{ if } 2b - \text{rotation.} \end{cases} \quad (2)$$

The ratios of the volumes of colored halos to the volumes of spark channels for two cases of the position of the rotation axis were calculated based on (1), (2) according to the expression:

$$V_L/V_s = \begin{cases} V_{La}/V_{sa} = \left(a_L b_L^2/a_s b_s^2\right) - 1, \text{ if } 2a - \text{rotation;} \\ V_{Lb}/V_{sb} = \left(b_L a_L^2/b_s a_s^2\right) - 1, \text{ if } 2b - \text{rotation.} \end{cases} \quad (3)$$

For two cases of the position of the rotation axis (coincides with the major axis $2a$ or coincides with the minor axis $2b$), the volumes of the rotation ellipsoids V_{sa} and V_{sb}, respectively, equivalent to the volumes of the spark cores of 67 plasma channels, (2) equivalent to the volumes of their color halos V_{La} and V_{Lb}, respectively, and (3) the ratios of the volumes of these regions of the channels V_{La}/V_{sa} and V_{Lb}/V_{sb}, respectively, were calculated by (1).

Statistical analysis of the distributions of the volumes of the components of plasma channels. For each sample of these volumes and their ratios with a total number of N elements, the following statistical moments were calculated: the mathematical expectation over the sample [41]:

$$M_S[V] = \frac{1}{N}\sum_{j=1}^{N} V_j , \quad (4)$$

the sample variance:

$$D_S[V] = \frac{1}{N}\sum_{j=1}^{N}\left(V_j - M_S[V]\right)^2 , \quad (5)$$

and the coefficient of variation for the sample:

$$\nu_S[V] = \sqrt{D_S[V]}/M_S[V] . \quad (6)$$

In the process of constructing discrete distributions of the above random variables, the following parameters were determined based on the measurement results: the minimum $V_{\min}$ and maximum $V_{\max}$ values of the corresponding volumes and their ratios by samples, the number of their values in each sample N, the number of intervals of discrete distributions n, the number of values in each interval N_j, the proportion in each interval $n_j=N_j/N$, the average value of the volume (or the ratio of volumes) $\overline{V}_{nj}$ in each j-th interval of discrete distributions, the mathematical expectation for the discrete distribution:

$$M_D[V] = \sum_{j=1}^{n} n_j \overline{V}_{nj} , \quad (7)$$

the variance according to the discrete distribution:

$$D_D[V] = \sum_{j=1}^{n} n_j\left(\overline{V}_{nj} - M_D[V]\right)^2 , \quad (8)$$

and the coefficient of variation for the discrete distribution:

$$\nu_D[V] = \sqrt{D_D[V]}/M_D[V] . \quad (9)$$

The rounded values of the above parameters are given in Table 1. The units of measurement of volumes and their mathematical expectations in Table 1 – mm^3, of variances of their distributions – mm^6, and the volume ratios and coefficients of variation are dimensionless quantities.

Table 1

Statistical parameters of sample volumes of plasma channels components and their ratios

Sample	$V_{\min}$	$V_{\max}$	N	$M_S[V]$	$D_S[V]$	$\nu_S[V]$	$M_D[V]$	$D_D[V]$	$\nu_D[V]$
V_{sa0}	0,02	17,57	67	0,96	6,20	2,61	1,78	4,24	1,16
V_{sa1}	0,02	6,26	66	0,70	2,05	2,03	0,94	1,80	1,42
V_{sa2}	0,02	2,80	61	0,32	0,29	1,65	0,39	0,22	1,21
V_{sb0}	0,02	19,34	67	1,17	8,36	2,47	2,09	5,76	1,15
V_{sb1}	0,02	7,77	66	0,89	3,41	2,07	1,16	2,73	1,42
V_{La0}	0,16	158,6	67	11,31	549,2	2,07	17,21	372,5	1,12
V_{La1}	0,16	66,73	66	9,08	223,8	1,65	10,81	174,8	1,22
V_{Lb0}	0,22	190,4	67	14,00	820,0	2,05	22,35	645,1	1,14
V_{Lb1}	0,22	88,11	66	11,32	353,9	1,66	14,11	300,6	1,23
$(V_{La}/V_{sa})_0$	1,96	143,0	67	21,79	499,9	1,03	22,26	489,3	0,99
$(V_{La}/V_{sa})_1$	1,96	74,00	65	18,62	167,5	0,70	18,68	155,1	0,67
$(V_{Lb}/V_{sb})_0$	2,70	92,30	67	19,92	239,4	0,78	19,93	224,6	0,75
$(V_{Lb}/V_{sb})_1$	2,70	63,00	66	18,79	156,4	0,67	18,77	150,0	0,65

As can be seen from Table 1, the statistical moments for samples (4) – (6) differ from the corresponding statistical moments for discrete distributions (7) – (9). This is due to the process of discretization of distributions of relatively small numbers of sample elements. Statistical moments for samples are primary information, therefore they more accurately reflect the parameters of the distributions.

When determining the optimal number of intervals of discrete distributions n [42], it is recommended to use the ratio $n \le \text{int}\left[\sqrt{N}\right]$. In the case of a uniform distribution, this ratio provides approximately the same number of distribution intervals and random variable values in each of them, which leads to close values of discretization errors both for intervals and for values in them. In addition, it is recommended that the number of intervals of the discrete distribution be in the range from 6 to 20. If the distribution is quasi-symmetric, then it is better to choose an odd number of its intervals. In the distributions considered here, N lies in the range from 61 to 67 (Table 1), therefore, taking into account the above, n=7 was chosen for all distributions.

When constructing discrete distributions based on the results of measurements of random variables, an important operation is to screen out «anomalous» values of the input data [43]. The distributions of the measurement results of any variable obtained in practice under quasi-identical conditions may differ significantly from the theoretical distributions of a random variable for such conditions. This may be due to a number of reasons.

Firstly, due to measurement errors, as a result of which some values of a random variable differ significantly from its mathematical expectation. Secondly, due to an insufficient number of measurements, which leads to inaccurate determination of the mathematical expectation, dispersion and other moments and parameters of the distributions of a random variable. Thirdly, due to an uncontrolled change in the parameters of real processes that affect the measurement results and violate the quasi-identicality of the experimental conditions. This can lead to the appearance of a certain number of «anomalous» measurement results, which make it impossible to qualitatively approximate discrete distributions obtained in practice by continuous theoretical distributions.

Several statistical criteria for screening out «anomalous» measurement results are known. Among them: Grubbs criteria [44], $2m$ – $3m$, Wright (another name 3σ) [45], $\acute{Z}$, Dixon, Charlier, Student coefficients, Irwin, etc. [43, 46]. But none of them guarantees screening out all «anomalous» results and preserving all error-free, and even more so eliminating all areas with zero values in the body of experimental distributions. In [43] it is shown that one of the most effective criteria for screening out «anomalous» measurement results is Wright criterion, which is why we used it in our studies.

In Table 1 – 5, the index «0» denotes the input samples without screening out «anomalous» measurement results. In Tables 1 – 5, their parameters are given in shaded rows. The index «1» denotes the samples in which screening out «anomalous» measurement results occurred in one iteration according to the Wright criterion. The index «2» denotes the sample in which screening out «anomalous» measurement results occurred in two iterations until all areas with zero values in the body of the experimental distributions were eliminated.

The screening out of «anomalous» measurement results according to the Wright criterion narrows the range of values that most of the considered random variables can take by more than 2 times, and screening out until all areas with zero values are eliminated by more than 6 times (Table 1). In all the considered samples, the largest values of the measured variables were screened out. The probability of measurement error of the largest values is much smaller than that of the smallest. When performing the screening operations, the mathematical expectations and variances, both for samples and for discrete distributions, as well as the coefficients of variation for samples, are noticeably reduced. These facts suggest that the values are screened out incorrectly.

The distributions of the volumes of spark cores, colored halos and their ratios are shown in Fig. 2 – 7. The discrete distributions obtained directly as a result of experiments are represented by histograms. The theoretical continuous distributions obtained from them, the values of the parameters of which are found by the method of statistical moments of the input samples, are represented by curves. The distributions for the cases when the major axes of the ellipsoids are their axes of rotation are shown in blue, and when they are minor are shown in red. The points at which the values of the theoretical distributions were calculated are marked in Fig. 2 – 7 with triangles with vertices at the top for cases when the major axes of the ellipsoids are their axes of rotation, and with the vertex at the bottom – when they are minor. Figures 2, 4, 6 present the distributions for all arrays of the obtained data without prior screening, and Fig. 3, 5, 7 – for data that have undergone preliminary screening according to the Wright criterion.

From the comparison of the pairs of Fig. 2 and Fig. 3, Fig. 4 and Fig. 5 and Fig. 6 and Fig. 7 it is seen that in all the considered cases, screening out of «anomalous» measurement results according to the Wright criterion does not lead to an improvement in the appearance of the distributions. Moreover, screening of the results significantly distorts the appearance of the distributions of the ratios of the volumes of colored halos to spark cores in Fig. 7 in comparison with Fig. 6.

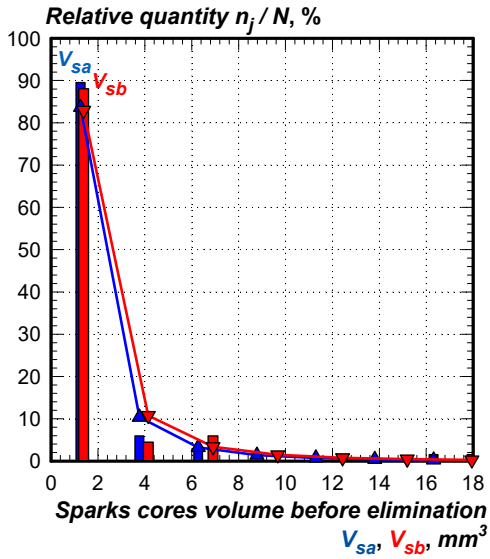

Fig. 2. Distributions of spark cores volumes before screening out

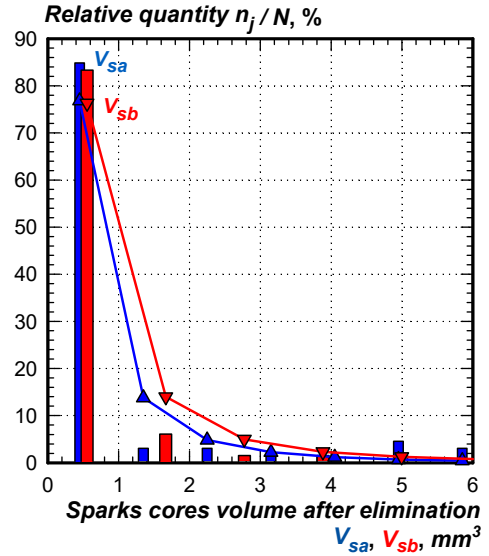

Fig. 3. Distributions of spark cores volumes after screening out

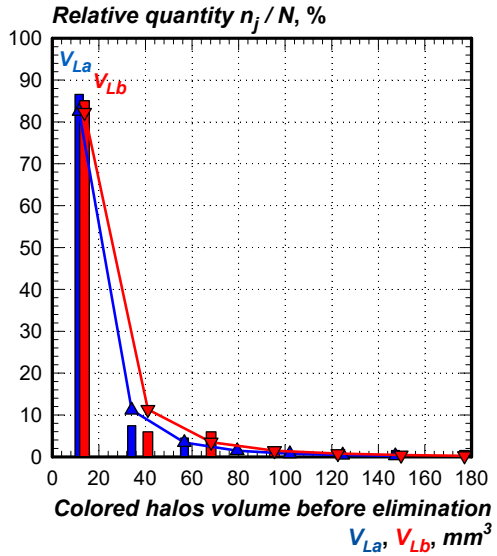

Fig. 4. Distributions of colored halo volumes before screening out

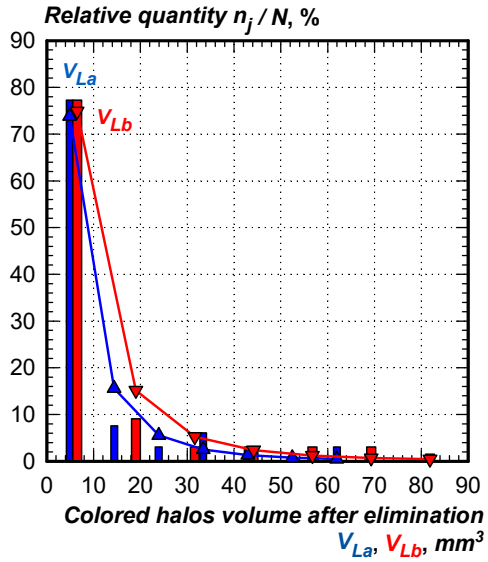

Fig. 5. Distributions of colored halo volumes after screening out

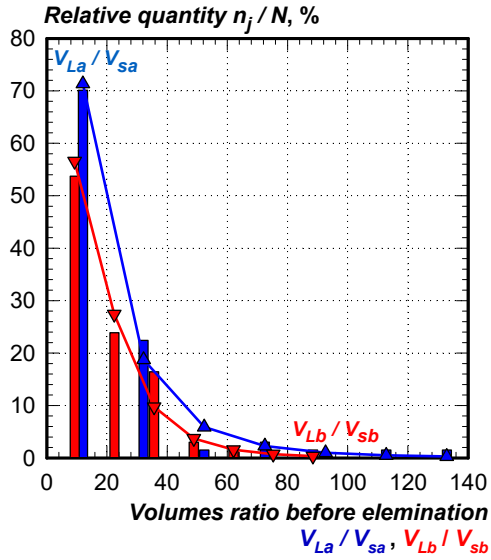

Fig. 6. Distributions of ratios of volumes of colored halos to volumes of spark cores before screening out

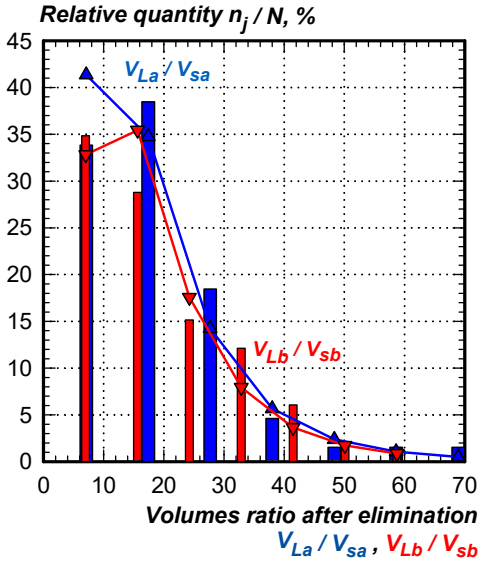

Fig. 7. Distributions of ratios of volumes of colored halos to volumes of spark cores after screening out

All distributions in Fig. 2, 4, 6 have similar shapes, which suggests that they can be described by one theoretical distribution with different parameter values. The volume distributions in which the equivalent ellipsoids were considered «flattened», i.e. the rotation axis was small (denoted by the index *b*) are more monotonic and match the theoretical distributions better than the volume distributions in which the equivalent ellipsoids were considered «elongated», i.e. the rotation axis was large (denoted by the index *a*). This is best seen in Fig. 6 for the distributions of the ratios of the volumes of colored halos to spark cores. This suggests that under the considered conditions, most of the components of the plasma channels are more correctly approximated by «flattened» rotation ellipsoids than by «elongated» ones.

The values of the volumes of the «flattened» ellipsoids in Fig. 2 – 5 were always slightly larger than the values of the volumes of «elongated» ellipsoids under the same conditions, which follows from the analysis of (1), (2). As for the ratios of the volumes of colored halos to spark cores (Fig. 6, 7), the opposite trend is observed there.

Approximation of the distributions of the volumes of the components of plasma channels and their ratios by theoretical distributions. Based on the type of discrete distributions, the values of their coefficients of variation, and the most typical cases of application of theoretical distributions [47], the following were considered to find the best one: log-normal, Weibull, and Rosin-Rammler [48].

The probability density of a random variable V according to the log-normal law is determined [49]:

$$f_{LN}(V)=\frac{1}{V\alpha\sqrt{2\pi}}\exp\left[-\frac{(\ln V-\mu)^2}{2\alpha^2}\right], \qquad (10)$$

where $\alpha=\sqrt{\ln\left[D[V]/M^2[V]+1\right]}$ is the standard deviation of the natural logarithms of a random variable;

$\mu = \ln\left[M[V] \Big/ \sqrt{D[V] \Big/ M^2[V] + 1} \right]$ is the average of the natural logarithms of a random variable.

The probability density of a random variable V according to the Weibull distribution [50]:

$$f_W(V) = \begin{cases} \frac{w}{\lambda}\left(\frac{V}{\lambda}\right)^{w-1} \exp\left[-\left(\frac{V}{\lambda}\right)^{w}\right], & V \geq 0; \\ 0, & V < 0, \end{cases} \quad (11)$$

where w is the shape factor; λ is the scale factor.

The probability density of a random variable V according to the Rosin-Rammler distribution is determined [51]:

$$f_R(V) = \begin{cases} 1 - \exp\left[\ln(0{,}2) \cdot (V / P_{80})^m\right], & V \geq 0; \\ 0, & V < 0, \end{cases} \quad (12)$$

where P_{80} is the 80th percentile of the distribution; m is the distribution range parameter.

The theoretical distributions we have considered are given on the intervals of change of the random variable $V \in (0; +\infty)$ for (10) and on $V \in [0; +\infty[$ for (11) and (12), while the distributions obtained in the course of experiments are given on much smaller intervals (Table 1). Therefore, to ensure the value of 100 % of the distribution functions in the real intervals of change of their arguments, the probability density of each theoretical distribution law $f(V)$ in each case must be multiplied by the corresponding correction coefficients of the ranges:

$$k = 100\% \Big/ \int_{V_{\min}}^{V_{\max}} f(V) \mathrm{d}V . \quad (13)$$

Finding the optimal values of the parameters of the theoretical distribution laws was carried out using two main groups of methods: statistical moments and the least deviation of theoretical values from the experimental results [48].

Statistical moments methods, unlike the methods of the least deviation of theoretical values from the experimental results, give unambiguous results, and not an infinite number of groups of parameters of the distribution laws. Therefore, if possible, these methods should be preferred.

However, in situations where the number of sample elements is relatively small, as in our studies, it is very difficult to accurately calculate the values of the parameters of the Rosin-Rammler and Weibull distributions using the first group of methods. For example, it is almost impossible to accurately find the value of P_{80} using our samples. Then the second group of methods comes in handy. For each j-th interval of the discrete distributions obtained as a result of the experiments, the differences between the number of objects observed in it n_{jO} and the number of objects that should be in it according to the continuous theoretical distribution law n_{jE} were found. Using all the obtained differences in accordance with the selected optimization function, its value was calculated. Then, using the «Solver» add-in of the English-language program Microsoft Office Excel 2003, the search for optimal values of the parameters of the theoretical distribution laws was performed under the condition of the smallest value of the selected optimization function.

We used the following as such functions: sum of squared differences (SSD) of the values of the discrete and continuous theoretical distributions obtained during the experiment:

$$S = \sum_{j=1}^{n} \left(n_{jO} - n_{jE}\right)^2 , \quad (14)$$

Pearson Chi-squared consistency criterion [52]:

$$\chi_n^2 = \sum_{j=1}^{n} \left(n_{jO} - n_{jE}\right)^2 \Big/ n_{jE} , \quad (15)$$

and the average modulus of relative deviations of the values obtained during the experiments of the discrete and continuous theoretical distributions:

$$|\delta| = \frac{100\%}{n} \sum_{j=1}^{n} \left| \left(n_{jO} - n_{jE}\right) \Big/ n_{jO} \right| . \quad (16)$$

The SSD (14) is one of the oldest optimization functions in the processes of finding coefficients of approximating functions. It is very easy to use and does not require large amounts of calculations. However, it is necessary to pay attention to the shortcomings of the SSD as an optimization function and as a criterion of the quality of approximation. The SSD uses squares of absolute, not relative, estimates, therefore, the quality of approximations under the condition of the minimum value of the SSD will be higher in those areas where the approximating function has large values and lower in areas where its values are small. The dependence of the SSD on the number of its members makes it not universal when comparing approximations of discretely given dependencies with different numbers of elements.

Traditionally, the possibility of using continuous theoretical distributions to approximate discrete distributions obtained as a result of experiments was assessed using the Pearson Chi-squared consistency criterion (15). Therefore, its choice as an optimization function is quite logical. But criterion (15) is also not without its shortcomings. Although, unlike (14), criterion (15) has a denominator, in its numerator there is the square of the difference. That is, criterion (15), like (14) is not dimensionless and universal. In addition, like (14) it depends on the number of intervals of the discrete distribution.

Among all the expressions considered here for optimization functions and criteria for the quality of approximation (14) – (16), only the average modulus of relative deviations (16) is universal. It provides a relative estimate, is dimensionless and does not depend on the number of elements of the discrete dependence. When using it as an optimization function, it should be noted that the quality of approximation in areas with small values of the approximating function may be higher than in areas with its large values. This is due to the use of relative, not absolute, estimates.

The disadvantage of the group of methods of the least deviation of theoretical values from the results of experiments is the ambiguity of the obtained results, due to the fact that the number of equations, which

corresponds to the number of intervals of discrete distributions, is greater than the number of parameters of theoretical distributions. That is, the system of equations is redundant and can have an infinite number of solutions (combinations of the values of the parameters of theoretical distribution laws). This leads to different results obtained by different optimization functions for the same distributions (Tables 2 – 4). The parameter values obtained in this way may be inconvenient for further calculations and be far from the values determined by the physical content of the quantities under study.

For all thirteen samples (Table 1), the values of the range coefficients (13) and the Pearson Chi-squared consistency criterion (15), found by the methods of the smallest values of the SCR (14), Chi-squared (15) and the average modulus of relative deviations (16), as well as the parameters of the theoretical distribution laws are given in Table 2 – 4. For the Weibull distribution – in Table 2, Rosin-Rammler – in Table 3, log-normal distribution – in Table 4. The decision on the correspondence or inconsistency of the theoretical law with the experimental data was made using the classical method of rejecting or accepting the null hypothesis about the consistency of the frequencies of occurrence of a discrete random variable in the specified intervals of its distribution, which were obtained during the measurement, and the values of the theoretical density functions of the distributions of continuous random variables. The significance of the first-order error ξ of the rejection of the null hypothesis when it is true, that is, when the theoretical distribution is rejected, and in fact it is consistent with the experimental data, was set at the level of $\xi = 0.05$. The number of degrees of freedom of the Chi-squared distribution is determined by $\zeta = n–1$ and in the considered distributions is: $\zeta = 7–1 = 6$.

The value of the critical point of the Chi-squared distribution was calculated using the built-in function CHIINV(ξ; ζ) of the English-language program Microsoft Office Excel 2003 and for $\xi = 0.05$ and $\zeta = 6$ it is approximately $\chi_k^2 \approx 12.5916$. That is, if the values found by (15) are less than 12.5916, then with a significance level of the first-order error $\xi = 5$ %, the null hypothesis is not rejected and the theoretical distribution with the current parameters passes according to the Pearson Chi-squared consistency criterion (marked «pass» in Tables 2 – 4 and «p» in Table 5).

In cases where the values found by (15) are greater than $\chi_k^2 = 12.5916$, with a significance level of the first-order error $\xi = 5$ %, the null hypothesis is rejected and the theoretical distribution with the current parameters is failed according to the Pearson Chi-squared consistency criterion (marked «fail» in Table 2 – 4 and «f» in Table 5).

Table 2

Weibull distribution parameters found by least-value methods of three different optimization functions

Sample	min [S]					min [χ_n^2]					min [$\lvert\delta\rvert$]				
	w	λ	k, %	χ_n^2	p / f	w	λ	k, %	χ_n^2	p / f	w	λ	k, %	χ_n^2	p / f
V_{sa0}	0,3175	0,0413	4,7687	7,0	pass	0,3175	0,0413	4,7687	7,0	pass	0,2676	0,1033	8,8405	16,708	fail
V_{sa1}	0,2629	0,0222	20,466	17,0	fail	0,2629	0,0222	20,466	17,0	fail	0,2192	0,0625	27,132	22,287	fail
V_{sa2}	0,2629	0,0222	61,081	6,2162	pass	0,2629	0,0222	61,081	6,2162	pass	0,2629	0,0222	61,081	6,2162	pass
V_{sb0}	0,2417	0,0052	1,7299	7,9	pass	0,2417	0,0052	1,7299	7,9	pass	0,2117	0,0182	4,6001	14,974	fail
V_{sb1}	0,2565	0,025	16,193	14,6	fail	0,2565	0,025	16,193	14,6	fail	0,1805	0,0757	19,706	22,418	fail
V_{La0}	0,2417	0,0418	0,2072	5,2283	pass	0,2417	0,0418	0,2072	5,2283	pass	0,2417	0,4443	0,7664	13,015	fail
V_{La1}	0,152	0,0007	0,3723	7,3	pass	0,152	0,0007	0,3723	7,3	pass	0,1489	0,0752	1,5269	13,01	fail
V_{Lb0}	0,2220	0,0317	0,1664	5,2	pass	0,222	0,0317	0,1664	5,2	pass	0,2028	0,1163	0,4087	10,87	pass
V_{Lb1}	0,152	0,0007	0,2453	3,5411	pass	0,152	0,0007	0,2453	3,5411	pass	0,1608	0,0079	0,5841	5,2353	pass
$(V_{La}/V_{sa})_0$	1,3650	19,431	4,9005	5433,1	fail	0,5122	6,2985	1,8523	6,0046	pass	0,4049	5,2134	1,8523	7,8918	pass
$(V_{La}/V_{sa})_1$	0,0773	0,0303	0,772	26,01	fail	0,0773	0,0303	0,772	26,01	fail	0,1195	0,0259	0,9303	26,74	fail
$(V_{Lb}/V_{sb})_0$	1,0373	17,694	6,4297	4,3846	pass	0,9841	17,913	6,2926	4,0738	pass	0,8173	17,92	5,7197	5,3612	pass
$(V_{Lb}/V_{sb})_1$	0,0438	0,0205	0,5216	9,3733	pass	0,0438	0,0205	0,5216	9,3733	pass	0,0543	0,0181	0,6275	9,4	pass

Table 3

Parameters of the Rosin-Rammler distribution found by least-value methods of three different optimization functions

Sample	min [S]					min [χ_n^2]					min [$\lvert\delta\rvert$]				
	P_{80}	m	k, %	χ_n^2	p / f	P_{80}	m	k, %	χ_n^2	p / f	P_{80}	m	k, %	χ_n^2	p / f
V_{sa0}	0,1805	–2,386	1,7423	7,1642	pass	0,3056	–2,113	9,1709	4,7	pass	0,2109	–1,553	13,482	12,346	pass
V_{sa1}	0,0902	–2,151	5,7473	37,317	fail	0,0315	–1,586	3,21	14,3	fail	0,0688	–1,161	29,691	25,631	fail
V_{sa2}	0,0315	–1,586	11,352	2,9173	pass	0,0315	–1,586	11,352	2,9173	pass	0,0315	–1,586	11,352	2,9173	pass
V_{sb0}	0,2541	–2,365	3,1993	11,926	pass	0,3593	–1,987	12,585	6,9	pass	0,5663	–1,684	41,008	10,81	pass
V_{sb1}	0,0268	–2,032	0,4036	26,204	fail	0,0386	–1,577	3,2734	11,9	pass	0,0207	–1,321	3,2212	15,113	fail
V_{La0}	3,1312	–2,256	9,446	5,9963	pass	3,1485	–2,01	13,663	4,3	pass	2,0014	–1,535	14,892	10,414	pass
V_{La1}	0,3209	–1,759	1,7134	9,0664	pass	0,2343	–1,57	1,8828	6,7	pass	0,0545	–1,175	1,4054	12,782	fail
V_{Lb0}	4,7658	–2,172	17,249	6,0331	pass	9,3091	–2,054	64,144	5,0	pass	4,8744	–1,64	35,202	7,9189	pass
V_{Lb1}	0,6282	–1,774	3,2521	3,7653	pass	0,9564	–1,643	9,1006	2,9	pass	0,9436	–1,519	11,861	3,4959	pass
$(V_{La}/V_{sa})_0$	22,353	–3,877	140,96	19,576	fail	16,758	–2,465	143,2	4,861	pass	16,768	–2,225	153,39	5,925	pass
$(V_{La}/V_{sa})_1$	23,413	–4,757	274,1	3,6183	pass	21,604	–3,728	275,76	1,615	pass	21,751	–3,174	295,45	2,918	pass
$(V_{Lb}/V_{sb})_0$	14,942	–2,318	186,75	4,9948	pass	17,048	–2,613	195,52	4,663	pass	14,131	–2,215	183,03	5,269	pass
$(V_{Lb}/V_{sb})_1$	16,286	–2,381	289,31	1,8529	pass	17,945	–2,664	301,44	1,733	pass	16,182	–2,39	286,95	1,857	pass

Table 4

Parameters of the log-normal distribution found by least-value methods of three different optimization functions

Sample	min [S]					min [χ_n^2]					min [$\|\delta\|$]				
	α	μ	k, %	χ_n^2	p / f	α	μ	k, %	χ_n^2	p / f	α	μ	k, %	χ_n^2	p / f
V_{sa0}	8,6955	–103,7	$4\cdot10^{-31}$	7,309	pass	6,6476	–46,08	$1\cdot10^{-10}$	4,7	pass	6,2159	–17,82	0,1082	13,442	fail
V_{sa1}	18,404	–395,3	$9\cdot10^{-100}$	39,943	fail	49,085	–1365	$3\cdot10^{-168}$	14,23	fail	52,117	–394,6	$1\cdot10^{-12}$	24,06	fail
V_{sa2}	0,9723	–1,541	263,58	9,518	pass	10,205	–72,53	$8\cdot10^{-10}$	2,4384	pass	2,6315	–4,37	61,525	3,22	pass
V_{sb0}	24,509	–785,3	$1\cdot10^{-223}$	10,705	pass	5,5296	–27,49	$2\cdot10^{-5}$	6,9	pass	6,451	–19,36	0,062	12,971	fail
V_{sb1}	23,061	–559,1	$2\cdot10^{-127}$	29,516	fail	60,265	–1985	$6\cdot10^{-236}$	12,541	pass	$7,27\cdot10^{7}$	$2,71\cdot10^{7}$	$1,8\cdot10^{-6}$	29,51	fail
V_{La0}	20,409	–490,8	$3\cdot10^{-128}$	5,3465	pass	2,0235	–0,447	0,7664	5,0	pass	4,8108	–7,974	0,0998	10,885	pass
V_{La1}	19,56	–300,1	$1\cdot10^{-52}$	9,9285	pass	55,37	–1628	$1\cdot10^{-189}$	6,628	pass	15,135	–37,21	0,0348	12,773	fail
V_{Lb0}	3,936	–13,95	$1,2\cdot10^{-4}$	6,1062	pass	35,524	–1135	$2\cdot10^{-224}$	4,3916	pass	4,0878	–4,537	0,2195	9,6915	pass
V_{Lb1}	35,888	–1013	$4\cdot10^{-175}$	4,0159	pass	53,404	–1760	$6\cdot10^{-238}$	2,812	pass	4,1267	–4,297	0,731	4,6711	pass
$(V_{La}/V_{sa})_0$	0,5598	2,9365	6,028	98,108	fail	1,1351	2,5125	4,2804	5,6784	pass	2,2447	0,0739	1,1808	6,7514	pass
$(V_{La}/V_{sa})_1$	0,5845	2,8055	10,033	2,3175	pass	0,6167	2,8278	10,045	1,9421	pass	0,5339	2,7318	10,047	7,839	pass
$(V_{Lb}/V_{sb})_0$	0,8487	2,7798	7,699	3,0661	pass	0,7934	2,826	7,8837	4,0480	pass	0,98	2,8135	7,2359	5,0016	pass
$(V_{Lb}/V_{sb})_1$	0,7858	2,8143	2,023	11,356	pass	0,753	2,811	11,484	1,3663	pass	0,7623	2,6991	11,593	2,4707	pass

The following results emerge from the analysis of the data in Table 2 – 4.

1. Out of all 39 cases considered by the Pearson Chi-squared consistency criterion, the Weibull distribution passes in 25 cases, Rosin-Rammler in 32 cases, and the log-normal distribution in 30 cases.

2. Out of 18 cases considered for each of the three distributions for samples without screening out «anomalous» values by the Wright criterion, the following pass by the Pearson Chi-squared consistency criterion: the Weibull distribution in 14 cases, Rosin-Rammler in 17 cases, and log-normal in 15 cases.

3. For samples with one iteration of screening out «anomalous» values by the Wright criterion, out of 18 cases considered by the Pearson Chi-squared consistency criterion, the following pass: Weibull distribution in 8 cases, Rosin-Rammler and log-normal in 12 cases. For a sample with two iterations of screening out «anomalous» values according to the Wright criterion to the complete absence of areas with zero values, all distributions pass the Pearson Chi-squared consistency criterion in all cases. But the range of the random variable distribution in this case decreases by more than 6 times, which raises doubts about the feasibility of such screening.

4. The parameters found by the minimum values of the SSD (14) and Chi-squared (15) coincide in 12 cases out of 39. Perhaps this is due to the fact that both functions are built on absolute differences. The parameters found by the minimum values of (16) coincide with those found by other criteria only in 2 cases out of 39. Perhaps this is due to the fact that, unlike functions (14) and (15), function (16) uses relative, not absolute, estimates. Except for one case out of 39, the Chi-squared values for distributions whose parameters were found by the minimum value criterion (15) were less than or equal to the corresponding values for distributions whose parameter values were found by other criteria. This is logical and follows from the essence of the criterion for finding optimal values of distribution parameters by the minimum values of the function (15).

5. The values of the Chi-squared parameter found by the minimum value criterion of the Chi-squared function (15) for the Weibull distribution in samples without screening out «anomalous» values in 5 cases out of 6 were less than the corresponding values for samples with one iteration of screening out «anomalous» values. For the Rosin-Rammler and log-normal distributions, these values were distributed equally: 3 cases each for samples without screening out and with screening out.

6. Of all 13 samples, the Chi-squared values found by the criterion of the minimum value of the Chi-squared function (15) for the Weibull distribution were always greater than the corresponding values for the other distributions considered. The values of this parameter for the Rosin-Rammler and log-normal distributions coincided in 2 cases out of 13. In 7 cases out of 13 for the log-normal distribution, the values of this parameter were smaller than for the Rosin-Rammler distribution. Accordingly, in 4 cases out of 13, the values of this parameter for the Rosin-Rammler distribution were smaller than for the log-normal distribution.

7. For samples without screening out «anomalous» values, smaller values of the Chi-square parameter for the log-normal distribution were observed in 2 cases out of 6. In 2 cases out of 6, the value of this parameter coincided with the values found for the Rosin-Rammler distribution, and in 2 out of 6 cases, these values for the Rosin-Rammler distribution were smaller than the values for the log-normal distribution.

8. For samples with one iteration of screening out «anomalous» values, smaller values of the Chi-squared parameter for the log-normal distribution were observed in 4 cases out of 6, and for the Rosin-Rammler distribution – in 2 of 6. For the sample with two iterations of screening out «anomalous» values, the smallest values of the Chi-squared parameter were found for the log-normal distribution.

Summarizing the results of the above analysis, we note that of all the theoretical distributions considered, the Weibull distribution describes the discrete distributions obtained in practice the worst, and the log-normal one the best. Therefore, for it, the parameter values were also found by the method of statistical moments both from the input data and from the data of discrete distributions (Table 5).

Table 5

Parameters of the log-normal distribution, found by the methods of statistical moments from input data and discrete distributions

Sample	From input data					From discrete distribut.				
	α	μ	k, %	χ_n^2	p/f	α	μ	k, %	χ_n^2	p/f
V_{sa0}	1,433	–1,07	17,6	7,23	p	0,922	0,152	41,5	15,9	f
V_{sa1}	1,279	–1,17	86,6	31,4	f	1,053	–0,62	114	34,2	f
V_{sa2}	1,146	–1,78	222	5,66	p	0,951	–1,39	275	7,68	p
V_{sb0}	1,401	–0,83	17,6	9,51	p	0,917	0,317	38,5	16,9	f
V_{sb1}	1,289	–0,94	70,4	29,0	f	1,053	–0,41	93,0	33,1	f
V_{La0}	1,291	1,592	2,63	7,07	p	0,902	2,439	4,74	14,4	f
V_{La1}	1,146	1,549	9,61	18,2	f	0,956	1,924	11,5	21,6	f
V_{Lb0}	1,283	1,816	2,24	7,76	p	0,911	2,692	3,98	12,9	f
V_{Lb1}	1,151	1,765	7,09	11,1	p	0,959	2,187	8,65	13,3	f
$(V_{La}/V_{sa})_0$	0,848	2,722	5,27	8,92	p	0,829	2,759	5,36	9,07	p
$(V_{La}/V_{sa})_1$	0,628	2,727	10,3	3,84	p	0,607	2,743	10,2	3,41	p
$(V_{Lb}/V_{sb})_0$	0,687	2,756	8,23	6,68	p	0,670	2,768	8,27	7,09	p
$(V_{Lb}/V_{sb})_1$	0,606	2,750	11,9	3,97	p	0,596	2,755	11,9	4,32	p

Analysis of the data in Table 5 allows us to make the following generalizations.

1. In 12 out of 13 cases, the Chi-squared values for log-normal distributions, the parameters of which were found from the input data, were smaller than for similar distributions, the parameters of which were found from the data of discrete distributions. Only in one case the opposite situation was observed.

2. In all 6 cases considered, the log-normal distribution, the parameters of which were found from the input data without screening out «anomalous» values, passes the Pearson Chi-squared consistency criterion. The log-normal distribution, the parameters of which were found by the parameters of discrete distributions without screening out «anomalous» values according to the Pearson Chi-squared criterion, passes in 2 cases out of 6.

3. The log-normal distribution, the parameters of which were found by the input data with screening out «anomalous» values in one iteration passes by the Pearson Chi-squared consistency criterion in 3 out of 6 cases, and by the data of discrete distributions – in 2 cases out of 6.

From the above analysis it follows that for the considered samples the best results are shown by log-normal distributions, the parameters of which were found by the methods of statistical moments from the input data without screening out «anomalous» values.

Methodology for constructing distributions of the volumes of the components of plasma channels. One of the results of the above-described studies and analysis of the obtained data is the method of constructing distributions developed by us, which consists in the following.

1. To approximate the equivalent volumes of spark cores and colored halo of plasma channels, «flattened» ellipsoids of rotation are used.

2. «Anomalous» measurement results are not screened out.

3. To approximate the obtained discrete distributions, a continuous analytical log-normal distribution is used.

4. The parameters of the log-normal distribution are determined by the method of statistical moments according to (10) and (13) based on the input sample data without filtering out «anomalous» measurement results.

5. The hypothesis of the correspondence of theoretical distributions to the discrete distributions obtained in practice is checked using the Pearson Chi-squared consistency criterion.

6. To compare the quality of approximation of discrete distributions obtained in practice by continuous theoretical distributions, a universal dimensionless criterion is used – the average modulus of relative deviations of the values obtained during experiments of discrete and continuous theoretical distributions.

Comparative analysis of the distributions by the sizes of erosion particles and holes on the surface of granules and components of plasma channels. In [48] it is shown that the distribution of the diameters of spark erosion holes on the surface of aluminum granules is best described by the Rosin-Rammler distribution, and the particles obtained from them are best described by the normal distribution. The volume of a hole of average diameter in the hypothesis that it has the shape of a hemisphere is 15 % higher than the volume of a particle of average diameter in the hypothesis that it has the shape of a sphere. That is, the average parameters of erosion particles can be predicted by the average parameters of holes, but their diameter distributions are described by different laws and the maximum diameter of holes can be twice the maximum diameter of particles.

Therefore, the distributions of the volumes of colored halo plasma channels, their spark cores and their ratios are best described by the log-normal law, but can be described by the Rosin-Rammler law. The distribution of the diameters of erosion holes on the surface of the granules is described by the Rosin-Rammler law, and the distribution of the diameters of erosion particles is described by a normal distribution. That is, there is a probability that the correlation between the volumes of the constituent plasma channels and erosion holes on the surface of the granules is stronger than between the volumes of the constituent plasma channels and erosion particles. This suggests that the process of erosion particle formation is more complex than the condensation and solidification of the metal volume of one erosion particle from one erosion hole [53]. However, additional studies are needed to verify this.

Generalization and conclusions.

1. In the process of determining the volumes of spark cores and colored halo of plasma channels, they can be approximated with sufficient accuracy for statistical studies by ellipsoids of rotation. Judging by the quality of approximation by theoretical distributions of their size distributions obtained as a result of experiments in the hypotheses of «elongated» and «flattened» ellipsoids in the studied regimes, the probability of the appearance of «flattened» ellipsoids is higher than «elongated».

2. The distributions of the volumes of the components of the plasma channels and their ratios obtained as a result of measurements have a similar appearance and can be approximated by one theoretical distribution with different parameter values. Of all the theoretical distributions considered (Weibull, Rosin-Rammler and log-normal), the best approximation of the discrete distributions obtained as a result of measurements is provided by the log-normal, and the worst by Weibull.

3. Screening out «anomalous» measurement results according to the Wright criterion in the considered cases not only significantly narrows the range of distributions of random variables (more than 2 times with one iteration of screening and more than 6 times with two iterations), but also in the vast majority of cases leads to a deterioration in the quality of approximation of the discrete distributions obtained in practice by continuous theoretical distributions according to the Pearson Chi-squared consistency criterion. Therefore, in the considered conditions, it is impractical.

4. In most cases, the method of searching for optimal values of the parameters of the theoretical laws of distributions of random variables by the smallest deviation of theoretical values from the experimental results gives smaller Chi-squared values than the method of statistical moments. But the values of the distribution parameters found by the first method are not the only possible solution and do not always correspond to the physically determined ranges due to the redundancy of the systems of equations that are solved to find them.

5. Among all the considered optimization functions, the minimum values of which were used to find the optimal values of the parameters of the theoretical laws of the distribution of random variables by the method of the least deviations of theoretical values from the experimental results, the smallest values of the Chi squared are expected to be provided by the function based on the Pearson Chi squared consistency criterion.

6. The universality of the criterion for the quality of the approximation of distributions among all the considered functions is provided only by the average modulus of the relative deviations of the values of the discrete and continuous theoretical distributions obtained during the experiments, since it does not depend on either the number of intervals of the discrete distributions or the absolute values of the random variables.

7. The search for the values of the parameters of the theoretical laws of distributions of random variables by the statistical moments of the samples is more accurate than by the statistical moments of discrete distributions. The method of statistical moments ensures the uniqueness of the results and their correspondence to the physically determined ranges. In the case of consistency between the distributions obtained in practice and the theoretical one by the Pearson Chi squared criterion, the method of statistical moments ensures the finding of satisfactory values of the parameters of the theoretical distributions.

8. A method for constructing the volume distributions of the components of plasma channels has been developed, adapted specifically for such objects.

Acknowledgment. The work was carried out with the support of the Ministry of Education and Science of Ukraine (Project DB No. 0121U107443).

Conflict of interest. The authors of the article declare that there is no conflict of interest.

REFERENCES

1. Gilchuk A., Monastyrsky G. «Core–shell» nanoparticles produced from Ti-Ni-Hf and Ti-Ni-Zr alloys by spark erosion method. *Applied Nanoscience*, 2023, vol. 13, no. 11, pp. 7145-7154. doi: https://doi.org/10.1007/s13204-023-02864-9.

2. Jin C.H., Si P.Z., Xiao X.F., Feng H., Wu Q., Ge H.L., Zhong M. Structure and magnetic properties of Cr/Cr2O3/CrO2 microspheres prepared by spark erosion and oxidation under high pressure of oxygen. *Materials Letters*, 2013. vol. 92, pp. 213-215. doi: https://doi.org/10.1016/j.matlet.2012.10.126.

3. Berkowitz A.E., Hansen M.F., Parker F.T., Vecchio K.S., Spada F.E., Lavernia E.J., Rodriguez R. Amorphous soft magnetic particles produced by spark erosion. *Journal of Magnetism and Magnetic Materials*, 2003, vol. 254-255, pp. 1-6. doi: https://doi.org/10.1016/S0304-8853(02)00932-0.

4. Aur S., Egami T., Berkowitz A.E., Walter J.L. Atomic Structure of Amorphous Particles Produced by Spark Erosion. *Physical Review B*, 1982, vol. 26, no. 12, pp. 6355-6361. doi: https://doi.org/10.1103/PhysRevB.26.6355.

5. Hong J.I., Parker F.T., Solomon V.C., Madras P., Smith D.J., Berkowitz A.E. Fabrication of spherical particles with mixed amorphous/crystalline nanostructured cores and insulating oxide shells. *Journal of Materials Research*, 2008, vol. 23, no. 06, pp. 1758-1763. doi: https://doi.org/10.1557/JMR.2008.0199.

6. Perekos A.E., Chernenko V.A., Bunyaev S.A., Zalutskiy V.P., Ruzhitskaya T.V., Boitsov O.F., Kakazei G.N. Structure and magnetic properties of highly dispersed Ni-Mn-Ga powders prepared by spark-erosion. *Journal of Applied Physics*, 2012, vol. 112, no. 9. art. no. 093909. doi: https://doi.org/10.1063/1.4764017.

7. Harrington T., McElfresh C., Vecchio K.S. Spark erosion as a high-throughput method for producing bimodal nanostructured 316L stainless steel powder, *Powder Technology,* 2018, vol. 328, pp. 156–166. doi: https://doi.org/10.1016/j.powtec.2018.01.012.

8. Wang W., Zhu F., Weng J., Xiao J., Lai W. Nanoparticle morphology in a granular Cu–Co alloy with giant magnetoresistance, *Applied Physics Letters*, 1998, vol. 72, no 9, pp. 1118–1120. doi: https://doi.org/10.1063/1.120942.

9. Berkowitz A.E., Walter J.L. Spark Erosion: A Method for Producing Rapidly Quenched Fine Powders, *Journal of Materials Research*. 1987, no 2. pp. 277–288. doi: https://doi.org/10.1557/JMR.1987.0277.

10. Shen B., Inoue A. Fabrication of large-size Fe-based glassy cores with good soft magnetic properties by spark plasma sintering*, Journal of Materials Research,* 2003, vol. 18, no 9, pp. 2115–2121. doi: https://doi.org/10.1557/jmr.2003.0297.

11. Youssef F.S., El-Banna H.A., Elzorba H.Y., Gabal A.M. Application of Some Nanoparticles in the Field of Veterinary Medicine, *International Journal of Veterinary Science and Medicine*, 2019, vol. 7, no 1. pp. 78-93. doi: https://doi.org/10.1080/23144599.2019.1691379.

12. Batsmanova L., Taran N., Konotop Ye., Kalenska S., Novytska N. Use of a Colloidal Solutions of Metal and Metal Oxide-Containing Nanoparticles as Fertilizer for Increasing Soybean Productivity, *Journal of Central European Agriculture*, 2020, no 2 (21), pp. 311–319. doi: https://doi.org/10.5513/JCEA01/21.2.2414.

13. Petrov O., Petrichenko S., Yushchishina A., Mitryasova O., Pohrebennyk V. Electrospark Method in Galvanic Wastewater Treatment for Heavy Metal Removal. *Applied Sciences*, 2020, vol. 10, no. 15, art. no. 5148. doi: https://doi.org/10.3390/app10155148.

14. Goncharuk V.V., Shcherba A.A., Zakharchenko S.N., Savluk O.S., Potapchenko N.G., Kosinova V.N. Disinfectant action of the volume electrospark discharges in water. *Khimiia i tehnologiia vody*, 1999, vol. 21, no. 3, pp. 328-336. (Rus).

15. Shydlovska N.A., Zakharchenko S.M., Zakharchenko M.F., Mazurenko I.L., Kulida M.A. Physical and Technical-economic Aspects of Modern Methods of Water Treatment for Thermal and Nuclear Power Engineering. *Technical Electrodynamics*, 2022, no. 4, pp. 69-77. (Ukr). doi: https://doi.org/10.15407/techned2022.04.069.

16. Zakharchenko S.N., Kondratenko I.P., Perekos A.E., Zalutsky V.P., Kozyrsky V.V., Lopatko K.G. Influence of discharge pulses duration in a layer of iron granules on the size and structurally-phase conditions of its electroerosion particles. *Eastern-European Journal of Enterprise Technologies*, 2012. vol. 6, no. 5 (60), pp. 66-72. (Rus).
17. Shydlovska N.A., Zakharchenko S.M., Cherkaskyi O.P. Physical Prerequisites of Construction of Mathematical Models of Electric Resistance of Plasma-erosive Loads. *Technical Electrodynamics*, 2017, no 2, pp. 5-12. (Ukr) doi: https://doi.org/10.15407/techned2017.02.005.
18. Shydlovska N.A., Zakharchenko S.M., Cherkassky O.P. The Analysis of Electromagnetic Processes in Output Circuit of the Generator of Discharge Pulses with Non-linear Model of Plasma-erosive Load at Change Their Parameters in Wide Ranges. *Technical Electrodynamics*, 2016, no. 1. pp. 87-95. (Rus). doi: https://doi.org/10.15407/techned2016.01.087.
19. Shydlovska N.A., Zakharchenko S.M., Cherkaskyi O.P. Parametric model of resistance of plasma-erosive load, adequate in the wide range of change of applied voltage. *Technical Electrodynamics*, 2017, no 3, pp. 3-12. (Ukr) doi: https://doi.org/10.15407/techned2017.03.003.
20. Shydlovskaya N.A., Zakharchenko S.N., Cherkasskyi A.P. Nonlinear-parametrical model of electrical resistance of current-carrying granulated mediums for a wide range of applied voltage. *Technical Electrodynamics*, 2014, no 6, pp. 3-17. (Rus).
21. Zakharchenko S.M., Perekos A.O., Shydlovska N.A., Ustinov A.I., Boytsov O.F., Voynash V.Z. Electrospark Dispersion of Metal Materials. I. Influence of Velocity of Flow of Operating Fluid on Dispersity of Powders. *Metallofizika i Noveishie Tekhnologii*, 2018, vol. 40, no. 3, pp. 339-357 (Rus). doi: https://doi.org/10.15407/mfint.40.03.0339.
22. Carrey J., Radousky H.B., Berkowitz A.E. Spark-eroded particles: influence of processing parameters. *Journal of Applied Physics*, 2004, vol. 95, no. 3, pp. 823-829. doi: https://doi.org/10.1063/1.1635973.
23. Suprunovska N.I., Shcherba M.A., Roziskulov S.S., Synytsyn V.K. Improving the dynamic characteristics of electric discharge installations, which are significantly distant from the spark-erosion load. *Technical Electrodynamics*, 2022, no 3, pp. 16-21. doi: https://doi.org/10.15407/techned2022.03.016.
24. Kornev I., Saprykin F., Lobanova G., Ushakov V., Preis S. Spark erosion in a metal spheres bed: Experimental study of the discharge stability and energy efficiency. *Journal of Electrostatics*, 2018, vol. 96, pp. 111-118. doi: https://doi.org/10.1016/j.elstat.2018.10.008.
25. Gnedenko B.V. *Theory of Probability*. London, Routledge, 1998. 520 p. doi: https://doi.org/10.1201/9780203718964.
26. Shydlovska N.A., Zakharchenko S.M., Zakharchenko M.F., Kulida M.A., Zakusilo S.A. Spectral and optic-metric methods of monitoring parameters of plasma channels caused by discharge currents between metals granules in working liquids. *Electrical Engineering & Electromechanics*, 2024, no. 6, pp. 72-83. doi: https://doi.org/10.20998/2074-272X.2024.6.10.
27. Kim C.J. Electromagnetic Radiation Behavior of Low-Voltage Arcing Fault. *IEEE Transactions on Power Delivery*, 2009, vol. 24, no. 1, pp. 416-423. doi: https://doi.org/10.1109/TPWRD.2008.2002873.
28. Kozioł M., Nagi Ł., Kunicki M., Urbaniec I. Radiation in the Optical and UHF Range Emitted by Partial Discharges. *Energies*, 2019, vol. 12, no. 22, art. no. 4334. doi: https://doi.org/10.3390/en12224334.
29. Kozioł M. Energy Distribution of Optical Radiation Emitted by Electrical Discharges in Insulating Liquids. *Energies*, 2020, vol. 13, no. 9, art. no. 2172. doi: https://doi.org/10.3390/en13092172.
30. Kohut A., Ludvigsson L., Meuller B.O., Deppert K., Messing M.E., Galbács G., Geretovszky Z. From plasma to nanoparticles: optical and particle emission of a spark discharge generator. *Nanotechnology*, 2017, vol. 28, no. 47, art. no. 475603. doi: https://doi.org/10.1088/1361-6528/aa8f84.
31. Korytchenko K.V., Essmann S., Markus D., Maas U., Poklonskii E.V. Numerical and Experimental Investigation of the Channel Expansion of a Low-Energy Spark in the Air. *Combustion Science and Technology*, 2019, vol. 191, no. 12, pp. 2136-2161. doi: https://doi.org/10.1080/00102202.2018.1548441.
32. Lo A., Cessou A., Lacour C., Lecordier B., Boubert P., Xu D., Laux C.O., Vervisch P. Streamer-to-spark transition initiated by a nanosecond overvoltage pulsed discharge in air. *Plasma Sources Science and Technology*, 2017, vol. 26, no. 4. art. no. 045012. doi: https://doi.org/10.1088/1361-6595/aa5c78.
33. Mylnikov D., Efimov A., Ivanov V. Measuring and optimization of energy transfer to the interelectrode gaps during the synthesis of nanoparticles in a spark discharge. *Aerosol Science and Technology*, 2019, vol. 53, no. 12, pp. 1393-1403. doi: https://doi.org/10.1080/02786826.2019.1665165.
34. Raizer Yu.P. *Gas Discharge Physics*. Berlin, Springer, 1991. 449 p.
35. Baranov M.I. A generalized physical principle of development of plasma channel of a high-voltage pulse spark discharge in a dielectric. *Electrical Engineering & Electromechanics*, 2024, no. 1, pp. 34-42. doi: https://doi.org/10.20998/2074-272X.2024.1.05.
36. Korytchenko K.V., Shypul O.V., Samoilenko D., Varshamova I.S., Lisniak A.A., Harbuz S.V., Ostapov K.M. Numerical simulation of gap length influence on energy deposition in spark discharge. *Electrical Engineering & Electromechanics*, 2021, no. 1, pp. 35-43. doi: https://doi.org/10.20998/2074-272X.2021.1.06.
37. *ToupTek. Download*. Available at: https://www.touptekphotonics.com/download/ (Accessed: 28 June 2024).
38. Mishra P., Pandey C., Singh U., Gupta A., Sahu C., Keshri A. Descriptive statistics and normality tests for statistical data. *Annals of Cardiac Anaesthesia*, 2019, vol. 22, no. 1, pp. 67-72. doi: https://doi.org/10.4103/aca.ACA_157_18.
39. Arya R., Antonisamy B., Kumar S. Sample Size Estimation in Prevalence Studies. *The Indian Journal of Pediatrics*, 2012, vol. 79, no. 11, pp. 1482-1488. doi: https://doi.org/10.1007/s12098-012-0763-3.
40. Akagawa S., Odagaki T. Geometrical percolation of hard-core ellipsoids of revolution in the continuum. *Physical Review E*, 2007, vol. 76, no. 5, art. no. 051402. doi: https://doi.org/10.1103/PhysRevE.76.051402.
41. Menzies N.A. An Efficient Estimator for the Expected Value of Sample Information. *Medical Decision Making*, 2016, vol. 36, no. 3, pp. 308-320. doi: https://doi.org/10.1177/0272989X15583495.
42. Wu Z., Yang X., Tu J., Chen X. Optimal consistency and consensus models for interval additive preference relations: A discrete distribution perspective. *Journal of the Operational Research Society*, 2020, vol. 71, no. 9, pp. 1479-1497. doi: https://doi.org/10.1080/01605682.2019.1621219.
43. Burshtynska H.V., Yidunov A.V. The study of various statistical criteria in the processing of false points in the process of determining the elements of mutual orientation. *Geodesy, Cartography and Aerial Photography*, 1984, no. 39, pp. 114-118. (Rus).
44. Adikaram K.K.L.B., Hussein M.A., Effenberger M., Becker T. Data Transformation Technique to Improve the Outlier Detection Power of Grubbs' Test for Data Expected to Follow Linear Relation. *Journal of Applied Mathematics*, 2015, vol. 2015, art. no. 708948. doi: https://doi.org/10.1155/2015/708948.
45. Zhao Y., Lehman B., Ball R., Mosesian J., de Palma J.-F. Outlier detection rules for fault detection in solar photovoltaic arrays. *2013 Twenty-Eighth Annual IEEE Applied Power*

Electronics Conference and Exposition (APEC), 2013, pp. 2913-2920. doi: https://doi.org/10.1109/APEC.2013.6520712.
46. Barbato G., Barini E.M., Genta G., Levi R. Features and performance of some outlier detection methods. *Journal of Applied Statistics*, 2011, vol. 38, no. 10, pp. 2133-2149. doi: https://doi.org/10.1080/02664763.2010.545119.
47. Ventzel E.S. *Theory of Probability*. Moscow, Nauka Publ., 1969. 576 p. (Rus).
48. Shidlovska N.A., Zakharchenko S.M., Perekos A.O. Peculiarities of the diameter distributions obtained at submilisecond duration of discharge pulses spark-erosive aluminum particles and caverns on the surface of its granules. *Technical Electrodynamics*, 2021, no. 1, pp. 10-22. (Ukr). doi: https://doi.org/10.15407/techned2021.01.010.
49. Mitzenmacher M. A brief history of generative models for power law and lognormal distributions. *Internet Mathematics*, 2004, vol. 1, no. 2, pp. 226-251. doi: https://doi.org/10.1080/15427951.2004.10129088.
50. Cuff V., Lewis A., Miller S.J. The Weibull distribution and Benford's law. *Involve, a Journal of Mathematics*, 2015, vol. 8, no. 5, pp. 859-874. doi: https://doi.org/10.2140/involve.2015.8.859.
51. Kumar R., Gopireddy S.R., Jana A.K., Patel C.M. Study of the discharge behavior of Rosin-Rammler particle-size distributions from hopper by discrete element method: A systematic analysis of mass flow rate, segregation and velocity profiles. *Powder Technology*, 2020, vol. 360, pp. 818-834. doi: https://doi.org/10.1016/j.powtec.2019.09.044.
52. Franke T.M., Ho T., Christie C.A. The Chi-Square Test: Often Used and More Often Misinterpreted. *American Journal of Evaluation*, 2012, vol. 33, no. 3, pp. 448-458. doi: https://doi.org/10.1177/1098214011426594.
53. Kucheriava I.M. Multiphysics processes at spark erosion treatment of conducting granules. *Technical Electrodynamics*, 2017, no. 5, pp. 32-38. (Rus). doi: https://doi.org/10.15407/techned2017.05.032.

Received 03.07.2024
Accepted 20.08.2024
Published 02.01.2025

N.A. Shydlovska[1], *Corresponding Member of NAS of Ukraine, Doctor of Technical Science, Chief Research Scientist,*
S.M. Zakharchenko[1], *Doctor of Technical Science, Leading Research Scientist,*
M.F. Zakharchenko[2], *Candidate of Chemical Sciences,*
M.A. Kulida[3], *Candidate of Veterinary Sciences,*
S.A. Zakusilo[1], *Postgraduate Student,*
R.A. Yakovenko[1], *Postgraduate Student,*
[1] Institute of Electrodynamics
of the National Academy of Sciences of Ukraine,
56, Prospect Beresteiskyi, Kyiv, 03057, Ukraine,
e-mail: snzakhar@ukr.net (Corresponding Author)
[2] V.I. Vernadsky Institute of General and Inorganic Chemistry
of the National Academy of Sciences of Ukraine,
32/34, Prospect Palladina, Kyiv, 03142, Ukraine.
[3] National University of Life and Environmental Sciences of Ukraine,
16, Vystavkova Str., Kyiv, 03041, Ukraine.

How to cite this article:
Shydlovska N.A., Zakharchenko S.M., Zakharchenko M.F., Kulida M.A., Zakusilo S.A., Yakovenko R.A. Distribution of volumes of plasma channels components between metal granules in working liquids. *Electrical Engineering & Electromechanics*, 2025, no. 1, pp. 73-85. doi: https://doi.org/10.20998/2074-272X.2025.1.10

Матеріали приймаються за адресою:
Кафедра "Електричні апарати", НТУ "ХПІ", вул. Кирпичева, 2, м. Харків, 61002, Україна
Електронні варіанти матеріалів по e-mail: a.m.grechko@gmail.com

Довідки за телефонами: +38 067 359 46 96 Гречко Олександр Михайлович

Передплатний індекс: 01216